

INFORMATION TO USERS

This manuscript has been reproduced from the microfilm master. UMI films the text directly from the original or copy submitted. Thus, some thesis and dissertation copies are in typewriter face, while others may be from any type of computer printer.

The quality of this reproduction is dependent upon the quality of the copy submitted. Broken or indistinct print, colored or poor quality illustrations and photographs, print bleedthrough, substandard margins, and improper alignment can adversely affect reproduction.

In the unlikely event that the author did not send UMI a complete manuscript and there are missing pages, these will be noted. Also, if unauthorized copyright material had to be removed, a note will indicate the deletion.

Oversize materials (e.g., maps, drawings, charts) are reproduced by sectioning the original, beginning at the upper left-hand corner and continuing from left to right in equal sections with small overlaps.

ProQuest Information and Learning
300 North Zeeb Road, Ann Arbor, MI 48106-1346 USA
800-521-0600

UMI[®]

University of Alberta

**MANUFACTURING AND JOINING TECHNOLOGY OF
FIBRE-REINFORCED COMPOSITE MATERIALS FOR
TUBULAR COMPONENTS UNDER
BIAXIAL LOADING CONDITIONS**

by

Pierre Mertiny



A thesis submitted to the Faculty of Graduate Studies and Research
in partial fulfilment of the requirements for the degree
of Doctor of Philosophy

Department of Mechanical Engineering

Edmonton, Alberta

Spring 2005



Library and
Archives Canada

Bibliothèque et
Archives Canada

0-494-08273-9

Published Heritage
Branch

Direction du
Patrimoine de l'édition

395 Wellington Street
Ottawa ON K1A 0N4
Canada

395, rue Wellington
Ottawa ON K1A 0N4
Canada

Your file *Votre référence*

ISBN:

Our file *Notre référence*

ISBN:

NOTICE:

The author has granted a non-exclusive license allowing Library and Archives Canada to reproduce, publish, archive, preserve, conserve, communicate to the public by telecommunication or on the Internet, loan, distribute and sell theses worldwide, for commercial or non-commercial purposes, in microform, paper, electronic and/or any other formats.

The author retains copyright ownership and moral rights in this thesis. Neither the thesis nor substantial extracts from it may be printed or otherwise reproduced without the author's permission.

AVIS:

L'auteur a accordé une licence non exclusive permettant à la Bibliothèque et Archives Canada de reproduire, publier, archiver, sauvegarder, conserver, transmettre au public par télécommunication ou par l'Internet, prêter, distribuer et vendre des thèses partout dans le monde, à des fins commerciales ou autres, sur support microforme, papier, électronique et/ou autres formats.

L'auteur conserve la propriété du droit d'auteur et des droits moraux qui protègent cette thèse. Ni la thèse ni des extraits substantiels de celle-ci ne doivent être imprimés ou autrement reproduits sans son autorisation.

In compliance with the Canadian Privacy Act some supporting forms may have been removed from this thesis.

Conformément à la loi canadienne sur la protection de la vie privée, quelques formulaires secondaires ont été enlevés de cette thèse.

While these forms may be included in the document page count, their removal does not represent any loss of content from the thesis.

Bien que ces formulaires aient inclus dans la pagination, il n'y aura aucun contenu manquant.


Canada

ABSTRACT

Pressure-retaining tubular structures (e.g. pipes) could be advantageously produced from fibre-reinforced polymeric composites (FRPC). Due to favourable properties, e.g. material anisotropy and corrosion resistance, these structures frequently outperform traditional metallic components. The axisymmetric shape is suited for the efficient filament winding process, which facilitates automated and continuous production. Improvements in performance and economy may thus be realised. Despite these advantages a limited understanding of damage behaviour, deficient design methodologies, and a lack of economical joining techniques have hampered an extensive utilisation of FRPC in high-pressure applications.

A favourable design for all-composite piping ought to possess the following characteristics: (a) The pipe body possesses adequate strengths under biaxial loadings associated with installation and in-service conditions; (b) the structure exhibits leak-before-burst failure (i.e. fail-safe design); and (c) joining of pipe sections is field-friendly and economical. The current study investigates the feasibility of such structures. A unique approach encompassing the design, manufacturing and joining was employed. Firstly, the manufacturing process was studied to identify efficient winding conditions (such as fibre tensioning) for optimal pipe performance. Secondly, different fibre architectures were analysed with regards to strength and damage behaviour. Finally, a unique yet simple adhesive bonding technique was employed for the integration of subcomponents. Due to the lack of suitable criteria for leakage prediction (i.e. the predominant failure mode), here the emphasis is on experimental investigations under

monotonic loading conditions. Glass-fibre and thermoset resin were utilised to fabricate small-scale model as well as large-scale prototype specimens. Using an innovative permeability-based method and conventional strength-of-material approaches an investigation on specimen scaling/size effects was conducted. Experiments were complemented using analytical methods for the determination of material and structural properties (e.g. pipe wall thickness); the joint geometry was optimised using finite element techniques.

Best overall prototype performance was achieved for a multi-angle lay-up with exterior filaments inclined to provide axial reinforcement. Namely, a $[\pm 60_3, \pm 30]_T$ fibre architecture exhibited superior strengths under the applied loadings. Favourable winding conditions were identified producing intermediate fibre volume fractions (~60%) and low void contents (~1%). In conjunction with bonded overlap sleeve joints, which were employed for their field-friendliness and cost-effectiveness, prototype structures were able to satisfy the aforementioned design requirements.

ACKNOWLEDGEMENTS

The author wishes to extend his gratitude to his supervisor, Dr. Fernand Ellyin. Throughout the work culminating with this research report his guidance and role as a mentor on an academic as well as a personal level are highly appreciated. Further, the author wishes to express his thankfulness to Dr. Zihui Xia, who offered support, advice and encouragement on numerous occasions.

The author is thankful for the financial support provided by Dr. Ellyin and the following scholarship award programs: Luscar Graduate Scholarship in Environmental Engineering, Dissertation Fellowship at the University of Alberta, RR Gilpin Memorial Scholarship in Mechanical Engineering, Alan Wharmby Memorial Graduate Award in Mechanical Engineering, and GULF Canada Resources Ltd. Graduate Scholarship in Hydrocarbon Development.

For continuously providing inspiration, the opportunity for personal development, and for opening new horizons, gratitude is extended to the Airbus Deutschland company and their doctoral scholarship program.

It was a pleasure to meet the members of the Advanced Composite Materials Engineering Group, who joined or left the group during the last few years. Their company, which fostered new insights and the progress of research, was very enjoyable on a friendship as well as intellectual level.

The author wishes to acknowledge contributions made by several other individuals. The help and technical expertise of the technical staff of the Mechanical Engineering Department's machine shop, in particularly that of Bernie Faulker, were of significant importance for the completion of this research. Following the author's invitation of a research internship several students from the University of Hannover (Germany) also supported this research. Namely, the author wishes to express his gratitude to Arne Hothan and Bartek Zielniewicz for their help during the experimental work, and to Hubertus Eilers and Thilo Mahrenbach for their help developing the control logic and the bending device of the prototype testing apparatus respectively.

Last but not least, the author would like to thank his family and friends, here in Canada and overseas in Germany, for offering invaluable support beyond academics. Most importantly, the author is grateful for his wife without whom this endeavour never would have been undertaken. Her support and love make every day a special day.

TABLE OF CONTENTS

Chapter 1. Introduction	1
1.1 Background of Current Study	1
1.2 Introduction to Composite Materials	3
1.2.1 Fibre-Reinforced Polymeric Materials for Filament Winding	3
1.2.2 Damage Development in Fibre Composite Materials	4
1.2.3 Environmental Effects on Composite Materials	10
1.3 Review of Filament-Wound Pressure-Retaining Structures	11
1.4 Overview of the Current Research Work	14
1.4.1 Design Objectives for All-Composite Pipe Structures	14
1.4.2 Scope and Significance of Current Research Work	15
1.4.3 Outline of the Current Report	15
Chapter 2. Manufacturing of Composite Tubular Structures	17
2.1 Introduction to Filament Winding	17
2.2 Physical Properties of Filament Wound Composites	21
2.2.1 Fibre Volume Fraction	21
2.2.2 Void Content	25
2.2.3 Degree of Winding Band Interweaving	28
2.2.4 Engineering Elastic Constants	31
2.2.5 Specimen Wall Thickness	36
2.2.6 On the Effect of Using Average Laminate Properties	39
2.3 Composite Material System	43
2.4 Processing Parameters in Filament Winding	46
2.4.1 Introduction to Filament Winding Process Parameters	46
2.4.2 Effect of Process Parameters on Winding Bandwidth	50
2.4.3 Effect of Process Parameters on Fibre Compaction	52
Chapter 3. Experimental Procedures	55
3.1 Specimen Design Considerations	55

TABLE OF CONTENTS

3.2	Testing Facilities	56
3.2.1	Small-Scale Testing Apparatus	56
3.2.2	Model-Scale Specimen Design and Assembly	57
3.2.3	Prototype-Scale Testing Apparatus	61
3.2.4	Prototype-Scale Specimen Design and Assembly	62
3.3	Detection and Quantification of Specimen Failure	65
3.3.1	Specimen Failure Events	65
3.3.2	Specimen Failure Criteria	65
3.3.3	Fluid Permeability Criterion	68
3.4	Testing of Model-Scale Specimens for Structural Failure	70
3.5	Loading Considerations	71
3.5.1	Biaxial Tensile Loading Spectrum	71
3.5.2	Compilation of Failure Strengths into Biaxial Failure Envelopes	73
3.5.3	Specimen Loading Rates	75
Chapter 4. Performance Investigation of Composite Tubular Structures		77
4.1	Experimental Verification of Elastic Constants	77
4.2	Effect of Filament Winding Tension	80
4.2.1	Experimental Results	80
4.2.2	Analysis of the Experimental Observations	86
4.2.3	Implication for the Design of Tubular Components	90
4.3	Effect of Multi-Angle Filament Winding	91
4.3.1	Experimental Results	92
4.3.2	Analysis of the Experimental Observations	94
4.3.3	Implication for the Design of Tubular Components	102
4.4	Lay-Up Stacking Sequence Effects	102
4.4.1	Experimental Results	104
4.4.2	Analysis of the Experimental Observations	108
4.4.3	Analytical Damage Progression Analysis	110
4.4.4	Implication for the Design of Tubular Components	116

TABLE OF CONTENTS

4.5	Model-Prototype Scaling and Size-Effects	117
4.5.1	Experimental Results	119
4.5.2	Analysis of the Experimental Observations	119
4.5.3	Implication for the Design of Tubular Components	128
Chapter 5.	Integration of Tubular Sub-Components	129
5.1	Review of Joints in Tubular Composite Structures	130
5.2	Design Objectives for Composite Tubular Joints	135
5.3	Review of Adhesive Bonding	136
5.3.1	Surface Preparation Techniques and Bonding Mechanisms	136
5.3.2	Failure Mechanisms in Adhesive Joints	137
5.4	Description of Current Joining Methodology	141
5.4.1	Earlier Research Work Pertaining to Current Joining Process	141
5.4.2	Description of Current Joint Configuration	141
5.5	Experimental Investigation of Joint Prototype Pipe	147
5.6	Modelling of Adhesively Bonded Composite Joints	153
5.6.1	Statement of Problem	153
5.6.2	Review of Modelling Techniques for Adhesively Bonded Joints	154
5.6.3	Fracture Analysis Using the Virtual Crack Closure Method	158
5.7	Parametric Study for Joint Design Optimisation	162
5.7.1	Description of Current Numerical Model	162
5.7.2	Validation of Current Numerical Model	167
5.7.3	Parametric Study	175
5.8	Advanced Fabrication Technique for Improved Joint Performance	186
Chapter 6.	Conclusions	189
Chapter 7.	Bibliography.....	193
Appendix A:	<i>Filament Winding Facility.....</i>	214
<i>A.1</i>	<i>Facility Overview</i>	214

TABLE OF CONTENTS

A.2	<i>Description of Customised Components</i>	216
A.2.1	<i>Fibre Tensioning System</i>	216
A.2.2	<i>Resin Bath</i>	222
A.2.3	<i>Mandrel System and Curing</i>	223
Appendix B: Bandwidth Measurement Techniques.....		225
B.1	<i>Bandwidth Measurement using Tracer Threads</i>	225
B.2	<i>Bandwidth Measurement using Image Analysis</i>	226
B.3	<i>Comparison of Bandwidth Measurement Routines</i>	229
Appendix C: Prototype-Scale Testing Apparatus.....		232
C.1	<i>Design Requirements</i>	232
C.2	<i>Apparatus Description</i>	233
C.2.1	<i>Structural Components</i>	233
C.2.2	<i>Components for Load Application</i>	235
C.2.3	<i>Components for System Control and Data Acquisition</i>	238
C.3	<i>Design of Controller Logic</i>	240
Appendix D: Experimental Biaxial Stress Data.....		244
Appendix E: VCCT: Derivation and Example Calculation		247
E.1	<i>Example Derivation of VCCT for Mode I SERR</i>	247
E.2	<i>Calculation of Parabolic Displacement Interpolation Function</i>	251
Appendix F: ANSYS Batch Files.....		253
F.1	<i>Stress Analysis Model</i>	253
F.2	<i>Fracture Analysis Model</i>	263

LIST OF TABLES

2.3.1	Single filament mechanical properties of applied glass material as supplied by the manufacturer (Owens Corning, 1998).....	44
2.3.2	Properties of neat polymer castings of EPON 826/EPI-CURE 9551 epoxy polymer system as supplied by the manufacturer (Resolution Performance, 2001).....	46
2.4.1	List of filament winding process parameters examined in the present study.....	49
3.2.1	Typical properties of 3M DP-460 epoxy adhesive as supplied by the manufacturer (3M, 2002).....	60
3.2.2	Average fibre volume fraction and wall thickness for all types of produced tubular structures.....	64
3.5.1	Description of biaxial stress ratios.....	73
3.5.2	Test matrix summary of applied stress ratios.	74
3.5.3	Specimen average loading rates in terms of von Mises equivalent stress, in kPa/s.....	76
4.1.1	Average values of elastic constants from measurement and analytical analysis of the $[\pm 60_3]_T$, $[\pm 45, \pm 60_2]_T$ and $[\pm 30, \pm 60_2]_T$ lay-ups (Mertiny et al., 2004a).	78
4.1.2	Elastic properties of fibre and matrix material (Mertiny and Ellyin, 2004b).	78
4.3.1	Summary of structural failure modes correlating lay-up and loading configurations (Mertiny et al., 2004a).	95
4.4.1	Elastic properties from constituents of $[\pm 45, \pm 60_2]_T$ lay-up (Mertiny et al., 2004b).	112
4.4.2	Elastic properties from constituents of $[\pm 60_2, \pm 45]_T$ lay-up (Mertiny et al., 2004b).	113
4.5.1	Experimental pressures and stresses at failure.....	120
4.5.2	Pi-terms for the geometry and possible damage parameters.	127
5.1.1	Examples of mechanically fastened joints for connecting composite pipe.	131
5.7.1	Geometry parameters for baseline finite element model.....	163
5.7.2	Material data used in the finite element modelling of prototype specimens.....	167

LIST OF FIGURES

2.1.1	Developed view of the mandrel surface, and geometry of nominal winding band.	19
2.1.2	Schematic of a winding process for a three-circuits interwoven $\pm\theta$ cover.....	20
2.2.1	Close-packed uniaxial bundles of fibres with a fibre arrangement in square (left) and hexagonal (right) arrays.....	22
2.2.2	Reduction of ultimate transverse strain with increasing fibre volume fraction based on a glass-fibre/epoxy material system used in the current study.....	23
2.2.3	Photomicrograph of a partial cross-section of a filament-wound specimen showing the resin coat on the outside surface of a specimen.	24
2.2.4	Micrographs showing voids (dark areas) in a filament-wound specimen.	27
2.2.5	SEM micrograph magnification of a void in a filament-wound specimen.....	28
2.2.6	Filament winding unit cell (left) with sub-areas, and single sub-area with dimensions (right).	30
2.2.7	Elastic properties and associated loadings of a transversely isotropic unidirectional lamina under plane-stress conditions.....	33
2.2.8	Additional elastic properties for out-of-plane loading conditions.	34
2.2.9	Dimensions of an idealised rectangular winding band cross-section (left); and developed view of the mandrel surface, and geometry of winding bands (right).....	38
2.2.10	Schematic of laminated (top) and fully interwoven (bottom) cross-ply cover.	39
2.2.11	Interdependence of fibre volume fractions for a two-ply unidirectional laminate with an average fibre volume fraction of 70%.....	41
2.2.12	Difference of elastic constants based on (a) individual ply fibre volume fractions and (b) an average laminate value of 70% for a two-ply UD-laminate.....	42
2.3.1	Temperature schedule for the curing of filament-wound glass-fibre/epoxy components.	46
2.4.1	Influence of tow tension of average winding bandwidth. Tracer thread and image analysis measurement techniques were employed.....	51

LIST OF FIGURES

2.4.2	Relative change in winding bandwidth from 26.7 N to 44.5 N tow tension. Tracer thread and image analysis measurement techniques were employed.....	51
2.4.3	Influence of tow tension on average fibre volume fraction measured on specimens produced with 26.7 N and 44.5 N tow tension.....	52
2.4.4	Influence of relative tow weight on average fibre volume fraction measured on specimens produced with 26.7 N and 44.5 N tow tension.	54
3.2.1	Small-scale testing apparatus.....	57
3.2.2	Schematic of the model specimen.	59
3.2.3	Schematic of the model specimen gripping system, adopted from Wolodko (1999).....	60
3.2.4	Prototype-scale testing apparatus.	61
3.2.5	Schematic of the prototype specimen.	64
3.3.1	Visualisation of matrix cracking using fluorescent dye-penetrant.	66
3.3.2	Example of graph showing model specimen internal pressure versus normalised volumetric flow rate, $q/\Delta p$	70
3.4.1	Schematic of the bladder system for the investigation of structural failures, adopted from Wolodko (1999).	71
3.5.1	Loading scheme for tubular specimens (left) and applied biaxial stress condition (right).	72
4.2.1	Biaxial stress-strain response for pure hoop loading, ϵ_A , ϵ_H : axial and hoop strain (measured); ϵ_T , ϵ_P : (calculated) transverse and parallel to fibre strain (Mertiny and Ellyin, 2002).....	81
4.2.2	Biaxial stress-strain response for a [3H:1A] loading ratio, ϵ_A , ϵ_H : axial and hoop strain (measured); ϵ_T , ϵ_P (calculated) transverse and parallel to fibre strain (Mertiny and Ellyin, 2002).....	81
4.2.3	Biaxial stress-strain response for closed end loading, ϵ_A , ϵ_H : axial and hoop strain (measured); ϵ_T , ϵ_P : (calculated) transverse and parallel to fibre strain (Mertiny and Ellyin, 2002).....	82
4.2.4	Biaxial stress-strain response for a [1H:15A] loading ratio, ϵ_A , ϵ_H : axial and hoop strain (measured); ϵ_T , ϵ_P : (calculated) transverse and parallel to fibre strain (Mertiny and Ellyin, 2002).....	83

LIST OF FIGURES

4.2.5	Photograph of specimens failed under (a) [3H:1A], (b) [2H:1A] and (c) [1H:15A] loading conditions, and (d) undamaged specimen (from left to right) (Mertiny and Ellyin, 2002).	84
4.2.6	Biaxial functional and structural stress failure envelopes (Mertiny and Ellyin, 2002).	85
4.2.7	Relative functional strengths of $[\pm 60_3]_T$ model specimens.....	86
4.2.8	Strains parallel and transverse to fibres at functional failure loads (Mertiny and Ellyin, 2002).	87
4.2.9	Mohr's circle illustration for comparison of the [3H:1A] and [1H:0A] structural failure behaviour (Mertiny and Ellyin, 2002).....	89
4.2.10	Mohr's circle illustration for comparison of the [3H:1A] and [2H:1A] structural failure behaviour (Mertiny and Ellyin, 2002).....	90
4.3.1	Failures mode under [3H:1A] loading: Burst failure showing jagged fracture surfaces (Mertiny et al., 2004a).....	93
4.3.2	Failure mode under [2H:1A] loading: Localised burst failure (Mertiny et al., 2004a).	93
4.3.3	Failure modes under [1H:1A] loading: Localised burst/collapse unique to $[\pm 45, \pm 60_2]_T$ lay-up (left); burst unique to $[\pm 30, \pm 60_2]_T$ lay-up (right) (Mertiny and Ellyin, 2004a).	94
4.3.4	Experimental functional failure envelopes and points of failure of $[\pm 60_3]_T$, $[\pm 45, \pm 60_2]_T$ and $[\pm 30, \pm 60_2]_T$ tube specimens (Mertiny et al., 2004a).	96
4.3.5	Experimental structural failure envelopes and points of failure of $[\pm 60_3]_T$, $[\pm 45, \pm 60_2]_T$ and $[\pm 30, \pm 60_2]_T$ tube specimens (Mertiny et al., 2004a).....	96
4.3.6	Relative functional-to-structural strength for each lay-up/loading combination (Mertiny et al., 2004a).	97
4.3.7	Functional strength of each lay-up/loading combination relative to functional strength of baseline lay-up (Mertiny et al., 2004a).	98
4.3.8	Structural strength of each lay-up/loading combination relative to structural strength of baseline lay-up (Mertiny et al., 2004a).....	99
4.3.9	Stress/strain diagram for closed-end loading of $[\pm 60_3]_T$, $[\pm 45, \pm 60_2]_T$ and $[\pm 30, \pm 60_2]_T$ specimens (Mertiny et al., 2004a).....	100
4.4.1	Burst failure with jagged fracture surfaces as observed under [3H:1A] loading (left: $[\pm 45, \pm 60_2]_T$; right: $[\pm 60_2, \pm 45]_T$) (Mertiny et al., 2004b).....	106

LIST OF FIGURES

4.4.2	Localised burst failure close to end connection of tubular structure as observed under [2H:1A] loading (left: $[\pm 45, \pm 60_2]_T$; right: $[\pm 60_2, \pm 45]_T$ (Mertiny et al., 2004b).	106
4.4.3	Failure in form of a wall perforation within the specimen gauge section as observed under equi-biaxial loading (left: $[\pm 45, \pm 60_2]_T$; right: $[\pm 60_2, \pm 45]_T$) (Mertiny et al., 2004b).	107
4.4.4	Collapse of the composite structure as observed under (approximate) pure axial loading (left: $[\pm 45, \pm 60_2]_T$; right: $[\pm 60_2, \pm 45]_T$) (Mertiny et al., 2004b).	107
4.4.5	Experimental structural failure stress envelopes of $[\pm 45, \pm 60_2]_T$ and $[\pm 60_2, \pm 45]_T$ tube specimens (Mertiny et al., 2004b).	108
4.4.6	Experimental functional failure stress envelopes of $[\pm 45, \pm 60_2]_T$ and $[\pm 60_2, \pm 45]_T$ tube specimens (Mertiny et al., 2004b).	109
4.4.7	Experimental functional failure strain envelopes of $[\pm 45, \pm 60_2]_T$ and $[\pm 60_2, \pm 45]_T$ tube specimens (Mertiny et al., 2004b).	109
4.4.8	Poisson's ratios ν_{XY} and ν_{YX} for $\pm\alpha^\circ$ -covers with 70% fibre volume fraction (Mertiny et al., 2004b).	116
4.5.1	Winding pattern of model (left) and prototype-size specimens (right).	121
4.5.2	Stress/strain data from testing of model and prototype-size specimens under closed-end loading (Note that ordinate values are given in terms of applied hoop stress).	124
4.5.3	Stress/strain data from testing of model and prototype-size specimens under [3H:1A] loading.	124
4.5.4	Change in the axial modulus, D_A , of model and prototype-size specimens.	126
5.1.1	Schematic of common bonded joint configurations: (a) single lap joint, (b) butt strap joint, and (c) scarf joint (black colour indicates adhesive material).	133
5.3.1	Failure modes of adhesively bonded joints: (a) adherend failure, (b) adhesive failure, and (c) cohesive failure.	138
5.3.2	Adhesive fillet shapes: (a) square-ended, (b) concave/arc, (c) triangular and (d) convex/rounded shape; (b-d) feature smooth transitions to the substrate surface.	140
5.4.1	Schematic of the prototype pipe joint.	143

LIST OF FIGURES

5.4.2	Pipe alignment device: (a) coupler cage, (b) inflatable mandrel with support structure, (c) coupled prototype pipe, and (d) pipe alignment device assembly.	144
5.4.3	Pipe alignment device with prototype pipe/coupler.	144
5.4.4	Completed prototype pipe joint.	146
5.4.5	Schematic of coupler end geometries: (a) inside taper and (b) (outside) chamfer (i.e. the current design configuration).	146
5.5.1	Photograph of partial joint fracture.	148
5.5.2	Photograph, schematic and magnifications of partial joint fracture.	149
5.5.3	Schematic of the strain gauge arrangement for the determination of the crack growth direction.	150
5.5.4	Global applied axial stress and strain readings from different gauge locations for the determination of the crack growth direction.	151
5.5.5	Experimental biaxial failure envelope of prototype pipe specimens.	152
5.6.1	Local coordinate system and stress components in vicinity of crack tip.	158
5.6.2	4-noded quadrilateral elements at the crack tip.	159
5.6.3	8-noded parabolic elements at the crack tip.	160
5.7.1	Schematic of model for finite element analysis.	162
5.7.2	Finite element mesh within the joint vicinity for the stress analysis of undamaged specimens.	164
5.7.3	Finite element mesh within the joint vicinity for the fracture analysis in cracked specimens (deformed geometry and scaled displacements shown).	164
5.7.4	Schematic of finite element model showing coordinate system, loadings and constraint boundary conditions.	166
5.7.5	Refined finite element mesh employed for sensitivity analysis.	168
5.7.6	Comparison between peel (left) and shear (right) stress data for a [2H:1A] loading case, from a refined and unrefined finite element mesh. Stress data originate from within the joint region along a path at the centre of the pipe surface resin coat. Stress data were normalised with respect to the average pipe hoop stress, σ_{hoop}	170

LIST OF FIGURES

5.7.7 Comparison between peel (left) and shear (right) stress data for a [2H:1A] loading case, from a refined and unrefined finite element mesh. Stress data originate from along a path at the adhesive/coupler interface within the bondline. Stress data were normalised with respect to the average pipe hoop stress, σ_{hoop}170

5.7.8 Comparison between strain energy release rate values from analyses with 4-noded and 8-noded axisymmetric quadrilateral elements. For the finite element analyses 100 MPa axial load was applied to the prototype specimen model.171

5.7.9 Through-wall stress (left) and strain (right) distributions from numerical analyses, and strain data from experiments, taken at the gauge section centre of the plain pipe body. Top, centre and bottom graphs show data for 50MPa/16.6MPa, 50MPa/25MPa and 5.15MPa/10.3MPa stress ratios respectively.....174

5.7.10 Comparison of shear stresses between models with and without centre pre-crack for pure axial loading. Stress data originates from within the joint region along a path at the centre of the pipe surface resin coat. Stress data were normalised with respect to the average pipe axial stress, σ_{axial}176

5.7.11 Comparison of peel and shear stresses within the centre of the pipe surface resin coat between models with baseline coupling distance, and those with 25% and 50% length reductions. Stress data were normalised with respect to the average pipe axial stress, σ_{axial}177

5.7.12 Comparison of maximum principle stresses within the centre of the pipe surface resin coat between models with baseline coupling distance, and those with 25% and 50% length reductions. Stress data were normalised with respect to the average pipe axial stress, σ_{axial}177

5.7.13 Vector plot showing magnitude/direction of maximum principle stresses in the vicinity of the coupler edge for the baseline configuration under axial loading.....178

5.7.14 Comparison between SERR values from analyses of a prototype model with baseline coupling distance, and those with and 25% and 50% length reductions. For the finite element analyses 100 MPa axial load was applied.....179

LIST OF FIGURES

5.7.15	Comparison between total SERR values from analyses of a prototype model with baseline coupling distance, and those with 25% and 50% length reductions. For the finite element analyses 100 MPa axial load was applied.	179
5.7.16	Normalised peak maximum principle stresses for models with bondlines of 0.5 mm, 1 mm, 2 mm and 4 mm. Stress data originate from three locations within the bondline, and were normalised with respect to the average pipe axial stress, σ_{axial}	180
5.7.17	Comparison between strain energy release rate values from analyses of prototype specimens models with 0.5 mm and 1.0 mm bondline thickness. For the finite element analyses 100 MPa axial load was applied.....	181
5.7.18	Normalised peak maximum principle stresses for models with one $\pm 60^\circ$ cover added/removed to/from the baseline coupler. Stress data originate from three locations within the bondline, and were normalised with respect to the average pipe axial stress, σ_{axial}	182
5.7.19	Comparison of peel (left) and shear (right) stresses within the centre of the pipe surface resin coat between models with one $\pm 60^\circ$ cover added/removed to/from the baseline coupler. Stress data were normalised with respect to the average pipe axial stress, σ_{axial}	184
5.7.20	Comparison between strain energy release rate values from analyses of prototype models with one $\pm 60^\circ$ cover added/removed to/from the baseline coupler. For the finite element analyses 100 MPa axial load was applied.....	184
5.7.21	Comparison between total strain energy release rate values from analyses of prototype models with an $[\pm 30, \pm 60_2]_T$ and an inversed $[\pm 60_2, \pm 30]_T$ lay-up. For the finite element analyses 100 MPa axial load was applied.....	185
5.7.22	Normalised peak maximum principle stresses for models with 15° , 30° and 60° coupler chamfers. Stress data originates from three locations within the bondline, and were normalised with respect to the average pipe axial stress, σ_{axial}	186
5.8.1	Experimental biaxial failure envelope of prototype specimens. Solid symbols mark specimens utilising improved prototype pipe.	188

NOMENCLATURE

Greek variables:

α	parameter used in conjunction with the composite cylinder assemblage model
$\alpha_{chamfer}$	coupler chamfer angle
$\alpha_{critical}$	critical angle of creel rotation indicating tow breakage
β_f, β_m	parameter used in conjunction with the composite cylinder assemblage model
γ	parameter used in conjunction with the composite cylinder assemblage model
γ_{12}	shear strain in the lamina material axes (1 - parallel, 2 - transverse to fibre direction)
Δ	crack extension increment
ϵ_1, ϵ_2	strain components in the lamina material axes (1 - parallel, 2 - transverse to fibre direction)
ϵ_{2u}	ultimate transverse strain of a fibre composite
ϵ_A, ϵ_H	strain in the axial and hoop direction
$\epsilon_{f,A}$	axial strain at failure
ϵ_{mu}	maximum matrix strain
ϵ_T, ϵ_P	strain in the transverse and parallel to fibre direction
$\epsilon_{XX}, \epsilon_{YY}, \epsilon_{ZZ}$	strain in the axial, hoop and radial direction
$\{ \epsilon_{lamina} \}$	lamina strain (vector)
$\{ \epsilon_i \}$	unit vector
$\eta_{E_T}, \eta_{G_{IT}}$	parameter used in conjunction with the Halphin-Tsai model
θ	filament winding angle
λ	constant of proportionality, 'Pi-term'
μ	dynamic fluid viscosity
ν	Poisson's ratio
ν_{12}, ν_{21}	Poisson's ratios of a lamina
ν_f, ν_m	Poisson's ratio of fibres and matrix material
ν_{LT}, ν_{TT}	longitudinal and transverse (major) Poisson's ratio of a unidirectional lamina
$\nu_{XY}, \nu_{YZ}, \nu_{XZ}$	(major) Poisson's ratio in global coordinates
ξ	local crack tip coordinate transverse to the crack plane

NOMENCLATURE

ξ_{E_T}	reinforcing factor (longitudinal Young's modulus)
$\xi_{G_{LT}}$	reinforcing factor (longitudinal shear modulus)
ρ	local crack tip coordinate normal to the crack plane; used as parameter used in conjunction with the composite cylinder assemblage model as well
ρ_c, ρ_f, ρ_m	density of composite, fibre and matrix material
σ_1, σ_2	stress components in the lamina material axes (1 - parallel, 2 - transverse to fibre direction)
$\sigma_{axial}, \sigma_{hoop}$	average pipe stress, in axial and hoop direction
σ_{eq}	von Mises equivalent stress
σ_H, σ_A	average hoop and axial stress components
σ_p	opening/mode I stress components in vicinity of crack tip
σ_T, σ_P	stress in the transverse and parallel to fibre direction
$\sigma_{XX}, \sigma_{YY}, \sigma_{ZZ}$	stress in the axial, hoop and radial direction
$\{\sigma_{lamina}\}$	lamina stress (vector)
$\partial\sigma/\partial t$	monotonic stress loading rate
τ_{12}	shear stress component in the lamina material axes (1 - parallel, 2 - transverse to fibre direction)
$\tau_{\xi p}$	opening/mode I stress components in vicinity of crack tip

English variables:

a	crack length
$a_{1,2}$	stress distribution coefficients for SERR analysis
A	area
A_0	winding pattern unit-cell area
$[A_{cover}]$	cover stiffness matrix in global coordinates
$[\bar{A}_{cover}]$	cover compliance matrix in global coordinates
A_f	fibre cross-sectional area
A_u	undulation area within a winding pattern unit cell
b	actual winding bandwidth
B	nominal winding bandwidth
c	Adhesive bond overlap length
C	number of winding circuits required for the completion of one cover
CSA	cross-sectional area of a typical roving
D	specimen inside diameter

NOMENCLATURE

D_A	change in axial modulus
D_T	degree of interweaving
$\{e_i\}$	unit vectors
E	Young's modulus
E_1, E_2	Young's moduli of the lamina
E_f, E_m	Young's modulus of fibres and matrix
$E_{f,A}$	axial Young's modulus at 97% functional failure load
E_H, E_A	(initial) hoop and axial Young's moduli of tubular specimens
E_L, E_T	longitudinal and transverse Young's modulus
E_{XX}, E_{YY}, E_{ZZ}	Young's modulus in global coordinates
F	axial force
\dot{F}	axial force loading rate
$F_1, F_2, F_{12}, F_{11}, F_{22}, F_{66}$	strength parameters of the material for the Tsai-Wu quadratic failure criterion
F_{tow}	winding tow tension
$F_{\rho t}, F_{\xi i}$	nodal forces parallel and tangential to crack tip
$\mathcal{G}_I, \mathcal{G}_{II}$	mode I and mode II strain energy release rate
\mathcal{G}_c	fracture energy (critical strain energy release rate)
\mathcal{G}_T	total strain energy release rate
G	shear modulus
G_{12}	shear modulus of the lamina
G_f, G_m	shear modulus of fibres and matrix material
G_{LT}, G_{TT}	longitudinal and transverse shear modulus
G_{XY}, G_{YZ}, G_{XZ}	shear modulus in global coordinates
k	permeability
k'	intrinsic permeability
K'	characteristic intrinsic permeability at leakage failure
L	specimen gauge length
L_b	winding band of length
L_u	undulation length
m_c, m_f	weight of composite and fibre sample
$[M]$	coordinate system transformation matrix
n	number of covers
N	number of elements of a data set
N_c	number of circuits performed until a winding band is deposited adjacent to the first circuit
N_u	number of undulations within a winding pattern unit cell

NOMENCLATURE

p	pressure
\dot{p}	pressure loading rate
p_o	atmospheric pressure
$p_i, p_{internal}$	specimen inside pressure
Δp	difference between atmospheric and internal pressure
Δp_f	leakage failure pressure
$\{\nabla p\}$	pressure gradient across specimen wall
q	total volumetric flow rate through the specimen wall
Q	volumetric flow rate at leakage failure
$[Q], Q_{ij}$	lamina stiffness matrix in local coordinates
$[\bar{Q}], \bar{Q}_{ij}$	lamina stiffness matrix in global coordinates
r	distance from crack tip
R	mandrel radius
R_{creel}	fibre creel radius
s	effective specimen wall or laminate thickness (also used as normalised coordinate in the description of finite element shape functions)
\tilde{s}	average specimen wall thickness
$s_1^{FT}, s_2^{FT}, s_{12}^{FT}$	lamina tensile strengths in lamina material coordinates
$s_1^{FC}, s_2^{FC}, s_{12}^{FC}$	lamina compressive strengths in lamina material coordinates
s_N	standard deviation
$[S], S_{ij}$	lamina compliance matrix in local coordinates
t	cover or ply thickness (also used as normalised coordinate in the description of finite element shape functions)
t'	cover half thickness
t_a	laminate thickness
t_b	bondline thickness
\hat{t}	time
T_{actual}	actual creel torque
T_{ideal}	ideal creel torque for frictionless system
TEX	relative fibre weight
TOW	number of tows within winding band
u	leakage radial flow velocity
$\{u\}$	leakage flow velocity vector
\bar{u}	crack opening displacement, parallel to crack plane
U_r	creel follower arm feedback voltage of the tow tension system

NOMENCLATURE

\bar{v}	crack opening displacement, transverse to crack plane
$V_{f,a}$	average fibre volume fraction of sample or specimen
V_f, V_m, V_v	volume fractions of fibres, matrix and void
$Vol, Vol_f, Vol_m,$	volume of sample, fibres and matrix
W	work required for crack closure, according to Irwin
x_i	elements of a data set

CHAPTER 1

INTRODUCTION

1.1 Background of Current Study

For more than four decades significant research efforts in high-technology sectors such as the aerospace industry have been directed towards structures made from fibre reinforced polymeric composites (FRPC). One of the predominant driving forces behind this research was the need for materials that combine high strength with low relative mass. This was made possible with the advent of high-performance fibre materials made from carbon, ceramic, polymers (such as aramid) as well as glass. Examples are plentiful in which advanced fibres, in combination with equally advanced polymeric matrix materials, allowed for the design of structures that outperformed traditional metallic components. An often-cited quality linked to FRPC is the ability to tailor the fibre architecture (i.e. the orientation and lay-up sequence of layers of unidirectional fibres) to the particular loading conditions. The result is an efficient material utilisation, which, to a great extent, may realise sought after weight savings. FRPC are lesser known for favourable corrosion properties. Yet, high resistance against environmental attack is of significant importance if a component design is aimed at heightened performance and longevity. Other advantageous properties of FRPC are improved fatigue performance and favourable surface properties of the finished product (e.g. low-friction flow characteristics).

The use of FRPC is no longer limited to high-technology sectors. The innovative properties make this class of materials play an increasingly important role in the production of various industrial components and even consumer goods. A prerequisite for this development has been the development of cost-effective production methods. At the forefront of such methods in terms of efficiency and cost-effectiveness is the filament winding technique, which enables the economical fabrication of high performance

tubular components. This has also been recognised by various industries involved in the extraction, processing and transportation of chemical and petroleum products. These industries usually operate considerable amounts of various pipe systems in plants and structures. The location of these facilities (e.g. pipelines and offshore oilrigs) and/or the corrosiveness of the processed substances often pose a challenge to metallic components.

It is not surprising that composite piping is well established in the chemical industry, where metallic structures are simply not usable for a variety of processes involving corrosive substances (see e.g. Cheremisinoff and Cheremisinoff, 1978). However, there are new emerging markets for composite piping. For example, the offshore oil and gas industry has been moving towards drilling in deeper seawaters (see e.g. Kalman and Loper, 1998). This resulted in escalating weight of floating production vessels, which has been counteracted by the utilisation of lightweight composite piping underwater (e.g. production risers, see Baldwin et al., 1997) and as part of the floating vessel itself (e.g. firewater lines, see Sundt, 1993). Another example is the pipeline industry, where the combination of large distances, remote locations and environmental conditions pose a challenge towards safety and cost-effectiveness. It is known that the conventional steel pipe is prone to stress corrosion cracking. Monitoring the health of a pipeline is costly due to the remoteness and size of the respective structures. Polymeric pipe systems are seen to remedy these deficiencies while realising other cost saving measures as well. The glassy interior surface of a full-composite pipe results in excellent flow characteristics and less build-up, which in turn significantly reduces pumping costs (Cheremisinoff and Cheremisinoff, 1978). Hence, a push towards new material systems has been initiated. Recently, fibre-reinforced steel hybrid pipe has been the first step towards safer and more economical pipelines (see e.g. Anonymous, 2003).

Although the high potential of FRPC pipe structures has been recognised, reluctance exists towards the application of these materials in pressurised pipe systems. The reason for this is the incomplete understanding of the material behaviour and damage development under complex loading (multiaxial, creep and fatigue) and environmental conditions (Ellyin et al., 2000). In addition, methodologies for the integration (joining) of composite pipe are in their infancy state. Thus, considerable research efforts are required

before a similar level of confidence and knowledge will be achieved as exist for metallic structures. It is the aim of the present research study to contribute to these efforts.

1.2 Introduction to Composite Materials

1.2.1 Fibre-Reinforced Polymeric Materials for Filament Winding

By definition composite materials are composed of two or more constituents. The aim is to achieve favourable material properties that neither of the constituents possesses individually. Most common are bi-phase composites, which consist of a discontinuous reinforcement phase embedded in a continuous matrix phase. Particles, continuous and discontinuous (chopped) fibres are known forms of reinforcements. But, only continuous fibre material can be used for the filament winding of tubular components. The fibre phase is generally arranged in a unidirectional fashion to form an individual layer, a so-called lamina. Several unidirectional laminae with varying orientations are then stacked on top of each other to produce an (commonly) anisotropic laminate. The correct orientation and stacking sequence of unidirectional laminae yields the desired macroscopic properties of the structure.

Fibres from a variety of materials are available, e.g. glass, carbon and polymers. However, glass is presently the material of choice for the production of pipe and similar structures. This is attributable to the undemanding handling and processing characteristics, as well as the availability of glass-fibre with excellent strength-to-cost ratios and corrosion resistance. Only recently has a volume cost similar to high-quality glass-fibre been achieved for certain types of carbon-fibre. However, compared to glass-fibre, processing of carbon-fibre is generally less economical in a large-scale production environment. This is based on, but not limited to, the electrical conductivity and the brittleness of carbon-fibre. Hence, carbon-fibre requires special care during fibre routing and tensioning to prevent fibre damage, and to avoid electrical shorts from fibre-fly and carbon dust in electronic equipment in the vicinity. Note that carbon-fibre is particularly advantageous for structures with high demands towards stiffness, which is usually considered secondary for pipe structures.

In industrial applications only polymeric matrix systems are being utilised in connection with glass-fibre materials. There are two types of polymer matrix materials, namely thermoplastic and thermoset polymers. In the case of the former, heat is required to liquefy the polymer, whereas the latter type, usually supplied in a liquid state initially, hardens after the initiation of a chemical reaction. Generally, thermoset polymers are preferred for the filament winding process. Although the field of thermoplastic polymers is constantly evolving, and considerable improvements in strength and ductility have been achieved, their applicability remains limited. This is due in part to the rapid deterioration of mechanical properties with increasing temperature, which is not acceptable for many practical applications. Moreover, handling and processing of thermoplastics is more involved than that of thermosetting resins. Generally, heating and thus the liquefaction of thermoplastics is only possible within a process zone of limited size. Thermoset polymers, on the other hand, remain liquid during the entire processing, which is usually concluded by the hardening of the liquid matrix phase in a temperature-controlled curing oven. Such conditions are ideal for achieving complete filament wetting and high degrees of fibre compaction. Thus, a potentially higher reinforcement effect may be realised with thermoset resins.

1.2.2 Damage Development in Fibre Composite Materials

In order to limit experimental work and facilitate an efficient and successful design process, failure criteria for FRPC are required that enable a reliable prediction of damage. Unfortunately, the complexity of these materials has so far precluded the development of a universally accepted criterion. To date, no universal failure model, such as the yield criterion often used in conjunction with metals, has been found to predict damage in FRPC. In contrast to homogeneous materials, which are characterised by the initiation and self-similar propagation of a singular damage event, heterogeneous and anisotropic fibre composites exhibit interactive and competing failure modes in various structural scales.

Starting at the micro level, damage in the form of inter-fibre matrix cracking, fibre-matrix debonding, fibre breakage and fibre buckling may occur. In fact, due to the

heterogeneous nature of FRPC, elevated temperature curing and processing often causes these micro damage modes to be present even in a virgin material. With continued loading damage development from the micro scale into the macro level can be observed. Possible macro damage modes are: widespread (intra-laminar) matrix cracking, delamination (inter-laminar matrix cracking), progressive fibre failure, and (global) buckling failure of the structure.

For the prediction of damage in FRPC researcher have developed various failure criteria (see e.g. Soden et al., 1998). These criteria can be categorised to be either of a macro- or micro-mechanical nature. Moreover, damage may also be caused by fatigue loading, which requires appropriate life prediction methodologies. A comprehensive study of available criteria is beyond the scope of this work. Nevertheless, basic concepts as well as shortcomings of common approaches are briefly reviewed in the following.

Macro-mechanical failure models:

For macromechanical analyses the basic building blocks of a composite, i.e. the unidirectional laminae are generally assumed to be orthotropic and homogeneous in nature. This is also known as a meso-modelling philosophy. Inherently, micro-mechanical features and their influences on damage are not being considered by these methods. Macro-mechanical failure criteria are well suited for the prediction of damage initiation (*first ply failure*). However, *first ply failure does not necessarily terminate the life of a composite structure*. Subsequent damage is likely to occur, and ultimate failure is often reached at significantly higher load levels. Thus, the following criteria are known to generally give a conservative failure prediction. (More detailed information on subsequent macro-mechanical failure criteria can be found in e.g. Tsai and Hahn, 1980; Hyer, 1998; Gdoutos, 2000; Vasiliev and Morozov, 2001; Kollár and Springer, 2003).

The (plane-stress) maximum stress criterion is usually cited to be the most basic criterion in this context. It is based on the assumption that no damage will be present within a unidirectional lamina, while all of the following three inequalities are satisfied:

$$-s_1^{FC} < \sigma_1 < s_1^{FT}, \quad -s_2^{FC} < \sigma_2 < s_2^{FT}, \quad |\tau_{12}| < s_{12}^F \quad (1.2.1)$$

where σ_1 , σ_2 , and τ_{12} are the stress components in the lamina material axes (1 – parallel, 2 – transverse to fibre direction), and s_i^F are lamina strengths with superscript C and T denoting the compressive and tensile components, respectively.

Each strength component is generally determined by experiments, and hence, can be associated with a distinct damage mode. However, the maximum stress criterion does not consider any stress interaction. This may affect the predictability of whether damage will actually occur at any of the prescribed stress levels. For example, a unidirectional lamina may fail due by fibre buckling when the applied stress exceeds the corresponding compressive strength; however, an additional transverse compressive loading would likely support fibres laterally, thus causing buckling to occur at a higher stress level than prescribed by s_1^{FC} . Being incorporated within a laminated structure, laminae are rarely subjected to a uniaxial stress alone but to multiaxial stress states. Neglecting the interaction of stresses may therefore be regarded as the major shortcoming of this criterion. Hence, the need for interactive failure criteria becomes evident.

Of equally simple nature as the maximum stress criterion is the maximum strain criterion. This method ignores strain interaction, however, it allows for some stress interaction. This is due to the Poisson's effect, which is incorporated into this criterion according to the following inequalities:

$$-\frac{s_1^{FC}}{E_1} < \varepsilon_1 < \frac{s_1^{FT}}{E_1}, \quad -\frac{s_2^{FC}}{E_2} < \varepsilon_2 < \frac{s_2^{FT}}{E_2}, \quad |\gamma_{12}| < \frac{s_{12}^F}{G_{12}} \quad (1.2.2)$$

where $\varepsilon_1 = E_1^{-1}(\sigma_1 - \nu_{12} \sigma_2)$, $\varepsilon_2 = E_2^{-1}(\sigma_2 - \nu_{21} \sigma_1)$ and $\gamma_{12} = G_{12}^{-1} \tau_{12}$, with E_1 , E_2 , G_{12} and ν_{12} , ν_{21} are the Young's moduli and Poisson's ratios of the lamina respectively.

Most widely used for the prediction of damage are quadratic failure criteria, such as the Tsai-Wu criterion. For a plane stress condition a quadratic failure criterion is given by the following inequality:

$$F_1 \sigma_1 + F_2 \sigma_2 + F_{11} \sigma_1^2 + F_{22} \sigma_2^2 + F_{66} \tau_{12}^2 + 2F_{12} \sigma_1 \sigma_2 < 1 \quad (1.2.3)$$

where F_i and F_{ij} are strength parameters of the material.

The first five strength parameter in Eq.(1.2.3) are based on the material strengths presented above, i.e. $F_i = (s_i^{FT})^{-1} + (s_i^{FC})^{-1}$, $F_{ii} = (s_i^{FT} s_i^{FC})^{-1}$, for $i = 1, 2$, and $F_{66} = (s_{12}^F)^{-1}$. The remaining parameter, known as the interaction strength parameter, is obtained from tests with two nonzero stress components inside the material. Alternatively, it can be approximated as $F_{12} = -0.5\sqrt{F_{11}F_{22}}$ (Tsai and Hahn, 1980). Quadratic failure criteria were shown to yield more accurate predictions than the structural strength criteria presented above. However, they do not provide explicit information about the damage mechanisms, which is considered their major limitation.

Despite their shortcomings all of the above failure criteria are widely used for their utility. For example, employing classical lamination theory or numerical techniques (e.g. finite element analysis), stresses and strains within each lamina of a laminate can be computed, thus enabling the prediction of first ply failure. Subsequent failure of the remaining laminae can be incorporated in such models by discounting previously failed plies (by e.g. assigning a residual stiffness to failed laminae).

Unfortunately, the predictability of composite failure depends highly on how failure is defined in the first place. Particularly the effect of matrix damage is often not considered appropriately. From a structural point of view, matrix damage mainly causes reduced stiffness, and may be the source for consecutive damage modes, such as delamination. However, in the present context, i.e. the investigation of pressurised structures for the containment of fluids, the significance of matrix damage on leakage cannot be captured by any of the above failure criteria; thus the predictability of leakage type failures was found to be inadequate (Soden et al., 2004).

Micro-mechanical failure models:

Micro-mechanics were predominantly chosen for the investigation of basic damage modes in unidirectional lamina under simple loadings, i.e. fibre breakage, fibre buckling, fibre-matrix debonding and matrix cracking (for further information see e.g. Gdoutos, 2000). The term ‘micro-mechanical’ implies that the individual properties of the constituents, i.e. fibres and matrix, were considered for the analyses. In their investigations researchers focussed mainly on representative structures such as

single-fibre volume elements. The periodic repetition of representative volume elements (unit cells) and their properties is then assumed to obtain the behaviour of the entire structure. This approach has produced good results for the determination of global material properties such as stiffness. But, unit cell models are generally inadequate for the investigation of failure. In real laminates the distribution of fibre and matrix is usually characterised by a certain degree of irregularity; hence, the assumption of a periodic distribution is quite inaccurate. In addition, unit cell models are limited in their ability to capture the complex behaviour of general laminates (i.e. laminates having more than a single fibre orientation). To overcome this limitation some researchers incorporated micro-mechanical models into a framework of laminate theory (e.g. Li and co-workers, 1998; Ardiç et al., 1999). However, micro-mechanical models for the prediction of failure in general laminates are generally considered rather complex, and the determination of material and damage parameters is commonly quite involved. Hence, these theories have not found wide application for the prediction of laminate failure. Notwithstanding their limitations, micro-mechanical models are indispensable for advancing the understanding of composite failure behaviour and mechanisms. For example, models describing the effect of fibre proximity on matrix cracking were developed by Kies and Greszczuk (see Jang, 1994), of which the former will be discussed later in the present study.

Fatigue damage:

Designers require reliable fatigue failure models capable of predicting and describing the onset and evolution of damage. The same micro- and macro damage modes as observed under monotonic loading may occur under fatigue conditions. But, the sequence of damage events and their extent substantially depends upon the cyclic loading conditions and the fatigue characteristics of the fibre composite material. In general, three different phases can be distinguished for the cyclic failure of unidirectional plies and general laminations (see e.g. Jang, 1994; Gamstedt and Talreja, 1999; and Pantelakis and Labeas, 2000). (a) Firstly, localised micro damage events, i.e. fibre breakage, fibre-matrix interface debonding and transverse matrix cracking accumulate rapidly. (b) After damage has reached a saturation state in one phase, a gradual development of micro as well as macro damage of another mode commences, such as local fibre fracture and

delamination. (c) Finally, in the third stage rapid damage accumulation such as extensive delamination growth and fibre breakage quickly lead to catastrophic failure. During the first and last stage of the cyclic failure process a fast drop in stiffness can be ascertained. A more gradual stiffness reduction characterises the second phase, which usually also comprises the greater part of the structure's fatigue life. In contrast to tensile loading, fibre buckling and delamination were found to be the dominating damage modes under compressive loading conditions. Fully reversed tension-compression loadings are therefore considered the worst scenario, since damage characteristic to both loading conditions is involved.

Methodologies for the characterisation and prediction of fatigue damage can be categorised into three groups. Firstly, work was focussed on unidirectional laminae under cyclic loading parallel to fibres. For example, a micro-mechanical model was described by Gamstedt (2000), which accounts for the breakage of fibres and subsequent load redistribution. Secondly, the on- and off-axis cyclic behaviour of unidirectional laminae was investigated. An approach employing experimental best-fit Wöhler-type curves was shown to yield reasonable predictions (Hashin-Rotem, 1974). Other methodologies involve energy-based models (see e.g. Fawaz and Ellyin, 1994; and Plumtree and Cheng, 1999). And thirdly, models for inter-laminar fracture were developed, which are based predominantly on fracture mechanics principles.

Despite the extensive research in the field of fatigue in FRPC, Pantelakis and Labeas (2000) concluded that the capabilities of predicting cyclic damage are still limited. Several reasons were cited for this assertion. Fatigue damage in FRPC largely depends on the characteristics of the structure and the material (e.g. fibre orientation, lay-up sequence and constituent properties). Moreover, a universal governing fatigue damage parameter such as the crack length in metallic materials has not been identified yet for FRPC. Thus, in practical applications the combination of a certain FRPC structure and an applied loading condition usually represents a unique system to which aforementioned fatigue models have only limited applicability. These conditions challenge the adoption of a damage tolerance concept, and hence, extensive experimental characterisation of FRPC structures remains imperative.

1.2.3 Environmental Effects on Composite Materials

Long-term exposure of polymeric fibre composites to certain environmental conditions may have detrimental effects on their performance. FRPC can be affected by radiation, moisture, temperature, the presence of chemical substances, and combinations of the four (for further information and references, see Barkatt, 2001).

Degradation effects due to radiation such as ultraviolet light are rarely considered in the context with FRPC. This is due to the fact that most structures are either not exposed to significant radiation, or appropriate measures can be taken for their protection (e.g. coatings).

On the other hand, literature pertaining to the effect of moisture and temperature on polymeric composites is frequently found (e.g. Ellyin and Rohrbacher, 2000 and 2003, where further references are cited). Not surprisingly, considerable attention was given to tubular structures for the containment of fluids (e.g. Perreux and Suri, 1997; Perreux and co-workers, 2002; and Ellyin and Maser, 2004). It was established that moisture accumulates in FRPC, and a temperature-specific saturation state can be determined. Moisture was found to affect fibres as well as the matrix. The former mainly suffer from degradation of interface properties, resulting in poor shear load transfer capabilities, and thus, reduced strength of the composite. Long-term moisture exposure may also diminish the strength of glass and polymer fibres. The diffusion of moisture into the polymeric matrix usually causes a degradation of mechanical properties as well. This is generally attributed to hydrolytic depolymerisation. But moisture uptake is also known to cause swelling and plasticisation of the matrix. These may reduce manufacturing-induced thermal residual stresses, thus causing improved composite strength. A pre-damaged structure (e.g. matrix cracking) provides additional pathways for the fluid to enter the composite, thus facilitating a more rapid moisture uptake. Adverse influences of moisture on a composite were shown to increase substantially with increased temperature, whereas at room temperature damaging effects were found to be marginal to moderate (Ellyin and Rohrbacher, 2000; Ellyin and Maser, 2004).

Aqueous environments, and particular those being acidic or alkaline, were cited to have appreciable influences on FRPC, whereas effects of non-aqueous environments remained largely insignificant (Barkatt, 2001). In the context of this research program no specific harmful environment was considered; hence this issue will not be discussed further.

In closing, the magnitude and characteristics of environmental effects strongly depend on the material system, the substances the composite will be exposed to, temperature, loading scenarios and the damage history of the structure. These conditions are likely to vary significantly from case to case. For a specific application and environment a further experimental study would be required.

1.3 Review of Filament-Wound Pressure-Retaining Structures

Filament winding has been employed for the fabrication of mainly three kinds of pressure-retaining structures, i.e. storage tanks, pressure vessels and piping systems.

The use of fibre composites for the fabrication of storage tanks is common practice, which is reflected by the existence of industry standards, such as ASTM D3299 (1995). Tanks are frequently used for above- and underground storage of liquids such as petroleum products. Pressure ratings of filament-wound tanks are generally low (<1,000 kPa), and often these tanks are only designed to sustain hydrostatic pressure imposed upon the structure by the contained liquid. Thus, the use of fibre composites is mainly driven by aspects such as corrosion resistance and minimised unladen weight.

Having a long history in the aerospace and defence industry (since the middle 1960's) filament-wound pressure vessels have become indispensable components in numerous applications such as aircrafts, marine and space vehicles (Klinger and Wilson, 1990). The primary purpose of these components is the storage of substances used as propellants or for environmental and breathing systems. Substances are commonly of a gaseous nature, or are liquefied requiring a pressurised environment. In the commercial sector filament-wound pressure vessels are predominantly used as breathing apparatuses (such as oxygen packs for medical use, air supply tanks for scuba diving and fire fighting

equipment). A recently emerging field are pressure tanks for fuel storage in alternatively powered automotive vehicles (e.g. natural gas or hydrogen). An international standard for such components is available (ISO 11439, 2000). Considerable pressure ratings, exceeding 40 MPa in some cases, are commonly achieved for filament-wound pressure vessels. Winding processes employed for the fabrication of cylindrical and spherical pressure vessels are highly evolved. Automated systems exist that are specialised for a variety of fibre/matrix material systems (such as carbon, aramid or glass-fibre reinforced polymers). Machine capabilities range from simple circumferential wrapping techniques to complex fibre guiding mechanisms facilitating fibre paths for fully wrapped units. In the past, pressure vessels were regularly equipped with metallic liners. Their function was to act as a winding mandrel during the manufacturing, and as a leakage barrier during service. Moreover, a metallic substructure also eases the design and installation of pressure connections. In recent times an increasing number of pressure vessels features polymeric liners, of which use is motivated by additional reductions in cost and weight (Funck and Fuchs, 2001).

Filament-wound pipe systems also have an extensive history reaching back more than three decades. Applications are diverse and range from low-pressure line pipe for the transportation of fire extinction fluid/water, to the recently emerging high-pressure composite production risers for the offshore oil industry. This diversity is reflected in pressure capabilities reaching from less than 1,000 kPa to 100 MPa, respectively. The majority of filament-wound pipe products, particular those with high-pressure ratings, are restricted to diameters of less than 0.25 m. Nonetheless, in some applications pipe diameters of up to 4 m were realised (e.g. power plant cooling water intake lines). In oil-field installations most composite pipe for surface transport and down-hole injection is pressure-rated between 2.5 MPa and 14 MPa; yet, some specialised systems are able to sustain pressures of up to 41 MPa. Efforts towards standardisation of composite pipe have been only partially successful. For example, ASTM standard D2996 (1995) is available, which mostly applies to low-pressure systems. But, for various important industrial sectors, such as those employing high-pressure pipeline, appropriate standard

specifications have not been achieved thus far. This is certainly a consequence of inadequate knowledge and predictability of damage behaviour.

Being geometrically simple, the cylindrical shape of pipe does not require advanced manufacturing capabilities. Nevertheless, a high degree of automation is desirable to achieve high output for large-scale production. Notably, some unique facilities were reported for the fabrication of continuous pipe (Klinger and Wilson, 1990). For this task a 360° delivery system is employed that deposits fibre onto a continuous, disposable spiral-wrapped paper mandrel. While the mandrel translates down the line a series of stationary delivery systems perform rotating motions for the circumferential wrapping of filaments. Thus, a multi-layer fibre architecture can be produced in a continuous fashion.

Joining of composite pipe has not been resolved as yet to satisfy the high expectation of various industries. This is particularly the case for pressurised structures, where requirements towards strength and durability are increased. High levels of efficiency, reproducibility and safety have been achieved for the joining of metallic pipes. Unfortunately, it has not been feasible to realise the favourable attributes linked to mechanical fastening and welding in conjunction with composite pipe systems. Adhesive bonding is generally considered the preferable joining technique for fibre-reinforced structures (Tong and Steven, 1999). Due to advancements in adhesive technology and efficiency of bonding techniques, other fastening methods are being increasingly replaced by this method in high-technology sectors such as the aircraft industry. However, confidence in adhesive bonding of pipe is still lacking. This is often attributed to insufficient field-friendliness of these techniques. A joining methodology is considered field-friendly if high and consistent joint quality is paired with competitive cost. Since this has not been achieved yet, the issue of joining continues to challenge the large-scale application of composites in pipe systems.

1.4 Overview of the Current Research Work

1.4.1 Design Objectives for All-Composite Pipe Structures

Future pipe designs ought to outperform traditional metallic structures from an operational, safety and economical point of view. Due to the aforementioned favourable properties, it is promising that this task may be accomplished with fibre-reinforced polymeric composites. Because of its ability to produce quality components at competitive cost, filament winding is proposed for the fabrication of pipe sections as well as for components required for the pipe structure integration. Pipe systems are usually subject to different biaxial stress states resulting from installation and in-service (primarily high pressure) loading conditions. Hence, safe operation of a pipe system under appropriate biaxial stress ratios has to be ensured. Fail-safe designs are preferable, i.e. failure is characterised by leakage events instead of catastrophic burst. Nonetheless, constant slow-rate fluid loss is unacceptable, which may be caused by damage within the composite structure induced during manufacturing or installation (matrix cracking).

Present design solutions for the joining of composite pipe commonly entail pipe extremities with rather complex features (such as threaded or interlocking connections). This often causes weakening of the pipe body by e.g. introducing load concentrations. Yet, it is the industry practice to dimension pipe structures based on the load-bearing capacity of the pipe body. Since the pipe body also constitutes the dominant portion of the overall structure by volume and cost, it is undesirable to introduce joining techniques that adversely influence pipe strength. Moreover, aforementioned complex joint features require additional machining, which often has to occur on-site. This renders the fabrication more expensive and less field-friendly. To overcome these shortcomings the utilisation of an innovative, yet simple all-composite adhesively bonded overlap sleeve joint is proposed. Such a joint bears certain similarities to the single-lap joint designs from a functional point of view, i.e. it allows for a gradual transfer of axial load between pipe sections by shear. In addition, it intrinsically provides secure sealing against fluid loss without requiring gaskets or similar components. Note that bonded joints are generally considered inadequate for multiple assembly and disassembly cycles. This certainly is the case if pipe extremities are equipped with complex features that cannot be

replicated in the field. Thus, a bonded joint design ought to be of simple geometry. This allows for a relocation of pipe by sectioning the existing structure at various locations, and reinstalling resulting sections employing the original joining method.

1.4.2 Scope and Significance of Current Research Work

One objective of the present study is to investigate the feasibility of high-pressure all-composite pipe systems, including the integration of pipe sections. The design, manufacturing and joining of composite tubular structures have been discussed in the technical literature to some extent. However, no research work known to the author specifically addresses the mutual relationship between these issues (i.e. the design, manufacturing and joining), and the associated distinct features of resulting structures. In particular, the present work constitutes a unique approach by investigating all-composite pipe structures within a mutual context of manufacturability, design methodologies and damage characteristics. The present study showed that composite structures for pressure containment purposes are subject to unique damage behaviour (leakage). Conventional design methods do not account for these conditions. Hence, an investigation was conducted that identified damage characteristics and suitable design and analysis methodologies. A better understanding of the damage mechanisms was acquired, which led to the identification of a suitable fibre architecture that offers superior strength properties. A design solution for high-performance pipe was thus obtained that is within the capabilities of the economical filament winding method. Lastly, a technique for the integration of pipe components was developed that satisfies installation and operational requirements within manufacturing constraints. The damage behaviour of coupled pipe was investigated using experimental and theoretical means. This led to an appropriate methodology for the joint analysis and design optimisation.

1.4.3 Outline of the Current Study

An in-house filament winding facility enabled the production of pipe bodies and pipe joint components. Since the manufacturing process is not trivial, influences of manufacturing parameters were evaluated to ensure fibre architectures with most favourable properties while maintaining an economical fabrication process. A discussion on this subject is presented in Chapter 2, where also a review of the filament winding

method, the employed material system and essential physical properties of filament-wound composites is provided.

Due to aforementioned insufficiencies in modelling and predictability of damage in pressurised composite structures, emphasis was given to experimental analyses. Pipe structures are generally subjected to constant pressurisation; yet, fatigue loading conditions may be imposed upon pipe structures as well (McAllister, 1998). Cyclic loads may result from pressure fluctuations, and seasonal and daily changes in temperature, causing dimensional changes of the pipe structure itself and the environment the structure is installed in (e.g. the ground). Non-constant pressurisation is usually associated with the so-called waterhammer effect, which has its origin in the operation of valves and pumps (Gustafson and co-workers, 1993). In the present study, however, it was assumed that the frequency of pressure fluctuation is low and that the ratio between the applied minimum and maximum stresses is close to one. Moreover, qualification of large-scale pipe structures is generally performed using hydrostatic pressure testing, where applied pressures are substantially higher than those under operating conditions. Hence, monotonic testing under relevant biaxial loading ratios was considered adequate for the analyses. Testing was performed using in-house multi-axial test equipment, employing prototype-size samples as well as small-scale model specimens. A description of specimens, testing apparatuses and experimental procedures is given in Chapter 3.

Several fibre architectures were evaluated that are compatible with the filament winding process, and that varied in their lay-up configuration, lay-up sequence and degree of fibre compaction. Results pertaining to this study are presented in Chapter 4. Since two specimen sizes were utilised for the analyses, also an investigation on model-prototype scaling and size-effects was conducted.

In Chapter 5 the performance of plain prototype pipe and joined prototype structures was investigated. Since experimentally observed damage was found compatible with modelling techniques based on strength-of-materials and fracture mechanics principles, a theoretical approach was employed for the study of various joint geometry features. A parametric study was conducted arriving at a methodology for joint design optimisation.

CHAPTER 2

MANUFACTURING OF COMPOSITE TUBULAR STRUCTURES

2.1 Introduction to Filament Winding

Filament winding is a continuous fibre moulding process well suited for the production of tubular-shaped components (More complex shapes can be produced by employing additional processes). Filament winding has certain advantages over other composite fabrication techniques. A high degree of automation and the ability to use raw materials in their simplest form (i.e. fibres and uncured polymer resin) result in low material and labour cost, and good reproducibility (Kliger and Wilson, 1990; Peters et al., 1999.). For structures with high length-to-diameter ratios, such as pipe structures, helical winding machines are most suitable. (The other basic machine type are polar winders that are predominantly used for components with length/diameter ratios lesser than 1.5:1, see Kliger and Wilson, 1990). A filament winding installation is composed of several subsystems. These are the fibre delivery system (i.e. fibre tensioner, guiding devices and resin bath), mandrel, control system, curing oven and mandrel removal system. For the present research project an in-house helical filament winding installation was employed (Wolodko et al., 2001). The four axis, computer controlled winding machine was equipped with a unique numerically controlled tensioning device that allows for accurate fibre tension control. A description of the winding facility including its subcomponents is given in Appendix A.

Description of the filament winding process:

The filament winding process has the potential to produce laminated structures as well as highly complex (interwoven) fibre architectures. The degree of complexity may affect material properties and damage behaviour. Thus, a sound understanding of the winding process is required in order to decide on a suitable winding strategy, as well as to enable

the evaluation of material behaviour and structural performance. A description of the winding process is provided in the following. Note that subsequent considerations are limited to helical winding.

During the winding process, fibre is supplied from a translating delivery head onto a rotating mandrel. The delivery head of the present winding system is a circular pay-out eye mounted to the translating carriage arm of the filament winding machine. The winding angle, θ , which is determined by the ratio of the two relative motions, is measured with respect to the axis of the rotating mandrel. Winding angles range between 0° and 90° . Hoop winding is a special case of helical winding, where winding angles are of approximately 90° . Winding angles smaller than 45° tend to produce slippage of fibres along the mandrel. This is due to increased fibre forces along the mandrel axis. In such a case, devices called pin-rings are usually installed to prevent slippage.

During winding a resin-wet fibre band is deposited onto the mandrel surface in a helical pattern. A winding band usually consists of several fibre bundles called tows. Each tow consists of numerous filaments, and is individually dispensed from one creel. The linear relative weight of a single tow is described by the variable *TEX* (weight-per-unit-length).

A band of so-called nominal bandwidth, B , is required to produce complete coverage of the mandrel surface in one pass of the fibre delivery head. The nominal bandwidth is determined by the winding angle and the mandrel geometry. From the developed view of the mandrel surface shown in Fig. 2.1.1, the nominal bandwidth is given by

$$B = 2\pi R \cos(\theta) \quad (2.1.1)$$

where R is the mandrel radius.

During a pass of the fibre delivery head away from its home position, a layer with a $+\theta$ winding angle is being produced. On the return pass back to the home position, the corresponding $-\theta$ layer is deposited. During such a sequence, which is called a circuit, a double layer, i.e. a $\pm\theta$ cover is created. C is the number of circuits required for the completion of a single cover.

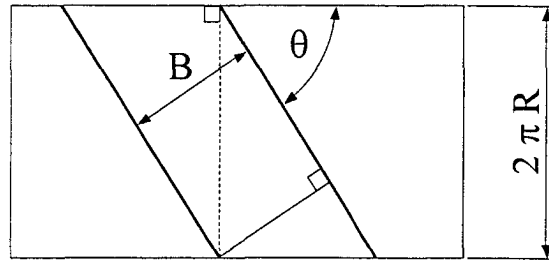


Figure 2.1.1: Developed view of the mandrel surface, and geometry of nominal winding band.

An actual winding band, b , is generally lesser in width than the nominal bandwidth, B . Thus, several circuits, C , are required to produce a complete cover. The location of subsequent bands may be adjacent-ahead or adjacent-behind a prior deposited band; this is termed lead or lag winding respectively. It is also possible to produce more complex winding patterns by separating consecutive winding bands by one or more shifts the size of a winding band. The actual bandwidth needs to be an integer fraction of the nominal bandwidth (i.e. $b = B/C$) to prevent any gapping or excessive overlapping. Note that the actual bandwidth is usually adjusted to provide a small overlap. This is done to account for the thinning of winding bands towards their shoulders, and to prevent gapping if small bandwidth fluctuations should occur. Gapping is unacceptable since areas of reduced or even missing reinforcement may be created. A repeatable and consistent bandwidth adjustment is therefore important for the production of quality parts. An investigation on bandwidth measurement and control is provided in Section 2.4.

If a winding band is of proper width to create complete mandrel coverage in one half circuit, a fibre architecture free of interweaving is produced. In this case a laminated structure with distinct layers is generated. This most likely occurs in the case of high winding angles (such as in hoop winding), where relatively small nominal bandwidths are required. However, if several circuits are necessary to produce a complete cover, an interwoven two-layer fibre architecture is created. Figure 2.1.2 shows a schematic of a winding process generating an interwoven fibre architecture. Here, three circuits are required to produce a $\pm\theta$ cover. Arrows denote the travel direction of the fibre delivery head. The developed mandrel surface is shown in dark colour, whereas the winding bands

are white and grey for the away and home travel direction respectively. After one and a half circuits 100% coverage is achieved, i.e. sufficient fibre material has been deposited to theoretically achieve complete coverage of the entire mandrel surface. Yet, due to the overlap of winding bands parts of the mandrel surface remain exposed, and an additional one and a half circuits are required to completely cover the mandrel.

Depending on the winding strategy filament-wound covers generally feature a certain 'degree of interweaving', which is the amount of undulations produced by crossovers of winding bands. In Subsection 2.2.3 a measure for the degree of interweaving is provided. (Note that interweaving is not unique to filament-wound structures. Fabrics used in composite production, such as in injection moulding procedures, and components produced by braiding also feature a high amount of undulations.)

Several covers with identical or different $\pm\theta$ fibre orientations are generally deposited onto the mandrel. The laminate geometry of a completed filament-wound tube is then

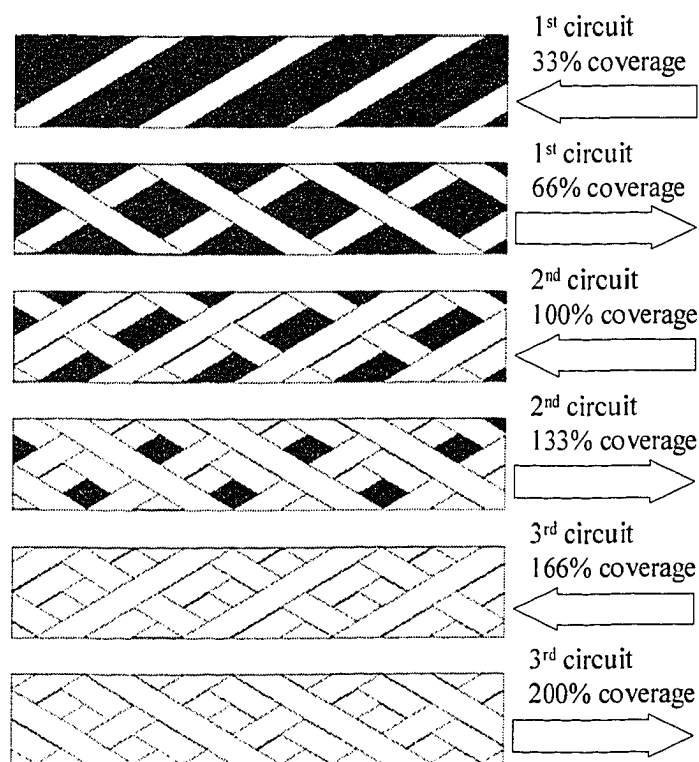


Figure 2.1.2: Schematic of a winding process for a three-circuits interwoven $\pm\theta$ cover.

defined by the fibre angles of each cover. A laminate geometry is coded by a sequence representing the cover order from the interior to the exterior of the tube. For example, $[\pm 45, \pm 60_2]_T$ denotes a three-cover fibre architecture, which features a $\pm 45^\circ$ cover on the inside of the tube followed by two $\pm 60^\circ$ covers.

2.2 Physical Properties of Filament-Wound Composites

In the present chapter, essential measures for the description of physical material properties of filament-wound composites are discussed. These measures will be used in subsequent investigations for the analysis and comparison of results. Necessary definitions are given, and theoretical foundations as well as measurement techniques are briefly explained. Thus, a framework for the interpretation of experimental as well as analytical results is provided.

2.2.1 Fibre Volume Fraction

The relative amount of fibre material in a composite is generally characterised by the fibre volume fraction. This parameter is of considerable importance, since it strongly affects stiffness and strength properties, among others. In a void-free fibre-reinforced composite of volume Vol with fibre volume Vol_f and matrix volume Vol_m , the fibre volume fraction, V_f , and the matrix volume fraction, V_m , are defined by

$$V_f + V_m = 1 \quad (2.2.1)$$

$$\text{with } V_f = Vol_f / Vol \text{ and } V_m = Vol_m / Vol \quad (2.2.1a \ \& \ b)$$

The theoretical maximum fibre volume fraction is given by the densest fibre packing within a unit volume. Note that in such a case, fibres come into contact with each other. For the square array fibre arrangement shown on the left-hand-side of Fig. 2.2.1, the maximum fibre volume fraction yields

$$V_f^{\max} = \frac{\pi R^2}{4R^2} = 0.785 \quad (2.2.2)$$

The highest fibre density is achieved by a hexagonal fibre array shown on the right-hand-side of Fig. 2.2.1. Here, the maximum fibre volume fraction becomes

$$V_f^{\max} = \frac{\pi R^2}{2\sqrt{3} R^2} = 0.906 \quad (2.2.3)$$

In practical applications these maximum values cannot be achieved since the fibre arrangement is not entirely uniform. Moreover, it is generally of little benefit to produce structures with fibre volume fractions close to the theoretical limits. As the matrix is required for transferring load between fibres, proper and complete coating of fibres with matrix material is crucial. Touching of fibres may also be considered flaws within the structure, since matrix damage may nucleate at these locations. Particularly transverse strength of fibre composites is affected negatively by high fibre volume fractions (Jang, 1994). During transverse loading, fibres act like hard inclusions. This enhances local stresses and strains in the material. Thus, high fibre volume fractions may lead to stress concentrations that cause reduced transverse strength. This occurs despite a gain in transverse modulus, which is raised by increasing the fibre compaction.

Based on a square fibre array, Kies (1962) provided a method for calculating the strain magnification effect due to increased fibre proximity in a square array model (see also Jang, 1994). In later work, Kok and Meijer (1999) confirmed that the analytical model of Kies reasonably approximates matrix strain magnifications. In terms of maximum matrix

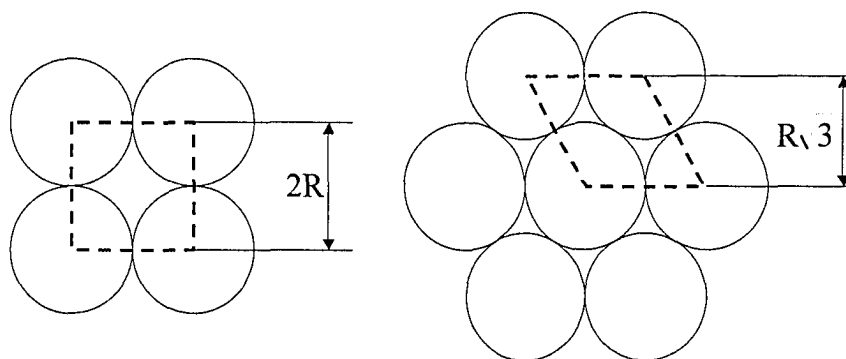


Figure 2.2.1: Close-packed uniaxial bundles of fibres with a fibre arrangement in square (left) and hexagonal (right) arrays.

strain, ε_{mu} , the ultimate transverse strain of the fibre composite, ε_{2u} , is reduced according to the following expression.

$$\frac{\varepsilon_{2u}}{\varepsilon_{mu}} = 1 - \sqrt{4V_f/\pi} [1 - (E_m/E_f)] \quad (2.2.4)$$

where E_m and E_f are the matrix and fibre Young's moduli respectively.

In Figure 2.2.2 the strain magnification effect is shown for the glass-fibre/epoxy material system used in the current study (see Section 2.3 for details on material properties). A significant reduction of the ultimate transverse strain can be observed with increasing fibre compaction. At 50% fibre volume fraction, for example, 24% of the ultimate matrix strain remains as the maximum transverse strain; this value is reduced to approximately 6% at 75% fibre volume fraction. These results underline the importance of considering fibre volume fraction during the design phase, as well as the necessity of controlling it during component production.

Fibre volume fraction measurement:

Several techniques have been reported for the measurement of fibre volume fraction (see e.g. Carlsson and Pipes, 1997). Most common are techniques that remove the

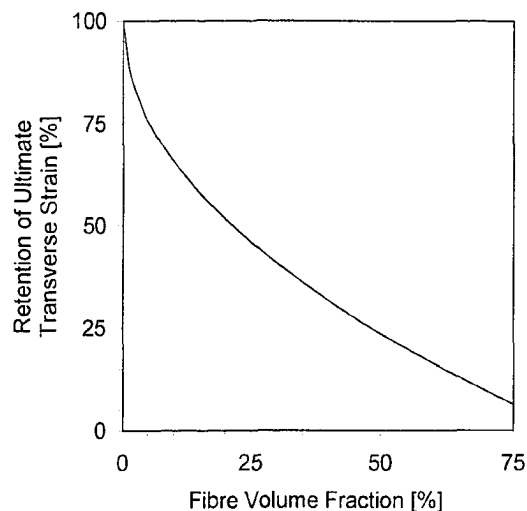


Figure 2.2.2: Retention of ultimate transverse strain with increasing fibre volume fraction based on a glass-fibre/epoxy material system used in the current study.

matrix material from the fibres. This can be achieved using chemical digestion techniques such as described in ASTM D3171 (1999), or matrix ignition methods, i.e. resin burn-off techniques (e.g. ASTM D2584, 2002). In either case, sample weights m_c and m_f are taken before and after the matrix removal process respectively. Knowledge of the densities of the matrix, ρ_m , and the fibre material, ρ_f , is required for a fibre volume fraction calculation according to Eq.(2.2.5).

$$V_f = \frac{\rho_m m_f}{\rho_m m_f + \rho_f (m_c - m_f)} \quad (2.2.5)$$

In the present study, the polymeric matrix was removed from the fibres according to ASTM D2584 (1994), i.e. by subjecting a minimum of three material samples in ceramic crucibles to an oxidation temperature of 538°C (1000°F) for three hours within a muffle furnace. In most cases, the outside surfaces of tubular samples were machined prior to the burn-off procedure, exposing the fibres on the top cover of the fibre bed. This preparation step was performed for the following reason. During the winding process the accumulation of excess resin produced a resin coat on the outside surface of tubular parts. The photomicrograph of a partial specimen cross-section in Figure 2.2.3 shows this resin coat, where inconsistency in thickness is clearly discernible.

The resin built-up exhibited significant variations in thickness over the surface of a specimen. This resulted in considerable data scatter when fibre volume fractions were measured without removing the resin built-up. Since the resin rich zones are practically

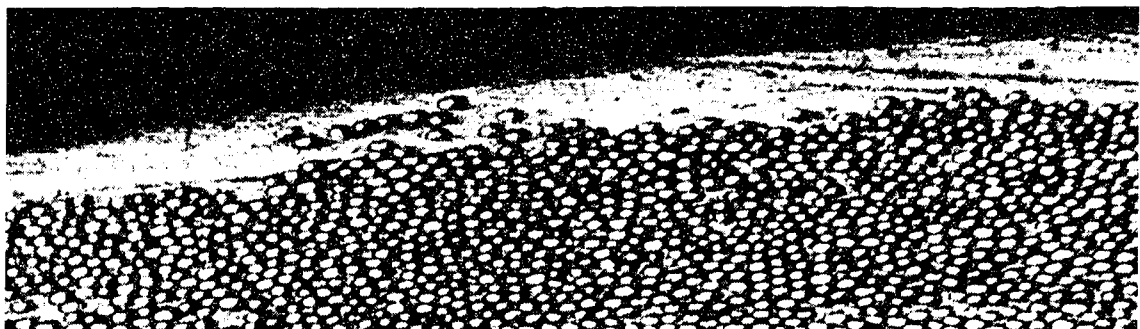


Figure 2.2.3: Photomicrograph of a partial cross-section of a filament-wound specimen showing the resin coat on the outside surface of a specimen.

free of fibre reinforcement, the resin built-up is not expected to contribute appreciably to stiffness or strength of the structure. Thus, the machining process was introduced, which yielded more consistent results albeit with higher fibre volume fraction values. The effect of removing the resin built-up is discussed further in Subsection 2.4.2.

Note that the abovementioned matrix removal methods generally eliminate any fibre sizing as well (i.e. a polymeric compound applied to the filaments to promote wetting and adhesion with the polymeric matrix material, and improve abrasion resistance). Standards for the determination of fibre volume fraction such as ASTM D2584 do not account for any fibre sizing loss. However, the amount of sizing applied to the surface of the glass material is approximately 1% by weight (Loewenstein, 1983). Thus, inaccuracies incurred by neglecting the presence of fibre sizing are generally considered negligible.

Other techniques for measuring fibre volume fraction employ photomicrographs of polished samples showing the fibre cross-sections (e.g. Cohen et al., 2001). Assuming a constant fibre-matrix ratio in direction perpendicular to the cross-sectional area, the fibre volume fraction is determined by the ratio of fibre area, A_f , to the total sample area, A :

$$V_f = A_f / A \quad (2.2.6)$$

Area measurements may be obtained employing manual as well as automatic techniques. However, only small sample areas can be captured by photomicrographs, and the fibre volume fraction may vary by location. Thus, numerous samples need to be analysed to give a representative result. This makes computerised image analysis techniques advantageous. Since the accessibility to such advanced equipment was limited, and the present study required the investigation of numerous specimens, the photomicrograph method was considered too cumbersome.

2.2.2 Void Content

During the manufacturing and curing process, insufficient wetting of fibres, entrapment of air and chemical reactions may cause gases and volatiles to remain as voids within the matrix material. The void content, V_v , is defined as follows:

$$V_f + V_m + V_v = 1 \quad (2.2.7)$$

Since voids may introduce stress concentrations and act like crack-like flaws (Rodopoulos, 2000), processes are generally optimised to reduce the void content to a minimum. Müller de Almeida and dos Santos Nogueira Neto (1994) showed that exceeding a critical level of porosity (i.e. 3%) has a detrimental effect on strength and fatigue life of carbon composites. In autoclave-cured parts a void content of less than 1% is commonly required (Carlsson and Pipes, 1997). In filament-wound components the level of porosity may be much greater (Peters et al., 1999). Rousseau (1997) reported the void content in filament-wound tubes to range from 2.0% to 2.5%. However, localised void contents of 5-10% were reported in areas with high void concentration. Areas of high porosity are particularly found in undulation regions, i.e. locations of the crossing-over of winding bands (Rousseau et al., 1999).

Void content can be quantified using a matrix burnout procedure (ASTM D2734, 2003), or photomicrographic techniques. To determine void content with a matrix burnout procedure, the density of the composite, ρ_c , needs to be determined with high accuracy. Appropriate procedures can be found in e.g. ASTM D792 (2000), ASTM D1505 (1998) and ASTM D3800 (1999). Assuming voids of zero weight, the void content can be calculated by Eq.(2.2.8).

$$V_v = \frac{m_c - (m_f / \rho_f + (m_c - m_f) / \rho_m) \rho_c}{m_c} \quad (2.2.8)$$

In the present case void content was determined for a sample specimen using an area fraction methodology and photomicrographs. A sample of a filament-wound tube was sectioned, polished and plated with a thin gold film. Images at five different locations around the circumference of the tube were taken using a scanning electron microscope (SEM). SEM imaging was employed for this task, since light microscope images were found to lack the depth-of-field and contrast for proper void recognition. Images were taken using magnification factors ranging from X50 to X100. Each image roughly covers an area of magnitude to the wall thickness square. Images are shown in Fig.2.2.4, and a magnified view of typical void is presented in Fig.2.2.5.

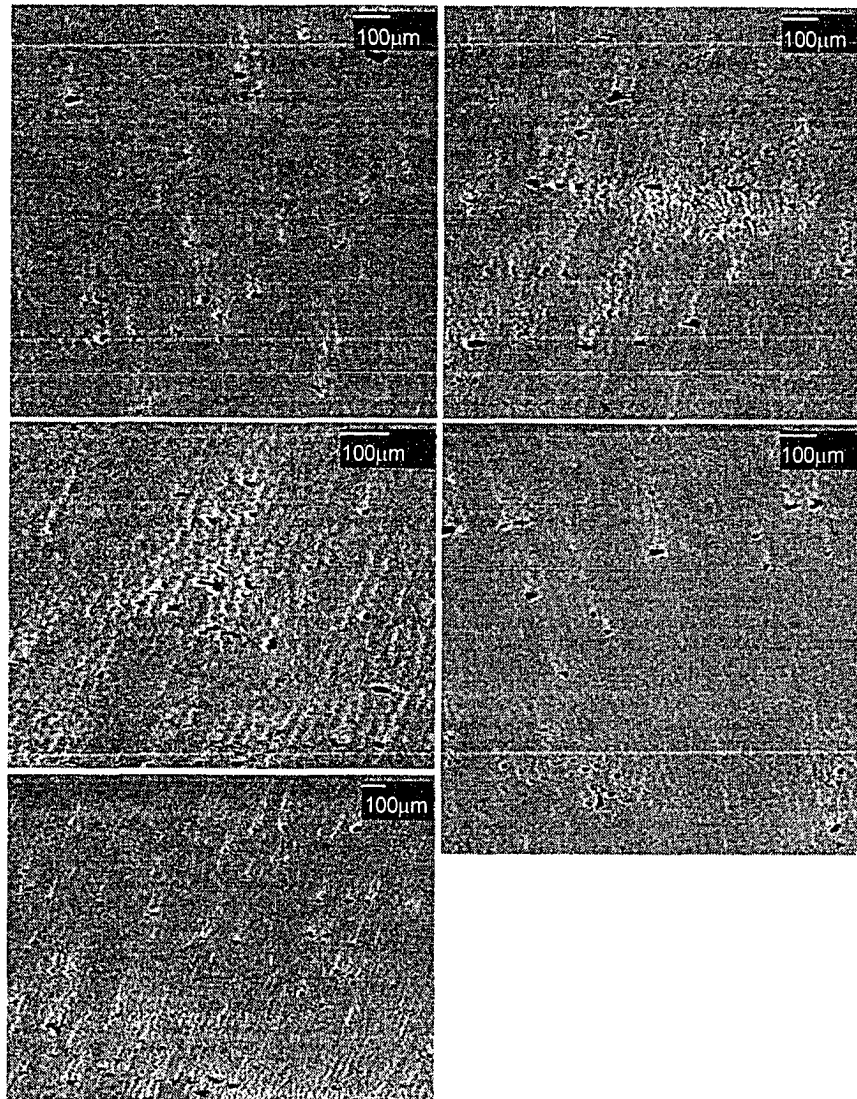


Figure 2.2.4: Micrographs showing voids (dark areas) in a filament-wound specimen.

Image analysis software (MATROX Inspector[®]) was employed for the measurement of area fractions of the five sample images, which is seen to reasonably approximate void fraction. Assuming a normal (standard) distribution for the sample data the average void area fraction is $0.7\% \pm 0.3\%$ for a confidence level of 99%. (Data variability is 0.3% measured by the standard deviation, see Eq.(2.2.9).) These values indicate that void fractions of present specimens are not necessarily within the aforementioned quality bounds (i.e. smaller than 1%), but still below the levels given in literature for other filament-wound structures.

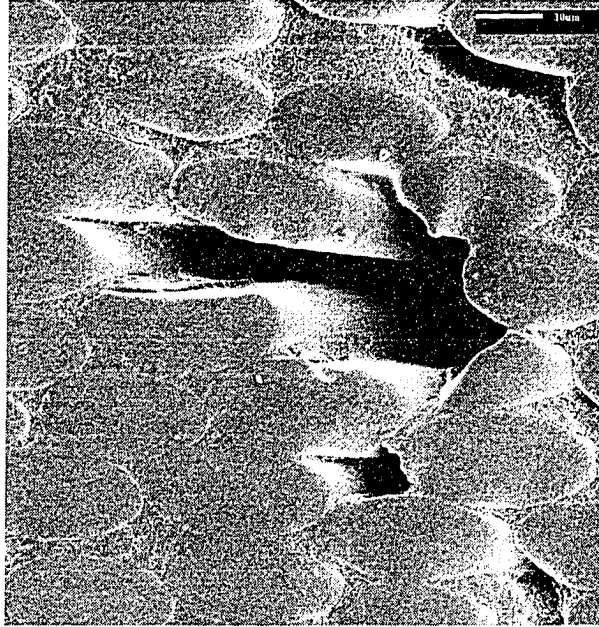


Figure 2.2.5: SEM micrograph magnification of a void in a filament-wound specimen.

$$s_N = \sqrt{\frac{N \sum_{i=1}^N x_i^2 - \left(\sum_{i=1}^N x_i \right)^2}{N^2}} \quad (2.2.9)$$

where s_N is the standard deviation with x_i are the elements of a data set with N elements.

2.2.3 Degree of Winding Band Interweaving

The degree of interweaving and its influence on component properties has been subject of several investigations. Zakrzhevskii and Khitrov (1988) investigated the performance of multi-angle composite tubes under torsion. An influence of the degree of interweaving on the in-plane shear modulus could not be found; however, the load-carrying capacity of certain specimens was increased by 50% by interweaving the fibres. In a later study Tarnopol'skii et al. (1996) established that increasing the degree of interweaving results in an increase in in-plane shear strength. Lossie et al. (1989) examined filament-wound specimens using a ring-split tensile test. Reinforcements were inclined to the load direction by $\pm 25^\circ$. Shear type failures were observed for specimens that were practically free of interweaving. For high degrees of interweaving failure

modes became increasingly fibre-dominated. Lossie et al. concluded that interweaving has a negligible effect on stiffness; however, a significant strengthening effect was observed. On the contrary, Rousseau et al. (1997 and 1999) recommended minimising the amount of interweaving. In tests on $\pm 55^\circ$ filament-wound tubular specimens under various biaxial loading conditions, they observed negligible or negative influences of interweaving on component strength and leakage thresholds, depending on the loading scenario. Tests furthermore revealed a minimal effect of interweaving on stiffness. Rousseau et al. (1999) suggested that improvements due to increased interweaving are limited to structures subjected to shear loading, which agrees well with aforementioned research results.

Measuring the degree of interweaving:

In the present study it was general practise to minimise the number of undulations by maximising the winding bandwidth. However, a certain degree of interweaving was inevitable, particular in the case of structures with large diameters. In order to assess possible interweaving effects, a measure for the degree of interweaving was adopted from Rousseau et al. (1999). The degree of interweaving, D_r , was defined as the percentage of disturbed area in an elementary cell of the winding pattern,

$$D_r = \frac{\text{undulation area}}{\text{unit cell area}} = \frac{A_u}{A_0} \quad (2.2.10)$$

Note that other definitions for the interweaving degree are available (e.g. Liang and Luo, 1996 and 1997; Tarnopol'skii et al., 1996). These methods quantify the interweaving degree based on an undulation count. However, the method by Rousseau et al. is advantageous, since an area-based definition makes this method independent from the width of the applied winding band. Hence, it is applicable to various woven structures.

A diamond-shaped unit cell with area A_0 is shown on the left-hand-side of Fig. 2.2.6. It is composed of C^2 diamond-shaped sub-areas shown on the right-hand-side of Fig. 2.2.6. From the geometry conditions given in Fig. 2.2.6, and the definition of winding bandwidth, see Eq.(2.1.1), the unit cell area is calculated according to Eq.(2.2.11).

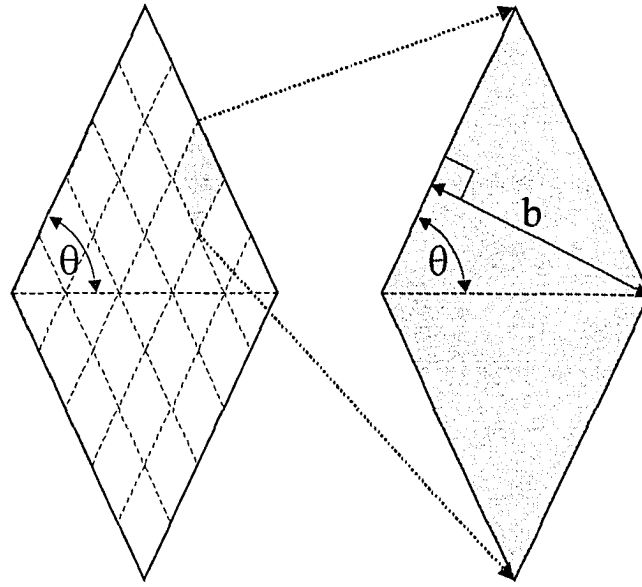


Figure 2.2.6: Filament winding unit cell (left) with sub-areas, and single sub-area with dimensions (right).

$$A_0 = \frac{2\pi^2 R^2}{\tan \theta} \quad (2.2.11)$$

Rousseau et al. introduced a parameter, N_c , for the number of circuits performed until the winding band is deposited adjacent to the first circuit. The greater is the parameter N_c , the more undulations are present within the structure. N_c can be determined arithmetically, or by graphically simulating the winding process. (The reference provides further information on this subject.) The latter method was used in the current study. From N_c , the number of undulations within a unit cell, N_u , is obtained according to

$$N_u = 4N_c(C - N_c) \quad (2.2.12)$$

The disturbed area within a unit cell, A_u , is calculated by multiplying N_u with the bandwidth, b , and the undulation length, L_u . From micrographs, Rousseau et al. measured the latter value to be 6 to 10 times the tow thickness (i.e. a half cover thickness, t'). In the current study, L_u is assumed to be 8 times the tow thickness. This is considered a reasonable assumption for all specimens used in this study since (a) identical reinforcement and matrix materials were used for all specimens; (b) the parameter D_T was

solely used for comparing the degree of interweaving between specimens (i.e. not for e.g. damage analysis); and (c) the degree of interweaving was only compared among specimens wound with the same winding tension. From the above considerations, the degree of interweaving is given by Eq.(2.2.13).

$$D_r = \frac{4N_u t' b \tan \theta}{\pi R^2} \quad (2.2.13)$$

2.2.4 Engineering Elastic Constants

In the present study, engineering material constants were required for modelling purposes, and comparison of analytical and experimental results. Several models for the calculation of elastic constants of interwoven fibre-composites have been presented (e.g. Ishikawa and Chou, 1982a,b and 1983; Carey et al., 2003). A summary on this subject was provided by Tong et al. (2002). But, these models were developed for textile composites, which generally feature a high degree of interweaving. As discussed in the preceding section, the effect of interweaving on stiffness is typically negligible for filament-wound composites. Anlaş et al. (1997) calculated elastic moduli of filament wound tubes based on lamination theory, and good agreement between calculated and experimental values was ascertained. The same approach was suggested by Kollár and Springer (2003). Smith and Swanson (1995) concluded that even for braided composites, lamination theory predicted stiffness on average as well as more involved models. Therefore, the following framework for the calculation of elastic moduli was adopted, which is based on micromechanics and lamination theory.

Engineering constants were determined in a two-step procedure. In a first step, elastic properties for a unidirectional lamina were derived from the constituent properties using micromechanics. In a second step, lamination theory was used to calculate elastic moduli for an orthotropic $\pm\theta$ cover. A filament-wound cover can be thought of as an interwoven structure of two unidirectional laminae. It is generally not possible to discern a lamina sequence, i.e. which lamina is on the top or at the bottom of a cover. Thus, properties of the $+\theta$ lamina and the $-\theta$ lamina were smeared such as to equal a homogeneous orthotropic material. The resultant homogeneous orthotropic cover properties were then

available for subsequent investigations employing numerical techniques (finite element analysis) and analytical models (classical lamination theory).

Determination of elastic moduli of unidirectional laminae using micromechanics:

Several micromechanical models for calculating engineering constants of unidirectional laminae from constituent properties have been given in literature (see e.g. Jang, 1994; Kaw, 1997; Hyer, 1998; Rosen and Hashin, 1987; and Xia et al., 2003). These include the strength of materials approach, numerical models based on e.g. finite element solutions, and elasticity solutions such as the composite cylinder assemblage model. It was shown that the strength of materials approach does not agree well with experimental results (Kaw, 1997), whereas the latter techniques are only available in graphical form or as complicated equations. This led to more convenient semi-empirical methods such as the one provided by Halpin and Tsai, see e.g. Halpin and Kardos (1976), Jang (1994) and Kaw (1997). Based on curve fitting to elasticity solutions they derived a simple set of equations for laminae under plane-stress conditions. Results produced by this method were found to agree well with experiments for a wide range of material combinations and fibre volume fractions, see Jang (1994). This was confirmed by Rosenow (1984), who found that up to the point of non-linearity the elastic response of filament-wound tubes was predicted accurately by the Halpin-Tsai model in combination with lamination theory. Note that the Halpin-Tsai equations were found to under-predict some elastic moduli for fibre volume ratios exceeding 70% (Halpin and Kardos, 1976).

Four parameters are sufficient to describe the elastic properties of the constituents (Note that this assumes isotropic constituent materials.). These are the fibre and matrix Young's moduli, E_f and E_m , and the respective Poisson's ratios, ν_f and ν_m . The corresponding shear moduli are derived according to

$$G = \frac{E}{2(1+\nu)} \quad (2.2.14)$$

A unidirectional lamina is considered transversely isotropic; thus, four in-plane elastic moduli (illustrated in Fig.2.2.7) are required to describe deformations under plane-stress conditions.

In the following the corresponding Halpin-Tsai equations are given.

Longitudinal Young's modulus: $E_L = E_f V_f + E_m V_m$ (2.2.15)

Transverse Young's modulus: $E_T = E_m \frac{1 + \xi_{E_T} \eta_{E_T} V_f}{1 - \eta_{E_T} V_f}$ (2.2.16)

where $\eta_{E_T} = \frac{(E_f/E_m) - 1}{(E_f/E_m) + \xi_{E_T}}$ (2.2.16a)

The so-called reinforcing factor, ξ_{E_T} , needs to be chosen based on the fibre geometry, fibre packing arrangement and loading conditions. For a circular fibre in a square array, $\xi_{E_T} = 2$ (Kaw, 1997), which is considered to sufficiently approximate a random fibre packing.

Longitudinal major Poisson's ratio: $\nu_{LT} = \nu_f V_f + \nu_m V_m$ (2.2.17)

Longitudinal shear modulus: $G_{LT} = G_m \frac{1 + \xi_{G_{LT}} \eta_{G_{LT}} V_f}{1 - \eta_{G_{LT}} V_f}$ (2.2.18)

where $\eta_{G_{LT}} = \frac{(G_f/G_m) - 1}{(G_f/G_m) + \xi_{G_{LT}}}$ (2.2.18a)

and $\xi_{G_{LT}} = 1 + 40V_f^{10}$ (2.2.18b)

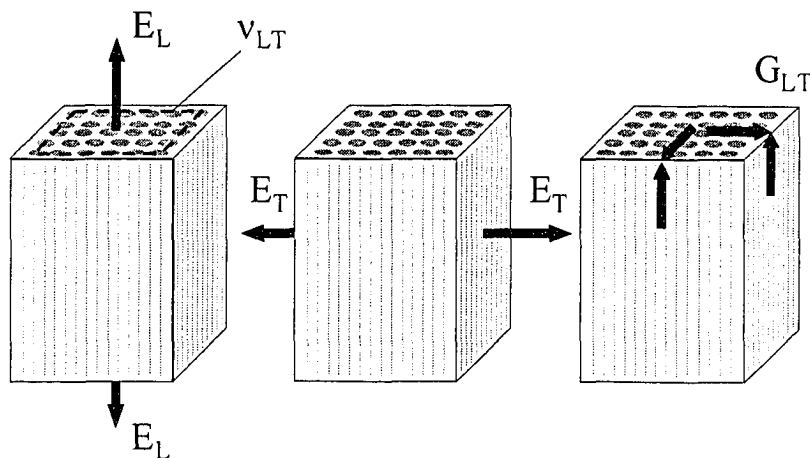


Figure 2.2.7: Elastic properties and associated loadings of a transversely isotropic unidirectional lamina under plane-stress conditions.

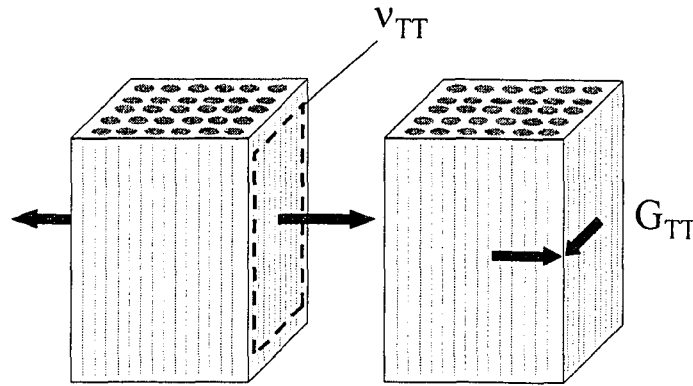


Figure 2.2.8: Additional elastic properties for out-of-plane loading conditions.

Certain investigations (i.e. numerical modelling of fracture damage events) do not permit the assumption of a plane-stress condition, because out-of-plane loadings need to be considered. Therefore, two more elastic moduli were required in addition to the four elastic moduli from the Halpin-Tsai model. These moduli are the transverse shear modulus, G_{TT} , and transverse Poisson's ratio, ν_{TT} , illustrated in Fig.2.2.8.

Since the Halpin-Tsai equations are based on an elasticity solution, the composite cylinder assemblage model was chosen to provide the missing parameters according to the following equations, see e.g. Hashin (1983) and Rosen and Hashin (1987). Note that this empirical model (among others) was compared with a finite element based meso/micro-mechanical unit cell model proposed by Xia et al. (2003); good agreement between the results from two models, and experimental data was ascertained.

$$G_{TT} = G_m \left[1 + \frac{(1 + \beta_m)V_f}{\rho - [1 + 3\beta_m^2 V_m^2 / (\alpha V_f^3 + 1)]V_f} \right] \quad (2.2.19)$$

$$\text{where } \alpha = \frac{\beta_m - \gamma \beta_f}{1 + \gamma \beta_f} \quad \rho = \frac{\gamma + \beta_m}{\gamma - 1} \quad (2.2.19a-b)$$

$$\text{and } \beta_m = \frac{1}{3 - 4\nu_m} \quad \beta_f = \frac{1}{3 - 4\nu_f} \quad \gamma = \frac{G_f}{G_m} \quad (2.2.19c-e)$$

Lastly, the transverse Poisson's ratio is found according to Eq.(2.2.14) using the transverse Young's and shear modulus.

Elastic moduli of an orthotropic cover:

The elastic moduli of a cover were computed by first defining a property matrix according to Eq.(2.2.20) for each of the two (interwoven) laminae.

$$\{\varepsilon_{lamina}\}_{lamina} = [S] \cdot \{\sigma_{lamina}\}_{lamina} \quad (2.2.20)$$

where $\{\sigma_{lamina}\}$ and $\{\varepsilon_{lamina}\}$ are the lamina stresses and strains respectively.

The compliance matrix, $[S]$, is given by

$$[S] = \begin{bmatrix} 1/E_L & -\nu_{TL}/E_T & -\nu_{TL}/E_T & \cdot & \cdot & \cdot \\ -\nu_{LT}/E_L & 1/E_T & -\nu_{TT}/E_L & \cdot & \cdot & \cdot \\ -\nu_{LT}/E_L & -\nu_{TT}/E_L & 1/E_T & \cdot & \cdot & \cdot \\ \cdot & \cdot & \cdot & 1/G_{TT} & \cdot & \cdot \\ \cdot & \cdot & \cdot & \cdot & 1/G_{LT} & \cdot \\ \cdot & \cdot & \cdot & \cdot & \cdot & 1/G_{LT} \end{bmatrix} \quad (2.2.21)$$

A matrix transformation was applied according to Eq.(2.2.22) to produce the material properties of the lamina in the global coordinate system of the tubular structure, where X, Y and Z denote the axial, hoop and radial direction respectively. (Note that a different coordinate convention is required for axisymmetric analyses by the finite element software employed for the investigation of adhesive joint behaviour, see Chapter 5: Subsection 5.7.1.)

$$[\bar{Q}] = [M]^T \cdot [Q] \cdot [M] = [M]^T \cdot [S]^{-1} \cdot [M] \quad (2.2.22)$$

$$\text{where } [M] = \begin{bmatrix} m^2 & n^2 & \cdot & \cdot & \cdot & -mn \\ n^2 & m^2 & \cdot & \cdot & \cdot & mn \\ \cdot & \cdot & 1 & \cdot & \cdot & \cdot \\ \cdot & \cdot & \cdot & m & n & \cdot \\ \cdot & \cdot & \cdot & -n & m & \cdot \\ 2mn & -2mn & \cdot & \cdot & \cdot & m^2 - n^2 \end{bmatrix} \quad (2.3.22)$$

$$\text{with } m = \cos(\theta), n = \sin(\theta).$$

Finally, e.g. see Kollár and Springer (2003), the elastic properties of a $\pm\theta$ cover were obtained according to

$$[A_{cover}] = \frac{1}{2}([\bar{Q}_{+\theta}] + [\bar{Q}_{-\theta}]) = \frac{1}{2}([M_{+\theta}]^T \cdot [Q] \cdot [M_{+\theta}] + [M_{-\theta}]^T \cdot [Q] \cdot [M_{-\theta}]) \quad (2.2.24)$$

The components of $[\bar{A}_{cover}] = [A_{cover}]^{-1}$ have the following properties:

$$E_{XX} = \bar{A}_{cover,11}^{-1} \quad G_{XY} = \bar{A}_{cover,66}^{-1} \quad \nu_{XY} = -\frac{\bar{A}_{cover,21}}{\bar{A}_{cover,11}} \quad (2.2.24a-c)$$

$$E_{YY} = \bar{A}_{cover,22}^{-1} \quad G_{XZ} = \bar{A}_{cover,55}^{-1} \quad \nu_{XZ} = -\frac{\bar{A}_{cover,31}}{\bar{A}_{cover,11}} \quad (2.2.24d-f)$$

$$E_{ZZ} = \bar{A}_{cover,33}^{-1} \quad G_{YZ} = \bar{A}_{cover,44}^{-1} \quad \nu_{YZ} = -\frac{\bar{A}_{cover,32}}{\bar{A}_{cover,22}} \quad (2.2.24g-i)$$

Note that for plane-stress conditions the preceding calculation was reduced to the two-dimensional case (Hyer, 1998). From the above results the elastic moduli for an entire tubular structure can be determined employing classical lamination theory (see e.g. Gürdal et al., 1999; Halpin, 1984; Hyer, 1998; and Jang, 1994) or numerical techniques (finite element analysis).

2.2.5 Specimen Wall Thickness

Since the calculation of stresses, among others, depends on the specimen wall thickness, it is imperative to determine this parameter in a consistent and repeatable manner. It is generally difficult to obtain consistent wall thickness measurements of filament-wound specimens using devices such as calliper gauges. The reason is the aforementioned resin coat on the surface of filament-wound parts. It is not feasible to remove the resin layer by machining without also taking away fibre material. Employing photomicrographs for wall thickness measurements is possible. However, since this method only produces highly localised results, a large number of sample images would be required for a single specimen. The photomicrograph method is therefore too cumbersome if large numbers of specimens need to be investigated. Hence, an analytical technique was required to reliably and conveniently determine wall thickness. A method

for calculating an effective wall thickness of filament-wound specimens was given by Mertiny and Ellyin (2001). The effective wall thickness will be used in the remainder of this study for the determination of stress values. For convenience it is henceforth simply referred to as specimen wall thickness, s .

A specimen wall thickness was defined as the sum of thickness of all covers, i.e.

$$s = \sum_{i=1}^n t_i \quad (2.2.25)$$

with t_i being the thickness of the i -th cover of a total of n covers.

Assuming a void-free structure the thickness of an individual cover depends on the amount of deposited glass-fibre material and the fibre volume fraction. From the amount of fibre material in a winding band of length L_b the following equation is derived.

$$Vol_f L_b^{-1} = A_f = TEX TOW \rho_f^{-1} \quad (2.2.26)$$

where TEX is the linear tow weight, and TOW is the number of wound tows.

From Eq.(2.2.1a), the cross-sectional area of a winding band, A , is found:

$$A = TEX TOW \rho_f^{-1} V_f^{-1} \quad (2.2.27)$$

Assuming a uniform cover thickness yields a rectangular winding band cross-section (as shown on the left-hand-side of Fig. 2.2.9). Therefore, Eq.(2.2.27) becomes

$$b t' = TEX TOW \rho_f^{-1} V_f^{-1} \quad (2.2.28)$$

From the right-hand-side of Fig. 2.2.9, which shows a developed view of the mandrel surface and the geometry of the winding band, the thickness of a cover can be derived according to

$$t = \frac{TEX TOW C}{\rho_f V_f \pi R \cos \theta} \quad (2.2.29)$$

Note that the cover thickness is given by $t = 2 t'$.

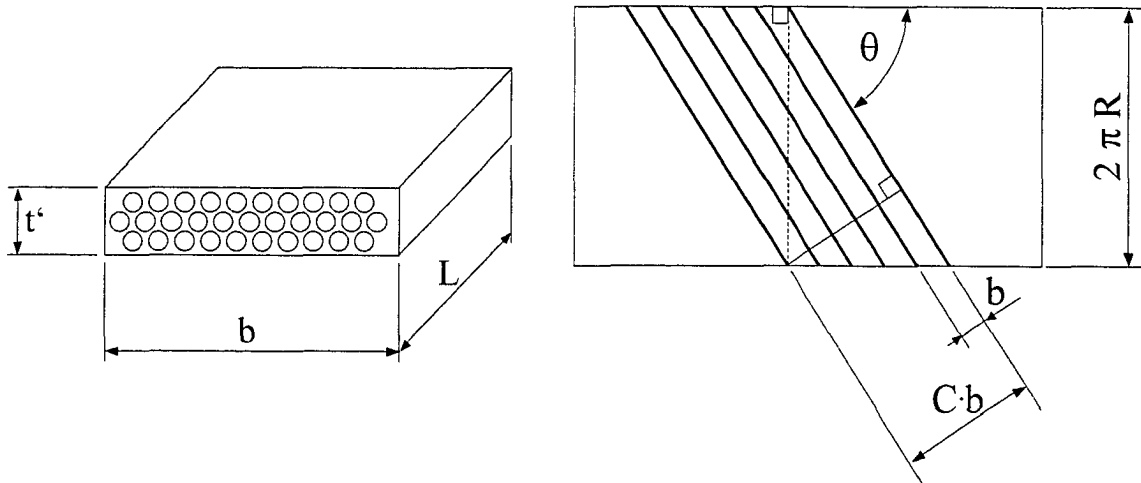


Figure 2.2.9: Dimensions of an idealised rectangular winding band cross-section (left); and developed view of the mandrel surface, and geometry of winding bands (right).

Strictly speaking, Eq.(2.2.29) is only valid for the first deposited cover. A more general expression for any i -th cover is given by

$$t_i = \frac{TEX TOW C_i}{\rho_f V_f \pi (R + \sum_{j=1}^i t_{j-1}) \cos \theta_i} \quad (2.2.30)$$

Note that an expression similar to the above was given by Peters et al. (1999). But instead of using typical tow properties (i.e. TEX , TOW , ρ_f and C), they based their method on a cross-sectional area of a typical roving, which was denoted the CSA value.

Influence of interweaving:

A wall thickness calculation according to Eq.(2.2.30) does not consider the effect of interweaving, since any out-of-plane transition of winding bands is not taken into account. In comparison to a laminated structure, an extra length of fibre material is necessary for the transition from one plane to another. The schematic shown in Fig.2.2.10 indicates this effect. Here, two extreme cases of a laminated cross-ply (top of figure) and a similar, however, totally interwoven structure (bottom of figure) are shown. The effect of interweaving on the cover thickness was approximated based on the ratio of unit cell areas of the two cases. The difference in average cover thickness is given by Eq.(2.2.31).

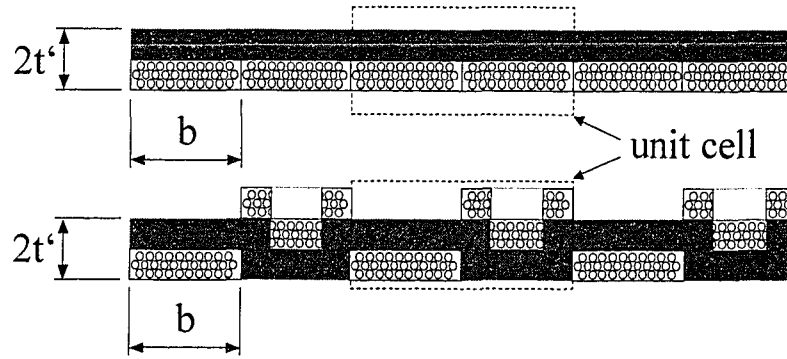


Figure 2.2.10: Schematic of laminated (top) and fully interwoven (bottom) cross-ply cover.

$$\frac{t_{undulated, average}}{t_{laminated, average}} = 1 + \frac{t'}{2b} \quad (2.2.31)$$

For the two different sizes of $\pm 60^\circ$ angle-ply specimens investigated in the current, i.e. small-scale models and large-scale prototypes, the cover and bandwidth dimensions were approximately 0.2 mm and 19 mm, and 0.5 mm and 26 mm, respectively. This yields a maximum difference in cover thicknesses between laminated and totally interwoven structures of 0.5% and 1% respectively. However, winding patterns used in this study feature a significantly lower degree of interweaving. Thus, the difference between calculated and actual cover thickness are expected to be considerably less than the aforementioned values, i.e. they are within the measurement accuracy of other key parameters such as the material densities. For this reason, the method presented for calculating wall thickness is considered adequate for providing consistent, repeatable, and accurate results.

2.2.6 On the Effect of Using Average Laminate Properties

Measurement techniques such as the matrix ignition method (see Subsection 2.2.1) yield an average fibre volume fraction for a complete sample. For convenience, Eq.(2.2.30) is intended to be used with an average fibre volume fraction. However, the degree of fibre compaction most likely varies with the thickness of a specimen due to (a) different levels of fibre compaction forces from the deposition of subsequent covers, and (b) differences in cover winding angles. The question then arises whether the use of

an average fibre volume fraction for the calculation of specimen wall thickness produces accurate results? This will be addressed in the following. Micromechanics and classical lamination theory were employed for this purpose. Note that for the subsequent investigation fibre plies of identical thickness were assumed. This assumption may not hold for thick laminates, where considerable variations in ply thickness may occur.

Consider the limit case of a unidirectional laminate of thickness, s , with an average fibre volume fraction of $V_{f,a}$. The laminate is assumed to be composed of two plies of areas A_1 and A_2 . Both plies are made from identical materials; however, they have different fibre volume fractions, V_1 and V_2 . Since the distribution of fibre material is constant between the two plies for any given laminate cross-section,

$$A_f = A_{f,1} + A_{f,2}$$

From Eq.(2.2.6) a relation for the average and the individual ply fibre volume fractions is found:

$$V_{f,a} = \frac{V_{f,1} A_1 + V_{f,2} A_2}{A_1 + A_2} \quad (2.2.32)$$

Assuming both plies to be of equal width and to have identical fibre cross-sectional areas, yields Eq.(2.2.33). This assumption was made for the issue at hand, i.e. to simulate a fibre volume fraction gradient across a composite layer.

$$A_f / 2 = A_{f,1} = A_{f,2} \quad (2.2.33)$$

Based on these assumptions, Eqs.(2.2.34) and (2.2.35) are found that completely determine the average laminate thickness and respective individual ply dimensions.

$$V_{f,1} t_1 = V_{f,a} t_a \quad \text{with} \quad t_a = s/2 \quad (2.2.34)$$

$$t_2 = 2t_a - t_1 \quad (2.2.35)$$

Based on above considerations, the interdependence of both ply fibre volume fractions can be computed. This is shown in Fig.2.2.11, assuming an average laminate fibre volume fraction of 70% for the glass-fibre/epoxy material system used in the present study (see Section 2.3 for details on material properties).

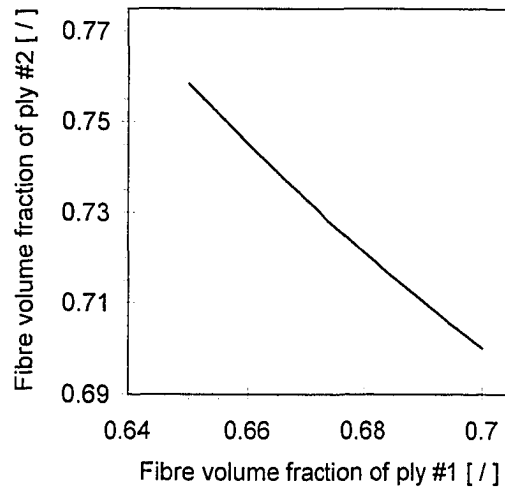


Figure 2.2.11: Interdependence of fibre volume fractions for a two-ply unidirectional laminate with an average fibre volume fraction of 70%.

Besides the dimensional properties of the individual plies, engineering constants may be affected by ply-to-ply variations in fibre volume fraction as well. Thus, elastic properties based on (a) individual ply fibre volume fractions and (b) an average laminate value will be compared in the following. For a plane stress condition, a compliance matrix, $[S]$, for each ply can be given according to Eq.(2.2.36).

$$[S] = \begin{bmatrix} E_L & -\nu_{LT}/E_L & \cdot \\ -\nu_{LT}/E_L & E_T & \cdot \\ \cdot & \cdot & G_{LT} \end{bmatrix} \quad (2.2.36)$$

where E_L , E_T , ν_{LT} and G_{LT} are given by Eq.(2.2.15-18).

Note that for a unidirectional laminate any transformation matrix reduces to the identity matrix. Thus, the laminate extensional stiffness matrix, $[A]$, is simply given by

$$A_{ij} = (Q_{ij})_1 t_1 + (Q_{ij})_2 t_2 = (S_{ij}^{-1})_1 t_1 + (S_{ij}^{-1})_2 t_2 \quad (2.2.37)$$

From the laminate extensional compliance matrix, $[\bar{A}] = [A]^{-1}$, the elastic moduli of the laminate are found according to Eqs.(2.2.37a-d).

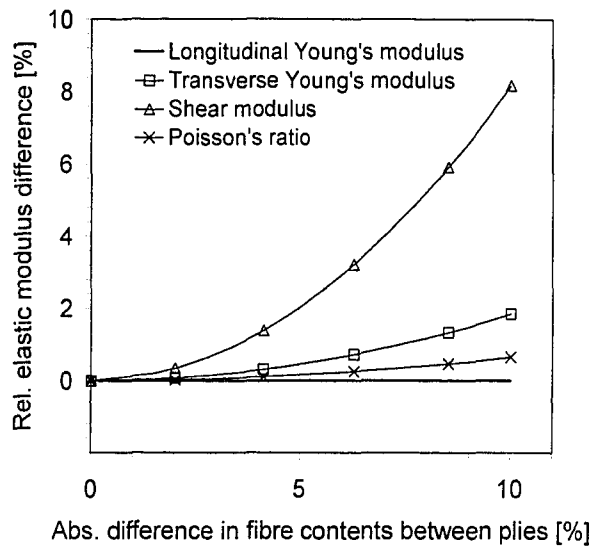


Figure 2.2.12: Difference of elastic constants based on (a) individual ply fibre volume fractions and (b) an average laminate value of 70% for a two-ply UD-laminate.

$$E_{xx} = (s \bar{A}_{11})^{-1} \quad E_{yy} = (s \bar{A}_{22})^{-1} \quad G_{xy} = (s \bar{A}_{33})^{-1} \quad \nu_{xy} = \bar{A}_{12} / \bar{A}_{11} \quad (2.2.37a-d)$$

The effect on the elastic constants is shown in Fig.2.2.12 for an average laminate fibre volume fraction of 70%. There is no discernable effect on the longitudinal Young's modulus using individual ply properties or an average value. Only small differences (<~2%) can be observed for the transverse Young's modulus and the Poisson's ratio, even when a maximum absolute variation in ply fibre volume fraction of 10% is assumed. A significant effect can solely be observed for the in-plane shear modulus. Here, the shear modulus varies by up to 8% for the aforementioned maximum difference in ply fibre volume fraction. Cohen and co-workers (2001) measured fibre contents variations between plies of similar magnitude (in large filament-wound pressure vessels). These differences were attributed to long winding hold-times (with magnitude of several hours), in which resin gelling occurred (Banerjee et al., 1998). Resin-rich layers were thus created after winding was resumed. Since present winding processes were continuous (i.e. the fabrication of each specimen was never interrupted for any appreciable length of time), it is reasonable to assume that differences in fibre contents

between layers are significantly less than those observed in the aforementioned works. Hence, the use of average laminate fibre volume fractions for the calculation of dimensional as well as stiffness properties is considered sufficiently accurate for subsequent investigations.

2.3 Composite Material System

Fibre reinforcement material:

The vast majority (>99%) of continuous glass-fibre reinforcement is produced from E-glass (Loewenstein, 1983), which is widely available at relatively low cost. More advanced glass-fibre materials are available, e.g. S2-glass, which exceeds the strength and Young's modulus of E-glass (Newman, 1990). Yet, due to its cost advantages E-glass is generally the preferred reinforcement material, particular for high volume applications. The material selected for the present study was 158B Type 30 roving from Owens Corning (Owens Corning, 1996 and 1997). Its specific glass composition (Owens Corning, 1998) combines electrical and mechanical properties of traditional E-glass and the higher corrosion resistance of E-CR-glass. Mechanical properties of single filament glass are provided in Table 2.3.1.

Type 30 roving is provided in the form of single-tow creels. The 158B designation stands for the type of fibre sizing applied to the filaments (also called fibre binder). The selected material was designed for use in filament winding applications in conjunction with epoxy polymers. The sizing was chemically optimised to promote fast and complete wet-out as well as good adhesion between glass and matrix. It also has lubricating and protective properties to prevent inter-filament abrasion. This allows for clean and smooth travel through guides without filament damage. Reduced filament damage and good fibre-matrix bonding are essential for achieving superior component strength. Fibre materials of 735 g/m linear weight (158B-AA-675) and 2000 g/m linear weight (158B-AC-250) were used in the present study. The average filament diameters are 13.4 μm and 15.6 μm respectively. Both materials have a specific gravity of 2.58 g/cm^3 .

Table 2.3.1: Single filament mechanical properties of applied glass material as supplied by the manufacturer (Owens Corning, 1998).

<i>Single filament tensile strength</i>	<i>3.1 – 3.8 GPa</i>
<i>Single filament elastic modulus</i>	<i>80 – 81 GPa</i>
<i>Maximum tensile elongation of single filament</i>	<i>4.6%</i>

Polymeric matrix material:

During the selection of a suitable polymeric matrix material, the first concern was with the mechanical properties of the polymer. Although the matrix is not the primary load-bearing component, its central role is to act as a carrier, protector and load-transfer medium around the fibre reinforcement. Within the fibre architecture the matrix material is exposed to a severe multi-axial stress state, which is even magnified by the non-uniform fibre distribution in a composite systems (Asp et al., 1995). Thus, high strength, elongation and fracture toughness are essential for good structural performance (i.e. to resist matrix micro-cracking). Moreover, mechanical performance needs to be maintained over a wide temperature range (including sub-freezing temperatures).

Secondly, it was imperative to consider the in-service environmental conditions that the structure would be exposed to. In the present study the focus is on pipe structures for the transportation and containment of hydrocarbon fluids. These fluids as well as soil contact may expose the composite material to corrosive chemical components and high humidity levels in an alkaline or acidic environment. The matrix material has to withstand such harmful media without losing its structural properties. It also has to protect the fibre reinforcement from any degrading influences. Thus, adequate chemical resistance and low moisture sensitivity are required properties.

With the EPON 826 epoxy resin and the EPI-CURE 9551 curing agent, a two-component thermoset polymer system with aforementioned properties was found. Properties of neat polymer castings are given in Table 2.3.2 (Note that in Chapter 4: Section 4.2, matrix as well as fibre mechanical properties are given that were determined by physical testing.). In its uncured stage this polymer has room-temperature

processing characteristics that are advantageous for filament winding: Low viscosity (1100 cP) promotes good fibre wetting, and a long gel-time (6.4 hours) provides sufficient processing time. Note that pre- and post-winding procedures (i.e. mixing and curing) were adjusted according to the manufacturer's recommendations. Their influence on part properties was not investigated in this research project.

Two procedures were used for resin dispensing and mixing: (a) volumetric dispensing with a static mixer nozzle, and (b) mixing of portions using a hand-held stirring device. The first method provides a clean and repeatable way of resin preparation, which is most suited for a large scale, continuous production. However, it was found that in a research environment the occasional use of the resin dispenser creates a problem with resin gelling. Hence, the second procedure was adopted. Resin and curing agent were blended according to a weight ratio of 100/36 (100/43.5 by volume).

After completion of the winding process, parts were placed into an electric air-circulating oven and cured according to the schedule shown in Fig.2.3.1. The same curing schedule was employed to produce castings of the neat polymer. From these, a specific gravity of 1.15 g/cm^3 was determined. Castings were used to investigate aforementioned methods for proper resin mixing and uniform curing. The surface of samples was cleaned (i.e. machined), and hardness tests were performed. Using a durometer type "Shore-D", the hardness was measured at 70 points over a sample area of approximately 40 cm^2 . Resin samples from methods (a) and (b) produced similar uniform hardness results (i.e. 86 ± 1 Shore-D hardness). Hence, both methods are suited to provide reliable and proper resin mixing.

It is important to note that epoxy resins such as the one used in this study, are subject to shrinkage during polymerisation. The shrinkage effect in fibre-composites was discussed by e.g. Zhang et al. (2004). It was shown that due to visco-elastic effects residual stresses and global shrinkage strain tend to small values. Yet, local residual strains within the matrix may remain significant affecting the response of the laminate and the damage development under subsequent mechanical loading. The determination of residual strains is beyond the scope of this thesis; however, their effect needs to be accounted for if one seeks to predict damage initiation and evolution.

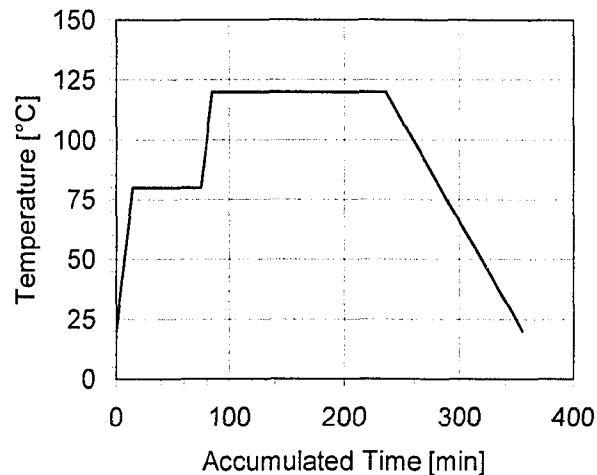


Figure 2.3.1: Temperature schedule for the curing of filament-wound glass-fibre/epoxy components.

Table 2.3.2: Properties of neat polymer castings of EPON 826/EPI-CURE 9551 epoxy polymer system as supplied by the manufacturer (Resolution Performance, 2001).

Glass transition temperature	110°C
Tensile strength	69.9 MPa (25°C) 90.3 MPa (-51°C)
Tensile Young's modulus	2.8 GPa (25°C) 3.4 GPa (-51°C)
Tensile maximum elongation	10.6% (25°C) 5.1% (-51°C)
Maximum water uptake (water immersion for 14days at 60°C)	1.8 wt%

2.4 Process Parameters in Filament Winding

2.4.1 Introduction to Filament Winding Process Parameters

The effect of process parameters on physical and mechanical properties of filament-wound components has, to a limited extent, been discussed in the technical literature. The key parameters were identified as the fibre tension, the resin take-up efficiency and the winding geometry (Hull and Clyne, 1996). Srinivas et al. (1999)

pointed out that the controllability of ply pre-stress forces (i.e. fibre tension) is one of the most desirable features. Cohen (1997) identified more than 50 process variables that contribute to part quality in filament wound pressure vessels. Using the design of experiment method (“DOE”), this set was subsequently reduced to the most significant parameters, i.e. tow tension during winding (winding tension), fibre strength variability, stacking sequence, winding time, fibre damage during winding and fibre wet-out. Winding tension was identified to be the most significant manufacturing parameter for the resulting mechanical properties. Increasing this parameter produced a higher fibre compaction and, at the same time, an increased strength of the composite structure. In a later publication Cohen et al. (2001) demonstrated a relationship between the fibre volume fraction in hoop-dominated laminae and the failure strength of filament wound pressure vessels. Note that in this specific case the fibre volume fraction was varied by a resin removal technique (i.e. running the fibres through an orifice after impregnation) instead of controlling the winding tension. Other studies of filament winding process parameters were focused on bandwidth effects (Lossie et al., 1989; Rousseau et al., 1997 and 1999).

Comprehensive theoretical models for the determination of component properties from filament winding process variables were also presented (Lee and Springer, 1990a and 1990b; Calius et al., 1990; Banerjee et al., 1998). These models simulate resin flow as well as thermo-chemical and thermo-mechanical conditions within the fibre architecture during winding and curing. This yielded descriptions for the fibre consolidation process, and thus, material properties. An application of these models, however, requires extensive thermo-chemical/mechanical material data. For most material systems, like the one used in the present study, a complete set of necessary data is not available from literature or manufacturers. Its determination would require significant experimental work. At this point two items from preceding discussions shall be recalled: Firstly, the focus of this research project is on the mechanical performance of filament-wound tubes. Secondly, analytical methods were found to possess limited abilities in predicting and quantifying damage in such structures (see Chapter 1: Section 1.3). Thus, the main

emphasis herein is on the experimental study for the investigation of physical and mechanical properties.

Definition of process parameters:

Mertiny and Ellyin (2001) defined two categories of filament winding process parameters. On the one hand, there are primary parameters. These can be selected, monitored and directly controlled by the operator. Secondary process parameters, on the other hand, are not directly controllable. Nevertheless, they may have a significant impact on the quality of the manufactured components. For example, it was discussed in Section 2.1 that the actual winding bandwidth requires adjustment depending on the nominal bandwidth. Attempts on in-situ bandwidth control have been reported (Koschmieder, 2000). But, necessary techniques for measurement and control are generally not available or practical. Hence, any adjustment is only feasible using primary parameters, with winding bandwidth being usually considered a secondary process parameter.

From the preceding literature review, certain process variables were identified to significantly affect a component quality; consequently, they were subjected to detailed investigation. Respective parameters are listed in Table 2.4.1. Their influence on physical and mechanical properties, as well as their impact on secondary process parameters was examined. Corresponding investigations can be found in subsequent sections of this thesis.

Note that the quality of constituent materials, i.e. fibres and polymer matrix, was not considered in this study. Initial winding trials were performed to select best quality fibre from among available products. Furthermore, the winding facility was designed to minimise fibre damage during winding, by e.g. converting outside-pull to centre-pull creels, and reducing sources of fibre friction using rollers and pulleys (see Appendix A for details). The result was a fibre quality above most industry standards. Any investigation with reduced fibre quality was therefore deemed unnecessary. Influences of the polymer system on component properties also were not considered, since chemistry as well as the processing characteristics of the polymer are beyond the scope of this

investigation. This includes fibre wet-out characteristics (e.g. winding speed). Nonetheless, parameters concerning constituent materials were carefully selected to provide good tubular specimen quality. Furthermore, these parameters were kept constant throughout the experimental program.

As component design parameters, the last three items in Table 2.4.1 were examined for their influence on physical properties in conjunction with the mechanical performance analysis discussed in Chapter 4.

Table 2.4.1: List of filament winding process parameters examined in the present study.

<i>Process parameter</i>	Type of process parameters / Remarks
<i>Fibre tension</i>	Primary parameter Special attention was paid to this parameter, which was predicted to have the most significant impact on component quality.
<i>Applied fibre quantity</i>	Primary parameter Linear tow weight, as well as the number of tows within a winding band, comprise this quantity.
<i>Winding bandwidth</i>	Secondary parameter This is the only process parameter of this list that is not directly controllable by the current winding facility.
<i>Mandrel diameter</i>	Primary parameter Besides being a process parameter, this is also a design/geometry parameter of a tubular component. Influences of this parameter on part properties were investigated in the context of component scaling and size effects in Chapter 4: Section 4.6.
<i>Winding angle</i>	Primary parameter Component design/geometry parameter
<i>Cover stacking sequence</i>	Primary parameter Component design/geometry parameter

2.4.2 Effect of Process Parameters on Winding Bandwidth

Of the above process parameters only the applied fibre quantity and tow tension are available for bandwidth adjustment. Use of the former is trivial: Increasing the number of tows or the linear tow weight results in increased bandwidth. However, winding trials are required to find the proper fibre quantity. Moreover, the proper arrangement and guidance of fibres through the pay-out eye need to be determined.

Since the winding facility features an active tension control, the use of tow tensioning is a potentially more convenient method for bandwidth adjustment. Thus, the influence of tow tensioning on winding bandwidth was examined (Mertiny and Ellyin, 2001). Being of 38.1 mm inside diameter, $[\pm 60_3]_T$ specimens made from eight tows of 0.735 g/m linear weight, were used for the current investigation. Note that this particular type of specimens will be referred to as ‘small-scale baseline configuration’ in the remainder of this thesis. Bandwidths were measured using tracer threads and automated image analysis (see Appendix B for details). Results are presented in Fig.2.4.1. Here, a general trend can be observed, i.e. the average winding bandwidth decreases with increasing tow tension.

In Fig.2.4.2 the change in average bandwidth (with respect to the lower tow tension) is presented for a tension increase of 67% from 26.7 N (6 lbf) to 44.5 N (10 lbf). A relative change of -2.7% and -3.7% was ascertained for measurement techniques using video analysis and tracer threads respectively. Using image analysis, results are more consistent showing an absolute variation of $\pm 1.1\%$ in contrast to $\pm 2.3\%$ when using tracer threads. But even in the former case, the reduction in bandwidth shows a large amount of scatter (i.e. $-2.7\% \pm 1.1\%$). This may result from non-controllable influences on the winding band such as sliding of fibres along the mandrel.

The above findings lead to the conclusion that decreases in bandwidth were rather small for even significant increases in tow tension. At the same time, high bandwidth variability of similar magnitude may occur. Difficult to control influences are suspected to be responsible for this behaviour. Due to the very complex fibre motion behaviour and the only limited influence of tow tension on winding bandwidth, the possibility of an in-situ bandwidth control appears to be impracticable.

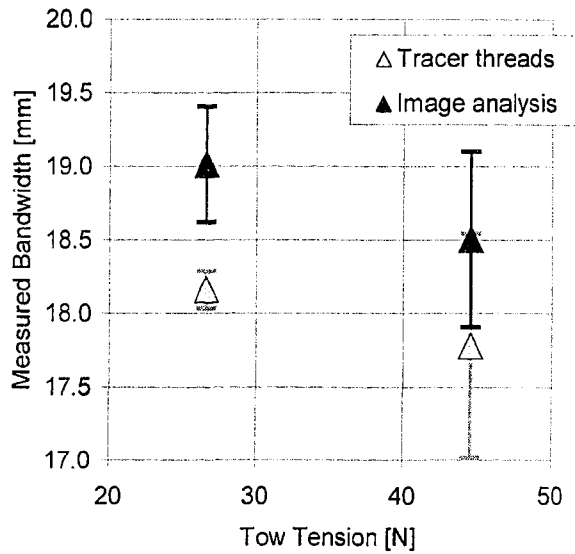


Figure 2.4.1: Influence of tow tension of average winding bandwidth. Tracer thread and image analysis measurement techniques were employed.

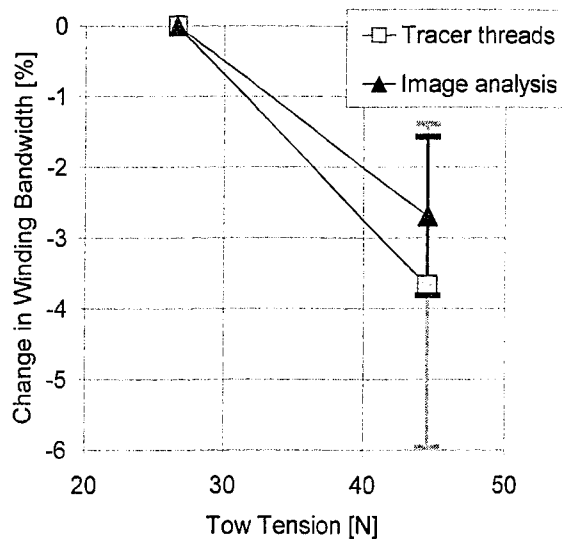


Figure 2.4.2: Relative change in winding bandwidth from 26.7 N to 44.5 N tow tension. Tracer thread and image analysis measurement techniques were employed.

2.4.3 Effect of Process Parameters on Fibre Compaction

It was shown in Section 2.2 that for a given material system, fibre lay-up and part geometry, the engineering moduli are governed by the degree of fibre compaction. Furthermore, the degree of interweaving was determined to have a negligible influence on component elastic constants, see Subsection 2.2.3. Thus, it is reasonable to assume that based on process parameters listed in Table 2.4.1, fibre volume fraction solely depends on tow tension and the applied fibre quantity. Investigations on this subject were conducted by Mertiny and Ellyin (2001, 2002); results are reproduced in the following.

Influence of tow tension on fibre compaction:

For small-scale baseline specimens the degree of fibre compaction was determined for certain tow tensions according to procedures outlined in Subsection 2.2.1. Average fibre volume fractions are shown in Figure 2.4.3 for two sample types: (a) specimens that were machined to remove the resin coat (solid symbols), and (b) unaltered specimens (open symbols).

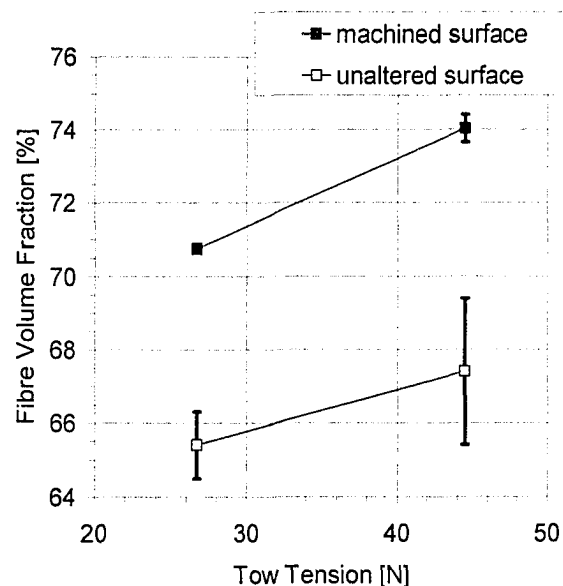


Figure 2.4.3: Influence of tow tension on average fibre volume fraction measured on specimens produced with 26.7 N and 44.5 N tow tension.

It can be observed, as to be expected, that fibre volume fraction was higher for samples with the machined surface. Here, a substantial increase of an absolute 3% from 70.8% to 74.0% was measured for 26.7 N and 44.5 N tow tension respectively. For the same forces, fibre volume fractions of 65.4% and 67.4% were obtained for the unaltered specimens. Machined specimens exhibited a maximum variation from the mean of less than an absolute $\pm 0.5\%$, compared to $\pm 2\%$ for the unaltered samples. The large data variability of the latter sample type made it impossible in some cases to note any increase in fibre volume fraction whatsoever. Therefore, the degree of fibre compaction was henceforth determined using machined specimens. Nonetheless, results clearly indicate that tow tensioning is an effective means for increasing fibre volume fraction.

Note that in Figure 2.4.3 data points were linearly connected only for illustrative purposes. A relation between tow tension and fibre volume fraction ought to be non-linear, since fibre compaction ultimately reaches a saturation state. Due to non-uniform fibre packing and the presence of undulations, the achievable fibre volume fraction is expected to be considerably lower than the aforementioned theoretical maximum of 90.6%. However, no attempt was made to investigate this matter in more detail, since selected tow tensions already represent the utmost useable force range, i.e. the tensioning device was unable to overcome friction within the system for tensions lower than 26.7 N, and fibre damage was observed for values higher than 44.5 N.

Influence of applied fibre quantity on fibre compaction:

In order to investigate the influence of the applied fibre quantity on fibre compaction, an alternative glass fibre material of similar filament size was used to produce a second set of small-scale baseline specimens. A 1.1 g/m fibre tow was provided by the FibreEx Company. Featuring a 67% higher linear weight than the aforementioned 0.735 g/m fibre material, this product was only used for the above purpose. For a rise in winding tension from 26.7 N to 44.5 N, fibre volume fraction was increased by absolute 3% and 5% for the 0.735 g/m (solid symbols in Figure 2.4.4) and 1.1 g/m (open symbols) relative tow weight respectively. This shows that the effect of fibre tension is more pronounced for heavier glass fibre material. This behaviour can be explained as follows: When winding a fibre band composed of tows of a relatively high weight, increased tension is necessary to

displace the liquid polymer matrix trapped under and within the fibre band, so as to achieve the same fibre volume fraction as when winding with lighter tows.

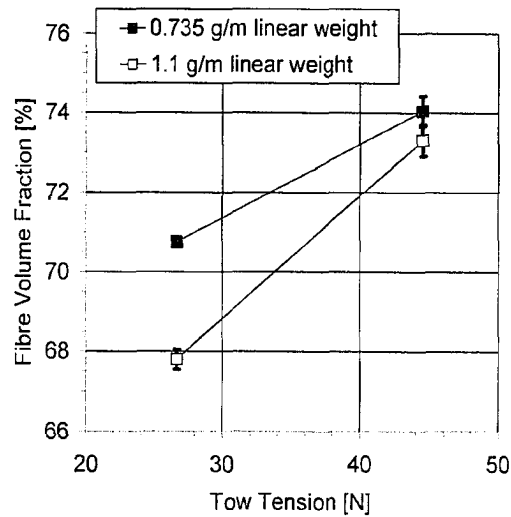


Figure 2.4.4: Influence of relative tow weight on average fibre volume fraction measured on specimens produced with 26.7 N and 44.5 N tow tension.

CHAPTER 3

EXPERIMENTAL PROCEDURES

3.1 Specimen Design Considerations

Several devices for the testing of fibre-composite tubes under biaxial loading conditions were presented in literature. Specimens tested by, for example, Soden and co-workers (1989 and 1993), and Gargiulo (1996) were equipped with circumferentially wound end reinforcements, which were tapered towards specimen gauge sections. In some studies, specimen extremities were also built up by reinforced or neat epoxy castings (e.g. Toombes et al., 1985; Swanson et al., 1988; Groves et al., 1992; Smith and Swanson, 1995 and 1997; Mertiny, 1999; Martens and Ellyin, 2000 and 2001). These methods were intended to reduce stress concentrations in the vicinity of the end connections. Consequently, failure generally occurred within the specimen gauge section, which is imperative for the successful experimental investigating of material behaviour.

The present research project, however, did not exclusively seek the examination of material behaviour, but also of structural performance. Testing of small-scale model specimens was required for phenomenological analyses of material and structural behaviour. In a later phase, large-scale testing of prototype specimens was conducted for the examination of scaling effects, and a feasibility study on pipe joining. Suitable specimen designs ought to be similar to actual structures, in which case special end reinforcements are considered prohibitive from an operational and cost point of view. Moreover, fabrication should be limited to the filament winding method. In the present work, end connections for an actual prototype structure were proposed in the form bonded sleeve couplers for the integration of pipe subsections (see Chapter 5: Section 5.2). Such end connections have to provide for proper sealing and load transfer in axial direction. Moreover, end connections with negative affects on pipe strength are considered unfavourable.

Fortunately, experimental set-ups were reported that successfully tested pipe structures devoid of any end reinforcement (e.g. Soden et al., 1978; Carroll et al., 1995a; and Ellyin et al., 1997). Wolodko (1999) developed a system for the testing of small-scale tubes under axial force and internal pressure. Specimens were installed into the testing apparatus using bonded metal end connections. This set-up was well suited for the present study, since it closely simulates the coupling of pipe subsections by adhesive bonding. The testing apparatus was consequently used for the experimental examination of model specimens. Based on experiences from small-scale testing, a new testing device was developed for the examination of prototype structures in a later stage of this research. More details on the employed testing devices and corresponding specimen designs are given hereafter.

3.2 Testing Facilities

3.2.1 Small-Scale Testing Apparatus

For experiments with model specimens the small-scale testing apparatus shown in Fig.3.2.1 was employed. Being briefly described in the following, its components are: load frame and gripping system, servo-hydraulic system, feedback and control system, and data acquisition and control computer. A detailed description of the testing apparatus was given by Ellyin and Wolodko (1997), and Wolodko (1999).

Specimens were installed into a gripping system, which was attached to the load frame and the axial actuator of the testing apparatus. Maximum specimen dimensions, i.e. length and inside diameter were 216 mm in length and 38.1 mm respectively. A chamber enclosing specimen and gripping system is available for external specimen pressurisation. But, in the present study the enclosure simply provided protection in the case of burst failures.

Through the servo-hydraulic system, four independent components can be operated, i.e. an axial and rotary actuator, and pressure intensifiers for external and internal specimen pressurisation. Since biaxial stress conditions were required for the present study, only the first and the last of the above features were employed for loading.

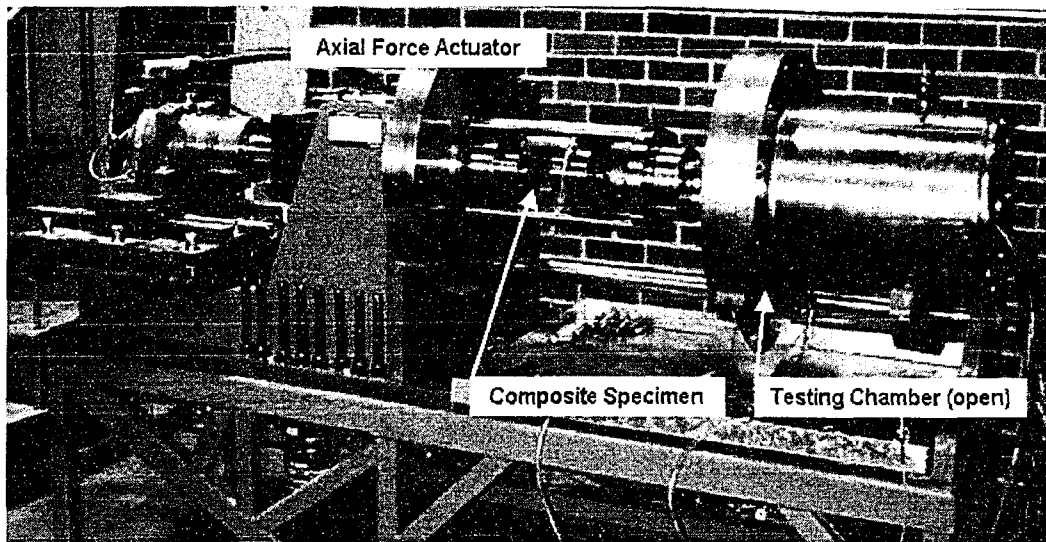


Figure 3.2.1: Small-scale testing apparatus.

Feedback signals were received from the respective transducers, i.e. load cells (located within the load-train of the machine) and pressure sensors (located at the pressure intensifiers). In addition, strain data were collected. Testing under deformation control as well as under load control is feasible; however, current testing was limited to the latter. The feedback and control system comprises several analogue controller modules, which ensure stable actuator control based on feedback and command signals. For the current testing program, transducers and control modules were chosen to process maximum pressure, force and strain signals of 67 MPa, 22 kN and 5% respectively.

Command signals were generated and data acquisition was handled by a personal computer. Signals were interfaced using two separate peripheral computer cards: a 16-channel analogue-to-digital card was used to collect input data; output signals were provided via a separate 4-channel digital-to-analogue device. Necessary computer software was developed in the context of an earlier study (Wolodko, 1999).

3.2.2 Model-Scale Specimen Design and Assembly

Model specimens were made from filament-wound tubes with an inside diameter of 38.1 mm. Tubes with various lay-up configurations were produced, in which the wall

thickness varied from 1 to 2 mm. Eight tows of 735 g/m linear weight were dispensed during winding, and 26.7 N tow tension was applied to for all but one specimen type (i.e. a batch of $[\pm 60_3]_T$ specimens was produced with 44.5 N tow tension). To avoid fibre slippage along the mandrel during the production of $\pm 30^\circ$ covers, pin-rings were applied. Layup configurations, fibre volume fractions and wall dimensions are summarised in Table 3.2.2 for all types of model specimens.

After curing, tubes were extracted from the chrome-plated steel mandrels. This was accomplished by pulling mandrels through a brass extraction eye using a servo-hydraulic testing machine. Sections of 190 mm length were machined from the tubes employing a custom-made cutting device (Wolodko, 1999). Specimens were cut by a circular saw while being held in a turning, motor-driven bracket. Thus, a planar cut perpendicular to the specimen centre-axis was produced. Pipe end-dwell sections, in which the winding angle changes to 90° , were discarded.

Aluminium end connections were applied to model specimens by adhesive bonding (see Chapter 5: Section 5.3 for a review on this matter). In Fig.3.2.2 a schematic of an assembled specimen is shown. The aluminium end-tabs are a two-part system, of which the inner part also has an alignment function. The individual end-tab parts were sandblasted to promote adhesion. For the same reason, specimen extremities were lightly abraded using 600-grid sanding cloth. After cleaning with acetone, the components were heated to about 50°C on a hotplate. This was done to remove any moisture, and to lower the adhesive viscosity during subsequent bonding. Employing a special assembly stand, tube and end-tabs were aligned in a vertical position. 3M DP-460 epoxy adhesive (3M, 2002) was inserted into the end-tab annulus, and the tube was lowered slowly into the same. (Basic adhesive properties are provided in Table 3.2.1.) Due to the reduced adhesive viscosity, complete coverage of the pipe extremities without the entrapment of air was achieved. After a 24-hour curing period, the second end-tab was applied to the other specimen end in the same manner.

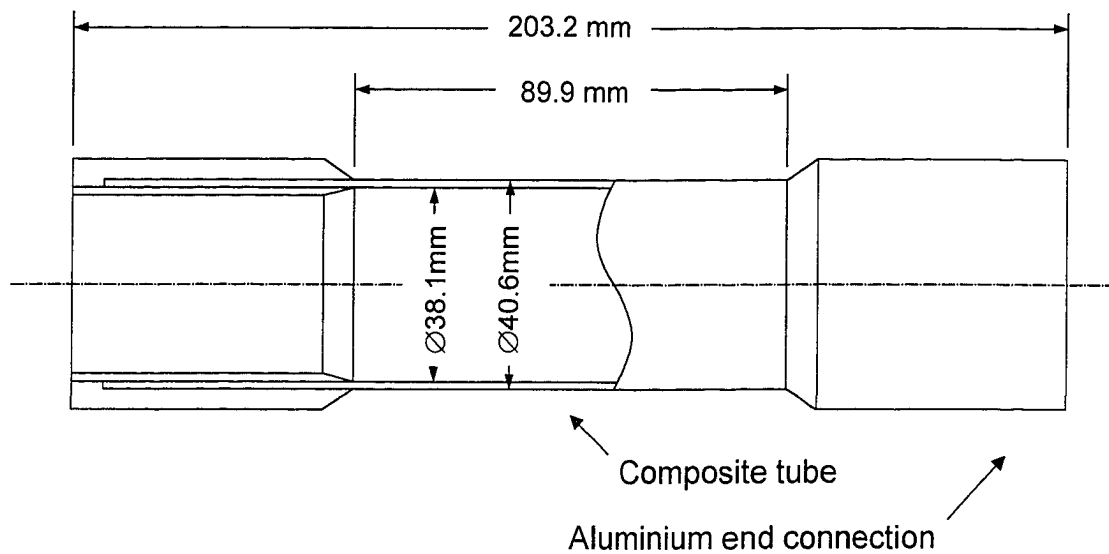


Figure 3.2.2: Schematic of the model specimen.

All specimens were equipped with two strain gauge rosettes with perpendicular grid (Micro-Measurement Company, type CEA-13-062WT-350). Gauges were aligned in axial and hoop direction of the tube, and bonded at the mid-length of the 90 mm specimen gauge section. Two rosettes were applied for the following reasons: (a) to allow the verification of symmetric loading, i.e. the absence of bending; and (b) to ensure continuous strain measurement even in the case of a strain gauge failure.

Preloading of the specimen grips preceded the installation into the testing apparatus. A schematic of the gripping system is shown in Fig.3.2.3. The grip assembly consists of two units, one for each specimen end. The units are identical except for a check valve system in one grip, through which specimen pressurisation occurs. Each grip has three major components: a tapered collet, a flanged hub, and a pre-loading plug. During the pre-loading procedure, force is imposed upon the pre-loading plug by a hydraulic screw-driven testing machine. Loading of the plug causes sliding of the collet into the flanged hub. Since both flange and collet are tapered, the collet is activated, imposing a clamping force upon the specimen end-tab. After both grips have been assembled in this manner, the specimen is filled with hydraulic fluid, and installed into the testing device.

Table 3.2.1: Typical properties of 3M DP-460 epoxy adhesive as supplied by the manufacturer (3M, 2002).

Mixing ratio B:A	2 : 1	by volume
	2 : 0.96	by weight
Viscosity at 23°C	~35,000 cps	of base (B)
	~11,000 cps	of accelerator (A)
Minimum worklife	60 minutes	of 20 g mixed
Overlap shear strength on various substrates, tested at 23°C, bondline thickness of ~0.47 mm	> 20 MPa	aluminium
	> 13 MPa	steel
	~5.5 MPa	FRP*

* fibre reinforced plastic

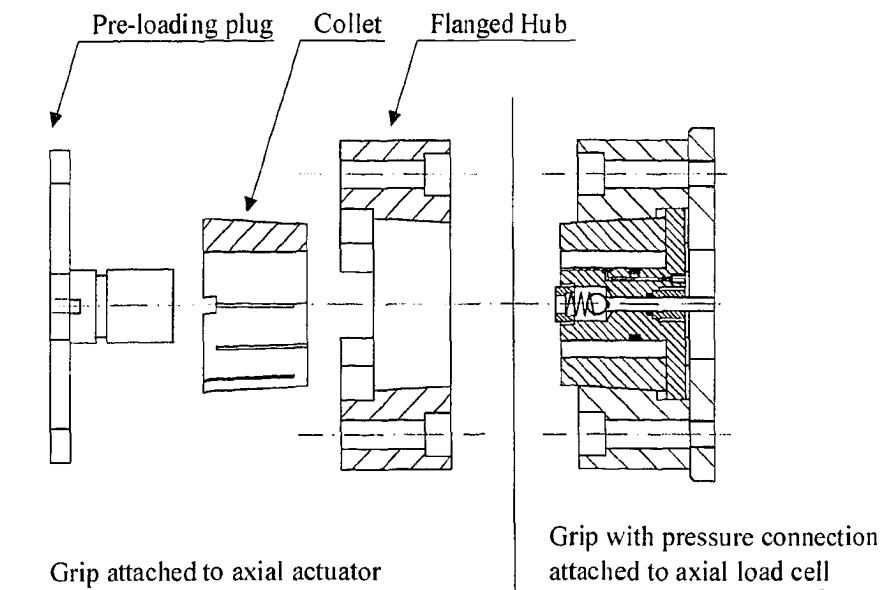


Figure 3.2.3: Schematic of the model specimen gripping system, adopted from Wolodko (1999).

3.2.3 Prototype-Scale Testing Apparatus

For the testing of large-scale tubular specimens the apparatus shown in Fig.3.2.2 was developed and built in-house by various members of the Advanced Composite Materials Engineering Group (from 2000 to 2002). Apart from being utilised for experiments this apparatus also serves as a mandrel extraction device. Basic features of this machine are summarised in the following. For a detailed description of this device see Appendix C.

The testing machine features two movable crossheads of which one houses the axial force actuator. The load frame of the testing apparatus was designed to accommodate pipe structures with a maximum inside diameter and length of 610 mm and 3,700 mm respectively. The load frame was provided with precision-machined rail and guide surfaces that ensure parallel crosshead alignment. Subjecting specimens to a combination of internal pressure and axial force facilitated biaxial loading. The test area can be enclosed by two hydraulically operated shields, which offer protection from debris in the event of a burst failure.

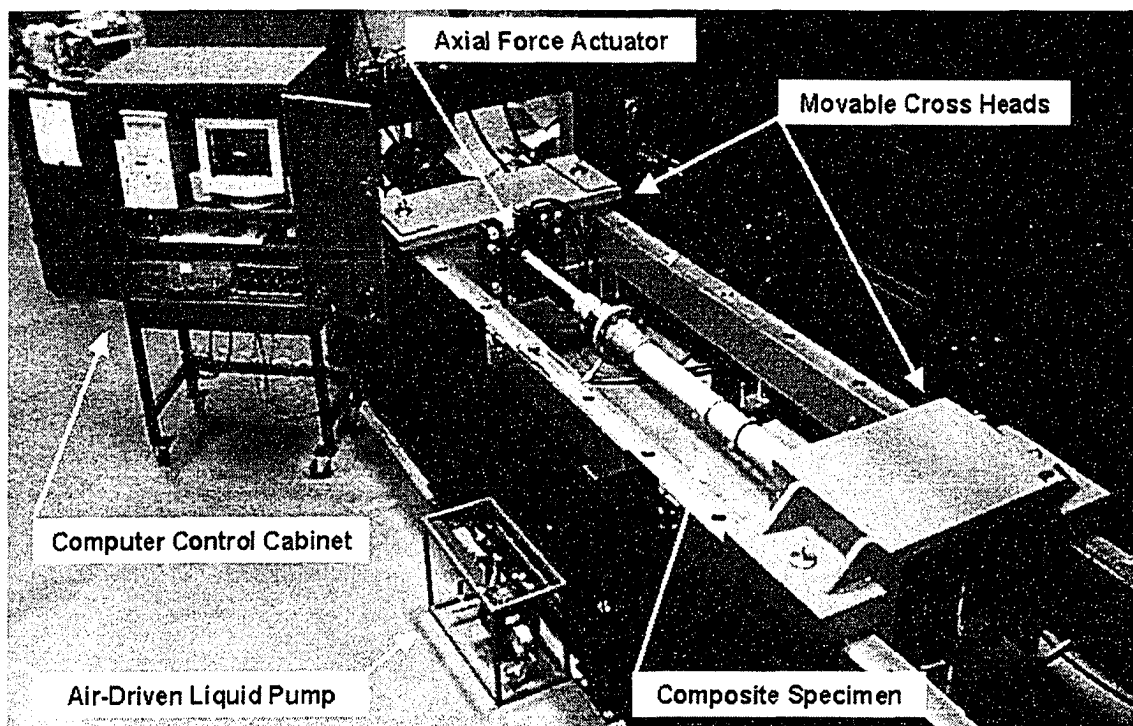


Figure 3.2.4: Prototype-scale testing apparatus.

Two separate systems are responsible for specimen pressurisation and axial loading. Specimens are pressurised using an air-driven reciprocating pump with a pressure capacity of 105 MPa. Water was chosen as the medium for specimen pressurisation. The air supply is proportional to the applied water pressure and is regulated using a continuously variable transducer/valve unit. Axial force is provided by a hydraulic actuator with maximum tensile and compressive capacity of 1054 kN and 1112 kN respectively. Hydraulic pressure in the axial actuator is adjusted by solenoid valves.

Hydraulic and pneumatic systems can be controlled manually, or by engaging a feedback and control logic run by a personal computer. Data acquisition is accomplished through the computer also. Respective software was developed based on the LabView™ program (for details see Appendix C). For the experimental study the software was designed to support load-controlled tests. Force and pressure feedback signals are sourced from a load-cell mounted in between specimen and hydraulic actuator, and a pressure transducer connected to one of the specimen end connections respectively. Five additional channels are available for the recording of strain gauge data. A peripheral computer card connected to an external switchbox establishes the interface between transducers/valves and computer.

3.2.4 Prototype-Scale Specimen Design and Assembly

Prototype specimens with wall thicknesses of 4 to 6 mm and different lay-up configurations were produced by filament winding. All prototype specimens were wound with ten tows of 2000 g/m linear weight with 26.7 N tow tensioning. Two prototype specimens were fabricated simultaneously on one 101.6 mm diameter ground steel mandrel. Pin-rings were again employed during the winding of $\pm 30^\circ$ covers. Details on fibre volume fractions, wall dimensions and layup configurations for all specimen types are provided in Table 3.2.2. After curing, the large-scale testing apparatus was employed to extract the mandrel from the tubular part. This occurred in a similar manner as described for the small-scale specimens, i.e. by pulling the mandrel through an extraction eye. Afterwards, the tubular part was sectioned into specimens of 1,676 mm length. End-dwell sections were rejected. Specimen extremities were either sandblasted or

machined in order to provide good adhesion. Isopropyl alcohol was preferred over acetone for the cleaning of composite tubes as well as end-tabs (see Chapter 5: Section 5.3 for details).

Prior to the installation into the testing machine, most prototype specimens were equipped with strain gauges in an identical manner as model specimens. The length of prototype gauge sections was approximately 1,250 mm.

In the case of biaxial loading, end-tabs analogous to the ones used in model testing were employed. Besides being significantly larger, end-tabs were made from steel; an inner end-tab part was provided solely for alignment purposes. A schematic of a prototype specimen with attached end-tabs is shown in Fig.3.2.5. End-tabs were sandblasted, cleaned and finally mounted onto the crossheads prior to pipe installation. A laser-pointer system was used to ease the coaxial alignment of the end connections. Afterwards, the composite pipe was inserted into one of the end-tabs. By means of the hydraulic actuator the pipe was moved towards the second end-tab until the pipe could be positioned onto the centre parts of both end connections. The actuator was then extended further, up to the point where contact between pipe and the back plates of both end tabs occurred. In order to prevent any premature loading of the pipe, force readings from the control system were monitored carefully during this procedure.

Composite tube and end-tabs were connected by adhesive bonding. Since this took place with the specimen already being mounted into the testing apparatus, a stress-free installation was ensured. A pneumatic adhesive gun was utilised to inject epoxy adhesive (3M, 2002) into the annuli in between pipe and end connections. Injection holes within the end-tabs' cylindrical body were provided for this task. Since bonding occurred in a horizontal position, a mould made of adhesive tape was required to prevent epoxy from dripping out of the annuli between composite tube and end-tabs. This procedure also resulted in the formation of adhesive fillets. After a 24-hour curing period, the liquid pump was connected to one end-tab, and air was bled from the specimen during the filling with water.

Table 3.2.2: Average fibre volume fraction and wall thickness
for all types of produced tubular structures.

Tubular structure:	Layup	Fibre volume fraction [%]	Wall thickness [mm]
model pipe ⁽¹⁾	$[\pm 60_3]_T$	74.0	1.21
model (baseline) pipe	$[\pm 60_3]_T$	70.7	1.27
model pipe	$[\pm 45, \pm 60_2]_T$	70.0	1.31
model pipe	$[\pm 60_2, \pm 45]_T$	70.6	1.29
model pipe	$[\pm 30, \pm 60_2]_T$	68.9	1.48
prototype pipe	$[\pm 60_3]_T$	63.3	5.16
prototype pipe	$[\pm 60_3, \pm 30]_T$	60.2	4.63
improved prototype pipe ⁽²⁾	$[\pm 60_3, \pm 30]_T$	63.6	4.39
prototype coupler sleeve ⁽³⁾	$[\pm 30, \pm 60_2]_T$	63.3	3.06

⁽¹⁾ model pipe wound with 44.5 N tow tensioning
⁽²⁾ for details on the improved prototype pipe see Chapter 5: Section 5.9
⁽³⁾ for details on the coupler geometry see Chapter 5: Section 5.4

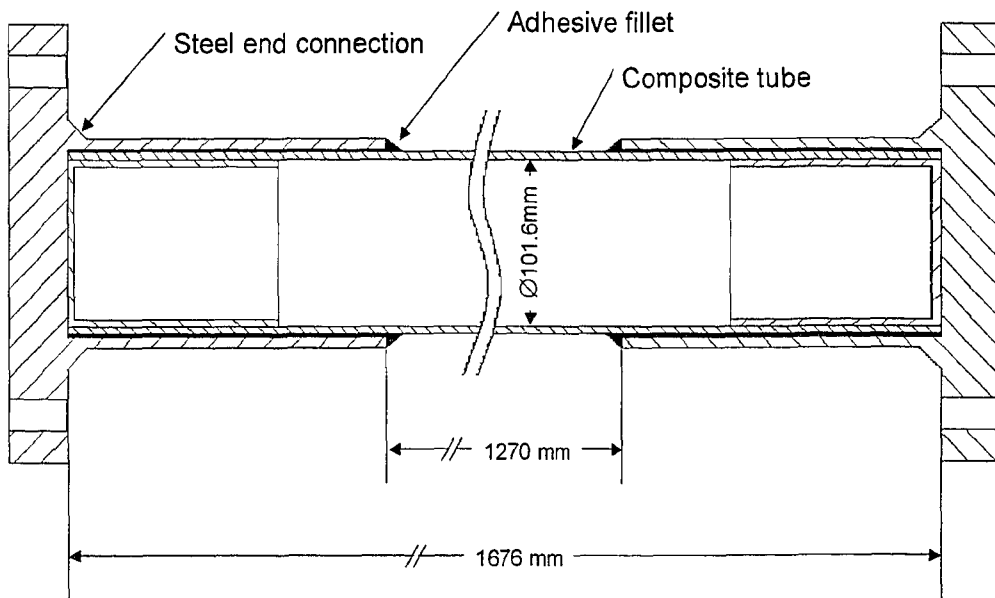


Figure 3.2.5: Schematic of the prototype specimen.

3.3 Detection and Quantification of Specimen Failure

3.3.1 Specimen Failure Events

Failure events in fibre-reinforced tubular structures under pressure loading can be divided into two categories. Firstly, the component may lose the ability to contain fluid. This condition is termed a functional failure, which generally terminates the useful life of the component. Any event associated with the loss of fluid, such as component leakage or burst, is considered a functional failure. However, even in the event of leakage the component may still be able to carry the applied loads. This leads to the second possible failure category, which is structural failure. Here, the component loses the ability to carry the applied loads (component burst or collapse). Consequently, functional and structural failures either coincide, or the latter follows the former.

A variety of damage mechanisms are responsible for the occurrence of aforementioned failure events. Also sequence and damage interaction play an important role. (A review on this subject matter was provided in Chapter 1: Subsection 1.3.2.) However, it may be a fair generalisation to attribute functional failure mostly to inter- and intra-laminar matrix damage. These damage modes result in the formation of networks of micro-cracks, which allows fluid to leak through tube walls. For example, Fig.3.3.1 shows the surface leakage pattern of a model specimen. The visualisation of the (lightly coloured) fracture lines was made possible by blending the hydraulic fluid with a fluorescent dye-penetrant.

Structural failure, on the other hand, is primarily caused by fibre breakage or matrix shear fracture. Note that strain gauge readings are not suited for detecting structural failure, as damage events associated with the functional failure (i.e. matrix cracking and fluid leakage) impair the gauge bond. Thus, strain gauge readings may be unreliable after the occurrence of leakage failure.

3.3.2 Specimen Failure Criteria

Loss of load bearing capability (burst or collapse)

A sudden drop of the internal pressure and/or the applied axial load straightforwardly indicates the loss of the load bearing capability of the component (structural failure).

Force and pressure recordings from the data acquisition system allow for an easy detection of structural failure.

Loss of fluid containment capability (leakage)

In earlier studies the point of leakage failure was generally defined by any of the following criteria: (a) Loss of a particular amount of fluid from the hydraulic system (Wolodko, 1999; Mertiny and Ellyin, 2002); (b) tangent curve intersection of the initial slope and the final slope in a leakage profile (Kujawski et al., 1998; Martens and Ellyin, 2000); (c) appearance of fluid spots on the specimen surface (Rousseau et al., 1999; Soden et al., 1989); (d) resistance change of a leak-detection wire wrapped around a specimen (Frost, 1994).

In the present study none of the above criteria could be used in conjunction with both specimen types. The enclosing test chamber of the small-scale testing device made visual inspection impossible, and the utilisation of oil as the medium for specimen pressurisation hampered the use of resistance wires. In the case of prototype testing, pressurisation occurred by a reciprocating pump, which did not allow for an accurate fluid loss measurement. Thus, different failure criteria were employed for the two specimen types.

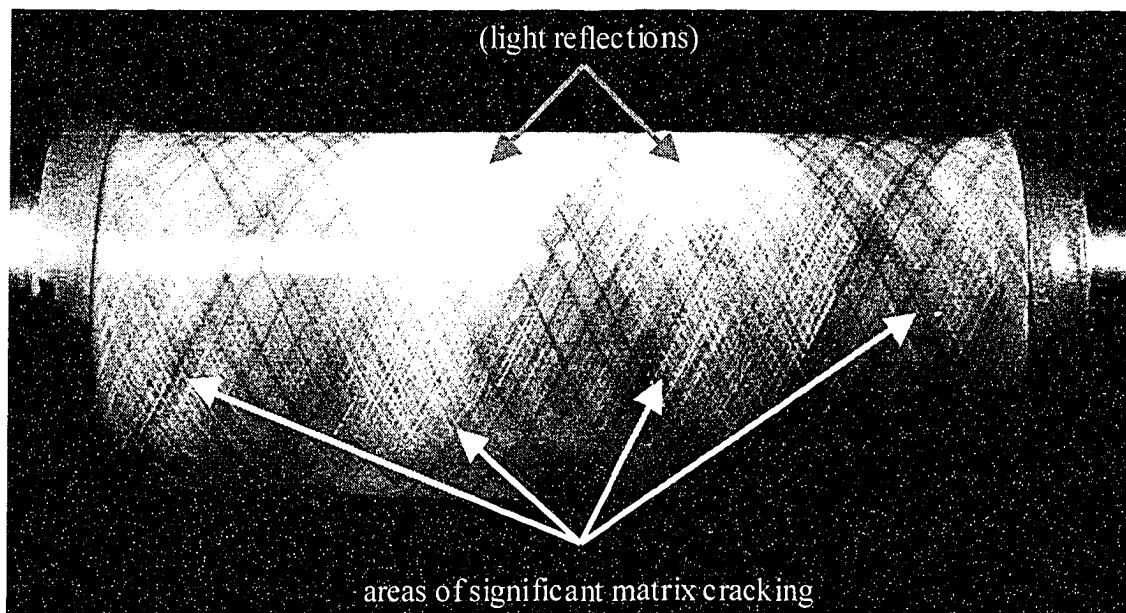


Figure 3.3.1: Visualisation of matrix cracking using fluorescent dye-penetrant.

For model specimens, a fluid loss of 1% inside volume, i.e. 2 ml, was defined as the point of leakage failure. Under certain loading scenarios with high axial stress components the control system failed to quantify the point of failure reliably, even though leakage could be observed visually. This is attributed to an insufficiently low internal pressure. In such a case, stress-strain recordings were examined as well, and a drop in hoop stiffness was used to verify the point of functional failure. For the present tests a slight reduction in hoop stiffness (i.e. a moderate non-linear stress-strain behaviour) could be observed up to functional failure. At functional failure, however, extensive matrix damage induced a noticeable change in specimen geometry, i.e. fibre realignment towards the axial direction took place. In the stress-strain diagram in the hoop direction this event is indicated by a significant decrease in slope of the stress-strain curve. A slope reduction to half of that of the initial slope at the start of the test was found to correlate well with pressure values at failure found by visual inspection. (An asterisk is used to mark tests that necessitated the use of the stiffness-based method within the summary of all test results in Appendix D.)

In the case of prototype specimens, leakage was defined as the point at which the reciprocating pump reached its maximum flow rate at maximum air-supply pressure (0.69 MPa). However, a uniform leakage failure criterion was required for the comparison of model and prototype test results. Hence, leakage failure was determined alternatively by the following permeability criterion.

Even though a reciprocating pump was used for the pressurisation of prototype specimens, dynamic effects are considered negligible. This assumption is justified by the low rate at which pump strokes occur for pressures approaching failure load. At these pressure levels the required fluid flow is small, which thus can be maintained by a limited number of pump strokes. Pump strokes occur slowly, i.e. due to low flow rates the pumping action is similar to the continuous fluid displacement found in pressure intensifiers.

3.3.3 Fluid Permeability Criterion

Following the works by e.g. Wolodko (1999) and Bates et al. (2000), a permeability criterion was used in the present study to determine the point of leakage failure for both specimen types in a consistent manner. Based on the observation that matrix damage resulted in the penetration of fluid through the tube wall, the damaged composite is assumed to act like a porous medium. This led to the conclusion that a certain damage state corresponds to a particular permeability. Since fluid penetration was a quasi-constant, slow flow, inertial effects were neglected. Thus, the flow regime was found to be in good agreement with Darcy's law (Darcy, 1983), where the permeability k of the porous medium is defined by Eq.(3.3.1).

$$\{u\} = -k \{\nabla p\} \quad (3.3.1)$$

where $\{u\}$ is the flow velocity vector and $\{\nabla p\}$ is the pressure gradient.

The permeability, k , depends on the penetrated medium as well as the fluid. Hence, the intrinsic permeability k' is introduced, which is defined as $k' = k \mu$, with μ being the dynamic viscosity of the fluid ($\mu_{\text{water}} = 0.0018 \text{ Ns/m}^2$, $\mu_{\text{oil}} = 0.0656 \text{ Ns/m}^2$). Assuming that any significant fluid flow occurs solely in radial direction uniformly through the entire wall of the tubular specimen, the flow velocity vector, $\{u\}$, and the pressure gradient, $\{\nabla p\}$, can be reduced to their radial components. The radial flow velocity u , is thus given by:

$$\{u\} = (0 \quad 0 \quad u)^T = u \{e_z\}$$

The differential pressure across the wall is given by:

$$\{\nabla p\} = \frac{\partial p}{\partial x} \{e_x\} + \frac{1}{z} \frac{\partial p}{\partial y} \{e_y\} + \frac{\partial p}{\partial z} \{e_z\} = \frac{dp}{dz} \{e_z\}$$

with $\{e_i\}$ being unit vectors.

The change from outside (atmospheric) pressure, $p_o = p(z + s)$, to inside pressure, $p_i = p(z)$, is assumed to be linearly distributed across the wall, i.e.

$$\frac{dp}{dz} = \frac{p(z+s) - p(z)}{z+s-z} = \frac{1}{s} \Delta p$$

where Δp is the difference between atmospheric and internal pressure. Thus, Eq.(3.3.1) becomes,

$$u = \frac{k' \Delta p}{\mu s} \quad (3.3.2)$$

Since the specimen inside wall surface, A , is given by $A = 2 \pi R L$, the total volumetric flow rate through the specimen wall, q , is given by Eq.(3.3.3).

$$q = \frac{A k' \Delta p}{\mu s} \quad (3.3.3)$$

Note that Eq.(3.3.3) assumes a thin-walled structure, i.e. $s \ll R$. Based on this equation, leakage failure for a particular loading ratio was determined as follows. At leakage failure, prototype specimens exhibited a large amount of fluid loss due to their large surface area. This inhibited further pressurisation (pressurisation stalled after leakage failure), as the reciprocating pump reached its maximum volumetric flow rate. Note that this flow rate depends on the pump output pressure as well as the air supply pressure. The latter was kept constant for all experiments. Performance charts (supplied by the pump manufacturer) were used to determine the volumetric flow rates at leakage failure, Q , from the air supply pressure and the maximum recorded pump output pressure (Note that $Q = q|_{failure}$). A characteristic intrinsic permeability at leakage failure, K' , was then calculated for the applied loading ratio from Eq.(3.3.3) (Note that $K' = k'|_{failure}$).

For the case of leakage failure, Eq.(3.3.3) can be written as,

$$\frac{Q}{\Delta p_f} = \frac{A K'}{\mu t} \quad (3.3.4)$$

where $Q/\Delta p_f$ is a characteristic value for the occurrence of leakage for a particular specimen, with Δp_f being the leakage failure pressure.

For model specimens, characteristic values for the occurrence of leakage, $Q/\Delta p_f$, were calculated from Eq.(3.3.4) using the dimensions of model specimens and characteristic intrinsic permeability values for the applied loading ratios, K' , which were determined

from prototype specimens. During testing of model specimens the fluid loss from the pressure intensifier as well as time and internal pressure data were recorded (besides others). Fluid loss data were normalised according to the compressibility and expansion characteristics of the hydraulic system, and differentiation with respect to time produced volumetric flow rate data, q . This enabled the calculation of $Q/\Delta p$. From this data, leakage failure pressures were found using the characteristic values for the occurrence of leakage, $Q/\Delta p_f$. As an example, a graph correlating specimen internal pressure and data according to $Q/\Delta p$ is shown in Fig.3.3.2. (Note that the expansion of the tube also contributes to the flow rate Q . Yet, this contribution to the flow rate is negligibly small, which is shown in Fig.3.3.2 for the lower pressure levels.)

3.4 Testing of Model-Scale Specimens for Structural Failure

Fluid loss at functional failure prevents any further specimen pressurisation, which renders the testing for structural failure impossible in most cases. To remedy this problem, researchers have developed bladder systems that allow for continued pressurisation until structural failure occurs (e.g. Hull et al., 1978). In the present study, a

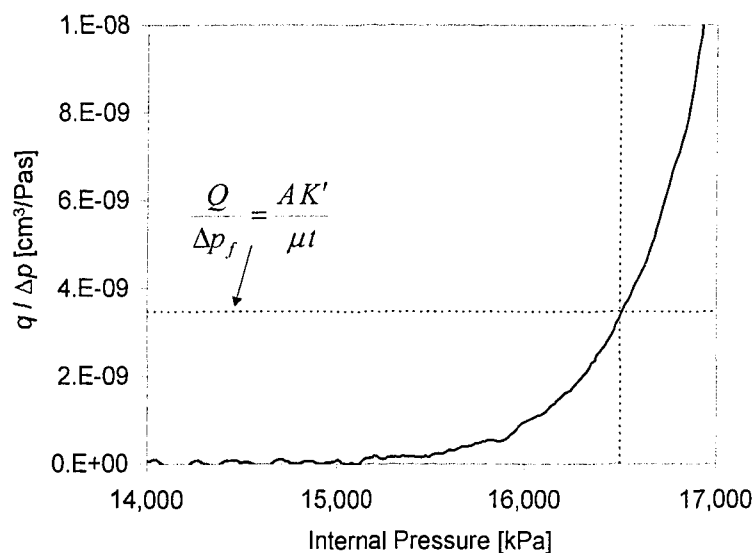


Figure 3.3.2: Example of graph showing model specimen internal pressure versus normalised volumetric flow rate, $q/\Delta p$.

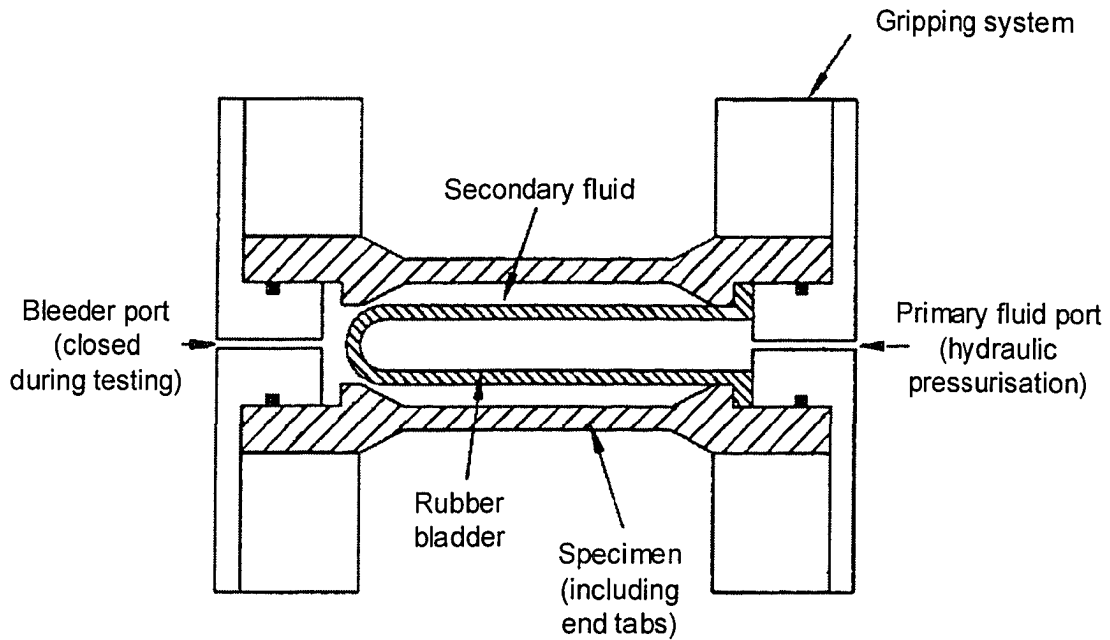


Figure 3.4.1: Schematic of the bladder system for the investigation of structural failures, adopted from Wolodko (1999).

bladder system developed by Wolodko (1999) was employed (shown in Fig.3.4.1). Here, a rubber bladder was placed inside the specimen. Hydraulic fluid filled the annulus between bladder and specimen wall, and pressure was applied from within the bladder. At functional failure the escaping fluid allowed the bladder to expand until it was pressed against the specimen wall. There it acted as a seal allowing for further pressurisation until ultimate failure of the specimen.

3.5 Loading Considerations

3.5.1 Biaxial Tensile Loading Spectrum

After the installation of model and prototype specimens into the respective testing machines, biaxial stress states with constant hoop-to-axial stress ratios were imposed upon the tubular structures. The control system of each testing apparatus ensured the application of a constant stress ratio using (a) axial force and pressure feedback signals,

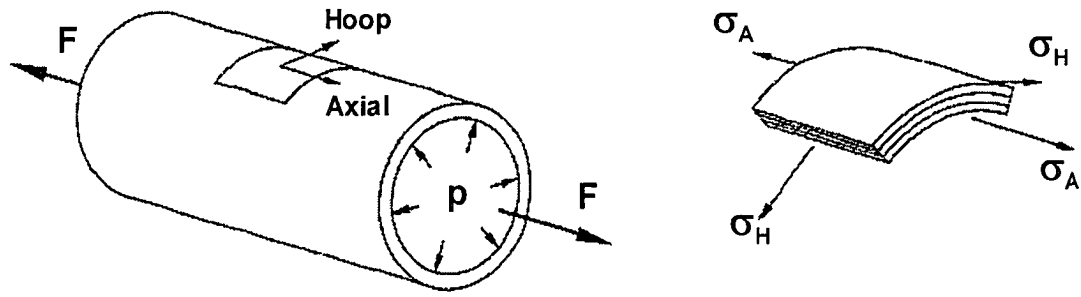


Figure 3.5.1: Loading scheme for tubular specimens (left) and applied biaxial stress condition (right).

and (b) information about the specimen geometry, which was entered by the operator. Consequently, all tests were performed under load control. To simplify matters an average specimen wall thickness, \tilde{s} , was entered for model and prototype specimens respectively, and used as a geometric parameter for the testing of each specimen type regardless of layup configuration. The computation of the necessary loads was based on the thin cylinder membrane theory, see Eqs.(3.5.1a) and (3.5.1b). The loading scheme and the resulting stress state are shown on the left-hand-side and right-hand-side of Fig.3.5.1 respectively. Note that internal pressurisation also produces radial stress. However, this stress component was neglected, since it is smaller by an order of magnitude in comparison to the other two stress components.

$$\sigma_H = \frac{\Delta p D}{2\tilde{s}} \quad \sigma_A = \frac{\Delta p D}{4\tilde{s}} + \frac{F}{\pi D\tilde{s}} \quad (3.5.1a-b)$$

where D is the specimen inside diameter, F in the applied axial force, and σ_H and σ_A are the average hoop and axial stress respectively.

In this research project, biaxial loading conditions were described by their hoop-to-axial stress ratios. For example, a two-to-one hoop-to-axial stress ratio is denoted by [2H:1A]. Applied stress ratios are listed in Table 3.5.1; and a test matrix correlating specimen types and loading conditions is provided in Table 3.5.2.

Table 3.5.1: Description of biaxial stress ratios.

<p>[1H:0A]: pure hoop (“open end”) loading condition</p> <p>[2H:1A]: “closed end” loading condition, also known as “pressure vessel loading”</p> <p>[3H:1A], [1H:1A] and [1H:3A]: stress ratios corresponding to netting theory for $\pm 60^\circ$, $\pm 45^\circ$ and $\pm 30^\circ$ angle-ply respectively (for details on netting theory refer to e.g. Tew, 1995; Grove, 1999)</p> <p>[1H:15A] and [1H:5A]: axial-dominated stress ratios for the investigation of axial capacity of model and prototype specimens respectively (internal pressure was applied to facilitate the observation of leakage)</p> <p>[0H:1A]: pure axial loading condition without the capability to investigate leakage (due to the lack of internal pressurisation)</p>
--

3.5.2 Compilation of Failure Strengths into Biaxial Failure Envelopes

After the completion of testing, stresses were computed in a post-processing operation; pressure and force recordings, and the specimen wall thickness, s , for each type of specimen and fibre architecture, were employed in conjunction with Eqs.(3.5.2) and (3.5.3) for the calculation.

$$\sigma_H = \frac{D(p_i - p_o) - 2s p_o}{2s} \quad (3.5.2)$$

$$\sigma_A = \frac{D^2(p_i - p_o) - 4p_o s(D + s)}{4s(D + s)} + \frac{F}{\pi s(D + s)} \quad (3.5.3)$$

The average hoop and axial stresses at functional and structural failure, i.e. functional and structural strengths were determined according to the criteria defined earlier (Subsection 3.3.2). Note that only data from successful tests are provided in this thesis. In some cases, unusually high leakage was encountered that could be traced back to defective seals. In such an instance, results were not included; hence, the number of

Table 3.5.2: Test matrix summary of applied stress ratios.

<i>H:A ratio:</i>	0:1	1:15	1:5	1:3	1:1	2:1	3:1	1:0
<i>Specimen type:</i>								
<i>model pipe, [$\pm 60_3$]_T</i>		X				X	X	X
<i>model pipe, [$\pm 45, \pm 60_2$]_T</i>		X			X	X	X	X
<i>model pipe, [$\pm 60_2, \pm 45$]_T</i>		X			X	X	X	X
<i>model pipe, [$\pm 30, \pm 60_2$]_T</i>		X		X	X	X	X	X
<i>prototype pipe, [$\pm 60_5$]_T</i>			X			X	X	X
<i>prototype pipe, [$\pm 60_3, \pm 30$]_T</i>			X			X	X	X
<i>prototype pipe, w/ coupler*, [$\pm 60_3, \pm 30$]_T</i>	X					X	X	
<i>improved prototype pipe**, w/ coupler, [$\pm 60_3, \pm 30$]_T</i>	X					X		

* for details on the coupler geometry see Chapter 5: Section 5.4

**for details on the improved prototype pipe see Chapter 5: Section 5.8

results for functional and structural failure may differ. Furthermore, stress ratios given by the [H:A] denote only the approximate applied ratios. This stems from the use of an average wall thickness as a geometry parameter for the control of the testing machines. The exact stress ratios can be calculated from given pairs of hoop and axial stress values. However, differences between the exact and approximate values are small, and are considered insignificant for the outcome of the experiments.

In the present study, functional and structural strengths were compiled into biaxial failure envelopes to illustrate the test results more clearly. Lines fitted through the average of each set of data points delineate each failure envelope.

3.5.3 Specimen Loading Rates

Model specimens:

Pressurisation of model specimens occurred with a constant rate of 4.63 kPa/s for all but two applied stress ratios. To produce axial-dominated stress ratios, i.e. [1H:15A] and [1H:3A], only relatively low internal pressures were required. In order to obtain test durations of the same order of magnitude, pressure rates were adjusted to 0.46 kPa/s and 0.92 kPa/s respectively.

During testing the analogue controller modules independently adjusted pressure and force based on respective command signals from the personal computer. Thus, it was necessary to supply the personal computer with pressure as well as with force rate values. Force rate were calculated from Eq.(3.5.4), which was obtained from Eqs.(3.5.2) and (3.5.3) by differentiation with respect to time, \hat{t} .

$$\dot{F} = \dot{p}_i \pi \left(\frac{A}{H} \frac{D(D+s)}{2} - \frac{D^2}{4} \right) \quad (3.5.4)$$

with $\frac{A}{H}$ is the inverse of the desired stress ratio [H:A].

Prototype specimens:

In the case of the large-scale testing apparatus, the use of a reciprocating pressure pump constrained the pressure adjustability; less consistent pressurisation rates were the result. For the [1H:0A], [3H:1A], [2H:1A] and [1H:5A] stress ratios, loading rates were 83.2 kPa/s (9.2 kPa/s), 62.7 kPa/s (14.7 kPa/s), 23.2 kPa/s (1.1 kPa/s) and 11.7 kPa/s (0.7 kPa/s) respectively. Values in parentheses quantify data variability given by the standard deviation.

Tests on prototype specimens were generally performed under pressure-control mode. The control mode refers to the parameter that is set versus the one being controlled; e.g. under pressure-control, specimen pressurisation simply followed a loading function, whereas the force was being adjusted based on the pressure feedback signal. However, the system was switched to force-control mode for large-scale testing under axial-dominated loading ratios, i.e. [1H:5A] and [0H:1A]. This was necessary since in

these cases applied pressures were too low to constitute a stable control signal, i.e. the force actuator was incapable to follow pressure fluctuations inherent to the reciprocating pump. Under these loading conditions, axial force was applied with a rate of 444.8 N/s.

In an earlier paper Carroll et al. (1995a) investigated the impact of the applied monotonic stress rate, $\partial\sigma/\partial\hat{t}$, on the strength of filament-wound composites ($\pm 55^\circ$ tubes with 49.5 mm inside diameter). Stress rates were given based on ‘von Mises’ equivalent stress, see Eq.(3.5.5).

$$\frac{\partial\sigma}{\partial\hat{t}} = \frac{\partial\sigma_{eq}}{\partial\hat{t}} \quad \text{with} \quad \sigma_{eq} = \sqrt{\sigma_A^2 - \sigma_A\sigma_H + \sigma_H^2} \quad (3.5.5)$$

The above equations were employed in the present research study to characterise loading rates independently from the control mode for each loading case and specimen configuration. Average stress rates for each specimen type and biaxial loading ratio are listed in Table 3.5.3. Note that loading rates for joint specimens are discussed in Chapter 5: Section 5.6. Data in Table 3.5.3 show that stress loading rates for model specimens were generally about an order of magnitude lower than those applied to prototype specimens.

Table 3.5.3: Specimen average loading rates in terms of von Mises equivalent stress, in kPa/s.

<i>H:A ratio:</i>	0:1	1:15	1:5	1:3	1:1	2:1	3:1	1:0
<i>Specimen type:</i>								
<i>model pipe, [$\pm 60_3$]_T</i>		105.7				63.1	64.2	72.8
<i>model (baseline) pipe, [$\pm 60_3$]_T</i>		100.7				60.1	61.2	69.7
<i>model pipe, [$\pm 45, \pm 60_2$]_T</i>		97.6			67.3	58.3	59.3	67.3
<i>model pipe, [$\pm 60_2, \pm 45$]_T</i>		99.1			68.3	59.2	60.2	68.3
<i>model pipe, [$\pm 30, \pm 60_2$]_T</i>		86.4		31.5	59.5	51.6	52.5	59.5
<i>prototype pipe, [$\pm 60_5$]_T</i>			527.8			197.8	544.4	819.1
<i>prototype pipe, [$\pm 60_3, \pm 30$]_T</i>			588.3			220.4	606.7	912.9

CHAPTER 4

PERFORMANCE INVESTIGATION OF COMPOSITE TUBULAR STRUCTURES

4.1 Experimental Verification of Elastic Constants

Hoop (E_{YY}) and axial (E_{XX}) Young's moduli and Poisson's ratios (ν_{XY}) were calculated from the initial (approximately linear) stress-strain responses of model specimens tested under pure hoop and approximated pure axial loading (i.e. [1H:15A]). Results are shown in Table 4.1.1 for model specimens with $[\pm 60_3]_T$, $[\pm 45, \pm 60_2]_T$ and $[\pm 30, \pm 60_2]_T$ lay-ups.

To confirm data provided by the suppliers of the constituent materials, respective Young's moduli were computed from experimental data of specimens with $[\pm 60_3]_T$ lay-up. The computation followed the methodology described in Subsection 2.2.4, and a numerical code was developed accordingly. Lamina properties were determined first, and the properties of the constituents were then fitted using the aforementioned Halphin-Tsai and Rosen-Hashin models. Fibre and matrix Poisson's ratio's were taken from Kaw (1997) and Hu et al. (2003) respectively (fibre: $\nu_F = 0.2$, matrix: $\nu_M = 0.42$). This yielded fibre and matrix Young's moduli of 81.5 GPa and 3.4 GPa. These results agree well with data provided by the manufacturers (see Section 2.3) and Hu et al. (2003).

In a subsequent step, elastic properties of the $[\pm 45, \pm 60_2]_T$ and $[\pm 30, \pm 60_2]_T$ lay-ups were calculated employing the above constituent properties and the average fibre volume fraction of each specimen type. Again, the computation was based on the described micro-mechanical methodology and classical lamination theory. Elastic properties of the two layups are also provided in Table 4.1.1. Comparison between data found by measurement and those based on micro-mechanical analysis confirms good agreement and consistency between experimental and analytical results. In the analyses to follow the computed constituent properties were used as listed in Table 4.1.2.

Table 4.1.1: Average values of elastic constants from measurement and analytical analysis of the $[\pm 60_3]_T$, $[\pm 45, \pm 60_2]_T$ and $[\pm 30, \pm 60_2]_T$ lay-ups (Mertiny et al., 2004a).

	$[\pm 60_3]_T$ *	$[\pm 45, \pm 60_2]_T$	$[\pm 30, \pm 60_2]_T$
E_{XX} , from experiments	20.6 GPa	20.6 GPa	25.8 GPa
Standard deviation	NA	NA	4.0 GPa
(E_{XX} , from constituents)	(19.9 GPa)	(20.8 GPa)	(25.6 GPa)
E_{YY} , from experiments	36.3 GPa	31.7 GPa	29.5 GPa
Standard deviation	3.2 GPa	NA	1.0 GPa
(E_{YY} , from constituents)	(36.3 GPa)	(31.0 GPa)	(27.9 GPa)
ν_{XY} , from experiments	0.23	0.35	0.32
Standard deviation	NA	NA	0.04
(ν_{XY} , from constituents)	(0.30)	(0.36)	(0.38)

* baseline specimen configuration

Table 4.1.2: Elastic properties of fibre and matrix material (Mertiny and Ellyin, 2004b).

E_F	Young's Modulus of Fibres	81.5 GPa
ν_F	Poisson's Ratio of Fibres	0.20
E_m	Young's Modulus of Matrix	3.4 GPa
ν_m	Poisson's Ratio of Matrix	0.42

Effect on fixed-end loading condition:

The operating conditions of pipe are often equivalent to a fixed-end loading condition (e.g. the pipe is buried in the ground). No tests were conducted that specifically applied such a condition. However, it will be shown that a fixed-end loading is adequately approximated by one of the applied biaxial stress ratios. The analysis to follow is based on the principle stress-strains relations for an orthotropic material, given by Eqs.(4.1.1) (see e.g. Kollár and Springer, 2003).

$$\begin{pmatrix} \varepsilon_{11} \\ \varepsilon_{22} \\ \varepsilon_{33} \\ \gamma_{23} \\ \gamma_{13} \\ \gamma_{12} \end{pmatrix} = \begin{bmatrix} \frac{1}{E_{11}} & -\frac{\nu_{21}}{E_{22}} & -\frac{\nu_{31}}{E_{33}} & 0 & 0 & 0 \\ -\frac{\nu_{12}}{E_{11}} & \frac{1}{E_{22}} & -\frac{\nu_{32}}{E_{33}} & 0 & 0 & 0 \\ -\frac{\nu_{13}}{E_{11}} & -\frac{\nu_{23}}{E_{22}} & \frac{1}{E_{33}} & 0 & 0 & 0 \\ 0 & 0 & 0 & \frac{1}{G_{23}} & 0 & 0 \\ 0 & 0 & 0 & 0 & \frac{1}{G_{13}} & 0 \\ 0 & 0 & 0 & 0 & 0 & \frac{1}{G_{12}} \end{bmatrix} \begin{pmatrix} \sigma_{11} \\ \sigma_{22} \\ \sigma_{33} \\ \sigma_{23} \\ \sigma_{13} \\ \sigma_{12} \end{pmatrix} \quad (4.1.1)$$

A relationship for the hoop-to-axial stress ratio σ_{YY}/σ_{XX} under fixed-end loading is found from the elastic material properties, and the assumption of zero axial displacement,

$$\varepsilon_{XX} = \frac{\sigma_{XX}}{E_{XX}} - \nu_{YX} \frac{\sigma_{YY}}{E_{YY}} = 0 \Leftrightarrow \frac{\sigma_{YY}}{\sigma_{XX}} = \frac{E_{YY}}{E_{XX}} \frac{1}{\nu_{YX}} \quad (4.1.2)$$

The relationship between the major and minor Poisson's ratios is defined by

$$\frac{\nu_{12}}{E_{11}} = \frac{\nu_{21}}{E_{22}}, \quad \frac{\nu_{13}}{E_{11}} = \frac{\nu_{31}}{E_{33}}, \quad \frac{\nu_{23}}{E_{22}} = \frac{\nu_{32}}{E_{33}} \quad (4.1.3)$$

Thus,
$$\sigma_{YY}/\sigma_{XX} = \nu_{XY}^{-1} \quad (4.1.4)$$

Stress ratios for the zero axial displacement condition for $[\pm 60_3]_T$, $[\pm 45, \pm 60_2]_T$ and $[\pm 30, \pm 60_2]_T$ model specimens are therefore [3.3H:1A], [2.8H:1A] and [2.6H:1A] respectively, based on data from micro-mechanical analysis provided in Table 4.1.1. Hence, the applied [3H:1A] loading ratio is seen to adequately approximate fixed-end loading conditions. Note that the above stress ratios for fixed-end loading were calculated assuming elastic material behaviour. Depending on the applied load levels these stress ratios may vary for materials that are non-linear viscoelastic or that experienced damage such as matrix cracking.

4.2 Effect of Filament Winding Tension[†]

In Section 2.4 filament winding tension was recognized to have an appreciable influence on component properties; the effect on physical properties and secondary process parameters was investigated. The focus of the present section is to investigate the effect of winding tension on the mechanical performance of pressurised composite tubes.

4.2.1 Experimental Results

Two sets of $[\pm 60^\circ_3]_T$ specimens were subjected to biaxial stress states with varying tensile hoop-to-axial stress ratios (i.e. [1H:0A], [3H:1A], [2H:0A] and [1H:15A]). Specimens were produced with 26.7 N (baseline configuration) and 44.5 N tow tension respectively. Monotonic stress-strain characteristics, and the circumstances under which specimens exhibited failure, are described below. Note that the $[\pm 60^\circ_3]_T$ lay-up was chosen based on a numerical study by Thornton (1999), which identified this winding angle to be suited for a pipeline application under certain pressure, installation and operational loads.

Biaxial monotonic stress-strain response:

(a) [1H:0A]: Figure 4.2.1 shows the characteristic measured global stress-strain response along with the computed strains transverse (ϵ_T) and parallel (ϵ_P) to the fibres. In this test functional and structural failure of the tubular occurred almost simultaneously, i.e. gradual leakage was not observed. The presence of a negative transverse strain component is deemed to be the reason for this type of behaviour (see Subsection 4.2.2).

(b) [3H:1A]: Results from this test indicated a stress range with pronounced leakage between the functional and structural failure event (see Fig.4.2.2). Leakage occurred at a positive transverse strain of about 0.25%. After the occurrence of functional failure a strong non-linearity in the otherwise almost linear stress-strain response, prior to leakage, was recorded for the axial and transverse direction (i.e. the matrix-dominated directions).

[†]A version of this section appeared as: Mertiny, P. and Ellyin, F. (2002). Influence of the filament winding tension on physical and mechanical properties of reinforced composites. Composite Part A, Vol. 33A, 1615-1622.

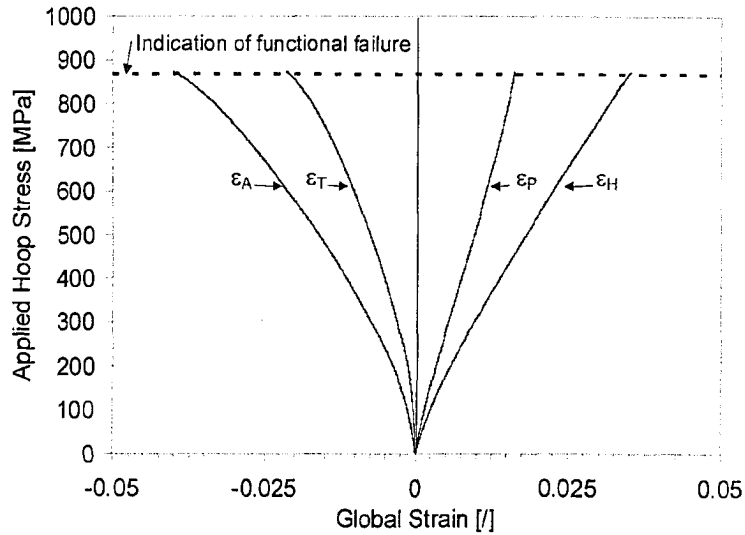


Figure 4.2.1: Biaxial stress-strain response for pure hoop loading, ϵ_A , ϵ_H : axial and hoop strain (measured); ϵ_T , ϵ_P (calculated) transverse and parallel to fibre strain (Mertiny and Ellyin, 2002).

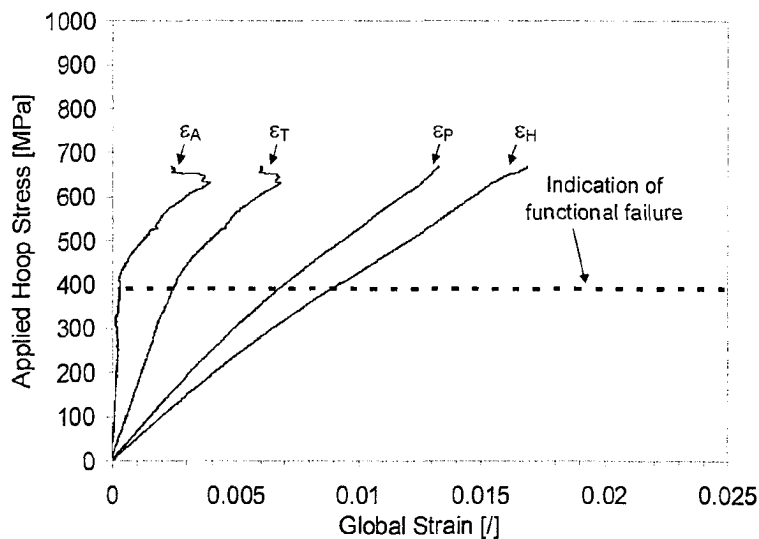


Figure 4.2.2: Biaxial stress-strain response for a $[3H:1A]$ loading ratio, ϵ_A , ϵ_H : axial and hoop strain (measured); ϵ_T , ϵ_P (calculated) transverse and parallel to fibre strain (Mertiny and Ellyin, 2002).

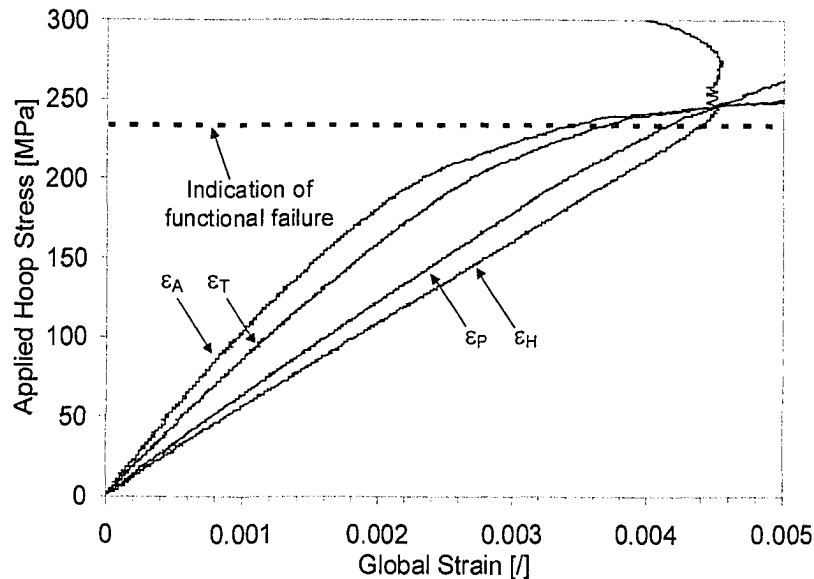


Figure 4.2.3: Biaxial stress-strain response for closed end loading, ϵ_A , ϵ_H : axial and hoop strain (measured); ϵ_T , ϵ_P (calculated) transverse and parallel to fibre strain (Mertiny and Ellyin, 2002).

(c) [2H:1A]: Similar to the preceding test, the hoop and parallel to the fibres stress-strain response of this loading (i.e. fibre-dominated components) is nearly linear before functional failure (see Fig.4.2.3). However, more pronounced non-linear behaviour is noticeable in the matrix-dominated directions. After functional failure at a transverse strain of 0.35% a non-linear behaviour was recorded. The matrix-dominated strain components trend towards high positive values, whereas the hoop strain shifts towards high negative values. This behaviour indicates a strong change in specimen geometry. After functional failure the matrix increasingly breaks down allowing the fibres to realign in the resultant loading direction. This behaviour was subsequently accompanied by a significant change in length and diameter of the specimen. However, these changes were not measurable with the test set-up, hence, stresses were calculated assuming unchanged specimen dimensions.

(d) [1H:15A]: Figure 4.2.4 shows the stress-strain response of a typical specimen in the almost pure axial loading case. Strains in fibre direction were negligibly small; thus

the load was carried to a great extent by the matrix material. At 0.32% transverse strain functional failure occurred at a low axial stress value. At this point the specimen also lost its load-bearing capability, consequently functional and structural failure coincided.

Structural failure characteristics:

Visual inspection of the fractured specimens provided further insights into the mechanisms accompanying structural failure. In Fig.4.2.5 the typical appearance of damaged specimens is presented for the [3H:1A], [2H:1A] and [1H:15A] loading cases. Note that a specimen tested under a pure hoop loading is not shown, since these specimens failed by burst leaving only fragments behind; thus, no localised damage could be assessed. This type of behaviour indicates that within the structure a high amount of energy was stored in an evenly distributed manner. Under a [3H:1A] loading, burst failures with fractured surfaces parallel to the fibre direction could be observed. Failure generally occurred within the gauge section of the specimen. This type of damage is characteristic of a fibre-dominated failure mode where fibres are loaded parallel to the resulting loading direction. The strength of the fibre structure is well utilised in this

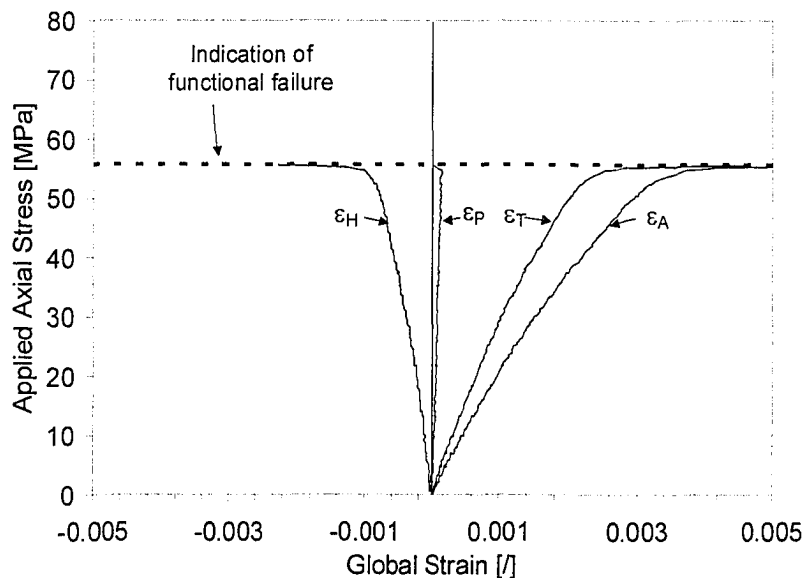


Figure 4.2.4: Biaxial stress-strain response for a [1H:15A] loading ratio, ϵ_A , ϵ_H : axial and hoop strain (measured); ϵ_T , ϵ_P (calculated) transverse and parallel to fibre strain (Mertiny and Ellyin, 2002).

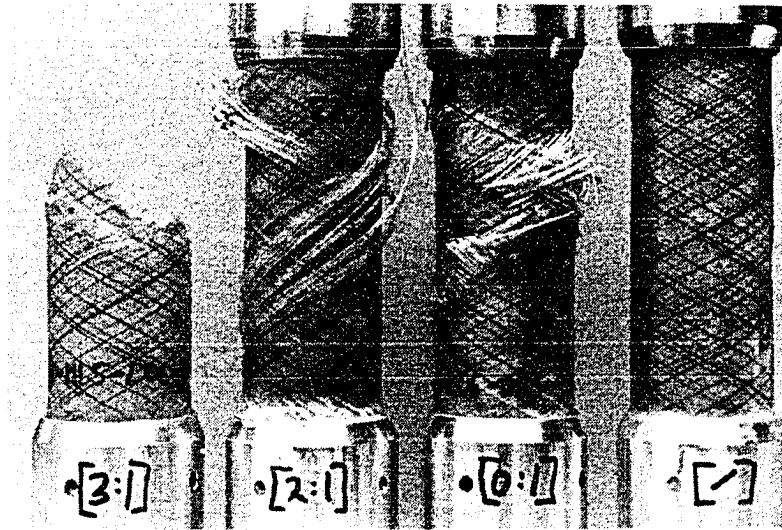


Figure 4.2.5: Photograph of specimens failed under (a) [3H:1A], (b) [2H:1A] and (c) [1H:15A] loading conditions, and (d) undamaged specimen (from left to right) (Mertiny and Ellyin, 2002).

loading/lay-up combination. In the [2H:1A] loading case, localised failure occurred near the end tabs, indicating a stress concentration in this zone. As the fibres were fixed in the annulus of the end-tabs, the aforementioned fibre realignment after matrix breakdown led to an additional localised fibre bending; thus, the potential of the fibre structure was not fully utilised. In the pure axial loading case the fibre bed immediately pulled apart after the breakdown of the matrix, indicating a poor utilisation of the potential strength of the structure.

Biaxial monotonic failure envelopes:

Test results for specimens were compiled into four biaxial failure stress envelopes (shown in Fig.2.4.6). Note that respective biaxial stress data are given in Appendix D. Structural failure envelopes encompass the functional type, as expected. In the pure hoop loading case, structural and functional failure points practically coincide at the highest recorded hoop stresses. Generally, failure stresses show a good consistency for the different loading ratios. The exception is the [3H:1A] loading case, where values exhibit considerable scatter. This is attributed to variations in the strength of the fibre structure, which is predominantly load bearing in this case. However, mean values still follow a

general trend that is similar for the structural and functional failure type. This trend can be described as follows: Under [3H:1A] loading a higher winding tension (i.e. higher fibre volume fraction) produced components with greater strength. However, in the case of the other loading ratios, a higher winding tension produced parts with equal or even less strength. In particular under increasingly matrix-dominated loading, i.e. [1H:15A] and [2H:1A], test results indicate that component strength was decreased by an increased tow tension. The above findings are summarised in Figure 4.2.7, where functional strengths in relation to the baseline configuration are portrayed. Note that a similar graph for structural failures would be virtually identical with that of the functional one.

Note that in the present study residual stresses induced during manufacturing were not considered for their influence on damage behaviour; neither was the time-dependent relaxation of these stresses due to the visco-elastic nature of the polymer matrix material, see e.g. Hu et al. (2003) and Chen et al. (2001). Yet, it is reasonable to presume that a

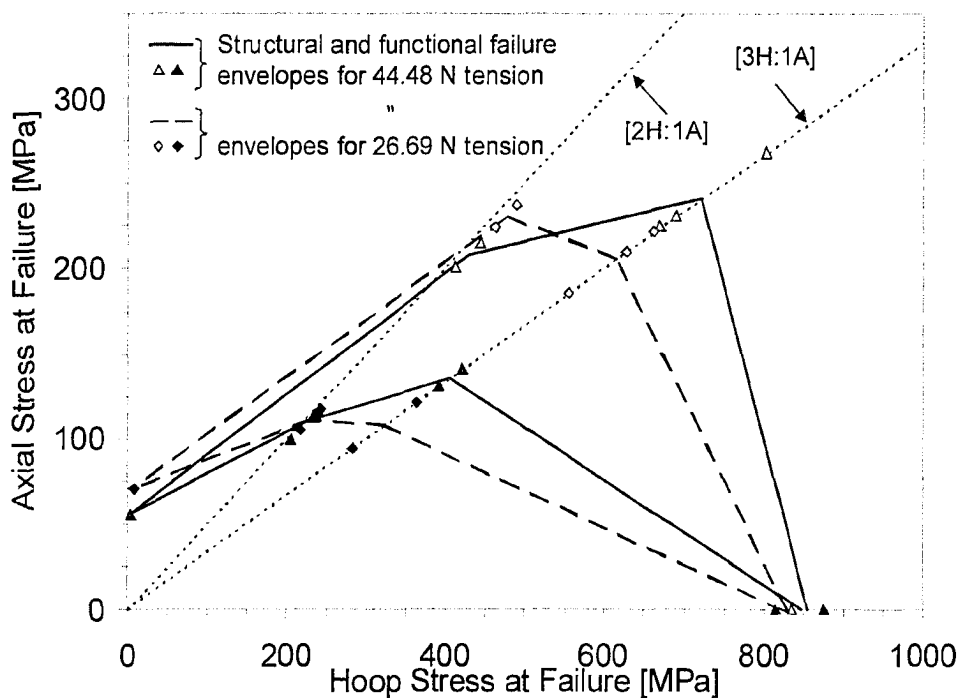


Figure 4.2.6: Biaxial functional and structural stress failure envelopes for $[\pm 60_3]_T$ model specimens (Mertiny and Ellyin, 2002).

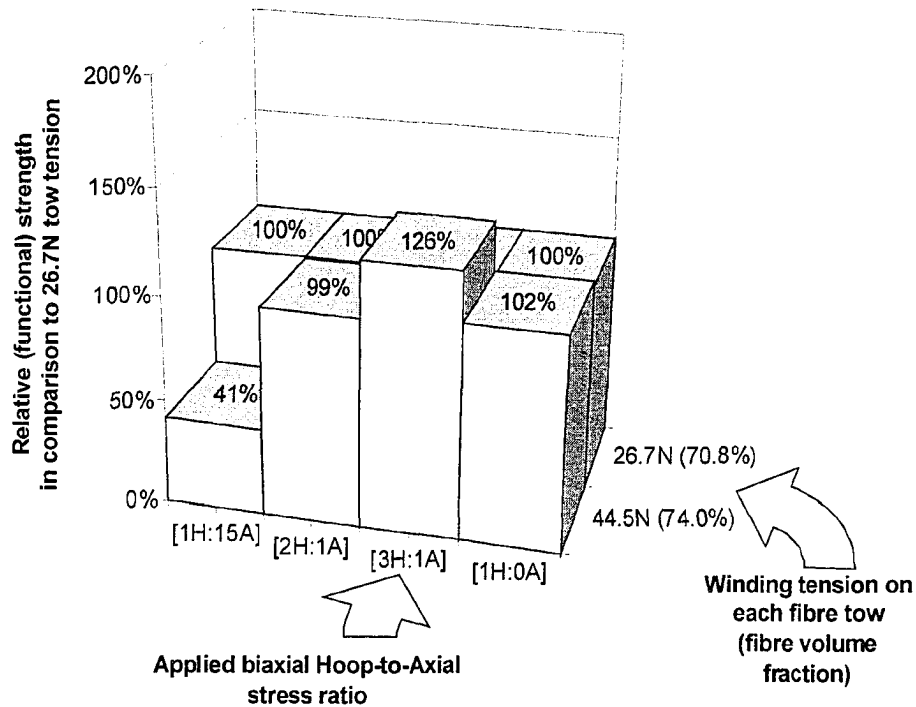


Figure 4.2.7: Relative functional strengths of $[\pm 60_3]_T$ model specimens.

distinct influence of the fibre volume fraction, i.e. the average fibre proximity, on component strength exists. This was shown by Cohen and co-workers (2001), who established a relationship between the relative fibre contents and the strength of filament wound pressure vessels. In that study the degree of fibre compaction was not adjusted by fibre tensioning but by employing a resin removal technique.

4.2.2 Analysis of the Experimental Observations

Qualitative analysis of functional failure events:

Matrix damage is regarded to be the primary cause for functional failure, as fluid weeping through the pipe wall could be observed, without any other visible damage to the pipe. This observation suggests that a network of cracks develops, starting from intra-laminar matrix damage. Cracks bridge inter-laminar zones and coalesce allowing fluid to penetrate through the wall of the tubular. It is reasonable to assume that intra-laminar matrix cracking is caused by strains acting transverse to the fibre direction.

Note that this leakage mechanism is only operative, if an opening mode, i.e. a positive displacement, is present. Hence, the typical leakage event was absent under [1H:0A] loading, where transverse strains were found to be compressive. From the recorded test data, strains parallel and transverse to the fibre direction at the leakage load were computed for the remaining three loading ratios. As shown in Fig.4.2.8, functional failure occurred approximately at an average value of 0.3% transverse strain, independent of the applied loading ratio. The exhibited scatter of data points is probably due to local geometric variations. In [3H:1A] loading, where principle stresses are aligned with the fibre direction, the observation of a common failure indicator (i.e. transverse strain) confirms that the material behaviour is in fact properly represented by the functional strength data. Since in case of the [2H:1A] and [1H:15A] stress ratios, principle stresses diverge from the fibre direction, more complex failure mechanisms need to be considered though, i.e. failure due to transverse as well as shear loading.

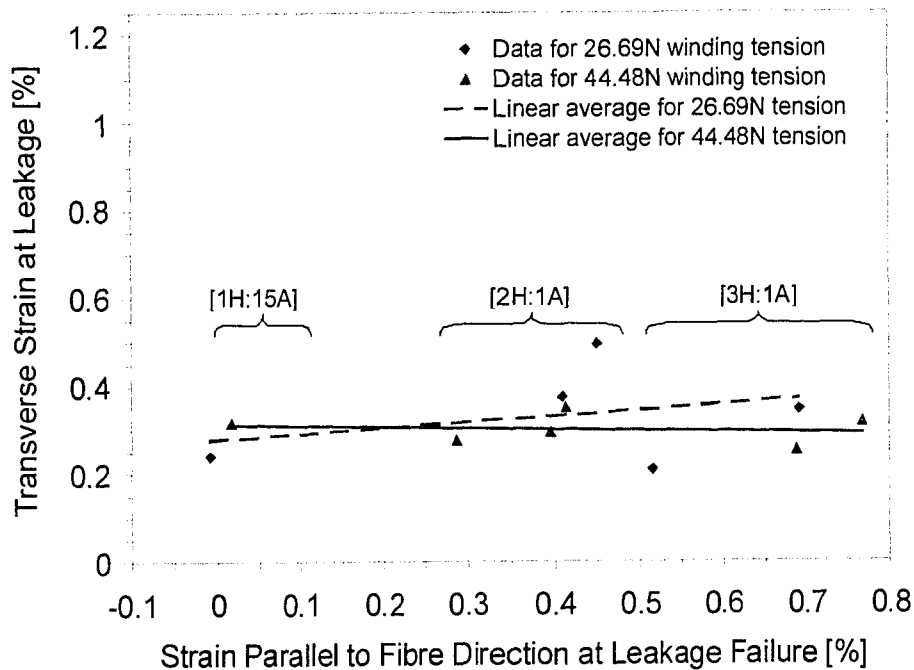


Figure 4.2.8: Strains parallel and transverse to fibres at functional failure loads
(Mertiny and Ellyin, 2002).

Based on a maximum elongation of the matrix material of 10.6% (Table 2.3.1), and the aforementioned Young's moduli of the constituents, the model by Kies (1962) (see Chapter 2: Subsection 2.2.1) predicts an ultimate transverse strain of the fibre composite of 0.7% and 0.9% for the specimens produced with 44.5 N and 26.7 N tow tension respectively. Values shown in Fig.4.2.8 are significantly lower. One reason for this discrepancy could be the non-uniform distribution of the fibres in the specimens, which causes numerous filaments being in closer proximity than assumed by a periodic fibre arrangement. Matrix damage and subsequent functional failure therefore develop at lower loads than predicted by the Kies model.

Qualitative analysis of structural failure events:

A unidirectional fibre/matrix structure is preferably loaded in fibre direction. Failure occurs when the tensile load exceeds a certain critical value (the maximum tensile strength, σ_{Pmax}). In the following, the observed structural failure behaviour will be qualitatively analysed applying the same principle. In the [3H:1A] loading case the resulting stress caused by the biaxial loading coincides with the applied winding angle of 60°. The stress/strain response and the investigation of fractured specimens indicated that for this case, fibres were actually experiencing a predominantly tensile loading. Hence, the stress parallel to the fibres at structural failure under [3H:1A] loading is assumed to be the maximum tensile strength of the fibre/matrix structure, σ_{Pmax} .

Mohr's circles were chosen to illustrate the conditions under pure hoop loading, see Fig.4.2.9. The [3H:1A] loading condition is represented by the top circle acting as a scale for comparison with the circle for the [1H:0A] loading case (shown below). The second circle was constructed using the maximum tensile strength of the fibre/matrix structure, σ_{Pmax} , and the given loading ratio. It can be observed that the hoop stress, σ_H , is necessarily greater than that in the first circle. This corresponds with the behaviour shown in the structural failure envelope (Fig.4.2.6). Moreover, the transverse stress, σ_T , for the pure hoop loading case is shown to be considerably less than that under [3H:1A] loading. This supports the assumption that significant matrix cracking did not occur under the pure hoop loading.

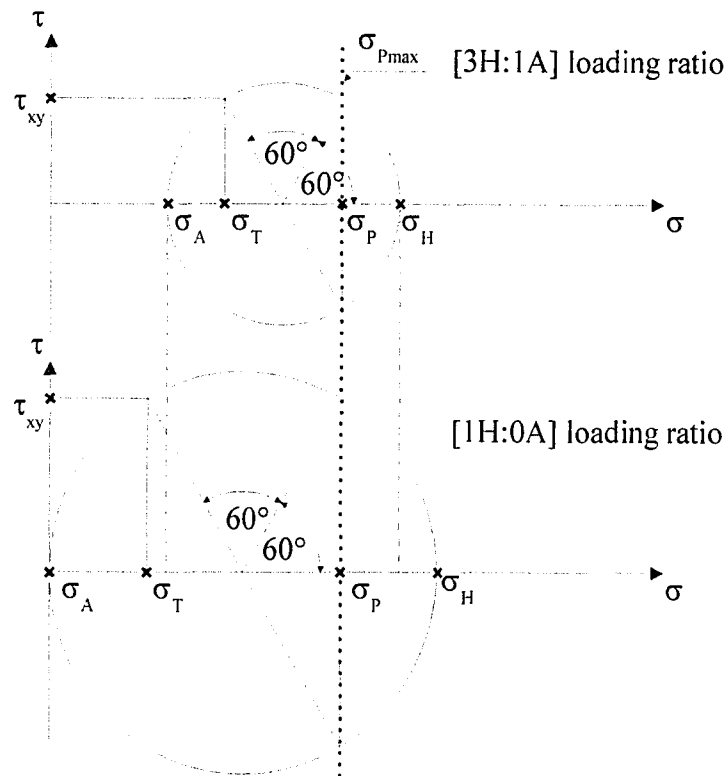


Figure 4.2.9: Mohr's circle illustration for comparison of the [3H:1A] and [1H:0A] structural failure behaviour (Mertiny and Ellyin, 2002).

Comparing the failure behaviour under [3H:1A] and [2H:1A] loading using a similar approach as presented above supports the assumption of a localised load concentration in the fibre structure under closed-end loading. In the bottom part of Fig.4.2.10, a Mohr's circle for the [2H:1A] loading was constructed using a fibre angle of 55° , which is the limit case for fibre realignment after matrix breakdown (found by conducting netting analysis for the particular loading ratio). Matching the stresses parallel to the fibre direction (i.e. $\sigma_P = \sigma_{Pmax}$) for the two considered loading ratios, resulted in nearly identical hoop stress values σ_H . This does not correspond with the experimental results, where the hoop stress is found to be less in the [2H:1A] loading case. However, incorporating a decreased maximum strength of the fibre structure (i.e. $\sigma_P < \sigma_{Pmax}$) gave a representation that quantitatively matched the experimental findings. Such a decrease was already suggested in Section 4.2.1 based on the presence of additional bending loads near

the specimen end tabs. Depending on the amount of strength reduction, axial stresses at failure, σ_A , can be higher or lower than the corresponding axial stresses in the [3H:1A] loading case; thus explaining the intersection of the structural failure envelopes for the high and low fibre volume fraction.

4.2.3 Implications for the Design of Composite Tubular Components

The above investigation confirmed that the applied winding tension and the mechanical performance of filament-wound structures are correlated. Unfortunately, the damage behaviour does not follow a simple unidirectional trend. Generally, an increase in winding tension has a beneficial effect on the component strength in the case of fibre-dominated loading, whereas under matrix-dominated loading a slight decrease in the failure strength was observed for increasing fibre compaction. Since structures for the storage and transportation of pressurised fluid are generally subject to variable loading

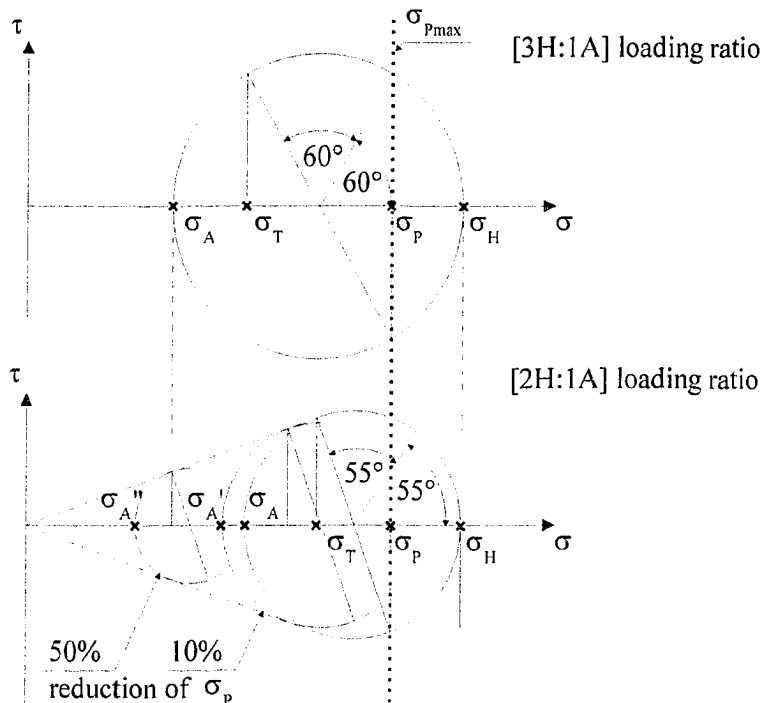


Figure 4.2.10: Mohr's circle illustration for comparison of the [3H:1A] and [2H:1A] structural failure behaviour (Mertiny and Ellyin, 2002).

conditions during installation and operation, the relatively low strength under matrix-dominated loading scenarios is of particular concern. Thus, fabrication with lower winding tensions is deemed desirable, to some extent, to enhance strength under axial loading. However, more significant improvements can be obtained by altering the specimen lay-up configuration (as described below).

4.3 Effect of Multi-Angle Filament Winding¹

Modern computer-controlled winding equipment permits the generation of almost any winding angle, see e.g. Giacoletto (2002). However, axial and hoop fibre lay-ups generally require pin-rings and hoop wrapping techniques with adjusted (small) bandwidths respectively. This reduces productivity, and thus, it is preferable to wind fibre helices at intermediate angles. Computer-controlled winding equipment also allows for an adjustment of the winding angle during the winding operation. This facilitates the production of multi-angle filament-wound structures. Lea and Yang (1998) described benefits of multi-angle filament-wound structures in comparison to such wound at the traditional $\pm 55^\circ$ angle (e.g. improved tension and bending characteristics).

The following design approach is common in industry: After a loading scenario has been identified, a uniform winding angle for the entire structure is based on a rather simplified design technique (e.g. netting theory). To a certain extent this approach has influenced the research direction, as evident from the amount of publications on strength and failure analysis of fibre composite pipe with fixed $\pm\alpha$ winding angles, e.g. Spencer and Hull (1978), Rosenow (1984), Amaldi and Marchetti (1992), Soden et al. (1993), Perreux and Thiebaud (1994, 1995), Carroll et al. (1995a), and Takayanagi et al. (2002).

Most investigations on multidirectional tubular composite structures, such as those presented by Ellyin et al. (1997) and Martens and Ellyin (2000), are limited to one lay-up configuration. Thus, these studies lack a systematic approach aimed at exhibiting benefits of multi-angle filament winding. In order to indicate potential benefits of multi-angle

¹ A version of this section appeared as: Mertiny, P., Ellyin, F. and Hothan, A. (2004a). An experimental investigation on the effect of multi-angle filament winding on the strength of tubular composite structures. *Composite Science and Technology*, Vol. 64, 1-9.

filament-wound structures, $[\pm 60_3]_T$ small-scale baseline specimens were experimentally compared to those with $[\pm 45, \pm 60_2]_T$ and $[\pm 30, \pm 60_2]_T$ lay-ups in the subsequent investigation. Specimens were tested employing the following biaxial stress ratios: [1H:0A], [2H:1A], [3H:1A], [1H:1A], [1H:3A] and [1H:15A].

4.3.1 Experimental Results

Observed modes of failure:

Independent from the applied loading ratios functional failures were characterised by the identical (visible) failure mode, i.e. weeping of fluid through the tube walls. Features of a structural failure, however, varied with the applied stress ratio. Even though every structural failure exhibited an individual appearance, certain common features were distinguishable. These characteristics were categorised into five structural failure modes described below.

(a) Under pure hoop loading, a “burst” type of failure was observed for all three lay-up configurations. Here, the entire structure of each specimen was destroyed and reduced to fragments.

(b) Under [3H:1A] loading burst failure also occurred, but specimens were generally split in two halves along the circumference. Jagged fracture surfaces were exposed, which were predominately parallel to the respective fibre direction. Fracture surfaces tend to be more frayed in the case of specimens with a multi-angle lay-up (see Fig.4.3.1).

(c) The [2H:1A] stress ratio produced failure close to one of the specimen end tabs. In the case of specimens with the $[\pm 30, \pm 60_2]_T$ lay-up an axially aligned crack-like perforation could be observed, whereas only a small localised perforation appeared with the other lay-up configurations. Pipe walls were perforated with frayed fibre strands protruding from the opening (see Fig.4.3.2). For a single $[\pm 45, \pm 60_2]_T$ specimen the fracture extended around the circumference of the tube.

(d) A complete or partial collapse of the specimens could be observed for tests under axial-dominated loadings of [1H:15A] and [1H:3A], respectively (Note: only $[\pm 30, \pm 60_2]_T$ specimens were tested in the latter stress ratio case.). Unlike other structural failure modes an apparent damage to the fibres was not noticeable. Failure is caused by

matrix damage: After extensive cracking of the matrix material, the fibre structure was broken up into loose fibre strands. Consequently, the structure lost its rigidity, and only insignificant loads could be carried by the structure. Fibre strands aligned into the direction of loading due to the action of the applied axial traction.

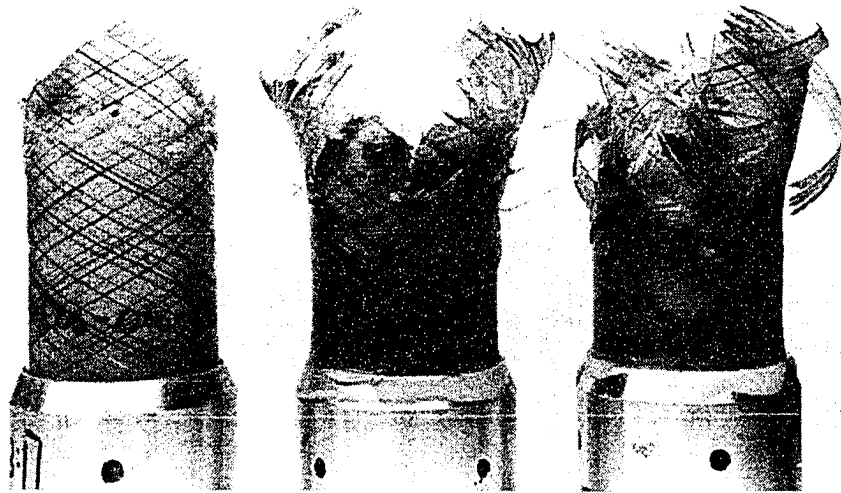


Figure 4.3.1: Failures mode under [3H:1A] loading: Burst failure showing jagged fracture surfaces (Mertiny et al., 2004a).

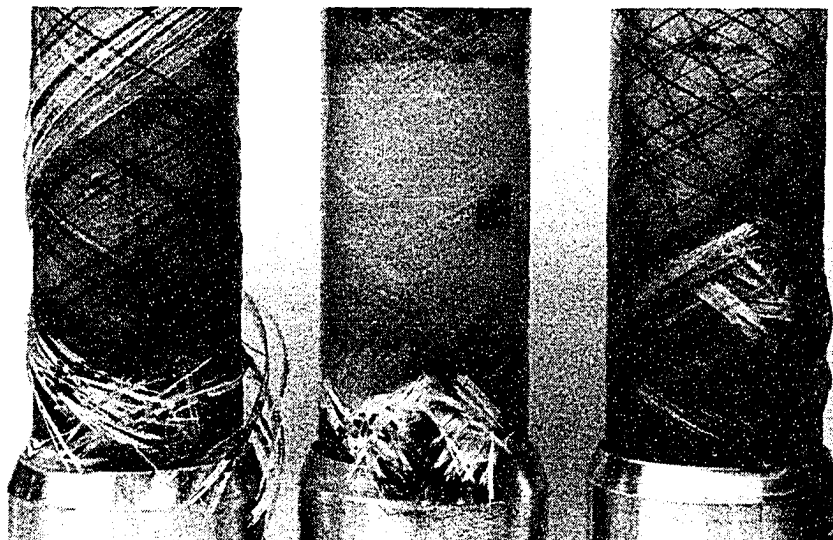


Figure 4.3.2: Failure mode under [2H:1A] loading: Localised burst failure (Mertiny et al., 2004a).

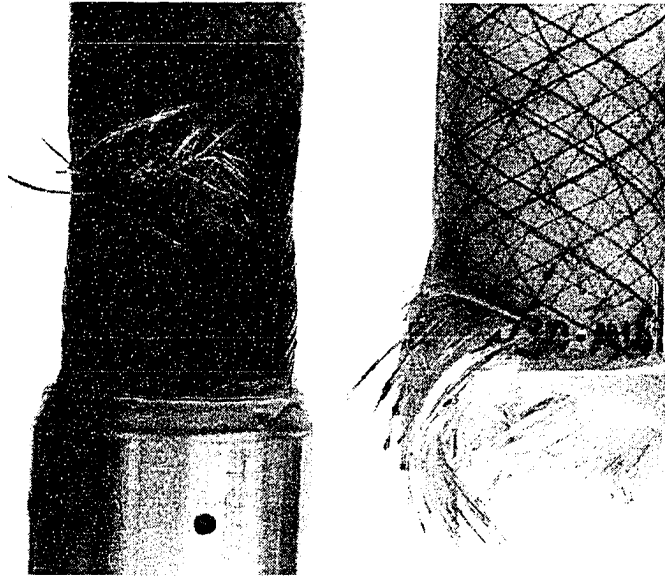


Figure 4.3.3: Failure modes under $[1H:1A]$ loading: Localised burst/collapse unique to $[\pm 45, \pm 60_2]_T$ lay-up (left); burst unique to $[\pm 30, \pm 60_2]_T$ lay-up (right) (Mertiny and Ellyin, 2004a).

(e) This failure mode only appeared with $[\pm 30, \pm 60_2]_T$ specimens under equi-biaxial loading, $[1H:1A]$. Specimens were fractured around the circumference close to one aluminium end tab. The fracture extended into the end tab, where fibre strands were pulled out from within the annulus of the end tab (see right-hand-side of Fig.4.3.3). Failure under equi-biaxial loading of specimens with a $[\pm 45, \pm 60_2]_T$ lay-up resembled a combination of the failure modes described under (c) and (d), i.e. failed tubes showed a perforation within a partially collapsed fibre structure (see left-hand-side of Fig.4.3.3).

Table 4.3.1 provides an overview of the observed structural failure modes (denoted by the above lettering) for every lay-up and stress ratio combination. Structural failures that were accompanied by extensive matrix damage, e.g. case (d), are denoted by (+).

4.3.2 Analysis of the Experimental Observations

Stresses at functional and structural failure:

Functional and structural failure envelopes are presented in two separate graphs, Figs. 4.3.4 and 4.3.5, respectively. A comparison of functional and structural strengths

indicated that under [1H:0A] and [1H:15A] loading, functional and structural failures practically coincided for all but one lay-up configuration. Only the $[\pm 45, \pm 60_2]_T$ lay-up exhibited a significantly lower functional than structural strength under the [1H:15A] ratio. This is further illustrated by the column chart in Fig.4.3.6 presenting the (average) relative functional-to-structural strengths for four types of loading and each lay-up. For the abovementioned stress ratios the relative strength was significantly below that of the reference case only in the case of the $[\pm 45, \pm 60_2]_T$ lay-up (i.e. 69%).

From Fig.4.3.6 it is noted that under [3H:1A] and [2H:1A] loading, the functional strength was significantly lower than the structural strength. Particularly in the latter case, tests indicated a low functional-to-structural strength ratio. A minimum value of 48% was found for specimens with the $[\pm 60_3]_T$ baseline lay-up. Without employing the pressure containing system (i.e. bladder) the usability of these structures would be limited by functional failure; therefore, improving functional strength becomes an important issue in order to fully utilise the potential of this kind of structure. This is, to some degree, achieved by the $[\pm 30, \pm 60_2]_T$ lay-up. In comparison to the baseline lay-up this multi-angle filament-wound structure had functional-to-structural strength ratios that were higher by an absolute 10% and 34% under [2H:1A] and [3H:1A] loading, respectively.

Table 4.3.1: Summary of structural failure modes correlating lay-up and loading configurations (Mertiny et al., 2004a).

<i>Lay-up Ratio</i>	<i>1H:15A</i>	<i>1H:3A</i>	<i>1H:1A</i>	<i>2H:1A</i>	<i>3H:1A</i>	<i>1H:0A</i>
$[\pm 60_3]_T$	(d) (+)			(c)	(b)	(a)
$[\pm 45, \pm 60_2]_T$	(d) (+)		(c/d) (+)	(c)	(b)	(a)
$[\pm 30, \pm 60_2]_T$	(d) (+)	(d) (+)	(e)	(c)	(b)	(a)

(a) = total burst

(b) = burst along fibre direction

(c) = localised failure near end tabs

(d) = matrix cracking

(e) = fracture near end tabs

(+) Structural failures were accompanied by extensive matrix damage.

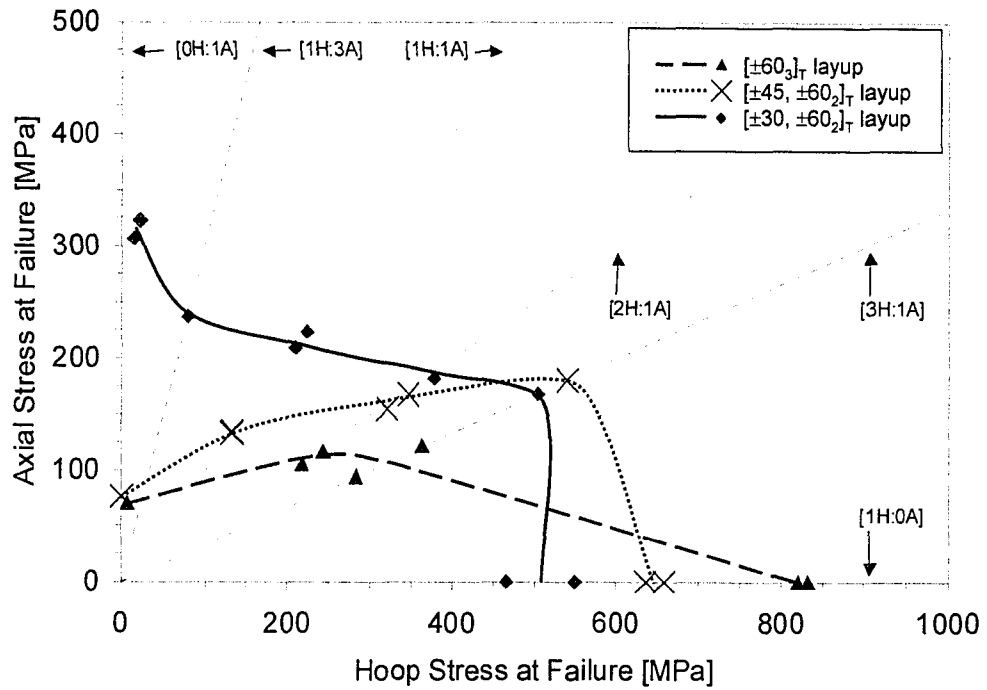


Figure 4.3.4: Experimental functional failure envelopes and points of failure of $[\pm 60_3]_T$, $[\pm 45, \pm 60_2]_T$ and $[\pm 30, \pm 60_2]_T$ tube specimens (Mertiny et al., 2004a).

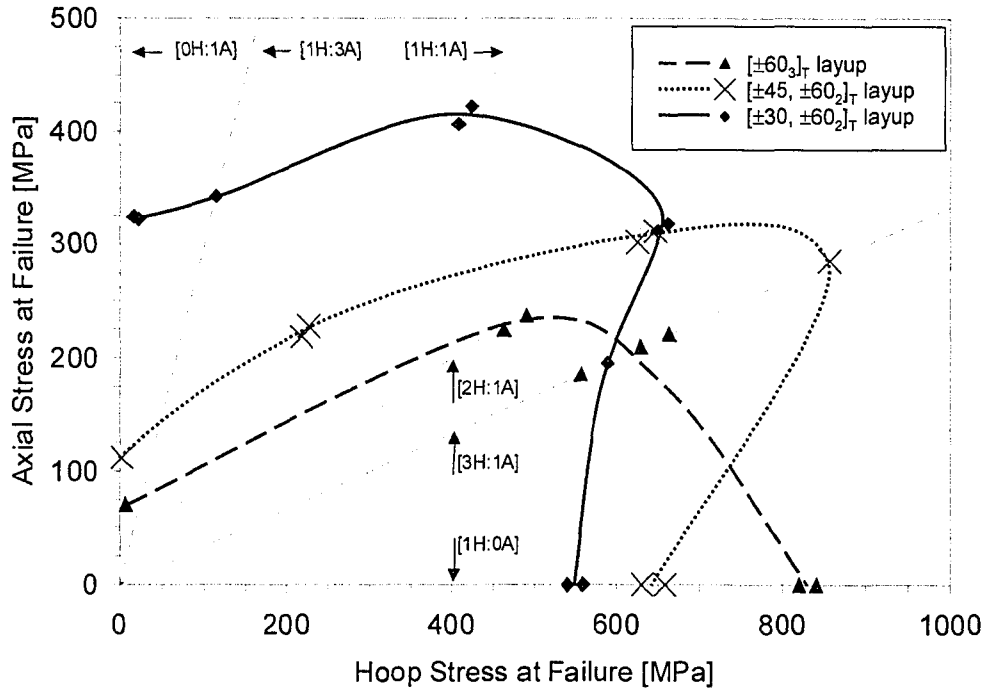


Figure 4.3.5: Experimental structural failure envelopes and points of failure of $[\pm 60_3]_T$, $[\pm 45, \pm 60_2]_T$ and $[\pm 30, \pm 60_2]_T$ tube specimens (Mertiny et al., 2004a).

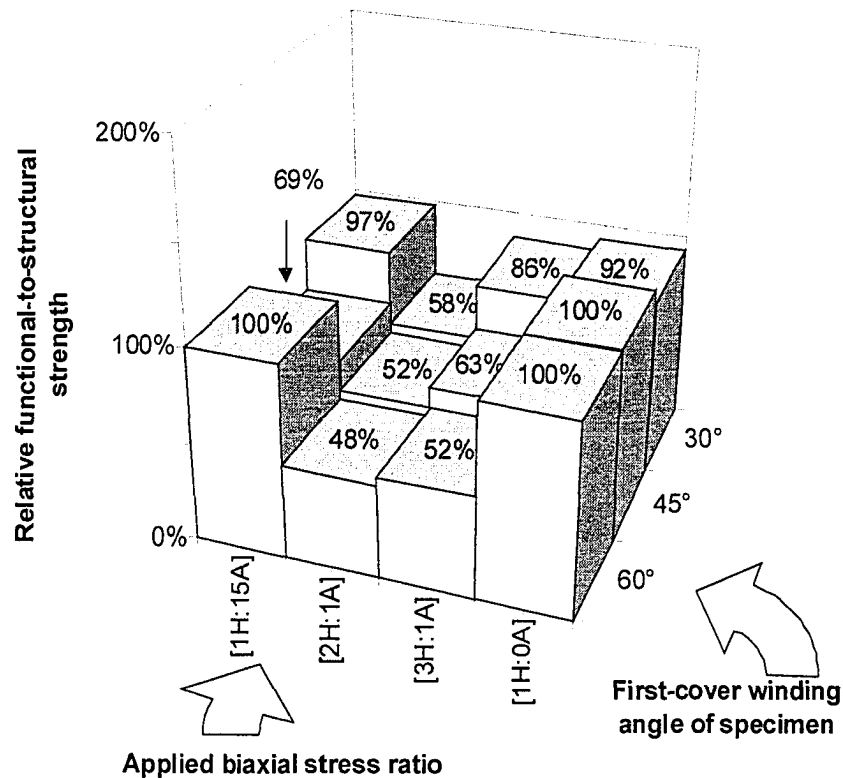


Figure 4.3.6: Relative functional-to-structural strength for each lay-up/loading combination (Mertiny et al., 2004a).

A notable feature of the $[\pm 60_3]_T$ lay-up is the high strength under pure hoop loading (i.e. 830 MPa hoop stress at failure). Under axial-dominated loading, however, strength was significantly reduced (i.e. 71 MPa axial stress at failure). Hence, this structure is preferably to be used under purely hoop-dominated loading conditions. The question whether there is a more versatile lay-up configuration that provides higher axial load capacity while still maintaining a high degree of hoop strength is addressed in Figs.4.3.7 and 4.3.8. These graphs present the (average) relative functional and structural strengths in comparison to the baseline lay-up of $[\pm 60_3]_T$ respectively. Regarding functional failure (see Fig.4.3.7) the $[\pm 45, \pm 60_2]_T$ lay-up only provided significantly improved strength under $[2H:1A]$ and $[3H:1A]$ loading (i.e. strength increased by 45% and 67%, respectively). The $[\pm 30, \pm 60_2]_T$ lay-up, however, also led to a substantial increase in axial strength (i.e. 345%) while maintaining a superior performance under the two

aforementioned stress ratios (i.e. strength increased by 64% and 56%, respectively). Only in the case of pure hoop loading was there a reduction in strength to 61% of that of the baseline lay-up. But, considering the overall gain in strength, this is only a minor penalty, which, if necessary, can be compensated for (e.g. by moderately applying more fibre material to the $\pm 60^\circ$ covers).

Observations are similar regarding structural failure (see Fig.4.3.8). Notable is the slightly reduced relative strength of the $[\pm 30, \pm 60_2]_T$ lay-up under $[3H:1A]$ loading. In this case and under pure hoop loading strength was only 96% and 66% of that of the baseline lay-up, respectively. Nonetheless, data confirm a superior overall performance of the $[\pm 30, \pm 60_2]_T$ lay-up under variable loading conditions (i.e. a significantly increased axial load capacity).

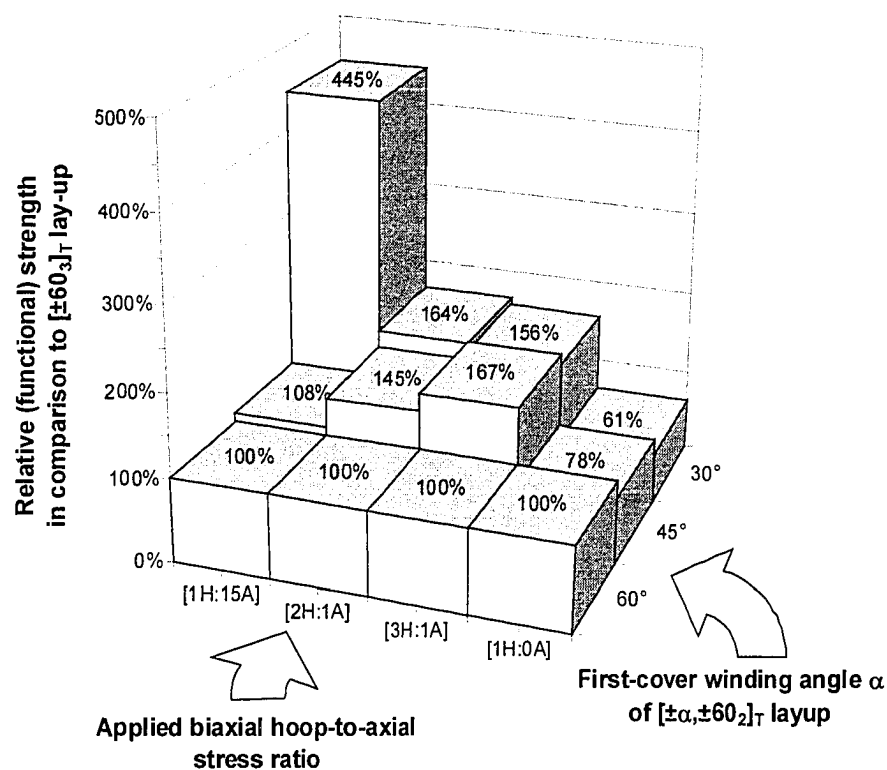


Figure 4.3.7: Functional strength of each lay-up/loading combination relative to functional strength of baseline lay-up (Mertiny et al., 2004a).

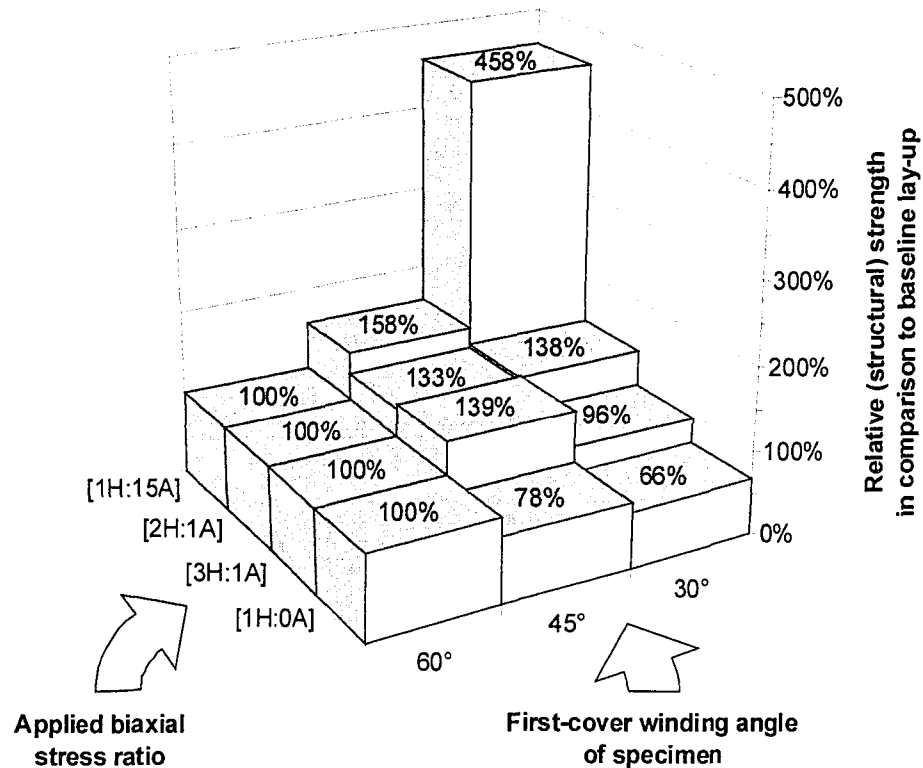


Figure 4.3.8: Structural strength of each lay-up/loading combination relative to structural strength of baseline lay-up (Mertiny et al., 2004a).

Improved functional strength by axial strain reduction:

Strains up to functional failure from tests under closed-end conditions are shown in Fig.4.3.9 for three specimens with different lay-up configurations: (a) $[\pm 60_3]_T$, (b) $[\pm 45, \pm 60_2]_T$ and (c) $[\pm 30, \pm 60_2]_T$. Functional failure occurred for all three specimens at axial strains in between 0.3% and 0.5%. This corresponds well to findings described by other researchers. Asp et al. (1996a) observed transverse strains (to fibres) at failure of as low as 0.3% for glass-fibre/epoxy composites with a fibre volume fraction of 70% was reported. For coupon specimens made from glass-fibre prepreg material, Hoover et al. (1997) reported strains at the occurrence of transverse cracking of 0.3% to 0.5% depending on the orientation of constraining plies.

The reinforcements of the first cover were increasingly oriented in an axial direction from specimen (a) to (c). This is accompanied by a reduction in axial strain and an

increase in hoop strain at comparable load levels. Note that this corresponds qualitatively to the Young's moduli presented in Table 4.1.1: E_{XX} increased and E_{YY} decreased with diminishing fibre angle of the first cover. Remarkably, the hoop strain at failure of the specimen with the $\pm 30^\circ$ cover was more than three times greater than that of the pure $\pm 60^\circ$ specimen (1.63% versus 0.48% strain). For the specimen with the $\pm 45^\circ$ cover the hoop failure strain (0.97% strain) was approximately twice that of the $[\pm 60_3]_T$ specimen. Regarding the axial orientation, differences between specimens (a), (b) and (c) were less pronounced with 0.45%, 0.39% and 0.32% axial strain at failure respectively. This particular case (i.e. a closed-end condition) clearly exemplifies the effect of introducing axially oriented reinforcement. By providing greater axial stiffness such reinforcement causes a significant strain reduction in the axial direction. In the $\pm 60^\circ$ covers transverse strains are reduced correspondingly. This delays the development of widespread matrix cracking. The $\pm 60^\circ$ covers therefore do not provide sufficient pathways for the leakage of fluid, and functional failure of the entire structure is shifted to higher load levels.

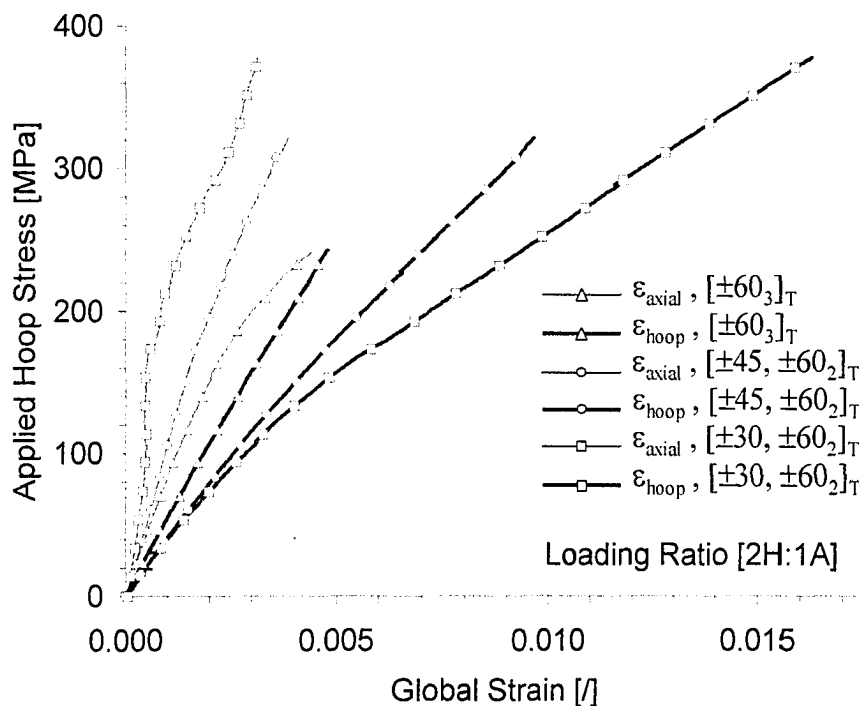


Figure 4.3.9: Stress/strain diagram for closed-end loading of $[\pm 60_3]_T$, $[\pm 45, \pm 60_2]_T$ and $[\pm 30, \pm 60_2]_T$ specimens (Mertiny et al., 2004a).

Effect of end connections:

After the occurrence of functional failure, matrix cracking increasingly weakened the composite structure. This facilitated fibre strands to commence to align into the direction of maximum principal stress. The end tabs, however, imposed a constraint, hence causing additional loads as fibres were subjected to bending. Note that it was possible to observe resulting dimensional changes visibly (i.e. fibre realignment caused an elongation of the specimens). However, strain gauges could not be used to detect these changes, as gauges malfunctioned at high strains, or a combination of cracking and leakage of fluid caused gauges to detach from the specimen surface. The additional bending loads are seen to be the cause for the proximity of burst failures to the end connections under [1H:1A] and [2H:1A] loading. Hence, it can be concluded that a particular structural feature rather than a uniform loading condition within the gage section caused structural failure. However, this failure mode was included in this study, as in most practical applications tubular structures would be equipped with constraining features such as frames, joints and pressure ports.

Influence of matrix damage on structural failures:

As described in Section 3.2 failure modes for the $[\pm 45, \pm 60_2]_T$ and $[\pm 30, \pm 60_2]_T$ lay-up under [1H:1A] loading did not bear resemblance to each other. The reason for this and also the increased structural strength of the $[\pm 30, \pm 60_2]_T$ lay-up under this loading is attributed to the reinforcing influence of the first cover. In the presence of the $\pm 30^\circ$ cover substantial axial reinforcement was provided, and specimens failed predominately due to fibre damage. (It is interesting to note that the fibres of this cover are aligned perpendicular to the ones in the $\pm 60^\circ$ covers.) If substantial axial reinforcement was absent, as in case of the $[\pm 45, \pm 60_2]_T$ lay-up, an extensive amount of matrix damage preceded final fracture, i.e. the composite structure was reduced into a network of fibre strands. The fibres of the $\pm 30^\circ$ cover suppressed matrix breakdown for a wide range of axial-dominated loadings. As a result structural failure was governed by fibre damage for a larger part of the load spectrum. An overall improved performance and usability of the structure under a variety of loading conditions was the outcome.

4.3.3 Implications for the Design of Tubular Components

Although the $[\pm 60_3]_T$ baseline lay-up performed best under pure hoop loading, low axial strength limits the usability of this structure under variable loading conditions. Under such conditions the $[\pm 30, \pm 60_2]_T$ lay-up performed particularly well. Compared to the baseline lay-up strength increased significantly under axial-dominated loading, and performance reductions under hoop loading may be acceptable. Moreover, the multi-angle configurations showed significantly improved strength over the baseline lay-up under closed-end and fixed-end loading conditions, which are the most common loading scenario in pressurised tubular structures. These findings lead to the conclusion that multi-angle filament winding is a superior method for producing tubular structures, particular if variable loading conditions need to be considered. In contrast to more extreme fibre alignments such as pure axial and circumferential orientations, the employed $\pm 30^\circ$ and $\pm 60^\circ$ covers are still of moderate inclination; thus, they do not considerably slow down manufacturing and add complexity to the winding process. In the present study prototype pipe and joint components were therefore produced featuring $\pm 30^\circ$ and $\pm 60^\circ$ fibre architectures.

4.4 Lay-up Stacking Sequence Effects¹

The design of multi-angle fibre architectures entails the selection of proper winding angles and stacking sequence. As shown in the preceding section, the former are usually chosen as to provide adequate axial and hoop stiffness and strength. Determination of the proper stacking sequence, however, requires further analysis, since the application of the component and imposed loadings need to be considered.

There are certain requirements towards a suitable stacking sequence when components are to be joined by adhesive bonding. Increased damage susceptibility was reported when placing hoop reinforcement adjacent to the joining surfaces, particularly under fatigue loading conditions (Johnson and Mall, 1986; Goeij et al., 1999). As the transfer of axial

¹ A version of this section appeared as: Mertiny, P., Ellyin, F. and Hothan, A. (2004b). Stacking sequence effect of multi-angle filament wound tubular composite structures. *Journal of Composite Materials*, Vol. 38, 1095-1113.

loads between bonded tubular sections occurs by shear, joining of hoop-dominated interface plies may result in transverse tensile failure within these layers. Polymeric matrices generally sustain only low transverse to the fibres strain (due to the low ductility of the matrix material and stress concentration effects caused by the presence of fibres, see e.g. Asp et al., 1995, 1996a-b; and Hoover et al., 1997). It has been shown that resulting localised matrix damage eventually propagates to more severe damage modes such as delaminations, see e.g. Hoover et al. (1997). Subsequent component failure by adherend delamination is the probable outcome, see e.g. MIL-HDBK 17, (1999). An increased strength of a bonded assembly featuring multi-angle filament wound components may thus be achieved by choosing stacking sequences that avoid hoop-dominated plies adjacent to joining surfaces.

But, a designer also has to consider that the stacking sequence may influence subcomponent strength. Unfortunately, only limited information on stacking sequence effects in multi-angle tubular composite structures is available in literature. Foral (1988) investigated tubes with 90° and $\pm 20^\circ$ layers under biaxial loading conditions. It was found that in the absence of inside hoop reinforcement, the so-called transverse fibre pullout occurred, i.e. inside helical layers were pulled away from the laminate. Respective structures failed at substantially lower loads than tubes with inside hoop layers. Foral concluded that any curved structure would be prone to this localised damage mode provided that inner fibre layers carry tension.

Carroll et al. (1995b) investigated stacking sequence effects in laminated structures. The stacking sequence was found to influence inter-laminar normal and shear stresses under monotonic and fatigue loading. This affected delamination growth and the ultimate strength of coupon specimens. Carroll et al. attributed this to free-edge and constraint effects. The former are necessarily absent in tubular structures. Here, free edges are only present at the tube ends, which are generally constrained by end connections. Nevertheless, Martens and Ellyin (2000) observed delamination damage in multidirectional glass fibre epoxy pipe, which occurred under biaxial loading conditions. Damage was located between layers of different fibre angles (i.e. between 0° and $\pm 66^\circ$ layers). However, the authors did not address the mechanisms responsible for the observed damage mode. Xia

et al. (2001) analytically investigated stacking sequence effects in tubular structures with 30° and 55° winding angles. It was shown that depending on the stacking sequence shear stresses of significant magnitude exist in between laminae. Furthermore, stress ratios of the individual laminae deviate from the overall applied stress ratio, and strains were found to be discontinuous in the through-thickness direction. Thus, a potential for the development of inter-laminar damage in multi-angle fibre architectures exists depending on the employed stacking sequence.

The location of axial reinforcement is also expected to influence the bending properties of a tubular structure. A location of axial reinforcement on the outside of the structure will cause an increase in bending stiffness, and may also, to some degree, suppress transverse cracking in hoop-dominated layers.

Lastly, stacking sequence effects may also influence fibre compaction. Winding of highly axial-dominated fibre reinforcement with high tow tensions is generally not feasible, since pin-rings for the prevention of fibre slippage can only sustain a limited degree of axial force. This in combination with the low wrap angle result in appreciably reduced fibre volume fractions. (Hoop-dominated windings are often placed on top of axially reinforced covers to eliminate this problem.). Note that in this investigation a $45^\circ/60^\circ$ angle combination was chosen, since in this case influences on the fibre volume fraction were found to be negligible (in contrast to e.g. a $30^\circ/60^\circ$ combination).

In the subsequent investigation two types of specimens, a $[\pm 45, \pm 60_2]_T$ lay-up and an inverted $[\pm 60_2, \pm 45]_T$ lay-up were tested under [1H:0A], [3H:1A], [2H:1A], [1H:1A] and [1H:15A] loadings. An analytical investigation of the two limiting stress states of pure axial and pure hoop stress accompanied the experimental study in order to provide further insight into the relationship between component strength and stacking sequence.

4.4.1 Experimental Results

For both lay-up configurations fluid weeping through the specimen wall was observed at functional failure. No damage to the fibre architecture was discernable. In fact, functional failure did not noticeably change colour or appearance of the specimens. In the case of structural failure, every specimen failed in a unique fashion. Nevertheless, certain

characteristic features were distinguishable, which in the following are related to the specific loading and lay-up configurations.

Modes of failure:

[1H:0A]: Under “open end” loading conditions, specimens were completely destroyed and fragmented by a “burst” type of failure for both lay-up configurations.

[3H:1A]: Specimens of both lay-up types were split in two halves within the gauge section. As shown in Fig.4.4.1, jagged fracture surfaces along the fibre directions as well as frayed fibre strands characterise this failure mode.

[2H:1A]: Under “closed end” loading, burst failure occurred in close proximity to one of the metallic end connections (see Fig.4.4.2). Damage to the fibre structure was limited to a small area. Only in case of a single $[\pm 45, \pm 60_2]_T$ specimen, damage extended around the circumference of the tube, separating the end connection from rest of the specimen.

[1H:1A]: Failure under this equi-biaxial loading ratio was caused by a single perforation of the specimen wall well within the specimen gauge section. In case of the $[\pm 60_2, \pm 45]_T$ lay-up, damage is extensive, as a substantial part of the outside $\pm 45^\circ$ cover was disrupted and loose fibre strands protrude from the specimen (see right hand side of Fig.4.4.3). Close examination also revealed a large delamination underneath the outside cover, which had been filled with hydraulic fluid. The $[\pm 45, \pm 60_2]_T$ layup, on the other hand, exhibited a much smaller area with disrupted fibres (shown on the left hand side of Fig.4.4.3). Instead of delamination extensive matrix damage to about half of the specimen could be observed. Hydraulic fluid penetrating this extensive network of cracks caused a noticeable discolouration of the specimen.

[1H:15A]: Under (approximate) pure axial loading, a collapse of the composite structure could be observed for both specimen types (see Fig.4.4.4). Fibre breakage is rare, and mainly damage to the matrix material was noticed including discolouration similar to the one mentioned above. Notably, the extent of matrix damage appeared to be greater in $\pm 45^\circ$ covers.

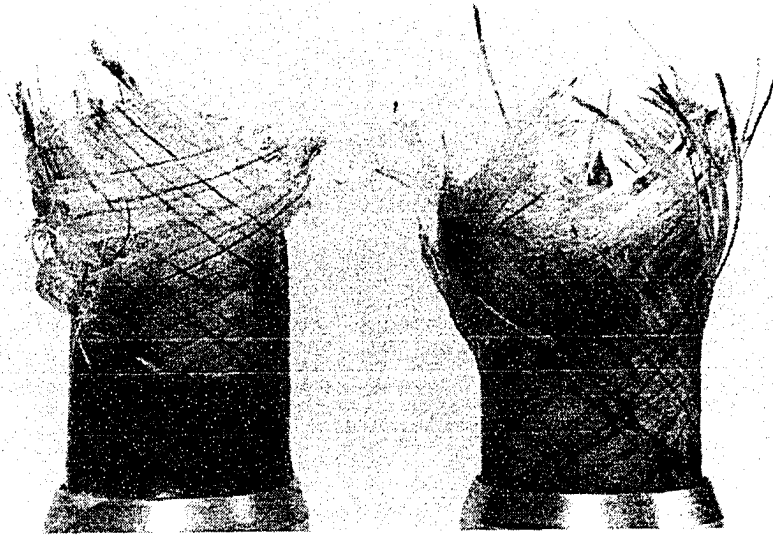


Figure 4.4.1: Burst failure with jagged fracture surfaces as observed under $[3H:1A]$ loading (left: $[\pm 45, \pm 60_2]_T$; right: $[\pm 60_2, \pm 45]_T$) (Mertiny et al., 2004b).

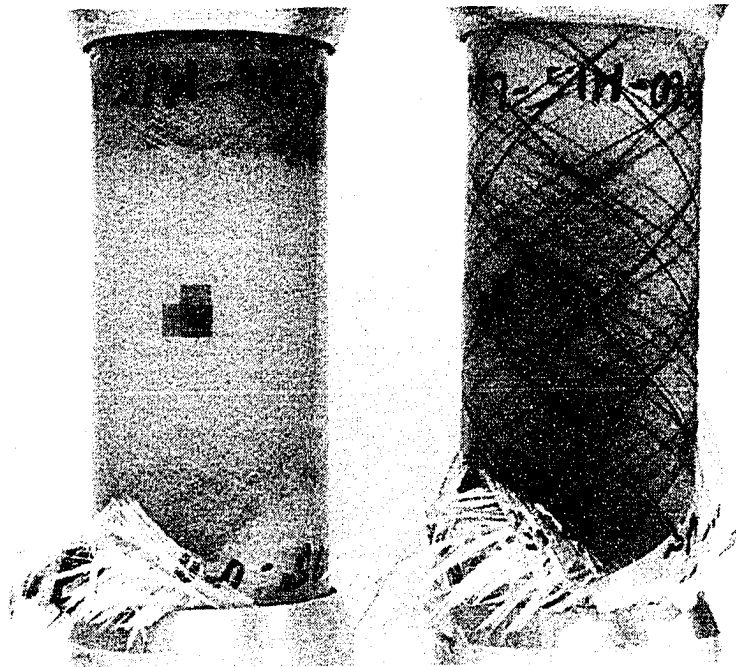


Figure 4.4.2: Localised burst failure close to end connection of tubular structure as observed under $[2H:1A]$ loading (left: $[\pm 45, \pm 60_2]_T$; right: $[\pm 60_2, \pm 45]_T$) (Mertiny et al., 2004b).

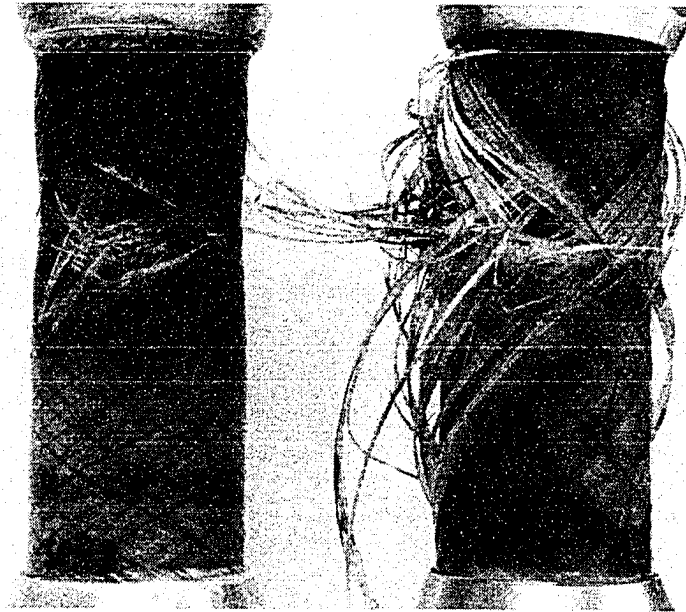


Figure 4.4.3: Failure in form of a wall perforation within the specimen gauge section as observed under equi-biaxial loading (left: $[\pm 45, \pm 60_2]_7$; right: $[\pm 60_2, \pm 45]_7$) (Mertiny et al., 2004b).

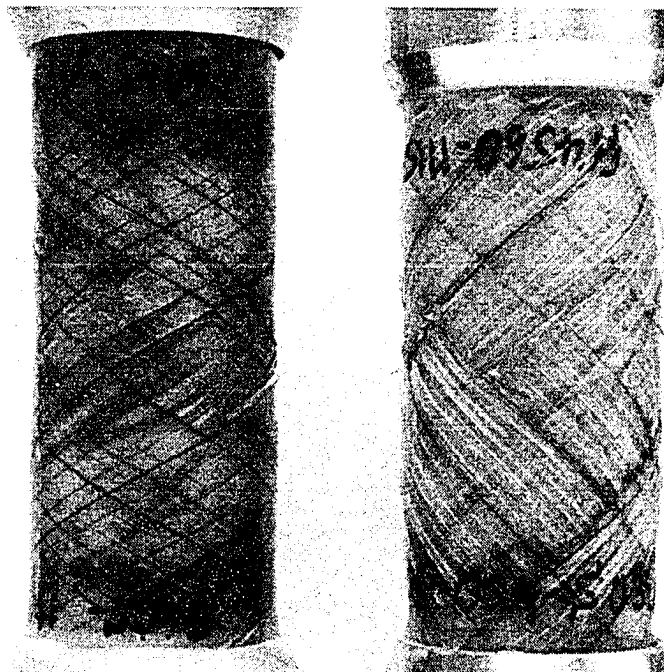


Figure 4.4.4: Collapse of the composite structure as observed under (approximate) pure axial loading (left: $[\pm 45, \pm 60_2]_7$; right: $[\pm 60_2, \pm 45]_7$) (Mertiny et al., 2004b).

4.4.2 Analysis of the Experimental Observations

Figures 4.4.5 and 4.4.6 show biaxial stress envelopes of similar shape for functional and structural failure respectively. In comparison to the $[\pm 60_2, \pm 45]_T$ lay-up an increased strength of the $[\pm 45, \pm 60_2]_T$ lay-up was observed at functional as well as structural failure under pure hoop loading. In the case of pure axial loading, equi-biaxial loading and pressure vessel loading the opposite trend is noted, i.e. the $[\pm 60_2, \pm 45]_T$ lay-up exhibited higher strength. (Under pure axial loading no difference in functional strength could be ascertained.) Under $[3H:1A]$ loading the $[\pm 60_2, \pm 45]_T$ lay-up showed an increased strength against functional failure; however, for the structural failure case a higher strength of the $[\pm 45, \pm 60_2]_T$ lay-up was recorded.

As shown in Fig.4.4.7, an examination of strains at functional failure did not reveal a distinct difference between the two lay-ups. Hence, strain is deemed a suitable failure indicator which is independent from the lay-up sequence. This led to the conclusion that changes of component stiffness occurred, which did not only depend on the biaxial stress ratios but also on the lay-up sequence. Besides non-linear matrix properties, changes

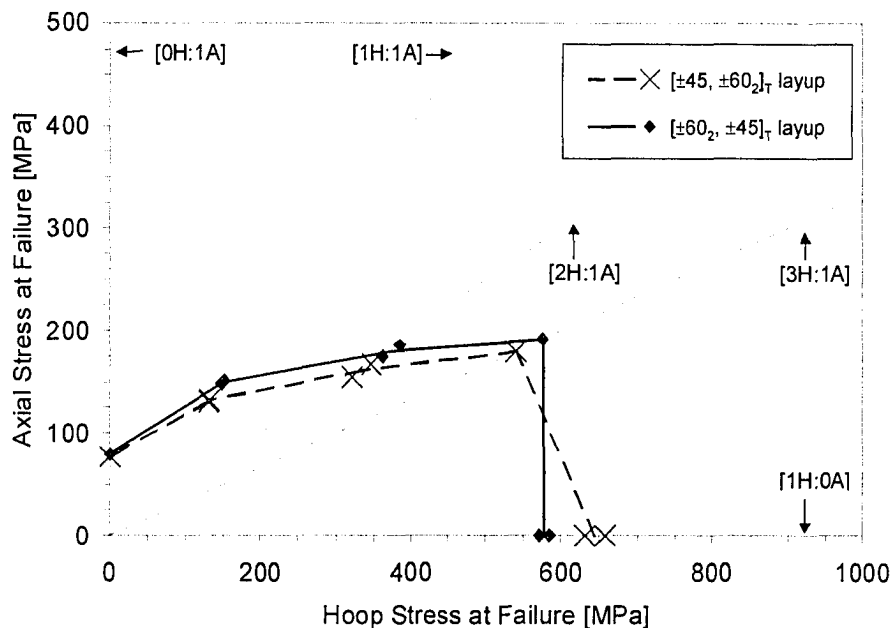


Figure 4.4.5: Experimental functional failure stress envelopes of $[\pm 45, \pm 60_2]_T$ and $[\pm 60_2, \pm 45]_T$ tube specimens (Mertiny et al., 2004b).

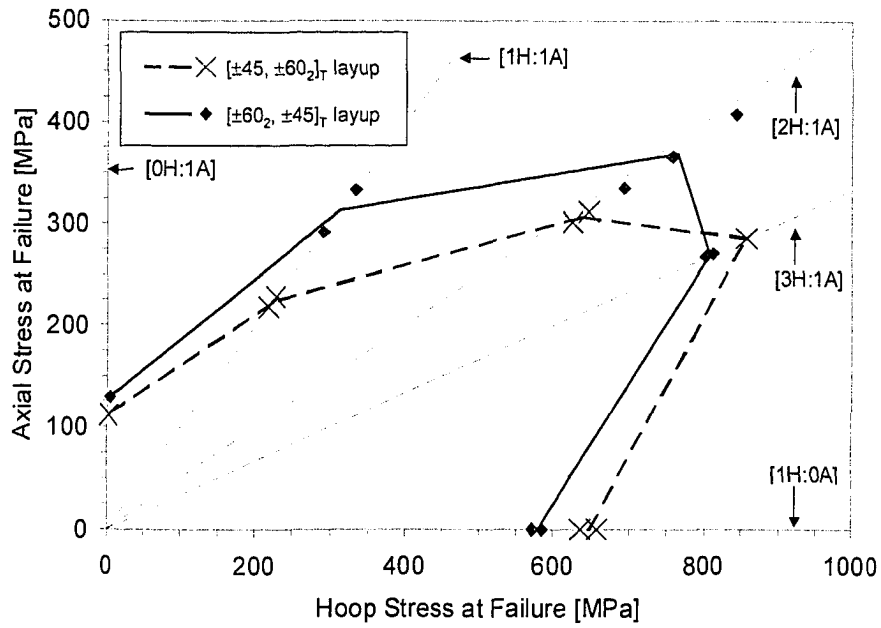


Figure 4.4.6: Experimental structural failure stress envelopes of $[\pm 45, \pm 60_2]_T$ and $[\pm 60_2, \pm 45]_T$ tube specimens (Mertiny et al., 2004b).

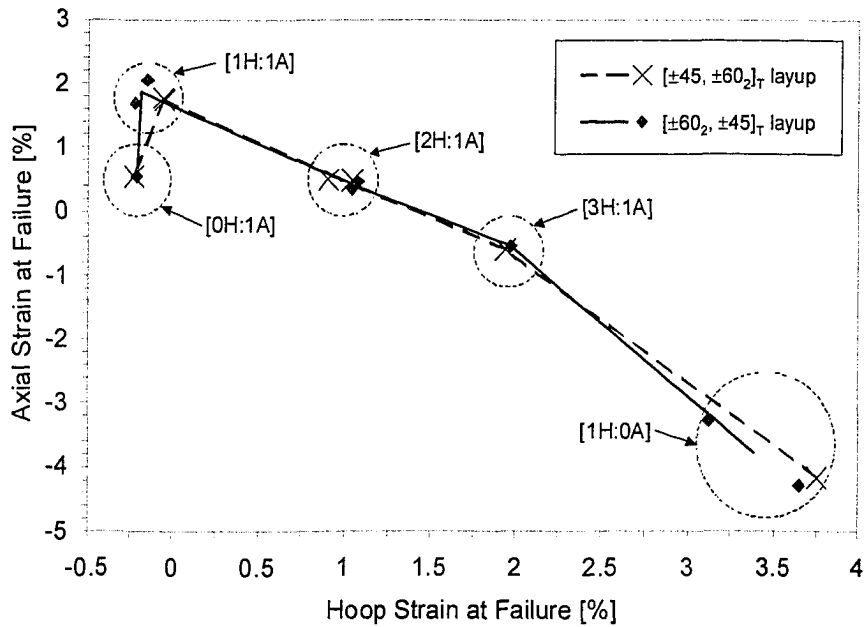


Figure 4.4.7: Experimental functional failure strain envelopes of $[\pm 45, \pm 60_2]_T$ and $[\pm 60_2, \pm 45]_T$ tube specimens (Mertiny et al., 2004b).

in stiffness are caused by damage events within the structure. Therefore, an influence of the layup sequence on the development of structural damage is discernable.

As already pointed out in Section 4.3, it is evident that the metallic end-connections influence the specimen failure behaviour under [2H:1A] loading, as damage always occurred close to the end-connections for both specimen types. This indicates that the composite structure experienced constrained deformation, and thus, elevated stresses in these areas. Failure was therefore premature compared to failures that might have occurred in a uniformly loaded specimen gauge section.

4.4.3 Analytical Damage Progression Analysis

The $[\pm 45, \pm 60_2]_T$ and $[\pm 60_2, \pm 45]_T$ lay-ups exhibited a different failure behaviour and different functional and structural failure strengths under the same loading conditions. In the following these effects are further investigated analytically for the pure hoop and pure axial loading case. In each case, covers are treated as fully decoupled entities, i.e. a damage state of complete delamination between covers is assumed, and therefore individual covers feature a maximum degree of freedom of deformation within the given structural constraints (e.g. end connections). Note that the development of extensive delaminations was not observed during experiments for the pure hoop and pure axial loading case, and hence, this assumption represents an (theoretical) extreme case. However, it is reasonable to assume that inter-laminar cracking and coalescence of such cracks occurs that facilitates the penetration of fluid through the tube wall.

Basic stress-strains relations of an orthotropic material were given by Eqs.(4.1.1). Assuming a state of plane-stress, i.e. $\sigma_{ZZ} \approx 0$, Eqs.(4.1.1) yield:

$$\text{axial strain:} \quad \varepsilon_{XX} = \frac{\sigma_{XX}}{E_{XX}} - \nu_{YX} \frac{\sigma_{YY}}{E_{YY}} \quad (4.4.1)$$

$$\text{hoop strain:} \quad \varepsilon_{YY} = \frac{\sigma_{YY}}{E_{YY}} - \nu_{XY} \frac{\sigma_{XX}}{E_{XX}} \quad (4.4.2)$$

$$\text{radial strain:} \quad \varepsilon_{ZZ} = -\nu_{XZ} \frac{\sigma_{XX}}{E_{XX}} - \nu_{YZ} \frac{\sigma_{YY}}{E_{YY}} \quad (4.4.3)$$

Pure hoop loading case:

For [1H:0A] loading, $\sigma_{XX} = 0$. Hence, Eqs.(4.4.1) to (4.4.3) can be rewritten as:

$$\text{hoop strain:} \quad \varepsilon_{YY} = \frac{\sigma_{YY}}{E_{YY}} \quad (4.4.4)$$

$$\text{axial strain:} \quad \varepsilon_{XX} = -\nu_{YX} \frac{\sigma_{YY}}{E_{YY}} = -\nu_{YX} \varepsilon_{YY} \quad (4.4.5)$$

$$\text{radial strain:} \quad \varepsilon_{ZZ} = -\nu_{YZ} \frac{\sigma_{YY}}{E_{YY}} = -\nu_{YZ} \varepsilon_{YY} \quad (4.4.6)$$

Elastic material properties were calculated based on the constituent properties given in Table 4.1.2. Elastic moduli of the $\pm 45^\circ$ and $\pm 60^\circ$ covers of the $[\pm 45, \pm 60_2]_T$ and $[\pm 60_2, \pm 45]_T$ lay-ups are given in Tables 4.4.1 and 4.4.2 respectively. Data were computed according to the method outlined in Chapter 2: Subsection 2.2.4.

For the $[\pm 45, \pm 60_2]_T$ layup, (according to Table 4.4.1),

$$\nu_{YX}^{(60^\circ)} = 0.55 \text{ and } \nu_{YZ}^{(60^\circ)} = 0.16 \text{ in the } \pm 60^\circ \text{ cover,}$$

$$\nu_{YX}^{(45^\circ)} = 0.50 \text{ and } \nu_{YZ}^{(45^\circ)} = 0.14 \text{ in the } \pm 45^\circ \text{ cover;}$$

and, for the $[\pm 60_2, \pm 45]_T$ layup (according to Table 4.4.2),

$$\nu_{YX}^{(60^\circ)} = 0.54 \text{ and } \nu_{YZ}^{(60^\circ)} = 0.16 \text{ in the } \pm 60^\circ \text{ cover,}$$

$$\nu_{YX}^{(45^\circ)} = 0.49 \text{ and } \nu_{YZ}^{(45^\circ)} = 0.15 \text{ in the } \pm 45^\circ \text{ cover.}$$

As the ends of a tubular section are constrained by bonded end connections, strains in axial direction, ε_{XX} , are assumed to be constant throughout the structure. As described above, it is assumed that the $\pm 60^\circ$ covers and the $\pm 45^\circ$ cover are fully decoupled. Then, from Eq.(4.4.5), for the $[\pm 45, \pm 60_2]_T$ lay-up,

$$\varepsilon_{YY} = -\frac{1}{\nu_{YX}} \varepsilon_{XX} = -\frac{1}{0.55} \varepsilon_{XX} = -1.82 \varepsilon_{XX} \text{ for the } \pm 60^\circ \text{ cover} \quad (4.4.7)$$

$$\varepsilon_{YY} = -\frac{1}{\nu_{YX}} \varepsilon_{XX} = -\frac{1}{0.50} \varepsilon_{XX} = -2.00 \varepsilon_{XX} \text{ for the } \pm 45^\circ \text{ cover} \quad (4.4.8)$$

Through testing (see Fig.4.4.7) it was shown that under [1H:0A] loading $\varepsilon_{XX} < 0$. Therefore, for the $[\pm 45, \pm 60_2]_T$ lay-up,

$$\varepsilon_{YY} = -1.82 \varepsilon_{XX} > 0 \text{ for the } \pm 60^\circ \text{ cover,} \quad (4.4.9)$$

$$\varepsilon_{YY} = -2.00 \varepsilon_{XX} > 0 \text{ for the } \pm 45^\circ \text{ cover;} \quad (4.4.10)$$

and, for the $[\pm 60_2, \pm 45]_T$ lay-up,

$$\varepsilon_{YY} = -1.85 \varepsilon_{XX} > 0 \text{ for the } \pm 60^\circ \text{ cover,} \quad (4.4.11)$$

$$\varepsilon_{YY} = -2.04 \varepsilon_{XX} > 0 \text{ for the } \pm 45^\circ \text{ cover.} \quad (4.4.12)$$

This shows that for either lay-up the hoop extension of the $\pm 45^\circ$ cover under pure hoop loading is greater than the hoop extension of the $\pm 60^\circ$ covers. In the case of the

Table 4.4.1: Elastic properties from constituents of $[\pm 45, \pm 60_2]_T$ lay-up (Mertiny et al., 2004b).

	$\pm 45^\circ$ cover	$\pm 60^\circ$ cover
V_f Fibre volume fraction	0.700	0.700
E_{XX} Young's modulus in axial direction	22.8 GPa	19.3 GPa
E_{YY} Young's modulus in hoop direction	22.8 GPa	35.5 GPa
E_{ZZ} Young's modulus in radial direction	20.4 GPa	20.3 GPa
G_{XY} Shear modulus	17.3 GPa	14.9 GPa
G_{XZ} Shear modulus	7.9 GPa	8.1 GPa
G_{YZ} Shear modulus	7.9 GPa	7.8 GPa
ν_{XY} Poisson's ratio	0.50	0.30
ν_{YX} Poisson's ratio	0.50	0.55
ν_{XZ} Poisson's ratio	0.14	0.17
ν_{ZX} Poisson's ratio	0.13	0.18
ν_{YZ} Poisson's ratio	0.14	0.16
ν_{ZY} Poisson's ratio	0.13	0.09

$[\pm 45, \pm 60_2]_T$ lay-up the $\pm 60^\circ$ covers act as a constraint for the $\pm 45^\circ$ cover. In contrast for the $[\pm 60_2, \pm 45]_T$ lay-up such a constraining action is not possible, as the outside cover expands more than the inside covers. This action would not occur if the $\pm 45^\circ$ cover and the $\pm 60^\circ$ covers were perfectly bonded. However, with the initiation and progression of matrix damage during loading, small localised delaminations are likely to occur. Therefore it is a reasonable assumption that the progression of damage within the structure, i.e. delaminations and penetration of pressurised fluid along the delamination zones, is more likely for the $[\pm 60_2, \pm 45]_T$ lay-up. This behaviour is considered to be the reason for the observation of reduced functional and structural strength of this lay-up in comparison to the $[\pm 45, \pm 60_2]_T$ lay-up under pure hoop and hoop dominated loading ratios.

Table 4.4.2: Elastic properties from constituents of $[\pm 60_2, \pm 45]_T$ lay-up (Mertiny et al., 2004b).

	$\pm 45^\circ$ cover	$\pm 60^\circ$ cover
V_f Fibre volume fraction	0.706	0.706
E_{XX} Young's modulus in axial direction	23.5 GPa	19.8 GPa
E_{YY} Young's modulus in hoop direction	23.5 GPa	36.2 GPa
E_{ZZ} Young's modulus in radial direction	20.7 GPa	20.7 GPa
G_{XY} Shear modulus	17.5 GPa	15.1 GPa
G_{XZ} Shear modulus	8.2 GPa	8.3 GPa
G_{YZ} Shear modulus	8.2 GPa	8.0 GPa
ν_{XY} Poisson's ratio	0.49	0.30
ν_{YX} Poisson's ratio	0.49	0.54
ν_{XZ} Poisson's ratio	0.15	0.18
ν_{ZX} Poisson's ratio	0.13	0.18
ν_{YZ} Poisson's ratio	0.15	0.16
ν_{ZY} Poisson's ratio	0.13	0.09

Pure axial loading case:

Under [0H:1A] loading, $\sigma_{YY} = 0$. Hence, Eqs.(4.4.1) to (4.4.3) can be written as:

$$\text{axial strain:} \quad \varepsilon_{XX} = \sigma_{XX} E_{XX}^{-1} \quad (4.4.13)$$

$$\text{hoop strain:} \quad \varepsilon_{YY} = -\nu_{XY} \sigma_{XX} E_{XX}^{-1} = -\nu_{XY} \varepsilon_{XX} \quad (4.4.14)$$

$$\text{radial strain:} \quad \varepsilon_{ZZ} = -\nu_{XZ} \sigma_{XX} E_{XX}^{-1} = -\nu_{XZ} \varepsilon_{XX} \quad (4.4.15)$$

where, for the $[\pm 45, \pm 60_2]_T$ lay-up (according to Table 4.4.2),

$$\nu_{XY}^{(60^\circ)} = 0.30 \text{ and } \nu_{XZ}^{(60^\circ)} = 0.17 \text{ in the } \pm 60^\circ \text{ cover,}$$

$$\nu_{XY}^{(45^\circ)} = 0.50 \text{ and } \nu_{XZ}^{(45^\circ)} = 0.14 \text{ in the } \pm 45^\circ \text{ cover;}$$

and, for the $[\pm 60_2, \pm 45]_T$ lay-up (according to Table 4.4.2),

$$\nu_{XY}^{(60^\circ)} = 0.30 \text{ and } \nu_{XZ}^{(60^\circ)} = 0.18 \text{ in the } \pm 60^\circ \text{ cover,}$$

$$\nu_{XY}^{(45^\circ)} = 0.49 \text{ and } \nu_{XZ}^{(45^\circ)} = 0.15 \text{ in the } \pm 45^\circ \text{ cover.}$$

It is again assumed that the displacement in axial direction is constant throughout the structure, i.e. $\varepsilon_{XX} = \text{const}$, and that the $\pm 60^\circ$ covers and $\pm 45^\circ$ cover are delaminated.

From Equation (4.4.14), for the $[\pm 45, \pm 60_2]_T$ lay-up,

$$\varepsilon_{YY} = -\nu_{XY} \varepsilon_{XX} = -0.30 \varepsilon_{XX} \text{ for the } \pm 60^\circ \text{ cover} \quad (4.4.16)$$

$$\varepsilon_{YY} = -\nu_{XY} \varepsilon_{XX} = -0.50 \varepsilon_{XX} \text{ for the } \pm 45^\circ \text{ cover} \quad (4.4.17)$$

From test results it is known that under [0H:1A] loading $\varepsilon_{XX} > 0$. Therefore, for the $[\pm 45, \pm 60_2]_T$ lay-up,

$$\varepsilon_{YY} = -0.30 \varepsilon_{XX} < 0 \text{ for the } \pm 60^\circ \text{ cover,} \quad (4.4.18)$$

$$\varepsilon_{YY} = -0.50 \varepsilon_{XX} < 0 \text{ for the } \pm 45^\circ \text{ cover;} \quad (4.4.19)$$

and, for the $[\pm 60_2, \pm 45]_T$ lay-up,

$$\varepsilon_{YY} = -0.30 \varepsilon_{XX} < 0 \text{ for the } \pm 60^\circ \text{ cover,} \quad (4.4.20)$$

$$\varepsilon_{YY} = -0.49 \varepsilon_{XX} < 0 \text{ for the } \pm 45^\circ \text{ cover.} \quad (4.4.21)$$

For either lay-up, the contraction in hoop direction under pure axial loading is greater for the $\pm 45^\circ$ cover than for the $\pm 60^\circ$ covers. This leads to the conclusion that the $\pm 45^\circ$ cover constrains the $\pm 60^\circ$ covers in the case of the $[\pm 60_2, \pm 45]_T$ lay-up. The opposite is happening in the case of the $[\pm 45, \pm 60_2]_T$ lay-up. That is, the inside cover contracts more than the outside covers leading to a separation between the $\pm 45^\circ$ and $\pm 60^\circ$ covers. As already stated in the preceding section, this mechanism is only operative in the event that the $\pm 45^\circ$ cover and the $\pm 60^\circ$ covers are delaminated. This is likely to occur in a localised fashion with initiation and progression of matrix damage during loading. Hence, the conclusions are similar to the above, i.e. the lay-up without the constraining effect is more prone to delamination and the penetration of pressurised fluid along the delamination zones. Under pure axial and axial-dominated loading conditions the $[\pm 45, \pm 60_2]_T$ lay-up does not exhibit this constraining effect resulting in the reduced functional and structural strength in comparison to the $[\pm 60_2, \pm 45]_T$ lay-up.

Influence of winding angle variation:

Combinations of 60° and 45° winding angles were chosen, because resulting lay-ups were found to have similar fibre volume fractions. However, these configurations do not represent an extreme case. Differences in the deformation behaviour between $\pm 60^\circ$ and $\pm 45^\circ$ -covers were addressed as the reason for the variation of strength between the two investigated lay-ups. These differences in deformation behaviour were associated with the Poisson's ratios ν_{XY} and ν_{YX} . In order to gain a better understanding of what a possible extreme case would be, the ν_{XY} and ν_{YX} Poisson's ratios were plotted in Fig.4.4.8 for covers with winding angles ranging between 1° and 89° . This figure shows that the biggest difference in Poisson's ratios can be found for an angle combination of approximately 34° and 89° . Note, however, that Fig.4.4.8 was produced under the assumption of a constant fibre volume fraction of 70%. Winding of tubes with a $[\pm \alpha_m, \pm \beta_n]_T$ and an inverted $[\pm \beta_n, \pm \alpha_m]_T$ lay-up with significantly different fibre angles would most likely result in a much more pronounced variation in fibre volume fraction between the two lay-ups. Therefore, the analysis of an extreme case should also consider lay-up effects on fibre volume fraction, which was not attempted in this context.

4.4.4 Implication for the Design of Tubular Components

An appreciable stacking sequence influence on functional and structural failure strengths was evident. The correlation between (functional and structural) strength and stacking sequence can be summarised as follows: Positioning of layers of axial reinforcement on the outside of the specimen provided higher strength under loadings with high axial stress components, whereas axial reinforcement on the inside of the tubes resulted in higher strength under strongly hoop-dominated loading scenarios. The analytical study gave strong indication that the individual deformation of each cover is responsible for the dependency of component strength on stacking sequence. It was shown that certain combinations of stacking sequence and stress ratio lead to a constraining effect, i.e. the outside cover acts as a constraint for subjacent covers. This effect likely causes a reduction in matrix cracking and delamination growth; hence, the strength of the structure is increased. The lack of the constraining effect only leads to an accelerated development of damage if an individual deformation of each cover is at least possible in a localised fashion. Hence, the constraining effect is only operative after the initiation of damage. This in turn suggests that stacking sequence effects on component properties under purely elastic conditions are absent (apart from bending).

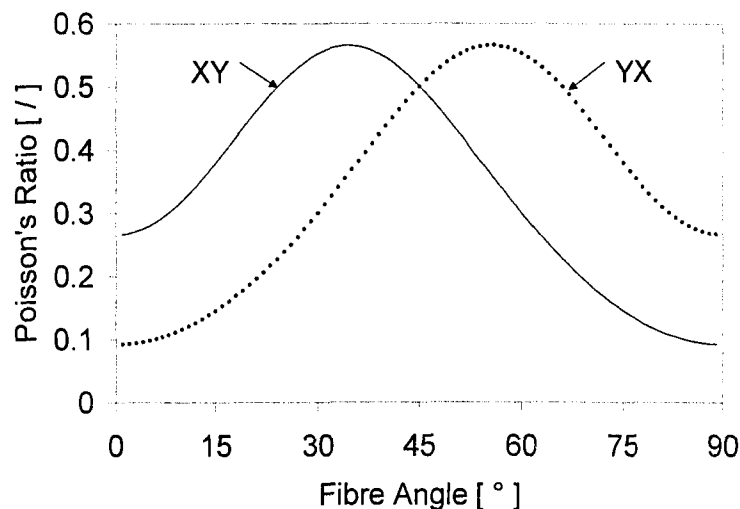


Figure 4.4.8: Poisson's ratios ν_{XY} and ν_{YX} for $\pm\alpha^\circ$ -covers with 70% fibre volume fraction (Mertiny et al., 2004b).

Based on these observations, a lay-up configuration for prototype specimens was chosen that features axial reinforcement on the specimen outside, i.e. $[\pm 60_m, \pm 30_n]_T$. An increased strength under the majority of loading conditions is anticipated due this lay-up, especially in the case of functional failure and loading scenarios with significant axial stress components. (Recall that resistance against functional failure is of particular importance, since it terminates the useful life of the structure.) Hoop loading scenarios are of lesser concern, as under these conditions tested lay-ups exhibited strengths of high magnitude. Moreover, the positioning of axial reinforcement on the outside of the tube promises better performance under bending and as a joint structure. Note that the selected stacking sequence will likely cause a reduction in fibre compaction in comparison to the inverted lay-up. However, this is seen to have negligible, possibly even beneficial effects on the overall performance of the structure, see Section 4.1.

4.5 Model-Prototype Scaling and Size-Effect¹

In the present study small-scale model specimens were extensively employed for the phenomenological analysis of material and structural behaviour. Yet, it is unclear to what extent these findings are applicable to quantitatively and qualitatively predict the behaviour of prototype-scale structures. An investigation pertaining to this subject matter is presented in the following.

Scaling laws and strength size-effects have received much attention by researchers due to the potential benefits of scaled model testing. Similitude theory is generally used to determine the necessary conditions for model-prototype scaling. Such conditions ensure that experimental findings can be extrapolated to similar structures. Chouchaoui and co-workers (1999a-b) have presented valuable results in the field of laminated tubular structures. An analytical model was developed for predicting the behaviour of tubes under a variety of loading conditions. In this analytical model, geometry, mechanical properties, lay-up configuration and number of layers were considered. Structures were

¹ A version of this section has been submitted for publication as: Mertiny, P. and Ellyin, F. (2004c). Model/prototype testing of filament wound tubular composite structures for pressurised fluid containment. *Journal of Composite Science and Technology*, (accepted with revisions, Jan.2004), 38 manuscript pages.

modelled from coaxial cylindrical tubes of orthotropic, elastic material. Good agreement between analytical and experimental results in terms of stress and deformation, as well as burst pressures was obtained for composite/metal hybrid tubes (which are not subject to leakage failure). Yet, the authors cautioned that deformation/failure mechanisms need to be identical to ensure good predictions of prototype behaviour from model testing.

On size-effects in fibre-reinforced plastics, Wisnom (1999) provided a review of current research. He concluded that size-effect is not a single phenomenon, but depends on the mechanism of failure. Yet, testing under tensile, compressive and matrix dominated loading conditions showed tendencies for the strength of structures to decrease with increasing size. A discussion of available results on size-effects was provided by Bazant (2000). This included results from (a) elasticity/plasticity theory, in which size-effects are absent, (b) statistical size-effects, e.g. Weibull theory, and (c) linear elastic fracture mechanics (LEFM), which exhibit the strongest possible size-effect. Recent literature supports the understanding that none of the available theories sufficiently captures the wide range of size-effects. Examples can be found in papers by Jackson et al. (1992), Lavoie et al. (2000), and Okabe and Takeda (2002), where traditional statistical Weibull theory was found unsuitable to accurately predict failure of scaled coupon type specimens under tensile and flexural test conditions. Extended statistical models, though, resulted in improved failure predictions, see Okabe and Takeda (2002). Good agreement between experimental and analytical results was also obtained by Bazant et al. (1996). They proposed a logarithmic size-effect law for notched tensile specimens, which bridges plasticity theory and LEFM. Large-scale damage modes such as delamination were found to follow scale models according to fracture mechanics principles, see e.g. Swanson (1994). However, a general size-effect law is presently far from reality. Since failure of composite structures usually involves various damage events on different dimensional scales, progressive damage models are required to achieve composite strength scaling (O'Brien, 1994).

The review of available literature on scaling laws and size-effects in fibre-reinforced plastics showed that research dealing with filament wound structures is limited, and work focussing on failure in structures that are intended for the containment of pressurised

fluids is particularly scarce. To investigate scaling and possible size-effects in these structures, an experimental study was conducted employing model and prototype-size tubes with $[\pm 60^{\circ}_3]_T$ (model baseline configuration) and $[\pm 60^{\circ}_5]_T$ lay-ups, respectively. Specimens were tested under [1H:0A], [3H:1A] and [2H:1A] loading ratios.

4.5.1 Experimental Results

All model and prototype-size tubes exhibited functional failure with the exception of model specimens under pure hoop loading. In this case specimens were completely destroyed by burst type failures. Apart from the leakage of fluid, a functional failure did not change the specimen's appearance, and damage to the fibre architecture was not discernable. In the case of prototype-size samples, cracking of the resin coat on the pipe surface could be observed. Failure pressures were determined based on the described permeability criterion except for the burst type failures, which are marked by asterisks in Table 4.5.1. Failure pressures and stresses as well as values of the average characteristic intrinsic permeability at leakage failure, K' , are listed in Table 4.5.1. It can be observed from this data that strength (in terms of stress) was consistently lower for prototype-size specimens. For comparison, Table 4.5.1 also shows (in parentheses) failure stresses and pressures based on the leakage fluid loss criterion used earlier.

4.5.2 Analysis of the Experimental Observations

Impediments to true model-prototype scaling arising from manufacturing processes:

Although high flexibility exists for producing specimens of different dimensions, the filament winding manufacturing process inherently constrained the capability to produce model and prototype-size specimens with identical material properties. This was caused by the circumstance that tow weights, winding bandwidths and tow tensioning were only adjustable within a limited range (rather than by the fixed dimensions of certain components, e.g. the fibre pay-out eye). Two properties are significantly affected by these constraints: (a) winding pattern and (b) fibre compaction. These are discussed below.

In the present study, model-prototype scaling was predominantly achieved by varying the applied number of tows (8 or 10) and the relative tow weight (735 g/m or 2000 g/m).

Table 4.5.1: Experimental pressures and stresses at failure.

Stress ratio	Specimen number	Spec. type	Characteristic permeability at failure, K' [10^{-13} cm^2]	Internal pressure at failure [MPa]	Experimental failure stresses [MPa]	
					Hoop stress	Axial stress
[1H:0A]	S019 *	M	N/A	55.394	833	0
	S032 *	M		54.572	820	0
	P004	P	0.71	47.656	468	1
	P008	P		49.764	489	2
[3H:1A]	S029	M	1.91	26.293 (24.239)	394 (363)	132 (121)
	S030	M		23.027 (18.887)	345 (283)	115 (94)
	P003	P		21.297	209	70
	P010	P		21.603	212	71
[2H:1A]	S017	M	2.67	16.496 (16.227)	247 (243)	119 (117)
	S026	M		15.251 (14.544)	228 (217)	110 (105)
	P005	P		16.429	161	80
	P007	P		16.461	161	81
	P009	P		14.536	142	72

* Burst type failure was observed.

M = Model, P = Prototype-size specimen

Values in parentheses are based on the leakage fluid loss criterion, see Section 3.3.2.

Consequently, winding bands for prototype-size samples were 3.4 times the relative weight of bands used for model specimens. Despite this difference, bandwidths differed significantly less (by a factor of about 1.25). As a consequence the dissimilar winding patterns shown in Fig.4.5.1 were selected to achieve full mandrel coverage. (Note that the unit-cell patterns shown in Fig.4.5.1 are not to scale.) Of concern is the amount of interweaving associated with these winding patterns, as the presence of undulation regions was found to decrease the threshold (in terms of stress) for the initiation of weepage (see e.g. Rousseau et al., 1997 and 1999).

According to Eq.(2.2.12) the degree of interweaving, D_T , was calculated as 7% and 15% for model and prototype-size specimens respectively. Rousseau et al. (1999) reported that for similar degrees of interweaving, i.e. 8% and 16%, weepage initiation thresholds were 75% and 84% of a structure without undulations respectively. But, the

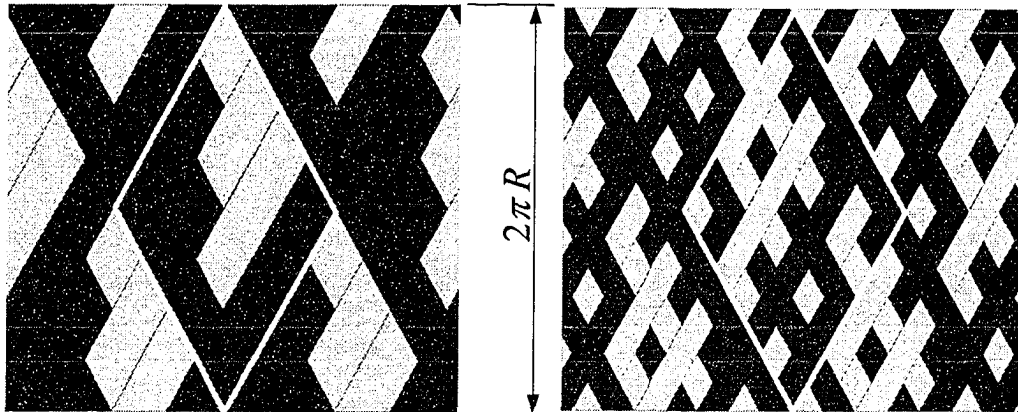


Figure 4.5.1: Winding pattern of model (left) and prototype-size specimens (right).

higher degree of interweaving (16%) produced a threshold for weepage initiation as well as final weepage failure that was by a factor of 1.12 higher than that of the lower degree of interweaving (8%). This is contrary to the trend observed in the present investigation. Thus, it is not reasonable to associate the increased degree of winding band interweaving of prototype-size samples with the observed strength disparity.

The third process parameter considered to affect model-prototype scaling is fibre tensioning. Even though the applied tow tension was controlled at 26.7 N for model and prototype-size specimens, the average fibre volume fraction of prototype-size samples was, by an absolute value, 7.4% lower than that of models. This is attributed mainly to the larger diameter of prototype-size samples, the increased wall thickness and the larger bandwidth. The former reduces radial forces that allow tows to displace resin during their settlement, and the latter two are responsible for trapping an increased amount of resin material within the structure.

Investigations by Asp et al. (1996) and de Kok and Meijer (1999) demonstrated that in glass-fibre/epoxy composites, fibre volume fraction influences the transverse strength. (The latter being the stress causing cracking of the matrix.) More specifically, transverse strength was found to increase with increasing fibre compaction. These findings correspond with the trend observed in the present experimental study. However, strength reductions of similar magnitude (more than 30%) have not been reported for a relatively

small difference in the fibre volume fraction (i.e. 7.4%). De Kok and Meijer (1999), for example, found the strength to decrease by approximately 10% between fibre volume fractions of 73% and 60%. Present results also agree qualitatively with observations made in Section 4.2. There, under [3H:1A] loading, an increase in functional strength by the factor of 1.26 was ascertained between model specimens with 70.7% and 74% fibre volume fraction. But, no such effect was found in the case of [2H:1A] loading.

In the studies by Asp et al. (1996) and de Kok and Meijer (1999) strength was defined in a structural sense (i.e. strength is the stress at which a structure loses its load-bearing capability). In the present investigation, however, specimens predominantly exhibited functional failure (i.e. leakage). In this case, the multiplicity of matrix damage events and their interaction determine the degree of permeability, and thus the functional strength of the structure. Since these damage events strongly depend on the degree of fibre compaction, differences in fibre volume fraction might have played an important role in the observed high strength dissimilarities.

Impediments to true model-prototype scaling arising from testing methodology:

Akin to the manufacturing processes, truly identical conditions were also not achievable for the testing of specimens. This stems from the need for different size testing apparatuses that provided sufficient load capabilities for testing specimens up to failure, and adequate levels of sensitivity and controllability. The main functional difference between the testing machines used in the experiments was the method of pressurisation. This mostly affected the applied stress rates, $\partial\sigma/\partial\hat{t}$, which were 64.2 kPa/s and 544.4 kPa/s under [3H:1A] loading, and 63.1 kPa/s and 197.8 kPa/s under [2H:1A] loading for model and prototype-size specimens respectively (see Table 3.5.3). Note that stress rates provided in this section were calculated according to Eq.(3.5.5).

In an earlier paper Carroll et al. (1995a) found that, for $\pm 55^\circ$ filament-wound specimens with 49.5 mm inside diameter, the strength depends on the applied monotonic loading rate. Two stress rates of approximately 50 kPa/s and 500 kPa/s were applied. No rate-effect was reported under [2H:1A] loading, whereas under pure hoop loading strength was reduced by 11% from the faster to the slower stress rate. This was attributed to a rate-dependency of the matrix material. Consequently, a rate-effect was absent under

[2H:1A] loading, in which case fibres in the $\pm 55^\circ$ lay-up are primarily bearing the load (fibres are aligned in the principle stress direction). Perreux and Joseph (1997) also investigated the influence of loading rate on the strength of $\pm 55^\circ$ filament-wound composite tubes (with 60 mm inside diameter). Tests under pure axial loading were performed. Stress rates were significantly higher than the aforementioned ones. They varied between 15 MPa/s and 300 MPa/s. No rate effect on strength was ascertained.

Based on results from these studies, it is reasonable to assume that no appreciable rate effect was present for $\pm 60^\circ$ lay-ups under [3H:1A] loading (alignment of fibres in the principle stress direction). For the [2H:1A] loading case, a rate-effect cannot be excluded. However, since (a) the observed strength reduction is comparable in magnitude to the [3H:1A] loading scenario, and (b) significantly greater reductions were observed than indicated by other researches, a possible rate-effect is seen to be of minor influence in comparison to the observed high strength variation.

Comparison of initial and failure stress/strain response:

The preceding discussion indicates that the damage behaviour of model and prototype-size structures is responsible for observed strength disparities. This was further investigated by examining the stress/strain responses of both specimen types. Stress/strain responses for model and prototype-size tubes tested under [2H:1A] and [3H:1A] loading are shown in Figs.4.5.2 and 4.5.3 respectively. In the latter case axial strain data was plotted in conjunction with the applied hoop stress (i.e. three times the applied axial stress). This representation was chosen to enlarge the axial stress-strain curves for clarity. Note that the [1H:0A] loading case was omitted, as completely different failure modes, i.e. burst and weepage were encountered for model and prototype-size samples.

For model and prototype-size specimens under [2H:1A] and [3H:1A] loading, stress/strain responses of the fibre-dominated (hoop) direction exhibited approximately linear behaviour. Pronounced non-linear behaviour was observed for the matrix-dominated (axial) direction. Here, stress/strain curves of model specimens showed a progressively increasing curvature. The linear response in the fibre-dominated hoop

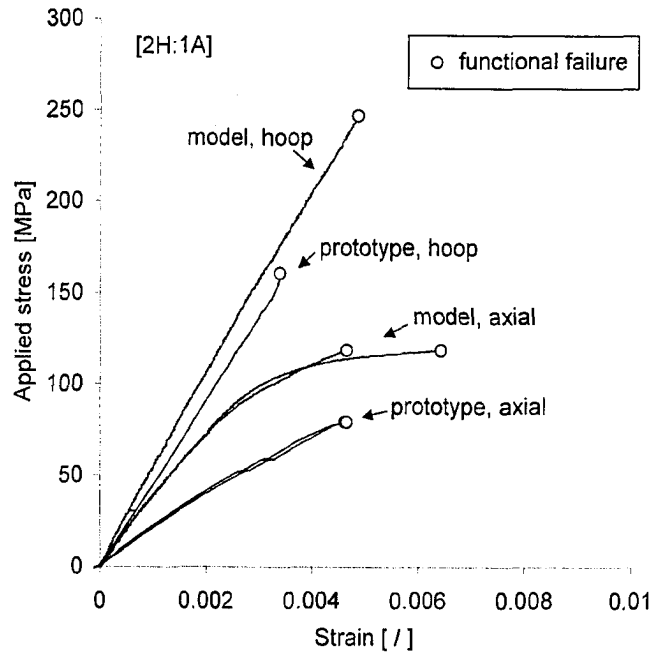


Figure 4.5.2: Stress/strain data from testing of model and prototype-size specimens under closed-end loading.

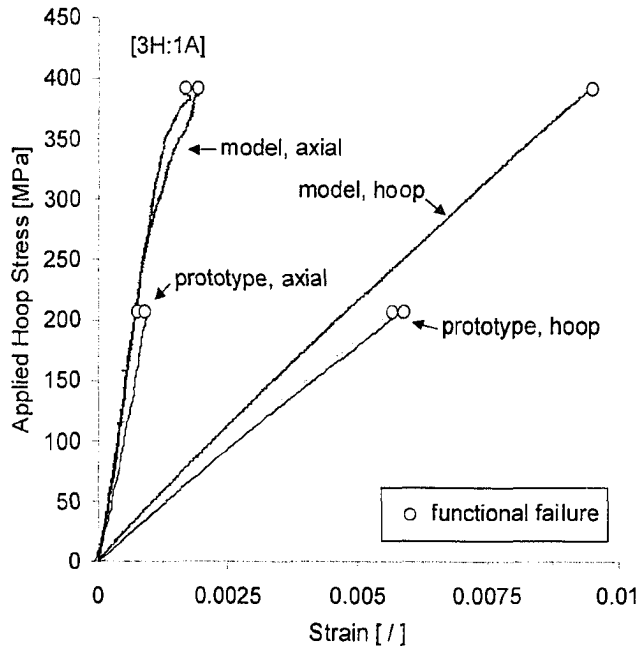


Figure 4.5.3: Stress/strain data from testing of model and prototype-size specimens under [3H:1A] loading (Note that ordinate values are given in terms of applied hoop stress).

direction indicates the absence of fibre damage. The non-linear axial strain, on the other hand, is attributed to the combination of the matrix material non-linear visco-elastic property and damage caused by cracking.

Degradation of the matrix material and associated non-linear stress-strain behaviour was ascribed to matrix damage by e.g. Perreux and Thiebaud (1995). The level of degradation was quantified by unloading and reloading of specimens and the evaluation of resulting hysteresis curves. This approach was not feasible with the present experimental set-up. In some cases strain gauges failed early during the tests, and readings from these gauges were omitted. Furthermore, some strain readings exhibited discontinuities, which were likely caused by damage events. These discontinuities, which particularly affected the axial component, were most frequently encountered at approximately 97% failure loads. Subsequent investigations were therefore limited to stress/strain data up to this load level.

In the present study the level of matrix material degradation is assumed to be quantifiable by a reduction of material stiffness. A parameter was adopted accordingly, i.e. the change in axial modulus, D_A , see Eq.(4.5.1). This parameter quantifies the change from the initial elastic axial modulus, E_A , (taken at a hoop stress level of 50 MPa) to the one at 97% failure load, $E_{f,A}$, given by Eq.(4.5.2). Results for the [2H:1A] and [3H:1A] loading cases are shown on the left and right hand side of Figure 4.5.3 respectively.

The change in axial modulus is defined by

$$D_A = \left| E_{f,A} - E_A \right| E_A^{-1} \quad (4.5.1)$$

$$\text{where } E_{f,A} = \frac{\sigma(\varepsilon_{f,A}) - \sigma(\varepsilon_{a,A})}{\varepsilon_{f,A} - \varepsilon_{a,A}} \quad (4.5.2)$$

with $\varepsilon_{a,A} \cong 0.98 \varepsilon_{f,A}$ and $\varepsilon_{f,A}$ is the axial strain at failure.

The present method does not allow for non-linear visco-elastic behaviour to be isolated from damage effects. However, it is reasonable to assume that influences of non-linear visco-elasticity are small compared to damage effects within the brittle matrix.

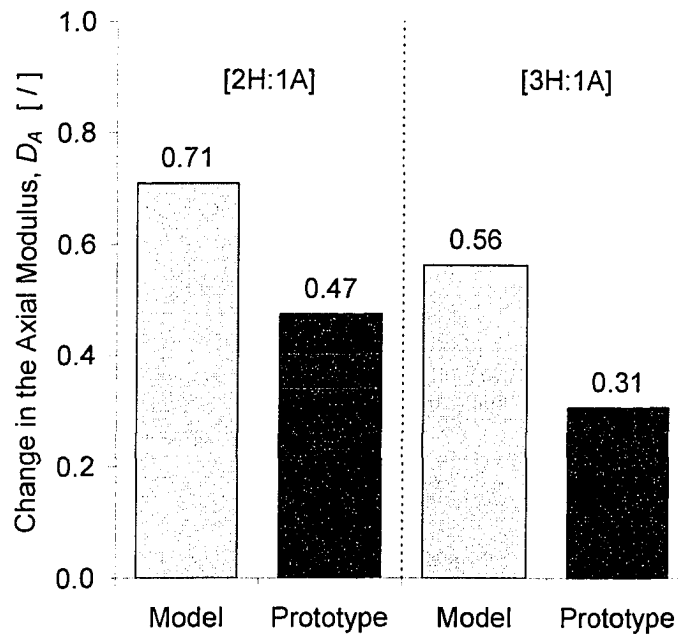


Figure 4.5.4: Change in the axial modulus, D_A , of model and prototype-size specimens.

Figure 4.5.4 shows that for both loading ratios the change in axial modulus is significantly higher for model than prototype-size specimens, despite equal permeability thresholds. This suggests that for the same permeability level the degree of matrix material degradation was higher in model specimens than in prototype-size samples. An explanation for the apparently dissimilar damage levels between model and prototype-size specimens may be found on a micro-mechanical level. However, this was not attempted in the context of the present study.

Similitude analysis:

The following similitude analysis on various geometrical and failure parameters concludes the present investigation. Similitude studies are commonly conducted for the identification of important physical variables that are responsible for the underlying scaling law for the structures in question. Such analyses often aim at enabling the prediction of prototype behaviour from constants of proportionality (i.e. Pi-terms) between the relevant variables used to describe the problem.

Aforementioned work by Chouchaoui and Ochoa (1999a-b), who made use of governing equations to provide scaling laws (based on an elasticity approach), is an excellent

example that similitude theory may indeed accurately predict prototype behaviour. The described method, however, does not succeed when dealing with progressive damage effects that violate elasticity theory. As shown by the analysis of stress/strain behaviour, this was the case in the present experiments. Since leakage failure was found to terminate the useful life of a structure, permeability was determined to be the governing damage parameter; and the permeability ratio, in other words, the permeability Pi-term between prototypes and models, $\lambda_K = K'_p / K'_m$, was set to unity. Generally, failure of structures is not quantified in terms of permeability. It is therefore of interest to ascertain how this criterion translates into other possible damage parameters, i.e. pressure, strength (stress) and strain. Pi-terms for these damage parameters along with Pi-terms for the geometry are given in Table 4.5.2. These data demonstrate that dimensional scaling between model and prototype-size specimens produced structures with (approximately) equal permeability and pressure containment capabilities. Strength and strain, on the other hand, were substantially compromised. Under [2H:1A] loading, for example, prototype failure pressures were expected to be approximately 1.5 times higher than model failure pressures based on geometry Pi-terms and a strength based failure criterion (i.e. the strength Pi-term is set to unity).

Table 4.5.2: Pi-terms for the geometry and possible damage parameters.

Average Pi-terms for	[/]	[2H:1A]	[3H:1A]
wall thickness,	λ_t		4.10
inside radius,	λ_R		2.67
permeability at failure,	λ_K	1.00	1.00
failure pressure,	λ_p	1.00	1.15
strength (failure stress),	λ_σ	0.65	0.57
hoop failure strain,	$\lambda_{\epsilon H}$	0.69	0.64
(at 97% failure load)		(0.69)	(0.62)
axial failure strain,	$\lambda_{\epsilon A}$	0.80	0.53
(at 97% failure load)		(0.87)	(0.51)

4.5.3 Implications for the Design of Tubular Components

Even though the conducted experiments indicated greatly reduced strengths and failure strains for the larger prototype-size samples, one could not attribute this solely to size-effects in the conventional sense. Leakage “damage mechanics” and appropriate modelling techniques for its prediction are not yet fully developed (Soden et al., 2004). Damage mechanisms for leakage failure, on the other hand, have been identified here. These are the interaction between matrix damage events on the micro-level (intra-laminar matrix-cracking), the meso-level (inter-laminar matrix-cracking, i.e. delaminations), and features enabling fluid penetration (e.g. crack opening, crack coalescence and extent of crack networks). Therefore, failure criteria based on structural properties (fibre-dominated properties) are inappropriate and will produce an ‘apparent size-effect’ unless they are correlated with properties that control the permeability of the structure. Consequently, for the prediction of prototype behaviour of pressurised filament-wound structures, scaling laws need to be applied that are based on aforementioned damage mechanisms and fluid penetration properties. These scaling laws are not available yet; however, the present investigation indicates the potential research direction, i.e. a combined investigation on micro- to macro-mechanical damage effects and the fluid permeability properties of the structure. However, until appropriate failure criteria become available, testing of prototypes will be imperative to obtain strength data, as well as to ensure equivalent model and prototype (damage) behaviour.

As detailed earlier, a $[\pm 60_m, \pm 30_n]_T$ fibre architecture was selected for subsequent prototype structures. Due to the lack of leakage-based scaling techniques, a conventional strength-based approach was adopted. Assuming identical strength for model and prototype structures, the lay-up of prototype structures was chosen as to achieve pressure capabilities of similar magnitude as the $[\pm 30, \pm 60_2]_T$ model lay-up. Based on the model configuration, scaling with regards to a hoop stress criterion dictates a prototype wall thickness of 4 mm. Employing fibre material of the aforementioned tow weight (i.e. 2000 g/m) the closest approximation of this target value was achieved by a $[\pm 60_3, \pm 30]_T$ lay-up (i.e. a 4.63 mm wall thickness). Note that this constitutes a 60°-cover to 30°-cover area ratio (with respect to the axial direction) of 2.41 for prototype pipe compared to 1.38 for the $[\pm 30, \pm 60_2]_T$ model specimens.

CHAPTER 5

INTEGRATION OF TUBULAR SUB-COMPONENTS

The subject matter of the present chapter is the integration of pipe subsections. Various technologies have been reported for the joining of tubular structures made from fibre-reinforced polymer composites. A brief survey of available research work on this subject is provided in the following (Section 5.1). Based on this information, objectives for the present composite tubular joint design were delineated (Section 5.2). It will be shown that adhesive bonding is the most advantageous method for the joining of composite pipe sections. This technique is briefly reviewed in Section 5.3, followed by the description of the joint configuration and bonding methodology for the current prototype pipe structures (Section 5.4). Joined prototype pipe was investigated experimentally along with plain pipe samples to assess performance and to examine the damage behaviour under different biaxial loading conditions. Results of this investigation are presented in Section 5.5.

A theoretical approach was chosen to accompany the experimental investigation of the proposed joint configuration. This was to obtain a better understanding of the damage behaviour and to improve the design of prototype pipe joints. The modelling and joint optimisation is discussed in the second part of the present chapter. A strength-of-materials and a fracture mechanics approach will be utilised for the analysis. Section 5.6 provides a review of modelling techniques for flat and tubular adhesive joints, which is followed by the description of the employed fracture analysis technique. The theoretical models are presented in Section 5.7, where validation of the models is also given. A parametric study of various joint features concludes this section. Finally, in Section 5.8 an altered fabrication process is presented that results in improved performance of joined prototype pipe.

5.1 Review of Joints in Tubular Composite Structures

Technologies for the joining of tubular composite structures can be divided into two groups: (a) mechanically fastened joints, and (b) adhesively bonded joints. While bonding produces a permanent connection, mechanical fastening is used to enable detachable joints. The latter may be achieved via flanged, threaded, or interlocking-sleeve connections. All of these solutions offer the ability for disassembly. However, great attention needs to be paid to the sealing of the connection. Firstly, a type of seal or gasket is required that is compatible with the service conditions. Secondly, compressive loads need to be imposed upon the seal to hold the joint leak tight. And thirdly, the seal and the joint assembly have to be able to sustain loads resulting from axial loadings and bending of the pipe assembly.

Various design solutions for mechanically fastened joints are available in the technical literature. Table 5.1.1 gives a summary of reviewed works, which represent examples of feasible design solutions for connecting composite pipe while allowing for detachability. However, all of these joints require tube segments to possess modified extremities with rather complex features (such as upsets, grooves or threads). It seems impractical to subject pipe segments to modifications outside the factory that will transform smooth, uniform pipe ends into the required shapes. Hence, repair work and replacement of pipe sections in the field might prove difficult. Moreover, requirements for assembly and sealing make for complex structures that involve multiple parts.

Analogous to welding of metallic pipe, adhesive bonding of composite pipe offers the advantages of integrated sealing, minimal part count and the ability to use uniform pipe sections without specific requirements towards the geometry of the pipe extremities. Thus, significant cost savings may be realised in comparison to mechanically fastened joints. The lap joint (cylindrical pipe extremities) and the scarf joint (conical or mating tapered pipe extremities) shown in Fig.5.1.1, are the two most common types of tubular bonded joints. Both design solutions are briefly reviewed in the following.

Table 5.1.1: Examples of mechanically fastened joints for connecting composite pipe.

<i>Type of joint</i>	<i>References / Remarks</i>
<i>Flanged connections:</i>	<i>Estrada and Parson (1997):</i> Pipe extremities feature tapered hubs (flaring towards the pipe end), which engage a metallic stub flange to transfer bolt loads to a gasket.
<i>Threaded connections:</i>	<p>Bell-and-spigot designs feature threads or helical grooves. Abrasive-resistant contact surfaces allow for multiple assembly and disassembly cycles.</p> <p><i>Simmons (1990 and 1995):</i> Winding onto a mandrel thread-form produced interlocking threads. Pressure tight sealing was achieved by a thread sealant.</p> <p><i>Ellsworth and Bauer (1992), Harte et al. (2003), Friedrich et al. (1996):</i> Threads were shaped by cutting into the fibre-reinforced pipe body. The first design features polymer contact moulded threads to provide sealing and consistent engagement properties. In the latter case a ductile key inserted into the resulting grooves functioned as an interlocking member. Sealing was achieved by the injection of a liquid adhesive sealant into an annulus formed by the facing contact surfaces and two parallel o-rings.</p>
<i>Interlocking sleeve connections:</i>	<i>Kaempfen (1983 and 1993), Jones (1989):</i> Joining is achieved by two semi-cylindrical half couplers, which are retained in a cylindrical coupler sleeve. The half couplers interlock with circumferential upsets on the pipe, flanged pipe ends, or circumferential grooves in the pipe surface. Pipe upsets or flanged ends result from winding over ring-type inserts or built-up hoop windings. Gaskets or seal rings are butted against the pipe ends to provide sealing.

Bonded tubular scarf joints:

Semb et al. (1995) reported that scarf joints generally achieve higher strength than lap joint designs. This was attributed to the thickness transition that reduces stress concentrations at the pipe ends. However, the application of scarf joints was found to be more complicated due to difficulties in machining and handling of slender scarf edges. A scarf joint design was investigated extensively by Cowling and co-workers (Hashim et

al., 1998; and Knox et al., 2000a-b, 2001). Testing and analysis conducted by these researchers focussed on a commercial pipe system (Ameron Company). Pipe connections were made according to the manufacturer's procedures (i.e. ends of two pipe sections were shaved into a conical shape with dimensions for a 2.5° taper/taper joint). A shallow scarf angle is required to minimise stresses normal to the bond surfaces. The preparation of pipe ends is usually conducted in the field using a portable shaver tool. Pipe sections were connected using a pre-manufactured glass-fibre reinforced epoxy socket coupling (which features corresponding inverse tapers). To prepare components for bonding, surfaces were primed, and adhesive was applied with a spatula. The components were subsequently mated, clamped and cured using a heat blanket.

Bonded tubular lap joints:

There is a considerable amount of literature pertaining to adhesively bonded tubular lap joints, i.e. the most basic design configuration. The joining of two tubular sections is usually achieved using butt-strap (sleeve) joints or bell-and-spigot type connectors (see Fig.5.1.1). In case of the latter connection type, which essentially constitutes a single lap joint, a tube with at least one specialised extremity is required. Notwithstanding their geometric differences, modelling and analysis of both connection types is generally performed employing comparable methodologies.

Bonded tubular lap joints subjected to torsion, such as in drive shafts, have been the subject of a considerable amount of research. Information on this topic and further references can be found in e.g. Graves and Adams (1981), Hipol (1984) and Kim and Lee (1995). However, torsional loading is not applicable to the present study; however, the analysis techniques employed were useful with regards to the current investigation.

Other research dealt with tubular lap joints under axial loading conditions. Early work on this subject was published by Lubkin and Reissner (1956), Yuceoglu and Updike (1980) and Adams and Peppiatt (1977). In the former two publications, closed-form solutions based on thin-shell theory were presented. More recently, Thomsen (1992) and Shi and Cheng (1993) extended the analytical modelling to elasto-plastic materials and thick adherends respectively. Using the finite element method, basic results by Lubkin

and Reisser (1956) were confirmed by Adams and Peppiatt (1977), who also included adhesive geometry effects in their study (i.e. adhesive fillets). They pointed out that even though closed-form theories are more conveniently incorporated into parametric studies, a more realistic representation of the joint geometry and extended joint optimisation capabilities are achievable with the finite element method. Despite the earlier research work, Whitcomb and Woo (1993) found a detailed understanding of tubular lap joints to be lacking. Employing numerical techniques in conjunction with linear elastic fracture mechanics they gained insight into the joint behaviour by comparing tubular single lap and butt-strap joints with the corresponding plate structures in terms of deformation, stress distribution and crack growth. Although important differences were found to exist, numerical modelling procedures for tubular and plate joint structures were shown to be basically compatible. Reedy and co-workers (1991 and 1993) and Guess et al. (1995) also performed finite element analyses to investigate the performance of tubular joints under tensile and flexural loadings (in wind turbine blades). Results were compared with experimental findings and good agreement was obtained. Note that the works discussed in this paragraph were primarily focussed on the mechanical behaviour of the bondline region; damage of the fibre-reinforced substrates was generally not considered.

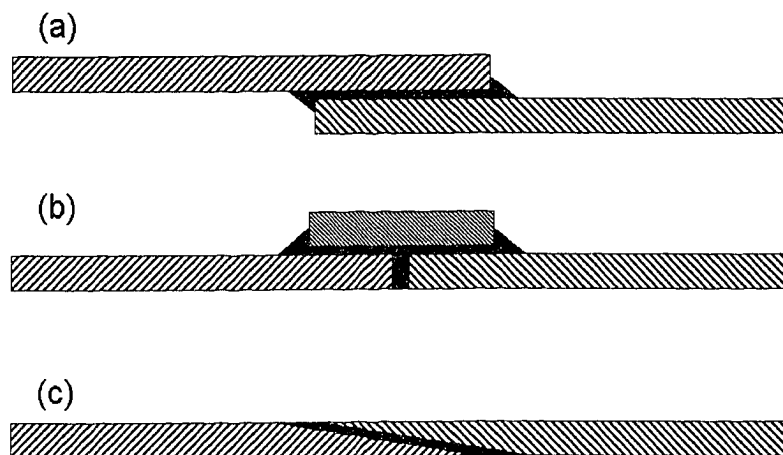


Figure 5.1.1: Schematic of common bonded joint configurations: (a) single lap joint, (b) butt-strap joint, and (c) scarf joint (black colour indicates adhesive material).

Although bonded tubular lap joints under torsion and axial loading have received considerable attention, available research on tubular joints in pressurised components is limited. Semb et al. (1995) (as well as Adams and Peppiatt, 1977) described the mechanisms causing stress concentrations in non-pressurised structures as differential straining of the adherends, bending of the adherends due to their non-collinearity, and end effects. A fourth mechanism was identified to be operative in pressurised structures, namely bending of the adherends due to differential radial displacement under applied internal pressure. Due to this added complexity, Semb et al. developed a finite element model for the investigation of butt-strap joined pipes under closed-end pressure loading.

Instead of sleeve connectors, some researchers have employed prepreg wrapping techniques to produce butt-strap joints for pressurised pipe. This type of design was reported by Stubblefield et al. (1998), and Huysman and co-workers (1996, 1997 and 1998). Pipe sections were placed end-to-end and prepreg material was wrapped about the two pipe extremities establishing the connection. The above studies reported that tapering of prepreg at the joint edges decreased the stress concentrations. Huysmans et al. (1998) also tapered the pipe ends (internally) to reduce the length of the artificial pre-crack. (Note that in the case of un-tapered butt-to-butt pipe coupling the pre-crack length is equal to the pipe thickness.) The resulting cavity between the pipe ends was filled with a gap filler material. It is interesting to note that composite wrapping is an emerging technique in various high-pressure piping applications. Wrapping of glass-fibre prepreg is being used as a repair technique for steel gas-pipelines, and as a part of the joining process of composite reinforced (steel) line pipe (see True, 1995; and Anonymous, 2003).

Similar modelling techniques as used for socket type connections were reported for joints produced by prepreg wrapping. Huysman et al. (1998) and Wahab and De Roeck (1997) examined joint performance using numerical techniques and a fracture mechanical approach. In complimentary papers by Griffin et al. (1991) and Yang (2000) an analytical model for the mechanical joint behaviour (under tension) was presented. In this analysis also possible pipe failure (due to shear delamination) was considered. Results were confirmed by comparison with experimental data and finite element solutions.

5.2 Design Objectives for Composite Tubular Joints

It is to be expected that mechanically fastened connections are required for the integration of valves and similar components within a composite pipe system. Nevertheless, in all probability only a small amount of such joints will be needed. The majority of connections within a pipe system therefore would be of a much simpler design ensuring low complexity, high reliability, ease of installation, and consequently low cost. Adhesively bonded joints are seen to comprise these objectives without compromise. A particular advantage of bonded connections is the ability to connect bare pipe ends. In contrast to mechanically fastened joints, bonded connections usually do not require pipe extremities with complex geometries. This offers the flexibility to segment pipe at any location along its length. Since apertures or depressions are not needed, the continuity of the fibre architecture within the pipe body can be preserved. Moreover, bonded tubular lap joints increase the quantity of load-bearing material locally; a reinforcement effect within the joint region may therefore be realised. A carefully designed joint may thus provide a load carrying capacity that is greater than that of the bare pipe body itself, without having any negative influence on the pipe strength. As a consequence, a “leak-before-burst” behaviour of the entire piping system may be realised. Hence, an adhesively bonded structure may possess all the properties considered imperative for a composite pipe system (see Chapter 1: Section 1.4). Bonding of composite connectors and pipe does not only provide for integrated sealing. It also constitutes an entirely non-metallic system, which inherently possesses sought-after properties such as enhanced corrosion resistance and a high strength-to-weight ratio. If all components of such a pipe system are producible by filament winding (or similar techniques), manufacturing advantages associated with this process may be fully utilised.

Based on the preceding discussion, it was decided to produce all components of the prototype piping system (i.e. connectors and pipe) by the filament winding method from glass-fibre reinforced epoxy material. For the aforementioned reasons, an overlap sleeve connection was favoured over a scarf joint configuration. Hence, in the current research project a joint design of adhesively bonded tubular overlap sleeves was selected for the integration of pipe sections with cylindrical extremities.

5.3 Review of Adhesive Bonding

In the following the employed adhesive bonding technique and the applied substrate priming procedures are briefly discussed. Further information on adhesive bonding can be found in publications by e.g. Ashbee (1993), Strong (2000) and Garbassi and Occhiello (2001). More recently a comprehensive review on adhesives, adhesion and surface treatment in composite material systems (as well as metallic alloys and polymers) was provided by Baldan (2004). In the second part of the current section a review of possible failure modes of adhesively bonded joints is provided.

5.3.1 Surface Preparation Techniques and Bonding Mechanisms

In the present research project, pre-manufactured composite components (i.e. prototype pipe sections) were to be joined using a liquid adhesive material. An essential prerequisite for proper adhesion is the ability of the adhesive to wet the bonding surfaces of the adherends. Thermodynamics dictates that wetting of the surfaces will only occur naturally, if the energy of the system is lowered in the process. Thus, the surface energy of the solid components has to be higher than that of the liquid, resulting in a reduced surface energy after wetting. In the present study the 3M DP-460 epoxy adhesive was chosen for its mechanical properties (see Chapter 3: Subsection 3.2.2 for details), and its ability to adhere to the glass-fibre reinforced epoxy composite adherends. But, even in the case of a properly chosen adhesive, the substrate surface energy is often significantly reduced, and wetting is consequently inhibited by surface contaminations such as oils and release agents. Hence, in the first stage of the preparation process, composite components were thoroughly cleaned using isopropyl alcohol. This solvent was preferred over acetone, because acetone's strong hydrophilic properties result in a substrate surface contamination with a micro water film. (Note that for the bonding of end-tabs to model type specimens a heating process was required in order to lower adhesive viscosity (see Chapter 3: Subsection 3.2.2). This also removed any moisture contamination from acetone use.)

The bonding of substrate surfaces can be ascribed to any of the following four mechanisms (Strong, 2000; and Baldan, 2004). The strongest possible bond between

adhesive and substrate is created by covalent bonds (i.e. the formation of new molecules by electron-sharing between non-metallic entities). The second possible mechanism is the attraction between substrate and adhesive due to phenomena such as hydrogen bonding and van der Waals forces. The third type of bonding is the diffusion of polymer molecules into the molecular network of the adherend material. And lastly, mechanical bonding may occur, i.e. the mechanical interlocking of adhesive in clefts on the substrate surface. The first three mechanisms depend entirely on the chemical composition of adhesive and substrate materials, which were predetermined by the manufacturers of the material system. To enable mechanical bonding, substrate surfaces were mildly abraded employing a sandblasting procedure. In the final step of the preparation process, the adherend surfaces were again wiped with isopropyl alcohol to remove any remaining surface contaminations resulting from the abrasion procedure.

Note that advanced techniques for modifying substrate surfaces are available that result in enhanced chemical bonding, e.g. flame or plasma treatment. However, such techniques were not considered in this research project, since they were shown to be most effective with thermoplastic material systems (Baldan, 2004). It will be shown in this chapter that excellent adhesion was achieved for the current thermoset materials employing the above described conventional techniques.

5.3.2 Failure Mechanisms in Adhesive Joints

Three basic failure modes can be distinguished in adhesively bonded joints (shown in Fig.5.3.1): (a) adherend failure, where joint strength exceeds the adherend load capacity; (b) adhesive failure, where debonding is found in the adherend/adhesive interface; and (c) cohesive failure, where crack growth occurs within the adhesive layer. Since adhesive failure is indicative of poor adhesion, it is usually linked to improper surface preparation and/or an incorrect adhesive material selection. As such, this failure mode should not occur for properly selected and primed materials. Moreover, no theoretical techniques exist for the prediction of this failure mode (Tong and Steven, 1999).

Bonded joints are subject to complex stress states. The locus of damage initiation depends on the stress distribution, and the properties of the adherend and adhesive

material (such as strength and ductility). However, stress or strain concentrations and corresponding fracture initiation sites are usually found within either the adhesive or the composite in the highly loaded regions at the ends of the adherends, i.e. in zones where load transfer from one adherend to another commences (see e.g. Adams and Peppiatt, 1977; Whitcomb and Woo, 1993; and Adams and Davies, 1996). From experiments with single lap joints Clark and McGregor (1993) observed failure to originate in the main body of the adhesive fillet.

After damage initiation, transverse normal (mode-I fracture) and in-plane longitudinal shear (mode-II fracture) stresses exceeding the material toughness generally cause a bonded joint to fail. Of particular concern are peel stresses acting transverse to the substrate surface, because structural adhesives as well as laminated composites exhibit significantly reduced strength under this loading condition (see e.g. Liechti et al., 1987; Adams and Davies, 1996). Mode-II fracture in brittle materials such as epoxy polymers was commonly described to originate from short microcracks inclined at 45° to the shear plane. With increasing load these cracks developed into ligaments or so-called “hackles”. Mode-II fracture growth was observed to occur due the collapse and coalescence of these features. Based on these observations it was postulated that the actual cause for mode-II fracture is the action of principle stress and the corresponding tensile failure (O’Brien, 1998; Lee, 1997).

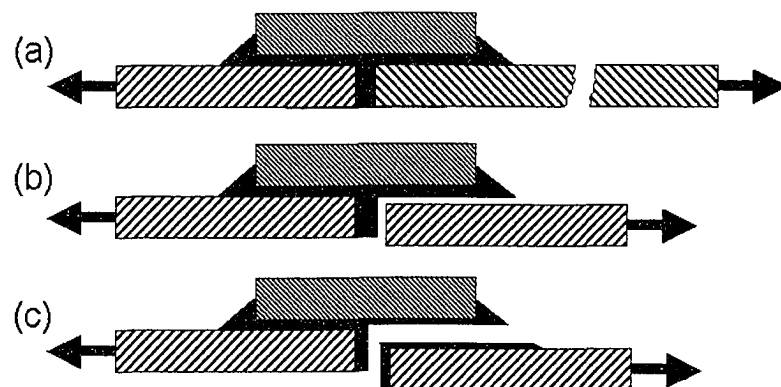


Figure 5.3.1: Failure modes of adhesively bonded joints: (a) adherend failure, (b) adhesive failure, and (c) cohesive failure.

The evolution of damage is usually characterised by some form of stable crack growth, followed by unstable fracture progression and final failure. This development is accompanied by a complex evolution of the stress field within the joint region. Cracking is therefore not limited to the adhesive or adherends, but commonly involves a combination of adherend and cohesive failure characteristics (see e.g. Bishop and Gilmore, 1989; and Tong and Steven, 1999). For example, it is not uncommon to observe crack growth within one of the adherends even after fracture initiation occurred inside the adhesive. Moreover, De Goeij et al. (1999) pointed out fundamental differences between static and fatigue-induced crack growth. Thus, joint performance does not only depend on the joint configuration but also on the type of loading (i.e. monotonic and cyclic loading). Note that Knox et al. (2000a) found visco-elasticity in adhesive joints to be insignificant compared to the overall creep deformation of pipe structures.

Further, it was demonstrated in the literature that specific features of overlap joints influence damage initiation and progression. Adherend tapering, adhesive fillets, adhesive layer thickness and overlap lengths were mainly cited in this context. Adams and Davies (1996), for example, emphasised the positive effects of adherend tapering and adhesive fillets. Tapering of lap joint adherends in conjunction with adhesive fillets was shown to maximise joint performance, with inside tapering yielding the best results. De Goeij et al. (1999) provided a survey on the influences of various joint parameters under static and fatigue loading conditions. The positive effects of adhesive fillets and adherend tapering were confirmed. Furthermore, an optimum overlap length and adhesive layer thickness were shown to exist. But, depending on the type of joint and the loading scenario the magnitude of performance enhancement due to any of these measures can be rather small; thus, it needs to be weighted against efforts in manufacturing.

In their early work Adams and Peppiatt (1977) pointed out that in practice, when an adhesive joint is made, fillets form by the displacement of excess adhesive. Concave, triangular or convex shapes with smooth transitions to the adherend surface are commonly observed fillet geometries formed by adhesive displacement on square-ended adherends, shown in Fig.5.3.2. These shapes correspond to fillet geometries in plate single lap joints that were investigated by Lang and Mallick (1998) (using finite element

analysis). For the abovementioned fillet geometries, appreciable reductions of shear, peel and axial peak stresses were reported compared to square-ended single lap joints (i.e. 50-60%, 73-87% and 31-35% respectively).

Failures reported for lap plate and lap tubular joint configurations often exhibit similarities. But, even for identical material systems and equivalent geometries the initiation and evolution of damage is not necessarily identical. This is due to the different deformation behaviour of the two joint types. Whitcomb and Woo (1993) showed that joint rotation is significantly decreased in tubular lap joints. Due to symmetry, joint rotation induces hoop stresses that in turn counteract and constrain adherend rotation. As a result reduced peak stresses at the ends of tubular joints were reported. Plate and tubular connections therefore do not share identical stress or deformation conditions, and consequently, initiation and progression of fracture may differ between the two.

Although concise in nature, the above review on damage in adhesively bonded joints clearly portrays the difficulties in predicting damage and failure in such structures. This was underlined by Tong and Steven (1999), who concluded that there is a lack of complete understanding and accurate modelling methodologies of failure mechanisms in adhesively bonded joints. Thus, the experimental investigation of a selected joint configurations is warranted, if not even necessary, to determine the nature of joint failure. Ensuing observations may then enable further optimisation of the bonded connection using numerical or analytical modelling techniques.

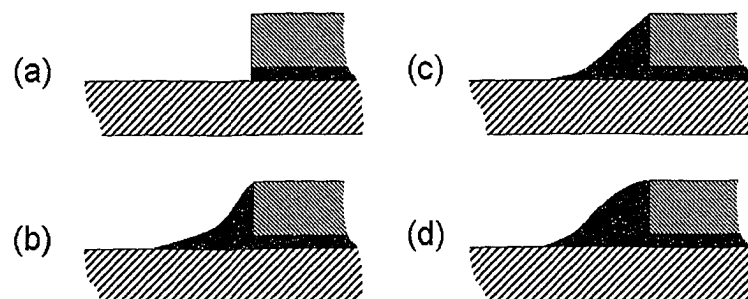


Figure 5.3.2: Adhesive fillet shapes: (a) square-ended, (b) concave/arc, (c) triangular and (d) convex/rounded shape; (b-d) feature smooth transitions to the substrate surface.

5.4 Description of Current Joining Methodology

5.4.1 Earlier Research Work Pertaining to Current Joining Process

The joining methodology for current prototype specimens is based on observations made in an earlier research study (Mertiny, 1999). In this work metallic overlap sleeves were employed in the making of adhesively bonded butt-strap connections for commercial fibre-glass/epoxy tubing. These tubes were dimensionally similar to present model-type specimens. Bonding was accomplished by an adhesive injection technique. Three equally spaced circumferential injection holes were introduced in the centre of the coupler sleeve. Particular attention was given to a complete adhesive impregnation of the adherends without air entrapment. This was confirmed by visualising the adhesive flow using polycarbonate sleeve couplers, and ultrasound inspection of the joined specimens. Mechanical testing of coupled tubes under closed-end loading conditions exhibited joint strengths exceeding the load capacity of the tubing itself.

A so-called 'pre-bonding' of the tube ends (butt-to-butt tube bonding) was established as a prerequisite for void-free adhesive layers and high joint performance. The coupler application was delayed until the adhesive used for the pre-bonding had gelled. Without the pre-bonding procedure, air pockets were observed to form in the centre of the annulus in between tube and coupler sleeve (i.e. air entered along the butt-to-butt connection). This was attributed to several possible mechanisms, i.e. adhesive shrinkage during curing, adhesive expansion and contraction due to thermal reactions, surface tension effects in the small gap in between the tubes and coupler, and the influence of gravity.

5.4.2 Description of Current Joint Configuration

Proposed pipe joint geometry:

In order to attain a field-friendly and inexpensive joining methodology, emphasis was given to a simple design and ease of assembly. Pre-manufactured cylindrical composite coupler sleeves were employed for the joining of prototype pipe. Recall that these pipes featured a $[\pm 60_3, \pm 30]_T$ lay-up configuration, see Chapter 4. All components were filament-wound following the procedures outlined in Chapter 3: Subsection 3.2.4. Details on the $[\pm 30, \pm 60_2]_T$ coupler lay-up were also provided earlier, see Table 3.2.2. A mandrel

of 113.3 mm diameter was employed for the coupler fabrication. This mandrel allowed for the simultaneous winding of three couplers, which were ultimately cut from the part. Coupler sleeves were 305 mm end-to-end, which constitutes a joint length of about three times the pipe diameter. Note that the coupler length, $2c$, was not determined based on structural requirements, but on space considerations for an unobstructed installation and adhesive application procedure. However, later in this text it will be demonstrated that the joint overlap length, c , was chosen conservatively, see Subsection 5.7.3. Coupler sleeves were completed by machining 30° chamfers on both ends. Providing compliant coupler ends ought to increase joint performance due to a more gradual load transfer and reduced peak stresses. A schematic of the proposed prototype joint is shown in Fig.5.4.1.

Pipe ends were machined to have mating 15° inside and outside tapers respectively. This is similar to the design reported by Huysmans et al. (1996, 1997 and 1998), who provided internally tapered pipe ends filled with gap-filler material. However, the mating inside/outside taper eliminates the need for any gap-filler (which is difficult to apply inside the pipe). Nonetheless, the current design is also aimed at shifting the initiation of damage to higher load levels compared to a basic butt-to-butt configuration. This can reasonably be presumed since the mating inside/outside tapering realises (a) an increase in load-transfer area, (b) a load-transfer by combined shear/tensile stresses between pipe end surfaces (instead of pure tensile stresses), and (c) the elimination of stress singularities. Joint strength is enhanced even further by internal pipe pressurisation, since superimposed compressive load normal to pipe end surfaces ought to reduce, possibly even eliminate, transverse tensile (peel) stresses. The selected geometry also eases the joining procedure by providing plane mating surfaces for the pre-bonding procedure, as well as a geometry that aids the coaxial centring of pipe sections. Note that despite certain similarities, the 15° inside/outside tapering should not be considered a scarf joint comparable to the design described by other researchers (e.g. Hashim et al., 1998). Firstly, the bulk of the substrates was kept to a cylindrical shape. Secondly, the present configuration (with a taper length of about 17.5 mm) is less shallow, and therefore also considerably less fragile, than the much longer conical-shaped pipe extremities of the reported scarf joint design (~ 70 mm overlap length for 3.5 mm pipe wall thickness).

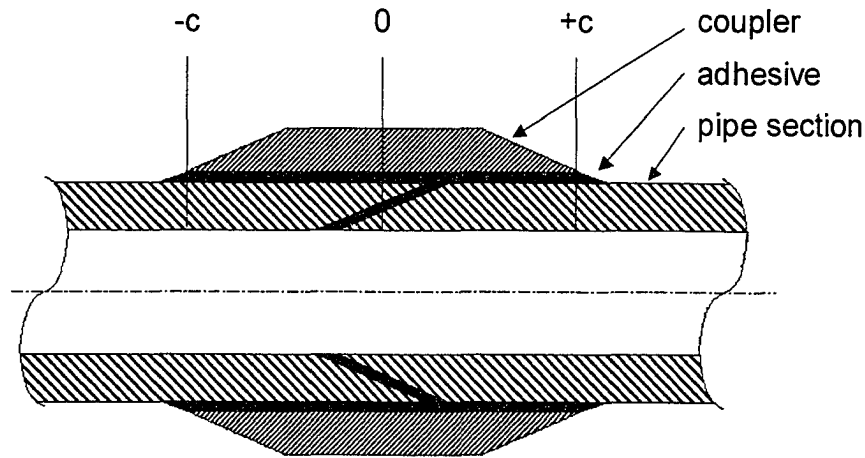


Figure 5.4.1: Schematic of the prototype pipe joint.

Proposed adhesive bonding procedure:

Prototype pipe joining was carried out analogous to the aforementioned joining methodology (Mertiny, 1999). Prior to the bonding process, four injection holes were machined in the centre of the coupler sleeve at loci equally spaced around the circumference. During the bonding procedure a special alignment device supported pipe sections and coupler sleeve (see Figs.5.4.2 and 5.4.3). Adhesive was applied using a pneumatic application gun. In a first step, an expandable mandrel was employed to provide coaxial alignment and axial compression of the pipe sections during the pre-bonding procedure of the mating pipe ends. A fixture encompassing the pipe/coupler assembly (i.e. the coupler cage) facilitated the ensuing coupler application. To position coupler and pipe relative to each other the coupler cage was equipped with a series of fasteners (bolts). Cut-outs were provided to ensure good accessibility of the coupler/pipe assembly and the injection holes. A uniform adhesive gap was adjusted by a shimming technique. Due to the resin coat on the outside pipe surface and its relative unevenness, a nominal bondline thickness, t_b , of 1.2 mm was adjusted (i.e. the nominal bondline thickness is calculated as the sum of the pipe inside radius and the effective pipe wall thickness, less the coupler inside radius). The actual bondline thickness varied considerably depending on the thickness of the resin coat; 0.5 mm and 1 mm were the approximate lower and upper bounds of the bondline thickness respectively.

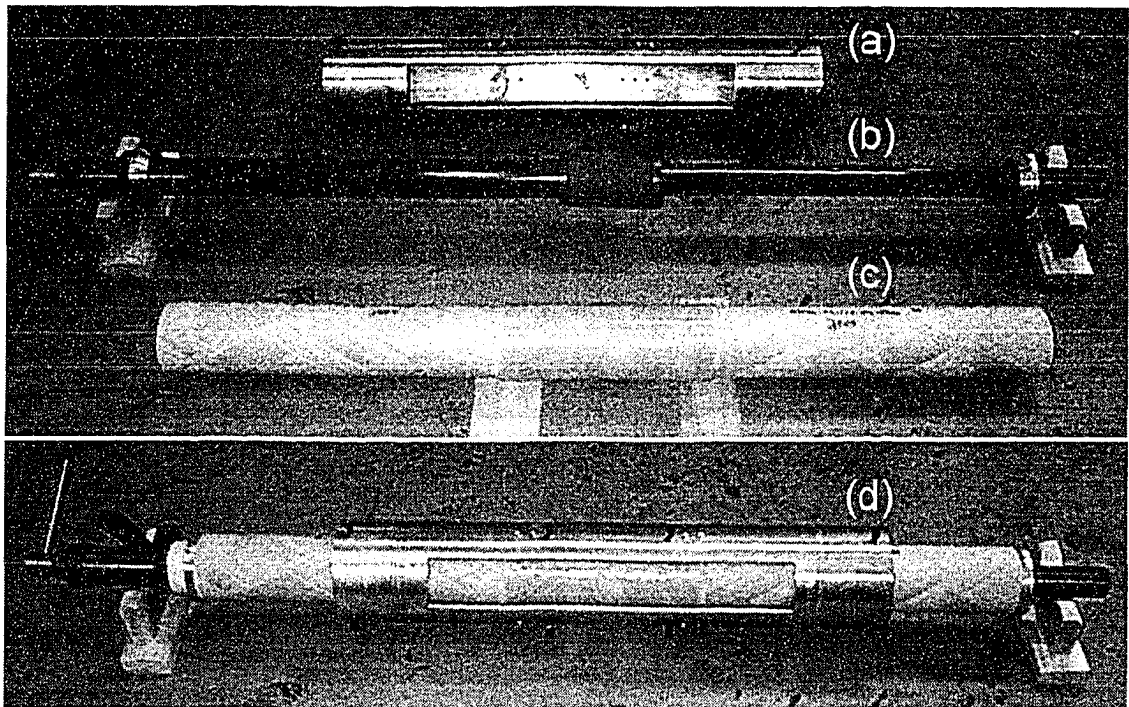


Figure 5.4.2: Pipe alignment device: (a) coupler cage, (b) expandable mandrel with support structure, (c) coupled prototype pipe, and (d) pipe alignment device assembly.

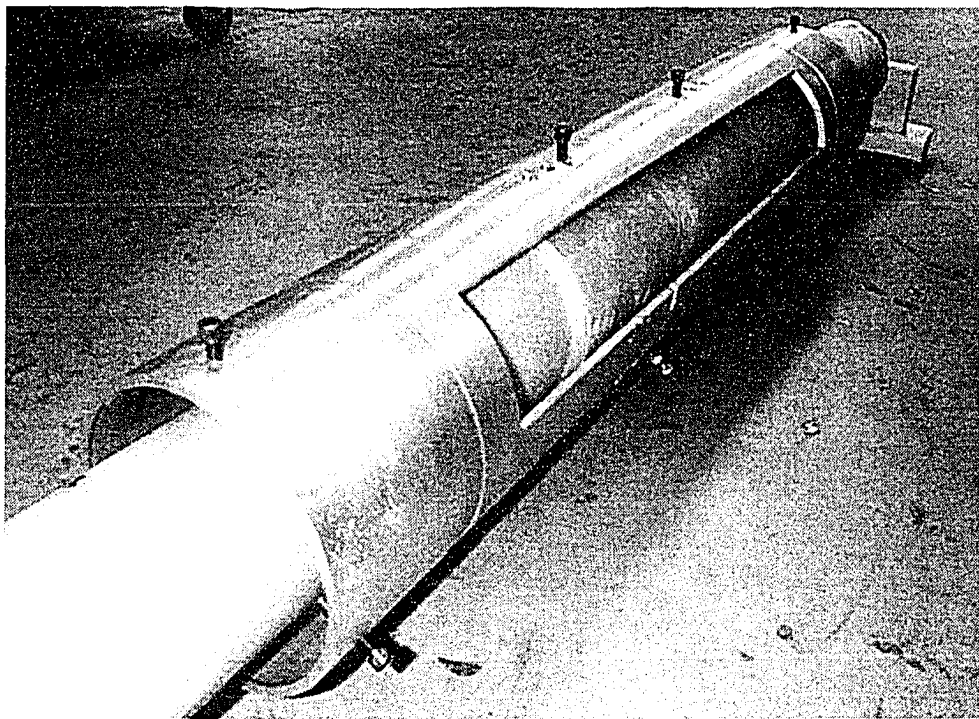


Figure 5.4.3: Pipe alignment device with prototype pipe/coupler.

After the adhesive applied for pre-bonding had set (gelling at room temperature occurs after about 60 min), adhesive material from the application gun was introduced into each injection hole until a bead of adhesive was visible at each coupler end. After switching to another injection hole the previous opening was covered by applying a sturdy adhesive tape. Tape was also wrapped tightly about the assembly in the vicinity of the coupler ends to support the formation of a uniform adhesive fillet. Note that tape was preferred over a solid mould, since the tape material conformed tautly to the uneven coupler and pipe surfaces. A tight enclosure was thus provided preventing any adhesive drip-off. During the injection process, adhesive flowing out of the pipe/coupler annulus filled the annular cavity formed by tape and coupler. Adhesive flow was maintained until the tape was visibly stretched and a small amount of adhesive was observed exiting small punctures made in tape for venting and pressure relieve. During curing at room temperature adhesive shrinkage resulted in a backflow of adhesive into the pipe/coupler annulus, thus preventing void formation. After a 24-hour curing period the tape was removed, and the specimen was taken out of the alignment device. A photograph of a completed joint and a schematic of the fillet geometry are show in Fig.5.4.4 and at the bottom of Fig.5.4.5 respectively.

Note that the bonding of a tubular joint shape poses additional difficulties compared to flat joint configurations. Therefore, the adhesive tape as well as the shimming/alignment technique were introduced. Without employing these aids moulding of the adhesive layer/fillet proved difficult, since gravity caused adhesive drip-off and a non-uniform adhesive bondline/fillet geometry. For the same reason (i.e. the tubular shape), coupler ends were equipped with (outside) chamfers instead of inside tapers (see Fig.5.4.5). Inside tapers were found to obstruct the application of shim spacers. Further, the large annular cavity in between coupler and pipe that is produced by inside tapering, and the lack of a smooth transition between coupler and pipe outer surfaces, were found to hinder the tape wrapping procedure by causing wrinkles, large creases and possibly tape incisions. Thus, inside tapering was not employed, even though better performance of this design was reported for flat joint configurations (Adams and Davies, 1996).

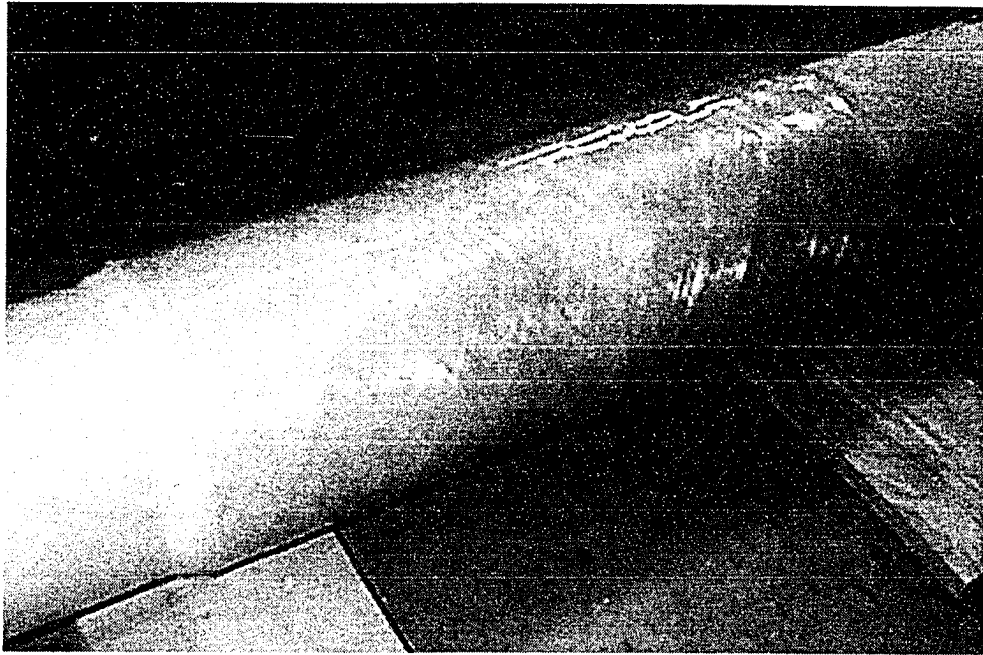


Figure 5.4.4: Completed prototype pipe joint.

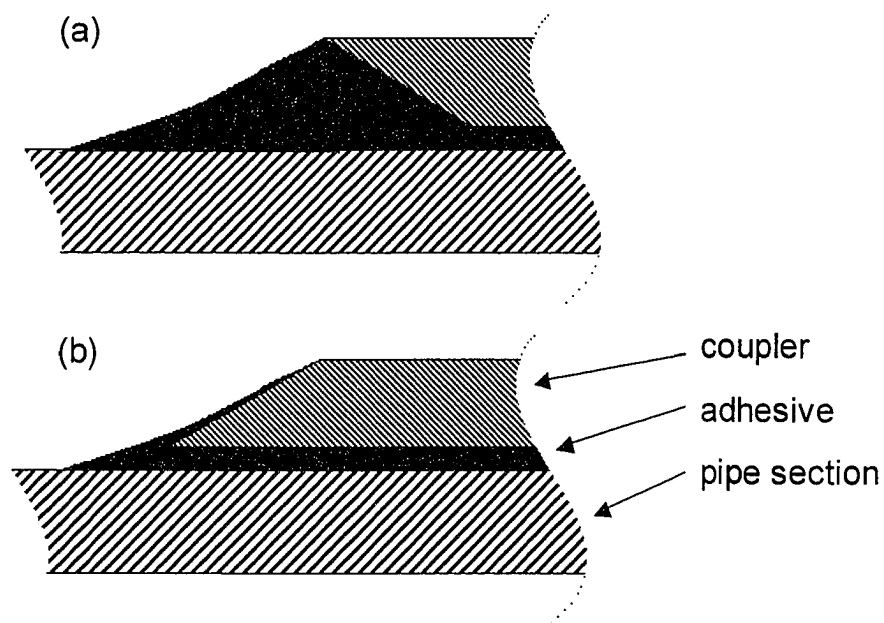


Figure 5.4.5: Schematic of coupler end geometries: (a) inside taper and (b) (outside) chamfer (i.e. the current design configuration).

5.5 Experimental Investigation of Coupled Prototype Pipe

An experimental study of coupled prototype pipe was conducted to identify the characteristic failure modes associated with this structure. Testing also allowed assessing the performance of the structure. Experimental results can be considered a benchmark in terms of strength, which can be used to evaluate future design optimisations as well as design configurations by other researchers. Plain prototype pipe and coupled prototype pipe sections were subjected to various biaxial loadings, i.e. [1H:0A], [3H:1A], [2H:1A], [1H:5A] and [0H:1A]. Plain pipe was tested in order to reduce efforts in specimen preparation. In this study corresponding data were only included after it was confirmed that failure under a particular loading ratio was clearly limited to the pipe body, i.e. pipe failure preceded and thus prevented joint failure.

Observed modes of failure:

Testing under biaxial loading revealed the occurrence of only two failure modes: (a) functional failure (i.e. leakage failure) of the pipe body, and (b) joint fracture leading to a separation of pipe and coupler. Leakage of fluid occurred for all biaxial stress ratios except pure axial loading. At the point of functional failure the aforementioned characteristic damage indicators were observed (i.e. fluid penetration dispersed over the pipe body). But, no leakage was noticeable within the coupler area, which remained dry. It was therefore concluded that the coupler produced a reinforcement of the joint region, which prevented the development of excessive matrix damage and associated leakage.

The second observed failure mode, i.e. the separation of pipe and coupler, occurred only under pure axial loading. Cracking sounds were heard during the testing, which suggested a progressive damage development instead of an instantaneous crack progression. Final failure was characterised by a complete separation of the coupler and one pipe section, which pulled out of the coupler. Note that this damage was not limited to a specific side of the joint, i.e. the pipe end with the inside or outside tapering.

The pullout of the pipe section caused substantial damage to the fracture surface. This rendered the examination of surface features, i.e. the study of fracture initiation and growth characteristics impractical. The specimen joint region was therefore segmented

after testing, which enabled further examination. This revealed that in some cases a crack grew only for a certain distance in between the remaining pipe section and the coupler. An example of such a partial joint fracture is shown in the photograph in Fig.5.5.1, where damage was highlighted using a dye penetrant. Fracturing was noticeable from the outside of structures in form of a crack line following the adhesive fillet around the circumference. The examination of samples further revealed a single dominant crack that grew parallel to the pipe surface. Cracks extended for an appreciable distance into joints (usually 25-50% of the overlap length). Extensive matrix cracking in the $\pm 60^\circ$ covers of the pipe was also discernable, see Fig. 5.5.1. Matrix cracking affected predominantly the pipe body away from the joint region and the area underneath the partial joint fracture.

A more detailed investigation of the damage associated with the partial joint fracture revealed that cracking occurred within the resin coat located on the outside of the pipe body. The adhesive layer exhibited only minor damage. Most noticeable was the cracking of the adhesive fillet at the coupler end. This fracture was inclined to the pipe surface by an angle of more than 45° but less than 90° . These features can be observed in Fig.5.5.2, where an overview of the partial joint fracture, a schematic of the coupler components, and magnifications of the crack are presented. Images labelled (b) to (d) in Fig.5.5.2 show damage akin to the type described by O'Brien (1998) and Lee (1997), i.e. the formation, collapse and coalescence of polymer ligaments/hackles. This observation suggests that the aforementioned specific type of mode-II fracture damage occurred within the brittle resin coat on the pipe surface, which eventually led to joint separation.

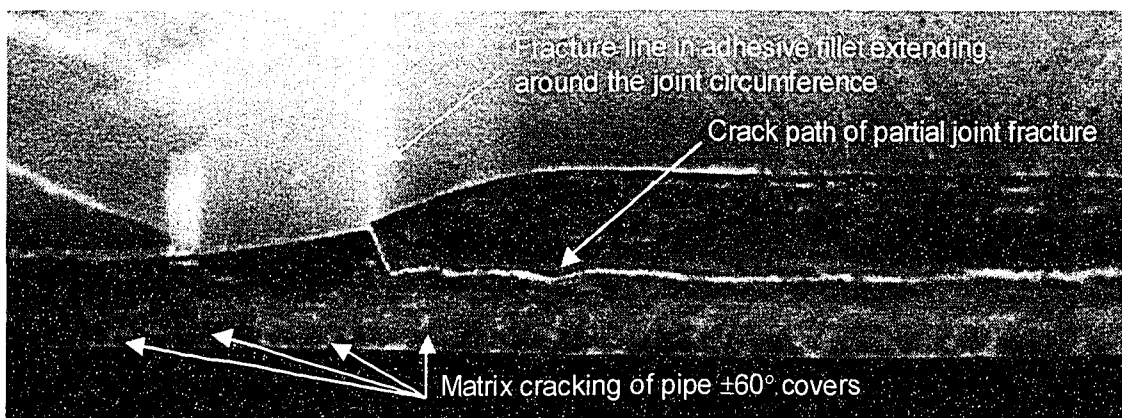


Figure 5.5.1: Photograph of partial joint fracture.

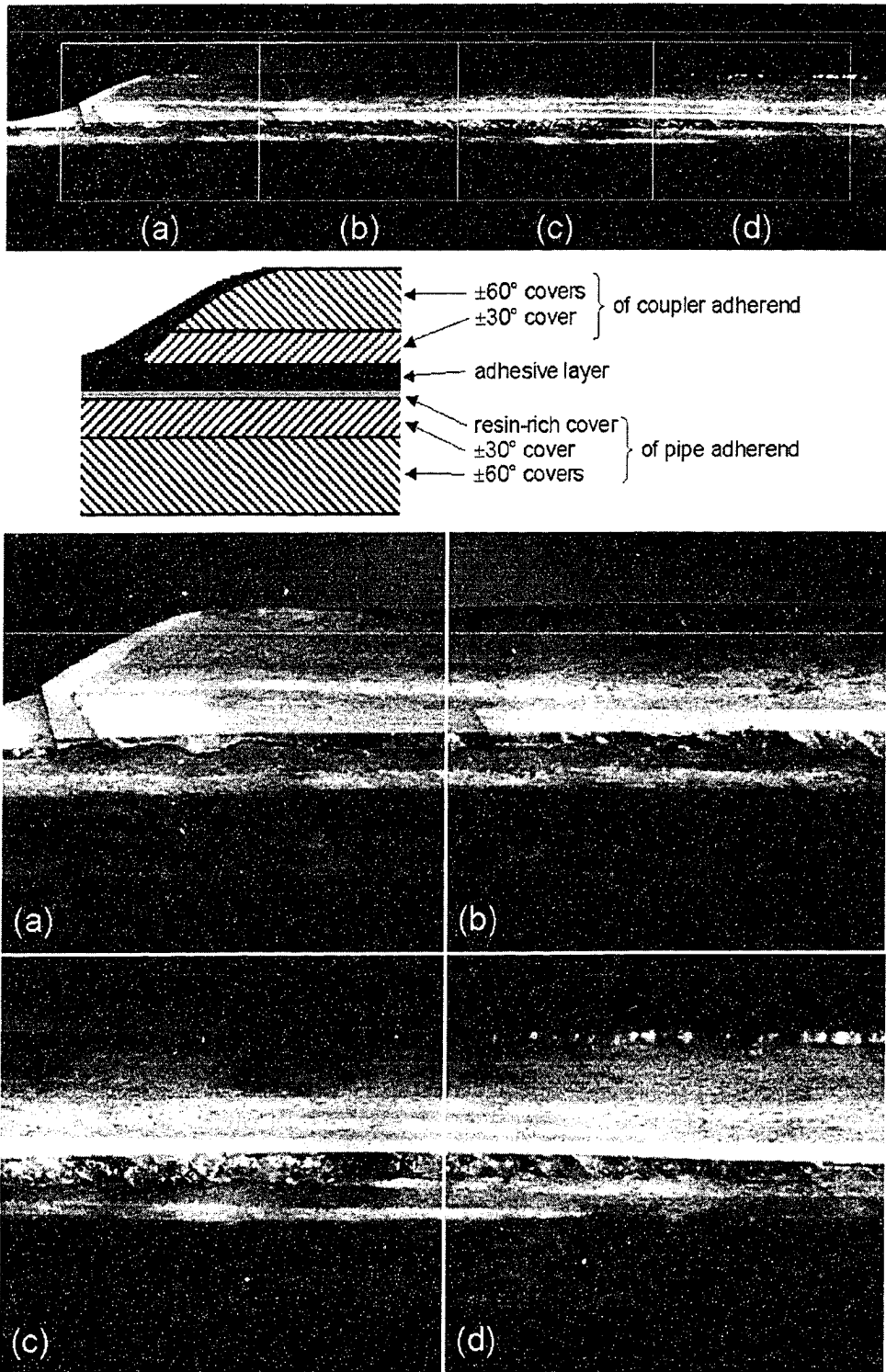


Figure 5.5.2: Photograph, schematic and magnifications of partial joint fracture.

It is reasonable to assume that the area of high stress concentration at the coupler edge is the location of fracture initiation. However, from the above observations the direction of crack growth cannot necessarily be inferred (i.e. whether the crack grew from the coupler end to the inside of the joint, or from within the joint towards the coupler edge). Proof for the above assumption was given by applying a number of strain gauges on the outside of the coupler as shown by the schematic in Fig.5.5.3. These gauges were adjusted to measure axial strain. Since an unloading of the coupler occurs in the wake of the crack, fracturing at a gauge location produces a sudden drop in the strain reading. Results for a specific test under [0H:1A] loading are shown in Fig.5.5.4. In this graph measured strains as well as the global applied axial stress (calculated from force data) were plotted with respect to time. It is evident that crack growth occurred over an extended period of time, i.e. about 30% of the duration of this particular test. Note that the applied load increased linearly with time. Consequently, crack growth occurred for approximately the final 30% of the load application. The sequence of strain reduction at the different gauge locations (i.e. gauge #4 to #1) clearly indicates a fracture progression from the coupler end to the inside of the joint. Note that failure at gauge #4 was preceded by a sudden strain increase recorded by strain gauge #1 (the gauge closest to the centre of the joint). It is assumed that this sudden increase was caused by the fracturing of the bondline in between the mating 15° inside/outside pipe tapers in the joint centre.

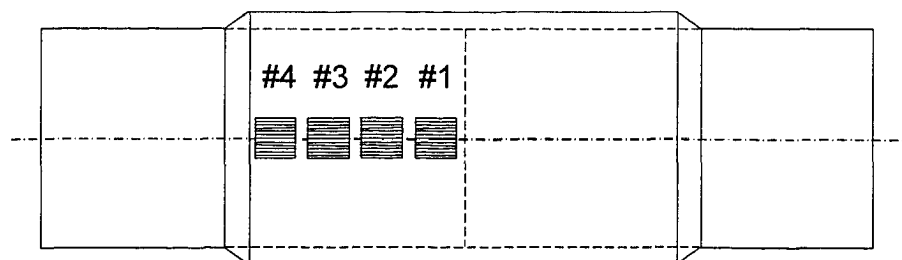


Figure 5.5.3: Schematic of the strain gauge arrangement for the determination of the crack growth direction.

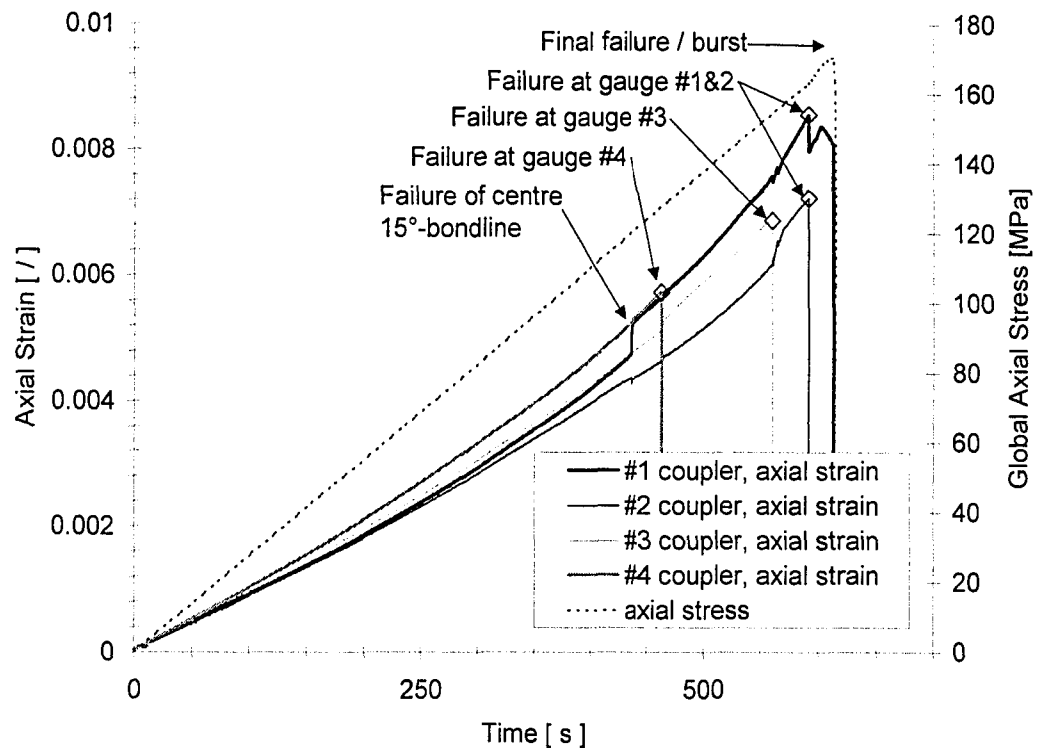


Figure 5.5.4: Global applied axial stress and strain readings from different gauge locations for the determination of the crack growth direction.

Analysis of failure stresses:

Strength data obtained from biaxial testing are delineated by the failure envelope shown in Fig.5.5.5. In general, low data variability was ascertained for specimens tested under the same loading conditions. The highest strength of about 400 MPa was observed under pure hoop loading. Under combined hoop and axial loading functional failure occurred at lower average (hoop) stress values, i.e. 263 MPa and 180 MPa under [3H:1A] and [2H:1A] loading respectively. Under pure axial loading, in which case joint failure was observed, the average axial strength was 176 MPa. Thus, for the present pipe configuration axial stress required for joint failure exceeded the axial strength of the pipe body for all loading configurations except for pure axial loading. Note that with the present experimental setup the determination of axial strength of prototype pipe was not feasible, since the testing of plain pipe sections caused similar fracturing in between the pipe and the metallic end connection.

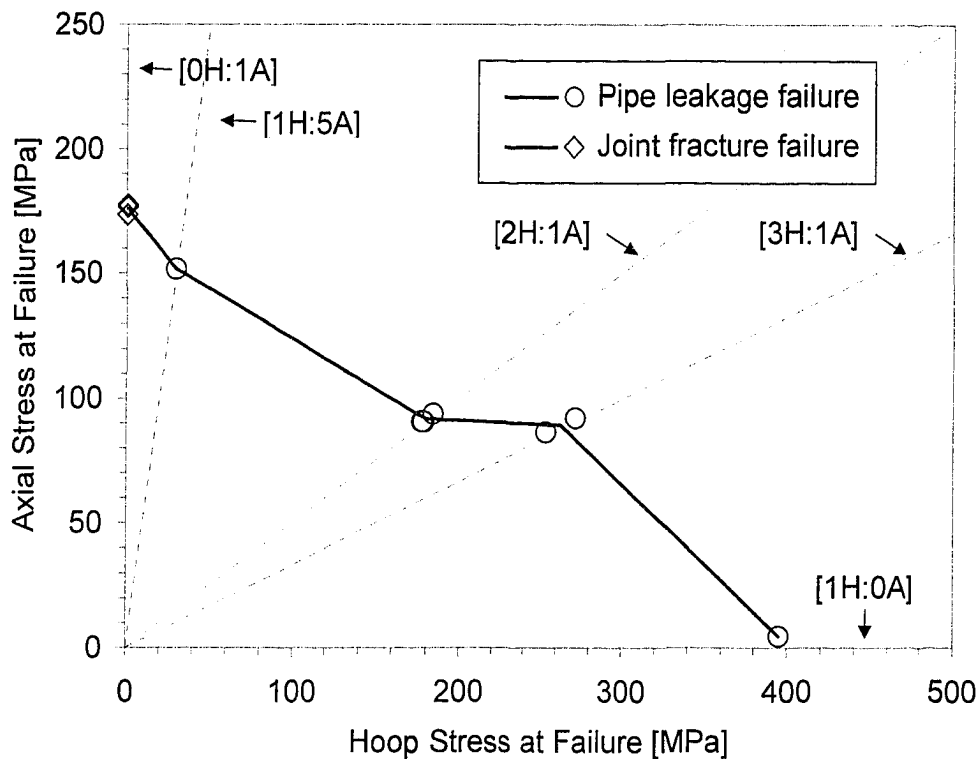


Figure 5.5.5: Experimental biaxial failure envelope of prototype pipe specimens.

It is interesting to note that the failure envelope in Fig.5.5.5 is qualitatively (but not quantitatively) similar to the functional failure envelope presented for $[\pm 60_2, \pm 30]_T$ model specimens (see Chapter 4: Subsection 4.3.2). Thus, the testing of model specimens also produced valuable results for the $30^\circ/60^\circ$ winding angle combination, even though the model lay-up does not represent a perfectly scaled prototype configuration (see Chapter 4: Subsection 4.5.3). However, under pure hoop loading model specimens exhibited burst type failures, whereas leakage was observed for prototype specimens. (An analogous behaviour was observed for model and prototype-scale specimens with pure $\pm 60^\circ$ angle-ply lay-ups, see Chapter 4: Subsection 4.5.1.) This supports the earlier conclusion that testing of prototypes cannot be entirely substituted by model testing.

Note that some coupled pipe structures were retested for axial failure after being subjected to either [3H:1A] or [2H:1A] loading. Stress values at joint failure show that damage to the pipe body associated with functional failure did not influence joint

strength. Hence, there appears to be no interaction between functional and joint failure, and one can conclude that completely different failure mechanisms were responsible for the observed failure modes.

5.6 Modelling of Adhesively Bonded Composite Joints

5.6.1 Statement of Problem

The comprehensive modelling of prototype behaviour requires the incorporation of two fundamentally different failure mechanisms, i.e. joint fracture and the leakage failure of the plain pipe body. Yet, as discussed earlier, no modelling technique is presently available that predicts the latter satisfactorily. As a consequence thereof, the preceding experimental investigation of model specimens as well as of full-scale prototypes was essential. Yet, modelling techniques such as those based on fracture mechanics principles were considered suitable for the investigation of the observed joint failure, i.e. the development of a single dominant crack. For example, similar fracture events (in plate structures) were reported by Ashcroft and co-workers (2001), and Potter et al. (2001), who also presented modelling in subsequent publications (Abdel Wahab et al., 2001; and Guild et al., 2001). Utilising a theoretical approach promises to significantly ease joint optimisation (by reducing experimental work). Moreover, the complex stress/strain field and associated damage make it difficult to separate influences of the various design parameters on purely experimental bases. Hence, a theoretical approach with experimental verification is deemed appropriate to provide a better insight into joint behaviour.

A suitable model had to take the following five joint features into account, which were considered characteristic of the present joint design: (a) joint overlap length, (b) adhesive bondline thickness, (c) coupler lay-up sequence, (d) coupler thickness, and (e) coupler chamfering. These features were subjected to further analyses to investigate their effect on joint performance. Note that the tapering of pipe sections was not included in this investigation, because testing indicated that such a tapering had an insignificant influence on failure. A parametric study on the various joint features was conducted (see

Subsection 5.7.3), in which effects on joint performance were evaluated relative to the employed prototype structure. Since quasi-static loading can best approximate the testing of prototypes, such conditions were assumed in subsequent theoretical investigations. A twofold course of action was chosen to study joint performance and to arrive at an improved joint design. First, the fracture initiation behaviour was analysed, followed by an examination of the fracture progression behaviour. In subsequent sections, analysis techniques for adhesively bonded joints are briefly reviewed, followed by the description of the employed fracture modelling technique.

5.6.2 Review of Modelling Techniques for Adhesively Bonded Joints

A strength-of-materials approach and/or methodologies based on fracture mechanics are usually employed for the modelling and shape optimisation of adhesively bonded (composite) joints. (Information on failure criteria and strength prediction methods for bonded joints can be found in e.g. Tong and Stevens (1999).)

Strength-of-materials approach:

The strength-of-materials approach employs criteria that compare stress/strain data relative to other design configurations, or with material allowables. This comparison is frequently based on the maximum principle stress or strain, or strain energy density values. Inherently, this approach is most suited for the prediction of damage initiation. The strength-of-materials approach is employed to provide damage criteria or optimisation criteria pertaining to the adhesive as well as to the substrates. The examination of the adherends is generally based on the same models and measures used for the damage prediction in laminated fibre composites (e.g. interactive failure criteria). (Respective models and criteria were discussed in Chapter 1: Subsection 1.3.2.) Criteria of the strength-of-materials approach are usually point-based, i.e. damage is assumed to occur at points where material allowables such as stress or strain are exceeded. However, for the analysis of the adhesive also zone-based criteria were proposed by e.g. Clark and McGregor (1993) (i.e. a damage parameter has to exceed a critical value at each point over a certain distance or area for damage to occur).

Various studies on adhesive joint performance employing a strength-of-materials approach have been reported in the technical literature. For example, (a) Lang and Mallick (1998), and (b) Rispler et al. (2000) dealt with the optimisation of adhesive fillet geometries; (c) Gleich et al. (2001) and (d) Kim (2003) investigated the influence of uniform and variable bondline thickness respectively; (e) Semb et al. (1995) examined the effects of coupler thickness, bondline thickness, and the coupler winding angle; and (f) Griffin et al. (1991) provided results on overlap length and bondline thickness. These were also analysed by (g) Yang (2000) along with effects of the coupler winding angle. Finite element analysis techniques were widely utilised in these investigations, i.e. (a-e). As well, analytical methods were presented, i.e. (d, f-g). The frequent use of finite element analyses is attributed to the ability of this method to capture a detailed joint geometry (e.g. adhesive fillets), which is generally not feasible employing analytical techniques.

Although it has been emphasised in the literature that structural adhesives are ductile (see e.g. Hart-Smith, 1987), various researchers have employed linear material models in their analyses (e.g. Adams and Peppiatt, 1977; Lang and Mallick, 1998; and Rispler et al., 2000). Non-linear material models are warranted if behaviour and failure of a real structure is to be predicted based on material data. However, for the purpose of design optimisation and comparison of different joint designs, a simplified linear-elastic approach is generally justified.

In the present study damage initiation behaviour was investigated using a strength-of-materials approach. Since the experimentally observed damage was confined to the adhesive and the resin coat on the pipe surface, an investigation of composite adherend failure was omitted. The initiation of the observed fracturing was considered consistent with a tensile failure caused by (principle) stress locally exceeding material allowables. Hence, the utilisation of a linear elastic analysis and a principle stress criterion were deemed reasonable. In order to enable the use of a single modelling technique for the analysis of each aforementioned joint feature, the investigation was conducted utilising a finite element simulation environment (ANSYS[®], 2002).

Fracture mechanics approach:

As detailed earlier, the testing of prototypes exhibited fracture growth to occur for a considerable part of the applied loading, i.e. 30% of the applied ultimate stress. Thus, it is of interest to conduct an investigation of the crack propagation behaviour. The observed damage is equivalent to a self-similar fracture problem, in which fracture occurs due to an opening mode I, a shearing mode II, or combinations of the two. The use of fracture mechanics is thus considered appropriate for the description of the observed fracture phenomena. By assuming a static crack at various loci along the crack path, valuable information about the crack propagation behaviour can be gathered from fracture parameters. This approach allows for the comparison of various joint geometries without the knowledge of critical material parameters (i.e. the K_c fracture toughness and \mathcal{G}_c fracture energy).

Various fracture criteria are well established for the evaluation of structures with crack initiation sites (i.e. pre-cracks or crack-like flaws). Namely, these are the strain energy release rate (SERR) criterion, the J-integral criterion, the stress intensity criterion and the crack tip opening displacement (CTOD) criterion. (Further information pertaining to fracture mechanics principles in polymers can be found in e.g. Krishnamachari, 1993.) A review of available literature on fracture in composites revealed the frequent use of energy methods, i.e. the former two criteria. In contrast to isotropic materials, where stress intensity criteria were applied extensively, SERR-related methods were found to be particularly convenient for the analysis of composites (O'Brien, 1982). If cracking occurs within a brittle polymer environment (i.e. a material with a small fracture process zone and plasticity effects), a framework of linear elastic fracture mechanics is suited for the analysis, i.e. the use of the strain energy release rate, \mathcal{G} . Corresponding techniques were most frequently employed for the analysis of delamination. Bonded composite structures were also studied employing SERR-related methods, see e.g. Whitcomb and Woo (1993), Pradhan et al. (1994), and Krueger et al. (2000). Since the present experimental work revealed fracture to occur primarily within a brittle polymer material, i.e. the resin coat on the pipe surface, a SERR method was deemed suitable for the investigation.

Moreover, the concentricity of the fracture plane facilitated the use of a two-dimensional axis-symmetric analysis employing mixed-mode I/II energy release rates.

Strictly speaking, the observed mode-II fracture features (hackles) and preceding microcracking are inconsistent with fracture mechanics' assumption of an idealised sliding of two crack planes relative to each other. Based on similar observation some researchers questioned whether mode II fracture energy, \mathcal{G}_{IIc} , constitutes the correct concept for a measure of shear fracture (Lee, 1997; and O'Brien, 1998). Furthermore, in homogenous materials a growing crack typically changes orientation to assume a pure opening mode I. Hence, in these materials the mode I fracture toughness, K_{Ic} , suffices for the description of fracture. In laminated composites and adhesively bonded structures, however, crack growth is commonly confined within resin-rich regions and bondlines respectively. This condition gave rise to the definition of the mode II fracture energy release rate. Owing to these observations Lee (1997) showed that \mathcal{G}_{IIc} is in fact related to \mathcal{G}_{Ic} , among other material properties. However, the controversy about \mathcal{G}_{IIc} is futile when employing mode II fracture energy release rates in conjunction with mixed-mode damage (or optimisation) criteria (O'Brien, 1998), because in such cases the determination of accurate \mathcal{G}_{IIc} values has little influence on the outcome of an investigation.

Various researchers have pointed out two particular SERR methods for their usefulness in conjunction with failure criteria that are highly dependent on the mixed-mode ratio (Raju, 1987; O'Brien, 2001; Krueger, 2002 and 2003). These methods are the virtual crack-closure technique (VCCT) and the crack closure method (CCM). (The latter technique is sometimes also called two-step virtual crack-closure technique.) The VCCT and the CCM are commonly implemented into finite element modelling, since analytical solutions are only available for specific (simple) geometries (e.g. double cantilever beam specimens). Moreover, these techniques do not require knowledge of the singular stress field near the crack tip, which greatly simplifies the analysis (O'Brien, 1982). In the present study, the VCCT was employed in conjunction with the finite element method for the analysis of fracture processes in prototype joints. In the following a discussion is provided on the theoretical background of these methods and their implementation into the current ANSYS® finite element environment.

5.6.3 Fracture Analysis Using the Virtual Crack Closure Technique

Irwin (1958) proposed that the energy released by an infinitesimal crack extension, Δ , from length a to $a + \Delta$, is equal to the work necessary to close the crack to its previous state. Using the notation of Fig.5.6.1 the energy released in the process is given by

$$W = \frac{1}{2} \int_0^{\Delta} \sigma_{\rho}(\Delta - r, 0) \bar{v}(r, \pi) dr + \frac{1}{2} \int_0^{\Delta} \tau_{\xi\rho}(\Delta - r, 0) \bar{u}(r, \pi) dr \quad (5.6.1)$$

where $\bar{u}(r)$ and $\bar{v}(r)$ are the crack opening displacements tangential and normal to the crack plane at distance r behind the crack tip at $a + \Delta$, respectively.

From Eq.(5.6.1) the strain energy release rate is calculated as

$$\mathcal{G} = \lim_{\Delta \rightarrow 0} \frac{W}{\Delta} = \lim_{\Delta \rightarrow 0} \frac{1}{2\Delta} \int_0^{\Delta} \sigma_{\rho}(\Delta - r, 0) \bar{v}(r, \pi) dr + \lim_{\Delta \rightarrow 0} \frac{1}{2\Delta} \int_0^{\Delta} \tau_{\xi\rho}(\Delta - r, 0) \bar{u}(r, \pi) dr \quad (5.6.2)$$

where the first and the second term represent the mode I, \mathcal{G}_I , and mode II, \mathcal{G}_{II} , energy release rates respectively (given in units of N/m, i.e. energy per fracture surface area).

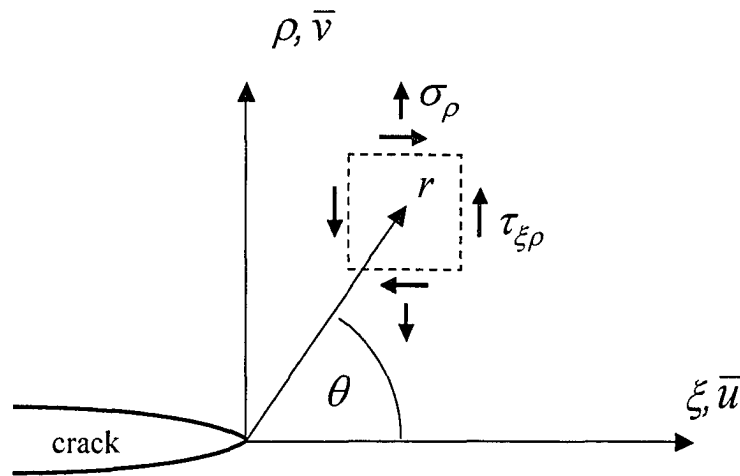


Figure 5.6.1: Local coordinate system and stress components in vicinity of crack tip.

Based on Eq.(5.6.2) Rybicki and Kanninen (1977) presented a procedure for the calculation of energy release rates employing the finite element method. This procedure utilises the product of nodal forces and the difference in nodal displacement to evaluate the energy available for crack extension. A virtual crack extension of one element length, Δ , is assumed. The following equations were derived based on constant element lengths for the element in the wake of the crack and in the front. For 4-noded quadrilateral elements (shown in Fig.5.6.2), the strain energy release rate equations are (given in units of N, i.e. energy per crack length for the 2-dimensional analysis)

$$\mathcal{G}_I = \frac{1}{2\Delta} \{F_{\rho i} (\bar{v}_k - \bar{v}_{k'})\} \quad (5.6.3)$$

$$\mathcal{G}_{II} = \frac{1}{2\Delta} \{F_{\xi i} (\bar{u}_k - \bar{u}_{k'})\} \quad (5.6.4)$$

where $F_{\xi i}$ and $F_{\rho i}$ are the nodal forces (given per unit length) at node i in the directions tangential, ξ , and normal, ρ , to the crack plane respectively, computed from elements I and J . In Eqs.(5.6.3) and (5.6.4) displacements \bar{u}_k and \bar{v}_k in the ξ and ρ directions were obtained from node k respectively.

The total energy release rate \mathcal{G}_T is calculated from the individual mode components as

$$\mathcal{G}_T = \mathcal{G}_I + \mathcal{G}_{II} + \mathcal{G}_{III} \quad (5.6.5)$$

with $\mathcal{G}_{III} = 0$ for the two-dimensional case.

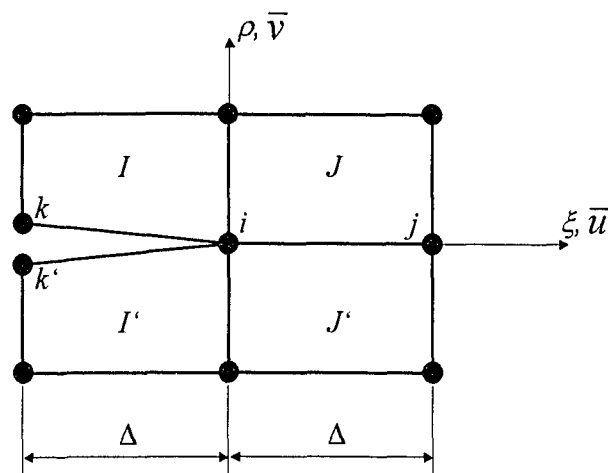


Figure 5.6.2: 4-noded quadrilateral elements at the crack tip.

Due to a small crack extension increment, Δ , it is reasonable to assume that a crack extension from length a to length $a + \Delta$, does not considerably change the conditions at the crack tip. Thus, the displacements in wake of the crack tip (node i) can be approximated by the displacement in the wake of the original crack tip (node k). This led to the formulation of the (one-step) VCCT, in which only one numerical analysis step is required to produce SERR results. To provide more detailed information on the VCCT, the derivation of Eq.(5.6.3) was included in Appendix E as an example.

Provided that a sufficiently fine element mesh was employed, Eqs.(5.6.3) and (5.6.4) were found to yield accurate SERR results (see e.g. Pradhan, 1994). However, an improved accuracy can be achieved using higher order elements. Solutions similar to Eqs.(5.6.3) and (5.6.4) but for higher order elements were derived by Raju (1988). In the present study 2-dimensional axis-symmetric 8-noded quadrilateral solids (as shown in Fig.5.6.3) were utilised for the numerical analysis. The corresponding equations for the energy release rates \mathcal{G}_I and \mathcal{G}_{II} were taken from literature (Raju, 1988; Krueger, 2002):

$$\mathcal{G}_I = \frac{1}{2\Delta} \{F_{\rho i} (\bar{v}_m - \bar{v}_{m'}) + F_{\rho j} (\bar{v}_l - \bar{v}_{l'})\} \tag{5.6.6}$$

$$\mathcal{G}_{II} = \frac{1}{2\Delta} \{F_{\xi i} (\bar{u}_m - \bar{u}_{m'}) + F_{\xi j} (\bar{u}_l - \bar{u}_{l'})\} \tag{5.6.7}$$

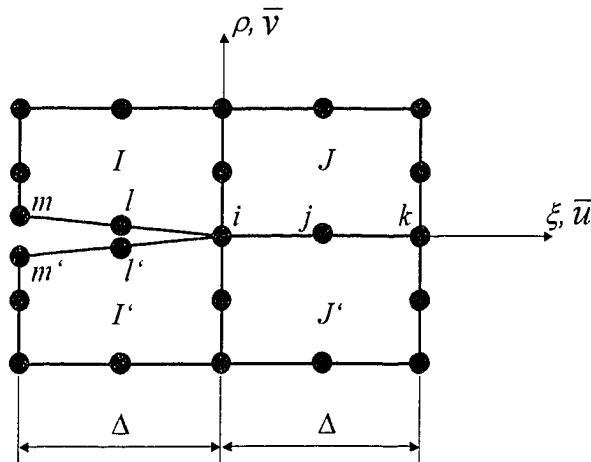


Figure 5.6.3: 8-noded parabolic elements at the crack tip.

Raju (1988) confirmed that Eqs.(5.6.6) and (5.6.7) are also applicable for triangular parabolic elements. Note that some researchers also proposed the use of quarter-point elements to model the $(r)^{-1/2}$ stress field singularity at the crack tip (Raju, 1988; Sethuraman and Maiti, 1988). This type of elements was employed particularly for the computation of stress intensity factors, K . However, Krueger (2002) pointed out that the VCCT as proposed by Rybicki and Kanninen (1977) does not necessitate such elements. The review of available research showed that for the most part singularity elements were not utilised. This was attributed to additional difficulties involving meshing and the implementation of a crack progression scheme. Hence, the present analysis was limited to conventional 8-noded quadrilateral elements.

Raju (1988) based the derivation of Eqs.(5.6.6) and (5.6.7) on a parabolic element shape function defined along nodes i - j - k . This function is given by

$$\bar{v}(\xi) = \left(1 - \frac{3\xi}{\Delta} + \frac{2\xi^2}{\Delta^2}\right) \bar{v}_i + \left(4\frac{\xi}{\Delta} - 4\frac{\xi^2}{\Delta^2}\right) \bar{v}_j + \left(-\frac{\xi}{\Delta} + 2\frac{\xi^2}{\Delta^2}\right) \bar{v}_k \quad (5.6.8)$$

In the second part of Appendix E it was shown that Eq.(5.6.8) and the shape function for the applied 8-noded quadrilateral solids (PLANE82), given by Eq.(5.6.9), are equivalent. Equation (5.6.9) was taken from the documentation of the finite elements software used in this investigation (ANSYS®, 2002).

$$\begin{aligned} \bar{v}(s, t) = & \frac{1}{4} [\bar{v}_i (1-s)(1-t)(-s-t-1) + \bar{v}_k (1+s)(1-t)(s-t-1)] \\ & + \bar{v}_m (1+s)(1+t)(s+t-1) + \bar{v}_o (1-s)(1+t)(-s+t-1)] \\ & + \frac{1}{2} [\bar{v}_j (1-s^2)(1-t) + \bar{v}_l (1+s)(1-t^2) + \bar{v}_n (1-s^2)(1+t) + \bar{v}_p (1-s)(1-t^2)] \end{aligned} \quad (5.6.9)$$

where coordinates s and t are normalized, going from -1.0 on one side of the element to +1.0 on the other.

5.7 Parametric Study for Joint Design Optimisation

5.7.1 Description of Current Numerical Model

Finite element model and meshing:

Two basic finite element models were developed for the examination of prototype specimens with $[\pm 60_3, \pm 30]_T$ pipe sections and $[\pm 30, \pm 60_2]_T$ coupler sleeves: one for the stress analysis of undamaged structures, and another for the analysis of fracture within the specimen joint region. Specimens were modelled according to the dimensions provided in Chapter 3. The thickness of the various composite layers was computed using information about the fibre volume fraction (see Table 3.2.2), and the procedure described in Chapter 2: Subsection 2.2.5. The thin resin coat on the outside of the pipe was included in the model as well, assuming a constant thickness of 0.2 mm. A summary of geometric parameters for the baseline finite element model is given in Table 5.7.1.

Due to the axis-symmetric specimen geometry and loading conditions, modelling was limited to a 2-dimensional cross-section. Since specimens were also symmetric about their centre-plane perpendicular the axis of rotation, only a quarter section of the specimen was analysed. Owing to the discussion in Subsection 5.6.1 the tapering of pipe ends was not explicitly modelled. However, the specimen behaviour before and after fracturing of the bondline in between the tapered pipe ends was approximated using appropriate boundary conditions (discussed below). In Fig.5.7.1 a schematic of the model is given (the full length of the pipe section was not shown for the sake of clarity).

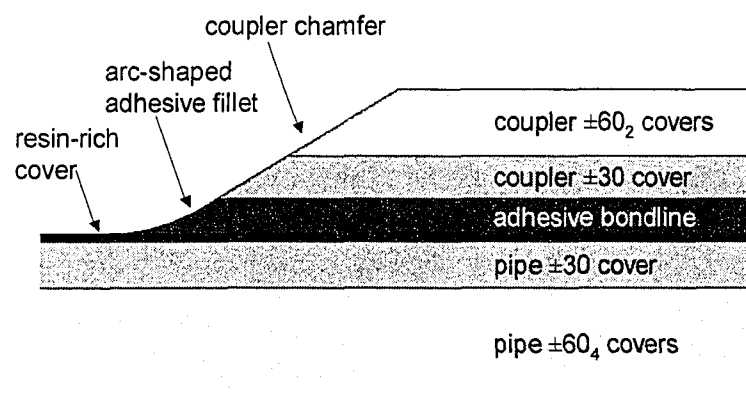


Figure 5.7.1: Schematic of model for finite element analysis.

Table 5.7.1: Geometry parameters for baseline finite element model.

<i>Pipe section:</i>	<i>length</i>	762.00 mm
	<i>inside diameter</i>	101.60 mm
	<i>wall thickness</i>	4.63 mm
<i>Thickness of resin layer on pipe surface:</i>		0.2 mm
<i>Thickness of adhesive layer:</i>		1.01 mm
<i>Length of arc-shaped adhesive fillet:</i>		2.78 mm
<i>Coupler sleeve:</i>	<i>length</i>	155.58 mm
	<i>wall thickness</i>	3.64 mm
	<i>chamfer angle</i>	30°
<i>Length of end connections:</i>		203.2 mm

Axis-symmetric 8-noded quadrilateral solids (PLANE82) were employed for the modelling. The finite element grids were produced using a mapped meshing procedure. Three and two elements were used in the through-thickness direction to model the adhesive layer and the thin resin coat (on the pipe surface) respectively. For the analysis of the undamaged structure, free meshing was required to adequately model the arc-shaped adhesive fillet and the upper corner of the coupler chamfer. The mesh was refined in the vicinity of the coupler edge; hence, the element size increases towards the specimen ends. Meshed models consisted of about 9000 elements depending on geometry features such as the chamfer angle. (Note that a mesh sensitivity analysis was conducted, which is presented in Subsection 5.7.2.) Details of the finite element grids within the joint vicinity are presented in Figs.5.7.2 and 5.7.3 for the stress and fracture analyses respectively. Note that despite certain differences both models are closely related geometrically, dimensionally and in terms of the applied finite element mesh.

The fracture behaviour was investigated employing a pre-cracked model geometry, which was based on the crack path observed in experiments (see Fig.5.5.1). As shown in Fig.5.7.3 this model features a discrete crack at the coupler edge that extends through the adhesive layer into the centre of the matrix-rich zone on the pipe surface. Since the adhesive fillet becomes separated by the pre-crack from the rest of the adhesive bondline,

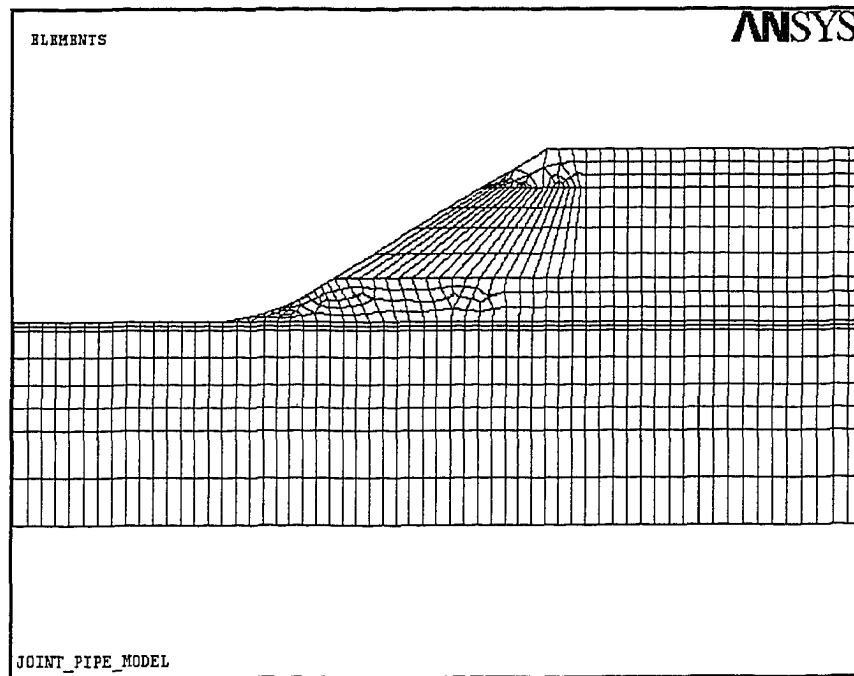


Figure 5.7.2: Finite element mesh within the joint vicinity for the stress analysis of undamaged specimens.

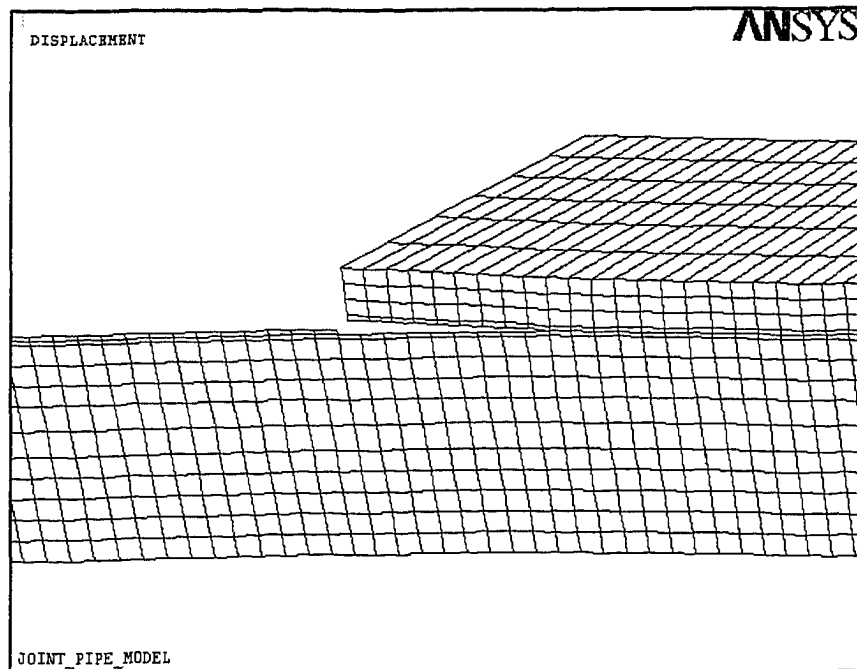


Figure 5.7.3: Finite element mesh within the joint vicinity for the fracture analysis in cracked specimens (deformed geometry and scaled displacements shown).

the fillet was not expected to have any appreciable influence on the crack growth behaviour. Thus, the fillet was not modelled in this case. Starting from the pre-crack, fracture growth was simulated according to the following procedure. Nodes from adjacent elements along the crack path were initially coupled by their translational degrees-of-freedom. A crack extension into the joint within the resin coat was then modelled by subsequently releasing constraints at the paired nodes. Nodes along the crack path were positioned equidistantly in order to comply with requirements of the VCCT (i.e. element lengths in front and behind the crack tip remain constant).

In some cases it might be necessary to link the upper and lower fracture planes using contact elements (e.g. TARGET169 and CONTACT172 elements) so as to prevent any irregular surface penetration. However, the use of contact elements entails a significant penalty regarding computational performance. Alternatively, the deformation behaviour was monitored using the ANSYS® Graphical User Interface and exaggerated displacement scaling. For the present test case, i.e. pure axial loading, irregular surface penetration could be ruled out. Nonetheless, for loading scenarios not investigated here, i.e. loadings involving internal pressurisation, the use of contact elements may be required for fracture analyses.

Boundary conditions and loading:

The specimen centre-plane symmetry (normal to the axis of rotation) was realised by imposing axial constraints on all nodes in this plane. A possible pre-cracking of the bondline in between pipe sections was simulated by removing respective constraints from all nodes belonging to the pipe structure, i.e. constraints on the coupler and adhesive were maintained (shown schematically by white in contrast to grey coloured constraint symbols in Fig.5.7.4). The specimen end-tabs were assumed to constrain radial displacement over a certain zone at the specimen ends. Thus, corresponding nodes were restricted in their radial degree-of-freedom. Note that a rigid end connection should also require constraints opposing relative axial displacement between the nodes. However, such a condition was considered redundant for the current study of joint behaviour. A schematic of the nodal degree-of-freedom constraints and loadings is given in Fig.5.7.4.

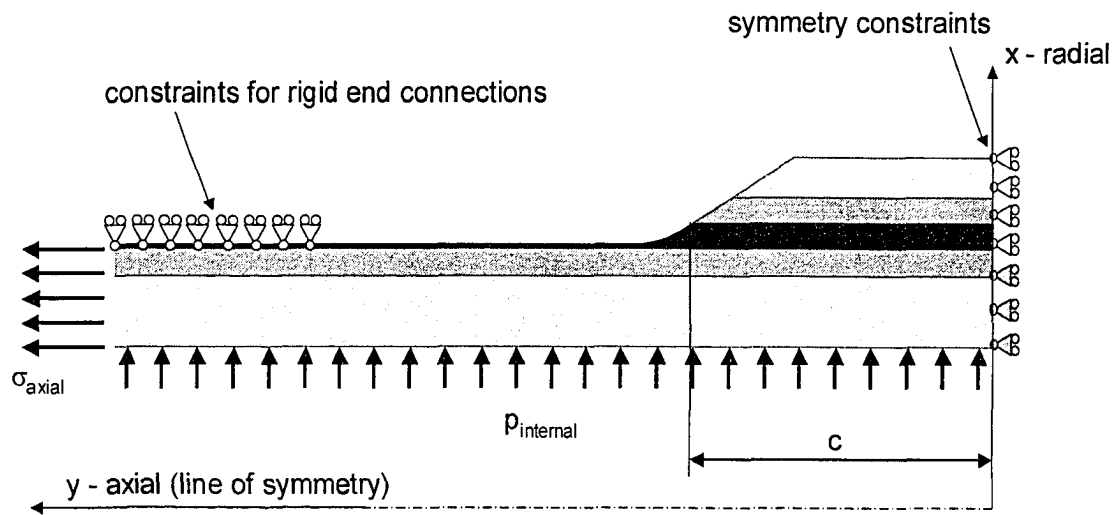


Figure 5.7.4: Schematic of finite element model showing coordinate system, loadings and constraint boundary conditions.

Note that the ANSYS[®] finite element platform requires a different coordinate convention for 2-dimensional axis-symmetric analyses than for full 3-dimensional models. For the axis-symmetric case coordinates x , y , z correspond to the radial, axial and hoop direction respectively.

A uniform tensile stress, σ_{axial} , was imposed on the end of the finite element pipe model. Since linear analyses were conducted, stress data taken from the model were usually normalised with respect to the average pipe stress, resulting in dimensionless (normalised) stress parameters. The finite element code also provides for the application of internal pressure, $p_{internal}$, which was only employed for model verification purposes (see the following chapter).

Material system:

A meso-scale approach was pursued for the modelling of the specimen adherends, i.e. the $\pm 60^\circ$ and $\pm 30^\circ$ fibre architectures were modelled as individual homogeneous orthotropic entities (see Fig.5.7.1). Since the $\pm 60^\circ$ and $\pm 30^\circ$ covers of coupler and pipe differed in fibre volume fraction (see Table 3.2.2), a separate set of properties was computed for each adherend using the procedures outlined in Chapter 2:

Subsection 2.2.4. The adhesive and the thin resin coat on the outside of the pipe were treated as isotropic materials. Hence, it was necessary to supply six sets of materials data to the finite element code. Corresponding data are given in Table 5.7.2.

5.7.2 Validation of Current Numerical Model

Expectations towards a suitable finite element model were to reproduce stress and deformation characteristics of the actual structure with reasonable accuracy. To verify that a model indeed delivers such results, two possible approaches are generally chosen: (a) Results from an additional model with a refined mesh and/or a more detailed geometry are employed to evaluate the accuracy of the initial model; and (b) results in terms of deformation are compared to actual measurements (i.e. strain gauge readings).

Table 5.7.2: Material data used in the finite element modelling of prototype specimens.

<i>Orthotropic material data⁽¹⁾: 60° covers {30° covers}</i>	<i>[±60₃, ±30]_T pipe</i>	<i>[±30, ±60₂]_T coupler</i>
<i>(Radial) Young's modulus E_{xx}</i>	<i>15.29 GPa</i>	<i>16.65 GPa</i>
<i>(Axial) Young's modulus E_{yy}</i>	<i>13.07 {26.87} GPa</i>	<i>14.55 {29.08} GPa</i>
<i>(Hoop) Young's modulus E_{zz}</i>	<i>26.87 {13.07} GPa</i>	<i>29.08 {14.55} GPa</i>
<i>Shear modulus G_{xy}</i>	<i>5.76 {5.0} GPa</i>	<i>6.38 {5.66} GPa</i>
<i>Shear modulus G_{xz}</i>	<i>5.0 {5.76} GPa</i>	<i>5.66 {6.38} GPa</i>
<i>Shear modulus G_{yz}</i>	<i>12.12 GPa</i>	<i>12.9 GPa</i>
<i>(Minor) Poisson's ratio⁽²⁾ ν_{yx}</i>	<i>0.176 {0.137}</i>	<i>0.171 {0.143}</i>
<i>(Minor) Poisson's ratio⁽²⁾ ν_{zx}</i>	<i>0.137 {0.176}</i>	<i>0.143 {0.171}</i>
<i>(Minor) Poisson's ratio⁽²⁾ ν_{zy}</i>	<i>0.697 {0.339}</i>	<i>0.663 {0.332}</i>
<i>Isotropic material data:</i>	<i>Polymer matrix⁽¹⁾</i>	<i>Adhesive⁽⁴⁾</i>
<i>Young's modulus</i>	<i>4.8 GPa</i>	<i>3.4 GPa</i>
<i>Shear modulus</i>	<i>1.8 GPa</i>	<i>1.2 GPa</i>
<i>Major Poisson's ratio⁽³⁾</i>	<i>0.34</i>	<i>0.42</i>

⁽¹⁾ Material data of constituents are given in Table 4.1.2.

⁽²⁾ Entered in ANSYS[®] code as minor Poisson's ratios using NUXY, NUYZ, NUXZ commands.

⁽³⁾ Entered in ANSYS[®] code as major Poisson's ratios using PRXY, PRYZ, PRXZ commands.

⁽⁴⁾ Data for DP-460 adhesive were taken from 3M (2002).

Both methods inherently have certain advantages and disadvantages. For example, a refined mesh and/or more detailed model may become too expensive computationally or even impossible to solve, depending on the computer platform and software configuration. And, in the latter approach, the ability to obtain information about critical parameters (such as stress concentrations) from the actual structure is generally limited. Because of these difficulties and associated uncertainties the subsequent verification of the present model employed both approaches, i.e. a comparison with actual measurements as well as a second numerical model with a refined mesh. In addition to the above, also the effect of the element type, i.e. 4-noded and 8-noded solids, on strain energy release rates was investigated.

Sensitivity analysis of the finite element model:

In order to investigate whether the chosen finite element mesh is properly sized and consistent results are generated, a sensitivity analysis was performed. An appreciable mesh refinement was achieved by reducing prescribed element sizes, i.e. the dominant part of the elements was effectively subdivided into four (see Fig.5.7.5). (The refined mesh consisted of 27,896 elements compared to 8,994 elements of the unrefined mesh.)

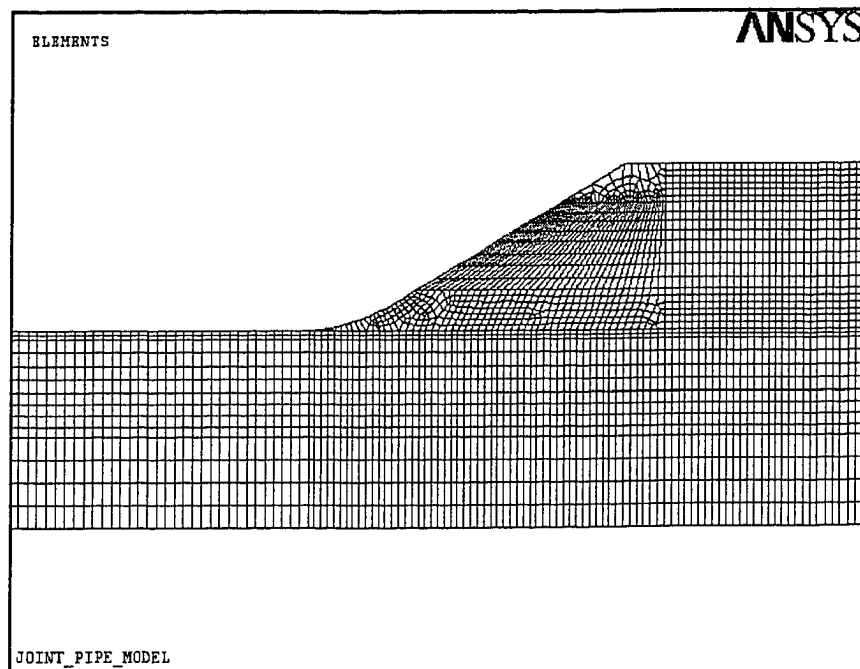


Figure 5.7.5: Refined finite element mesh employed for sensitivity analysis.

A comparison between results from both finite element grids is presented in Figs.5.7.6 and 5.7.7, where peel and shear stresses for a [2H:1A] loading are shown on the left and right-hand-side respectively. Data were taken within the joint region along straight paths at the centre of the resin coat on the pipe surface and at the adhesive/coupler interface within the bondline respectively. Abscissa values and stress data (ordinate axes) were normalised with respect to the coupler overlap length, c , and the average pipe hoop stress, σ_{hoop} , respectively. A sharp rise of stress values was observed in the vicinity of the coupler edge, $y/c = 1$. To make the various curves more distinguishable, abscissa values were scaled according to $\frac{y}{c} 1000^{(y/c-1)}$. This non-linear axis scaling resulted in an expansion of the data points in the proximity to the coupler edge, i.e. y/c values close to and greater than 1.

From the plots in Fig.5.7.6 it can be observed that the results for the two levels of mesh refinement are virtually indistinguishable. Even stress concentrations at the coupler edge were fully captured by the initial, coarser finite element grid. Nevertheless, close examination of the data in Fig.5.7.7 revealed differences between the peak peel and shear stresses of the fine and the coarse mesh respectively. Peak peel and shear stresses for the fine mesh were 18.4% and 1.2% greater than for the coarse mesh correspondingly.

Other researchers have also reported that peak stress values in close proximity to free surfaces are highly dependent on the mesh refinement (Gleich et al., 2001). In order to overcome this mesh dependency it was suggested to select alternative locations for the determination of stress parameters. For example, Gleich et al. (2001) suggested selecting the third node point along the chosen path away from the singularity location. Alternatively, the present parametric study was based on stress data extracted along paths (located in the vicinity of the adhesive bondline) that are free of stress singularities, i.e. paths that do not intersect free surfaces. As shown above the initial finite element model provided a sufficiently refined mesh for such an approach (see Fig.5.7.6). Nonetheless, for the investigation of each joint configuration also paths intersecting free surfaces were included initially. This was to ensure that for a variety of path locations similar trends could be observed.

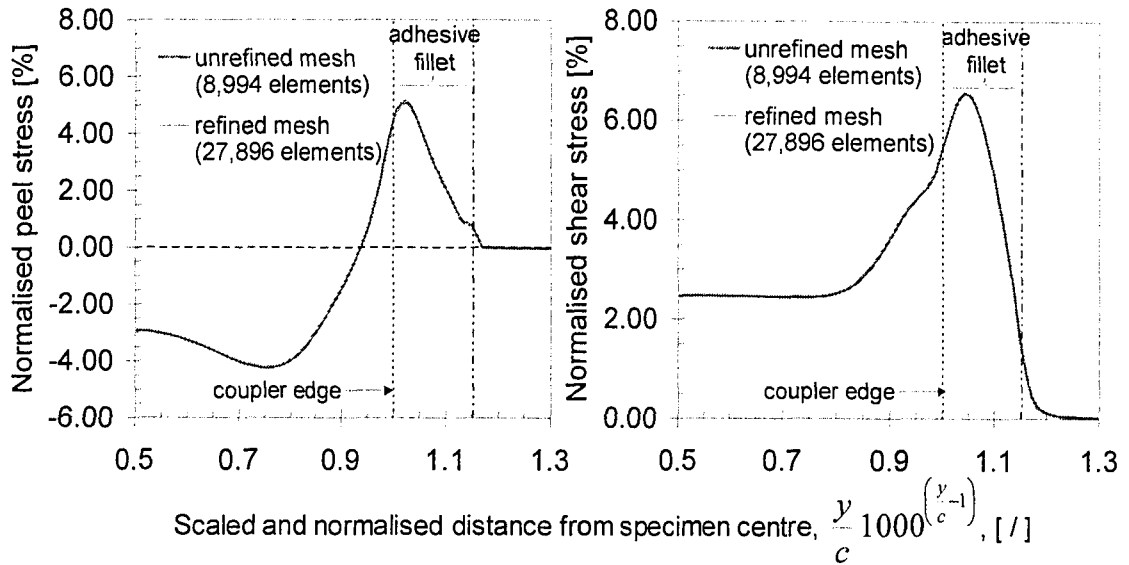


Figure 5.7.6: Comparison between peel (left) and shear (right) stress data for a [2H:1A] loading case, from a refined and unrefined finite element mesh. Stress data originate from within the joint region along a path at the centre of the pipe surface resin coat. Stress data were normalised with respect to the average pipe hoop stress, σ_{hoop} .

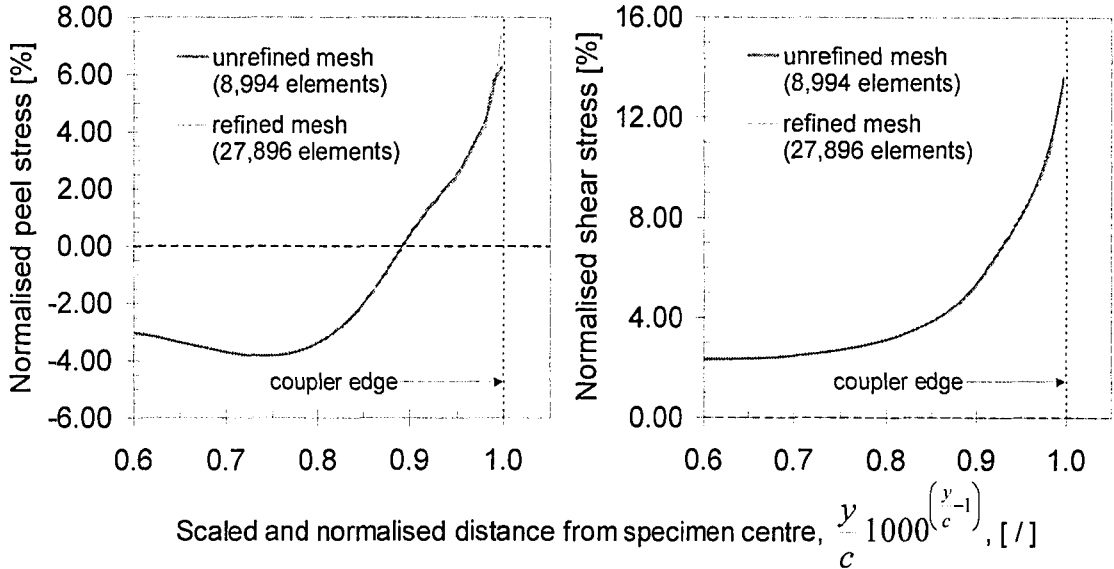


Figure 5.7.7: Comparison between peel (left) and shear (right) stress data for a [2H:1A] loading case, from a refined and unrefined finite element mesh. Stress data originate from along a path at the adhesive/coupler interface within the bondline. Stress data were normalised with respect to the average pipe hoop stress, σ_{hoop} .

Effect of element type on fracture analysis:

Whitcomb and Woo (1993) investigated the convergence of strain energy release rates for single lap tubular joints under tension modelled with 4-noded and 8-noded axis-symmetric quadrilateral elements. It was shown that convergence was achieved with fewer elements when higher-order elements were used. Due to this fact the 8-noded elements were favoured for the present fracture analysis. From Whitcomb and Woo's work it can also be deduced that an adequate mesh refinement is obtained when results from both element types converge to the same solution. Thus, for the current prototype specimen model two solutions were computed for an axial loading of 100 MPa that employed 4-noded and 8-noded axis-symmetric quadrilateral elements correspondingly. (Note that 100 MPa axial load were employed for all subsequent fracture analyses, if not stated otherwise.) Results are presented in Fig.5.7.8, where strain energy release rates for both element types were plotted over the normalised crack length (the crack length was extended to half of the coupler overlap length). It can be observed that the difference

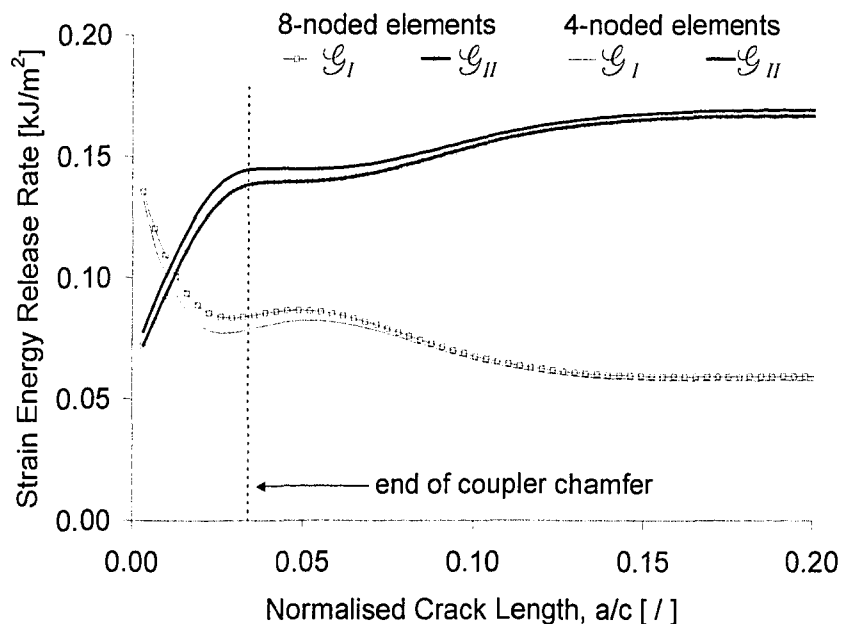


Figure 5.7.8: Comparison between strain energy release rate values from analyses with 4-noded and 8-noded axis-symmetric quadrilateral elements. For the finite element analyses 100 MPa axial load and boundary conditions were applied according to the schematic shown in Fig.5.7.4.

between each pair of curves is indeed small (i.e. a maximum (average) difference of 8.5% (2.1%) and 8.3% (3.4%) for \mathcal{G}_I and \mathcal{G}_{II} respectively). Thus, it was concluded that an adequately refined mesh was chosen for the analysis.

Although it is not the aim of the present fracture analyses to predict failure in terms of absolute values, it is of interest to compare the obtained SERR values with critical parameters from literature. In the analysis a maximum total SERR value, $\mathcal{G}_T = \mathcal{G}_I + \mathcal{G}_{II}$, of 0.228 kJ/m^2 was computed. Since the axial stress applied for the modelling, i.e. 100 MPa, was approximately the load level at which failure initiation was observed experimentally, computed SERR values should, to some extent, approximate critical material parameters. Unfortunately, data for the utilised material system were not available. Alternatively, the above SERR value was compared with related material data. For example, fracture energies \mathcal{G}_c for neat epoxy resins were described to range from 0.1 kJ/m^2 to 0.3 kJ/m^2 (Ashby and Jones, 1980). Swanson (1996) provided examples for mode I fracture energies, \mathcal{G}_{Ic} , of E-glass/epoxy composites, i.e. 0.207 kJ/m^2 and 0.227 kJ/m^2 . Values for mode II fracture are known to be generally higher than the mode I parameters, i.e. they represent an upper bound for a critical SERR envelope. However, \mathcal{G}_{IIc} values remain of the same order of magnitude; see Lee (1997), who proposed a relationship between \mathcal{G}_{IIc} and \mathcal{G}_{Ic} for the present matrix failure mode (microcracks and hackles). From this brief review of fracture parameters it can be deduced that the computed SERR values are of reasonable magnitude.

Comparison between numerical and experimental results:

In the following, strain gauge readings taken at the centre of the pipe gauge section are compared with results from the numerical simulation. Experimental data were obtained from altogether nine specimens (equipped with one or two strain gauges), which were tested at three different loading ratios, i.e. [3H:1A] (two specimens), [2H:1A] (three specimens) and [1H:2A] (one specimen). Average data points and error bars are presented in Fig.5.7.9, where also computed strain as well as stress distributions across the pipe wall are shown. (The wall thickness was measured from the inside outwards).

Stress and strain distributions were included for completeness, and to enable a discussion whether the numerical simulation yielded physically rational results.

The integrity and continuity of the structure necessitates a continuous strain distribution across the thickness of the pipe wall. Accurately, the numerical simulation predicted such behaviour, which can be observed in the graphs shown on the right-hand-side of Fig.5.7.9. Due to the different stiffness of the various layers, discontinuous stress distributions are noted (left-hand-side of Fig.5.7.9). Moreover, for the [3H:1A] and [2H:1A] loadings the highest stresses are discernible in layers having a $\pm 60^\circ$ fibre orientation, i.e. the inside layers. The opposite can be observed for the [1H:2A] stress ratio, where stresses reach their maximum in the $\pm 30^\circ$ layers. As predicted by the simulation stresses in the circumferential direction necessarily reach a maximum on the inside of the pipe wall for the hoop-dominated loading scenarios, i.e. the [3H:1A] and [2H:1A] ratios. On the outside of the pipe any load-carrying contribution of the resin coat is shown to be negligible. Clearly, the portrayed behaviour was to be expected, and hence, strong indication was given that the numerical model provides a quantitatively good approximation of the structure's actual behaviour.

In terms of absolute values good agreement between test results and simulation could be ascertained as well. Note that test data were taken at load levels within in the elastic range of the material. As shown in the graphs on the right-hand-side of Fig.5.7.9 the numerical model achieved a reasonably accurate prediction of the experimental strain data. Particularly the dominant strain components were predicted with good precision, whereas the simulation underestimated to some extent, the lesser strain components. The reason for this behaviour is unknown, however, may be rooted in the initial assumptions made with regards to constituent material properties (see Chapter 4: Section 4.1) and/or the micromechanical material modelling techniques (see Chapter 2: Subsection 2.2.4).

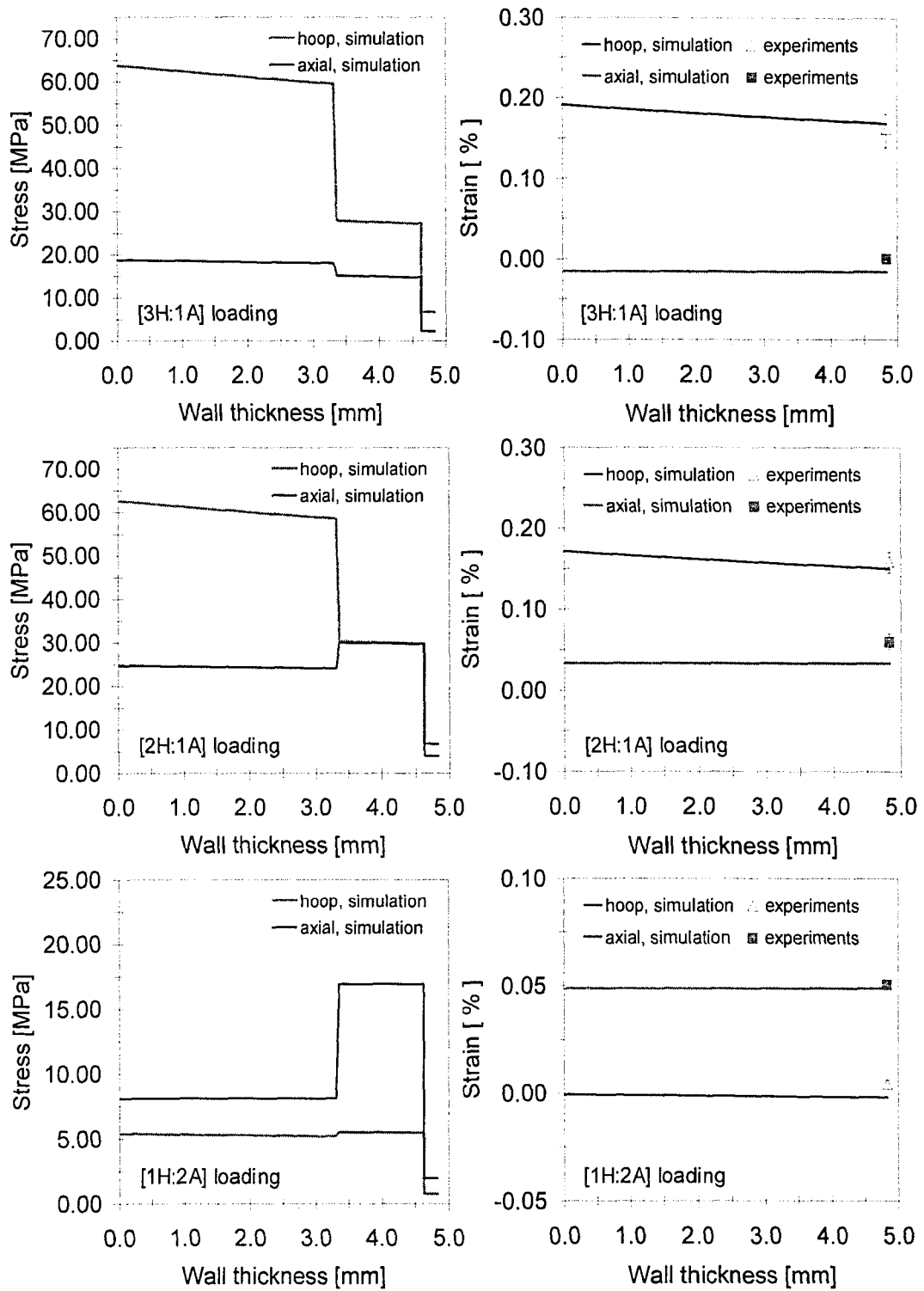


Figure 5.7.9: Through-wall stress (left) and strain (right) distributions from numerical analyses, and strain data from experiments, taken at the gauge section centre of the plain pipe body. Top, centre and bottom graphs show data for 50MPa/16.6MPa, 50MPa/25MPa and 5.15MPa/10.3MPa stress ratios respectively.

5.7.3 Parametric Study

After confirming that the numerical models yielded sensible results with reasonable accuracy the aforementioned characteristic geometry features were investigated. Corresponding results are presented and discussed in the following.

Effect of joint overlap length:

For the investigation of coupling length effects a pre-crack was assumed to exist in between the ends of joined pipe sections (for details on the corresponding boundary conditions see Subsection 5.7.1). Results for models with and without centre pre-crack are presented in Fig.5.7.10, where shear stress distributions located within the resin coat on the pipe surface are depicted. (Note that, once more, stress values and the distance from the centre of the joint, y , were normalised with respect to the average applied axial pipe stress, σ_{axial} , (as shown in Fig.5.7.4) and the coupler overlap length, c , respectively). It can be observed that different results were computed for the two models for the joint centre region (i.e. $y < c/2$). The model with centre pre-crack exhibited a shear stress distribution that almost mirrored stresses found at the coupler edge, whereas for the model without pre-crack shear stresses were absent in this region. Note that as a consequence of the centre pre-crack a stress singularity was present as well. But, since experiments revealed fracture to initiate at the coupler edge, the exact distribution and magnitude of stresses in the joint centre are of little relevance to this investigation. For this reason the centre pre-crack in its present form and the associated stress field approximation were considered adequate for the analysis. Moreover, it is reasonable to consider a joint has failed after a crack has exceeded half of the overlap distance. This assumption is supported by experimental evidence discussed in Section 5.5. As shown in Fig.5.5.4 fracture progressed rapidly leading to final failure as soon as the crack tip went beyond the midsection of the overlap. (In Fig.5.5.4, failure at strain gauge location #2 and #1 occurred in short succession as soon as the crack grew beyond gauge #3.) Thus, only half the coupling distance nearest to the coupler edge was considered for subsequent investigations.

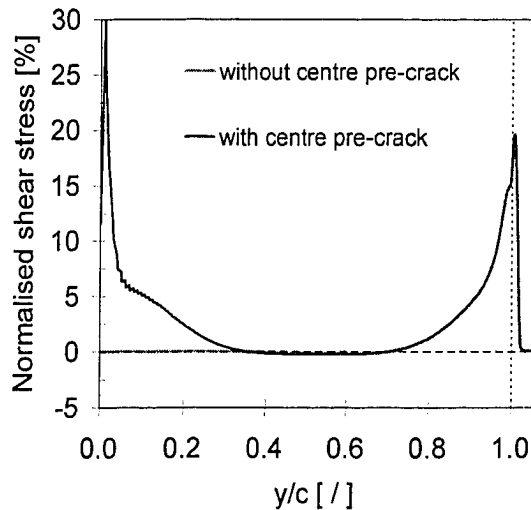


Figure 5.7.10: Comparison of shear stresses between models with and without centre pre-crack for pure axial loading. Stress data originates from within the joint region along a path at the centre of the pipe surface resin coat. Stress data were normalised with respect to the average pipe axial stress, σ_{axial} .

As shown in Fig.5.7.10, shear stresses decreased towards the middle of the coupling length, c . As a result, shear stresses for the model with centre pre-crack were negligible in the midsection of the overlap for approximately 30% of the overlap length. Consequently, this area does not contribute to any axial load transfer. This indicates that the coupler length of prototype specimens was indeed chosen conservatively.

Figures 5.7.11 to 5.7.15 address the question to what extent the overlap length could be reduced without increasing damage susceptibility. For the original baseline coupling distance (approximately 3 times the pipe diameter), and 25% and 50% length reductions, peel, shear, and maximum principle stresses within the pipe surface resin coat are shown on the left- and right-hand-side of Fig.5.7.11, and in Fig.5.7.12 respectively. It is noted that the magnitude of peak stresses at the coupler edge are not appreciably affected by the overlap distance. In fact, peel and maximum principle stress distributions remained virtually identical for each length variation. Hence, any influence of the investigated overlap geometries on damage initiation was considered insignificant. (For information, a

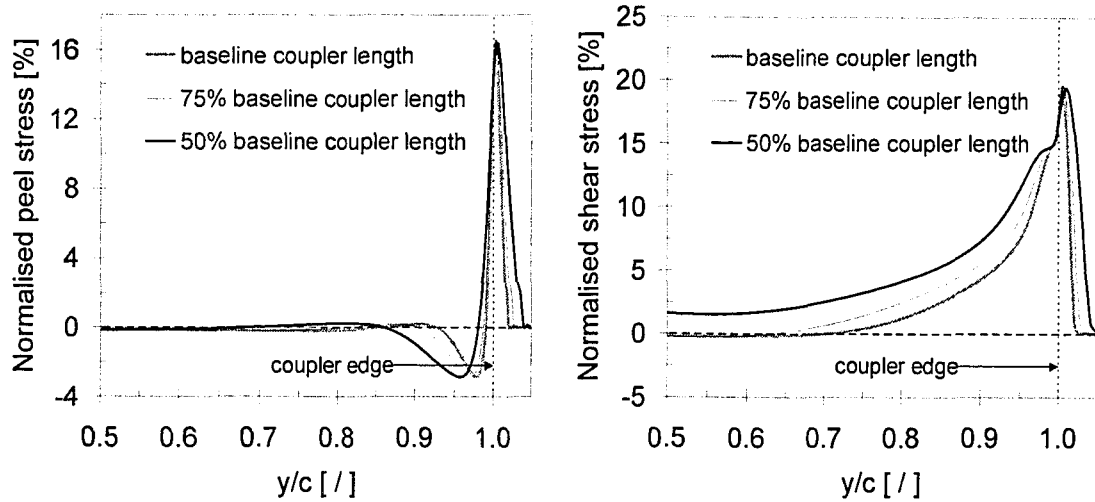


Figure 5.7.11: Comparison of peel and shear stresses within the centre of the pipe surface resin coat between models with baseline coupling distance, and those with 25% and 50% length reductions. Stress data were normalised with respect to the average pipe axial stress, σ_{axial} .

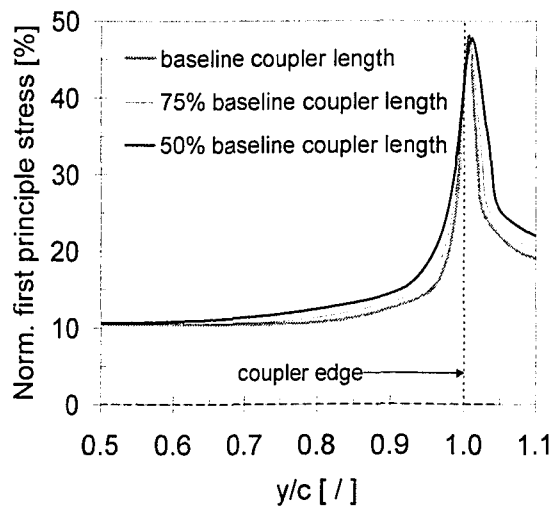


Figure 5.7.12: Comparison of maximum principle stresses within the centre of the pipe surface resin coat between models with baseline coupling distance, and those with 25% and 50% length reductions. Stress data were normalised with respect to the average pipe axial stress, σ_{axial} .

vector plot is provided in Fig.5.7.13, showing magnitude and direction of maximum principle stresses within the vicinity of the coupler edge for the baseline configuration.)

Notably, the shear stress distribution for the shortest coupling distance (i.e. 50% length reduction, which is equivalent to an overlap length of 1.5 times the pipe diameter) differs appreciably from the one of the baseline coupler, see right-hand-side of Fig.5.7.11. Here, the shear stress did not level off to zero in the middle of the coupling length. This is seen to affect the damage progression behaviour. Thus, Fig.5.7.14 and 5.7.15 were produced which show mode II and total strain energy release rates for the three joint configurations respectively. In contrast to the other joint lengths the model with the shortest overlap distance yields mode II and thus total SERR values that never reach a plateau, but increase constantly. In such a case the net energy supplied does not decrease below the threshold for crack extension; unstable crack growth is the outcome. This led to the conclusion that a reduction of the baseline overlap length beyond 25% (i.e. an overlap length equal to 2.25 times the pipe diameter) severely reduces joint strength, and promotes catastrophic failure.

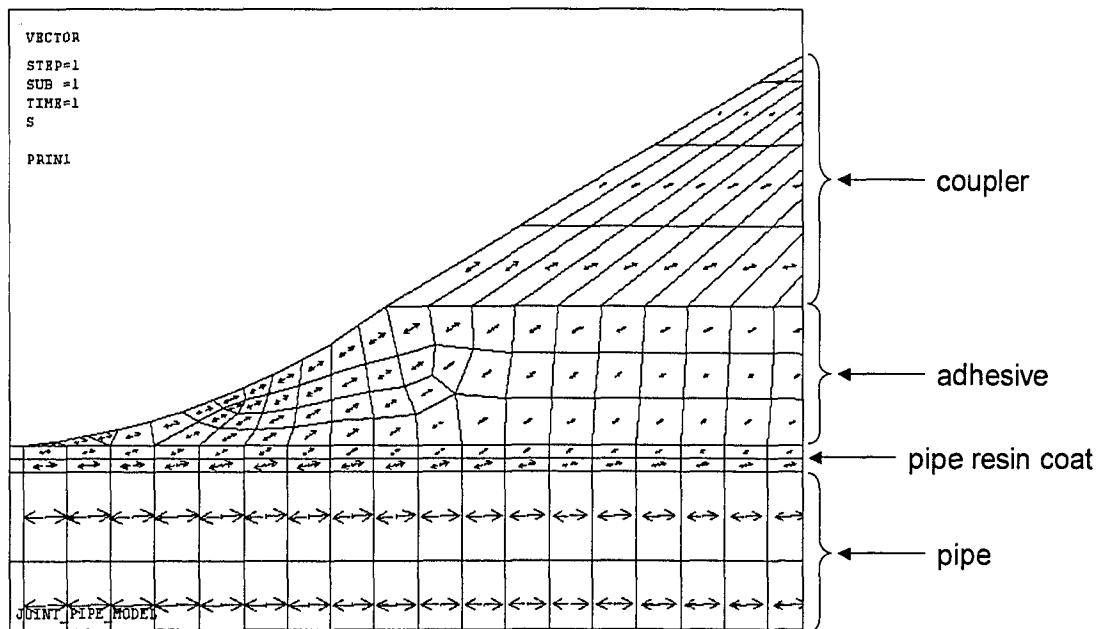


Figure 5.7.13: Vector plot showing magnitude/direction of maximum principle stresses in the vicinity of the coupler edge for the baseline configuration under axial loading.

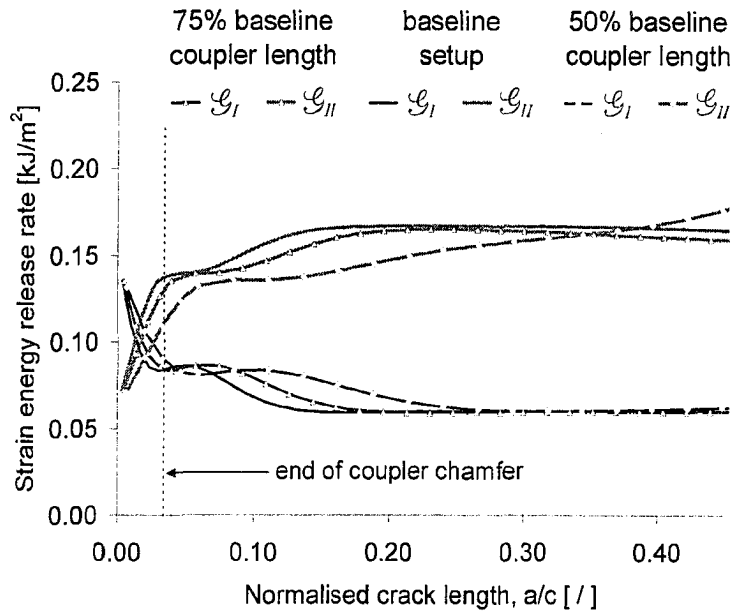


Figure 5.7.14: Comparison between SERR values from analyses of a prototype model with baseline coupling distance, and those with and 25% and 50% length reductions.

For the finite element analyses 100 MPa axial load was applied.

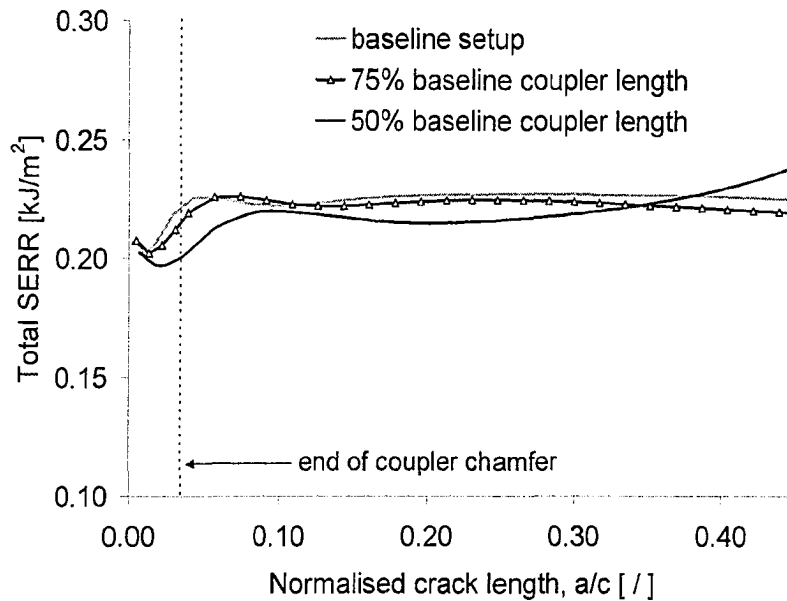


Figure 5.7.15: Comparison between total SERR values from analyses of a prototype model with baseline coupling distance, and those with 25% and 50% length reductions. For the finite element analyses 100 MPa axial load was applied.

Effect of adhesive bondline thickness:

It has been reported in the technical literature that theoretical analyses based on strength-of-materials theory yield optimal bondline thicknesses that are in disagreement with experimental observation (Gleich et al., 2001). Experiments revealed that an optimum bondline thickness is typically of about 0.1 mm to 0.5 mm (see e.g. Tomblin et al., 2002). On the contrary theoretical studies based on strength-of-materials theory commonly predicted joint strength to increase with increasing bondline thickness due to a reduction of peak stresses at the coupler edge (see e.g. Griffin et al., 1991; and Semb et al., 1995).

Figure 5.7.16 shows peak maximum principle stresses computed at various locations within the adhesive layer for four bondline thicknesses. All peak stresses were located in the vicinity of the coupler edge. Analogous to observations in literature, results shown in Fig.5.7.16 clearly indicate that an increase in bondline thickness leads to a reduction of peak stress values, and thus to lesser damage susceptibility.

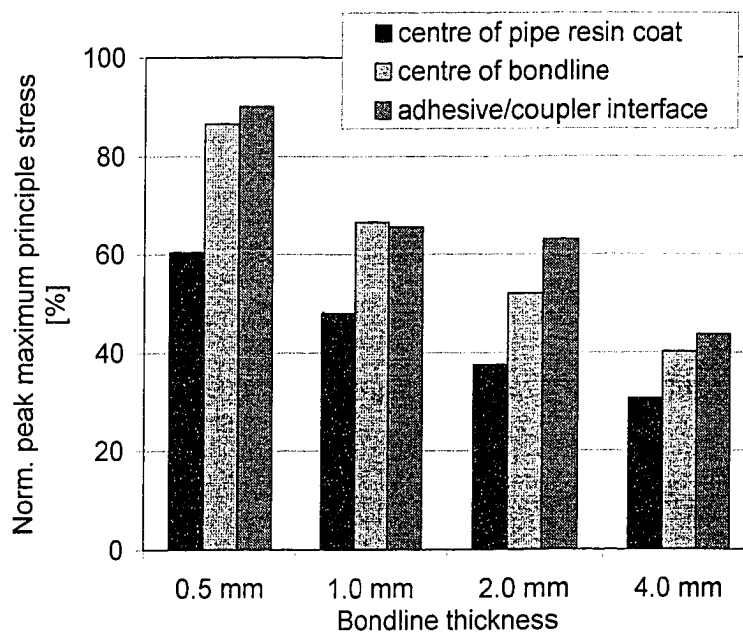


Figure 5.7.16: Normalised peak maximum principle stresses for models with bondlines of 0.5 mm, 1 mm, 2 mm and 4 mm. Stress data originate from three locations within the bondline, and were normalised with respect to the average pipe axial stress, σ_{axial} .

It is worth noting that increasing the bondline thickness and enlarging the adhesive fillet bear similarities in their effect of reducing peak stresses at the coupler edge. This explains favourable strength properties of joints with reverse adherend chamfering. Reverse chamfering (being promoted by various researchers, e.g. Adams and Davies, 1996, and Potter and co-workers, 2001) provides for a local increase in bondline thickness (i.e. at the adherend edge), an enlarged adhesive fillet and a more compliant adherend end.

Gleich et al. (2001) suggested that an investigation of bondline thickness effects based on fracture mechanics principles ought to yield results that are in better accordance with experimental observations. Therefore, in the present study a modified fracture model with a bondline thickness reduction of 50% was analysed (i.e. the thickness of the adhesive layer was 0.5 mm). Results are presented in Fig. 5.7.17, where data of the baseline configuration is also shown (i.e. 1 mm bondline). It is seen that initially higher values of

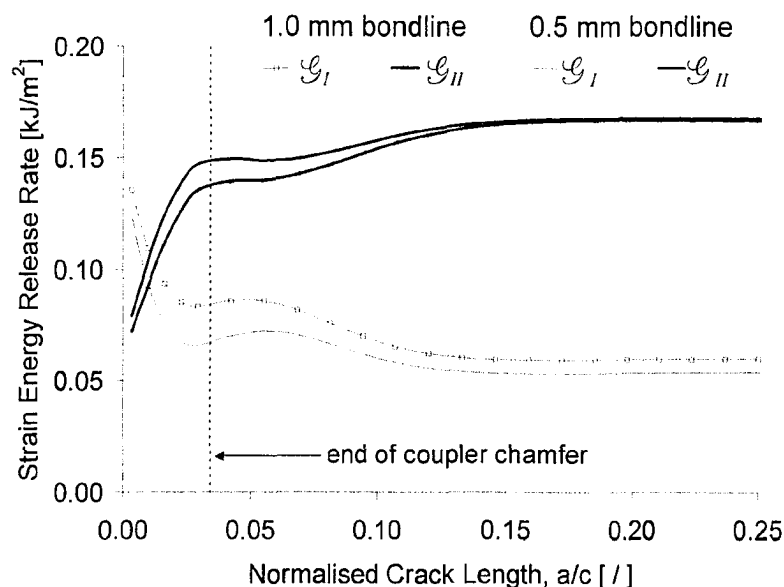


Figure 5.7.17: Comparison between strain energy release rate values from analyses of prototype specimens models with 0.5 mm and 1.0 mm bondline thickness. For the finite element analyses 100 MPa axial load was applied.

\mathcal{G}_{II} were found by the modified model. However, mode II SERR values eventually reached the same plateau as the baseline model. Mode I release rates, on the other hand, consistently remained lower than those of the baseline model (for the modified model \mathcal{G}_I values were reduced between 8.5% and 21% compared to the baseline configuration). This confirms experimental findings from literature, namely that joints featuring thinner bondlines are indeed superior to those with thicker adhesive layers. Unfortunately, as discussed earlier, the prototype structure in its present configuration did not allow for a thinner bondline due to the unevenness of the resin coat on the pipe surface.

Effect of coupler thickness and lay-up:

The effect of coupler thickness was evaluated by adding/removing a single $\pm 60^\circ$ cover to/from the baseline model (i.e. the $[\pm 30, \pm 60_2]_T$ baseline configuration was compared to $[\pm 30, \pm 60]_T$ and $[\pm 30, \pm 60_3]_T$ lay-ups). As shown in Fig.5.7.18, the comparison of peak maximum principle stresses from various locations within the bondline basically yielded inconclusive results. (Note that removing the $\pm 60^\circ$ cover resulted in small relative peak

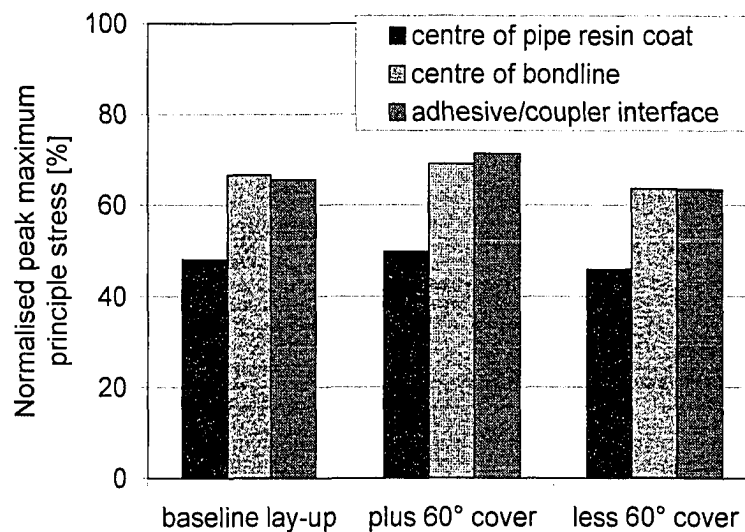


Figure 5.7.18: Normalised peak maximum principle stresses for models with one $\pm 60^\circ$ cover added/removed to/from the baseline coupler. Stress data originate from three locations within the bondline, and were normalised with respect to the average pipe axial stress, σ_{axial} .

stress reductions of 3.2% to 4.5%; however these reductions were considered too small to be of substantial influence.) As well, no significant difference could be ascertained between the different lay-up configurations in terms of peel and shear stress distributions, see the left and right-hand-side of Fig.5.7.19 respectively. Hence, the coupler thickness is not expected to have any substantial influence on damage initiation. This result was to be expected, since due to coupler chamfering a change in coupler thickness does not substantially affect compliance or deformation behaviour of the coupler edge, i.e. the region where peak stresses occur which promote crack initiation.

Fracture analyses, on the other hand, indicate that coupler thickness appreciably affects strain energy release rates. A strengthened coupler caused a significant increase in \mathcal{G}_{II} values, which were accompanied by only minor decreases in the mode I contributions (see Fig.5.7.20). The opposite is true for reducing coupler thickness. In this case, small increases in the mode I strain energy release rate and significant reductions of mode II SERR values were ascertained. Consequently, an average \mathcal{G}_T decrease of 11.5% was achieved. It therefore seems beneficial to reduce the coupler design to a $[\pm 30, \pm 60]_T$ lay-up; even the consideration of a pure $\pm 30^\circ$ lay-up appears to be worthwhile. However, the latter is considered unfavourable from a fabrication point-of-view. The low circumferential strength of a single $\pm 30^\circ$ cover combined with a coupler wall thickness of only 1.2 mm is thought to cause substantial difficulties in machining and handling.

One might also consider improving fracture behaviour by reversing the coupler lay-up sequence, i.e. the $\pm 30^\circ$ cover would be located on the outside of the coupler sleeve. But, as shown in Fig.5.7.21, the effect on total strain energy release rate and therefore the fracture behaviour is negligible assuming an unchanged crack path. Moreover, the highly stressed coupler chamfer would predominantly consist of $\pm 60^\circ$ layers. This might cause damage initiation to occur within the fibre architecture, possibly shifting the damage behaviour from fracture within the bondline region to an interlaminar damage mode.

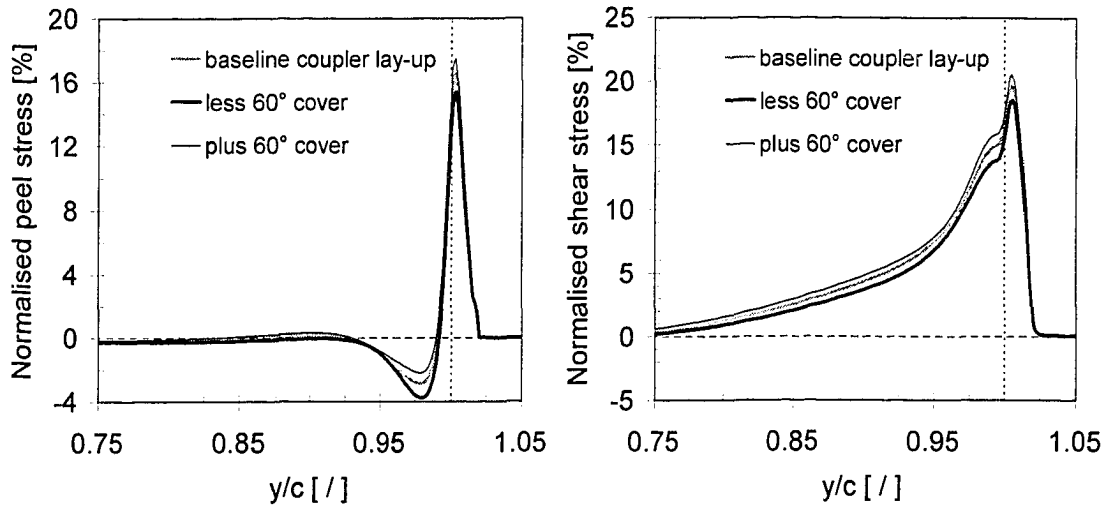


Figure 5.7.19: Comparison of peel (left) and shear (right) stresses within the centre of the pipe surface resin coat between models with one $\pm 60^\circ$ cover added/removed to/from the baseline coupler. Stress data were normalised with respect to the average pipe axial stress, σ_{axial} .

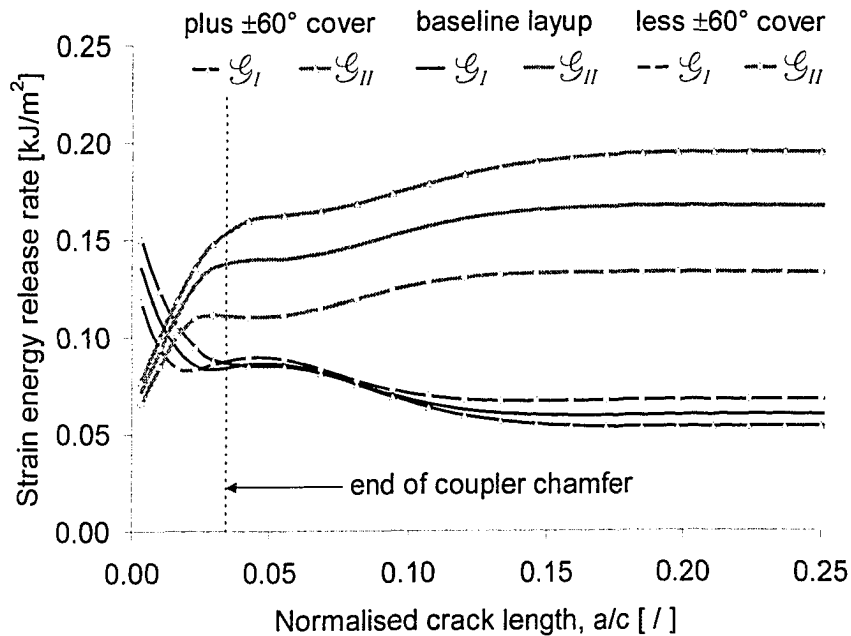


Figure 5.7.20: Comparison between strain energy release rate values from analyses of prototype models with one $\pm 60^\circ$ cover added/removed to/from the baseline coupler. For the finite element analyses 100 MPa axial load was applied.

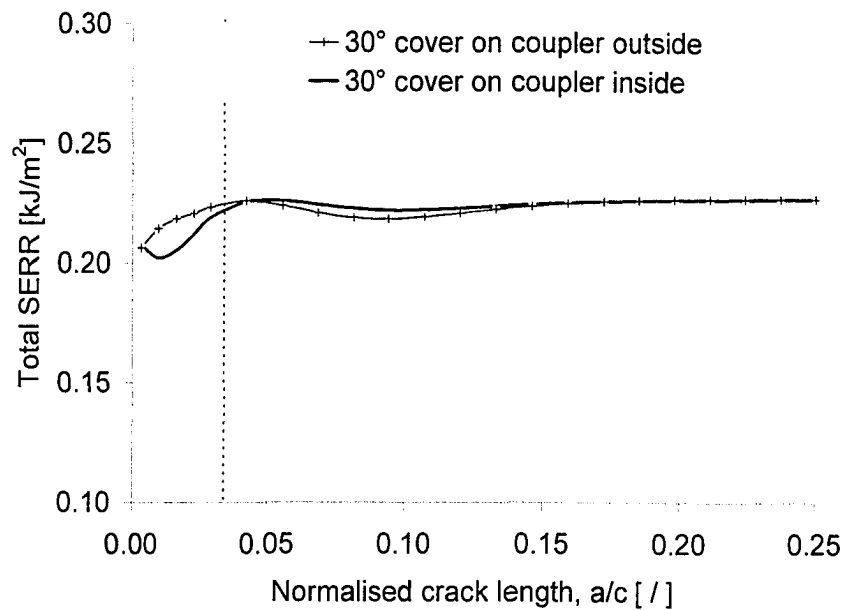


Figure 5.7.21: Comparison between total strain energy release rate values from analyses of prototype models with an $[\pm 30, \pm 60_2]_T$ and an inversed $[\pm 60_2, \pm 30]_T$ lay-up. For the finite element analyses 100 MPa axial load was applied.

Effect of coupler chamfering:

Coupler chamfering is limited in its ability to improve joint performance. An unloading of the coupler structure occurs in the wake of the crack tip, which renders the chamfer ineffective in an early stage of crack growth. Since the chamfer geometry has no influence on fracture growth behaviour, chamfering is only effective for delaying damage initiation. Consequently, the present investigation was limited to a strength-of-materials approach. Three coupler geometries with chamfer angles of 15°, 30° (baseline) and 60° were evaluated. In Fig.5.7.22 normalised peak maximum principle stresses are shown, which were determined along the three paths employed earlier. All peak values were again located within the vicinity of the coupler edge. Notably, peak stresses do not follow a common trend: An increased slenderness of the coupler chamfer caused a rise in peak values close to the adhesive/coupler interface (dashed line in Fig.5.7.22). The opposite can be observed for the pipe/bondline interface and the centre of the bondline, where the highest principle stresses were encountered for the bluntest coupler chamfer (solid lines

in Fig.5.7.22). Blunting of the coupler edge thus causes increased stresses in the resin coat, i.e. the zone where damage developed predominantly. It is therefore reasonable to assume that large chamfer angles affect joint strength negatively. On the other hand, the 15° chamfer produced a zone of high stress intensity in the adhesive close to the adhesive/coupler interface. Since neither the 15° nor the 60° chamfer provided for reduced loading of the bondline, the 30° chamfer is considered an adequate compromise offering moderate stressing of the bondline region.

5.8 Advanced Fabrication Technique for Improved Joint Performance

It was confirmed by experiments that fracturing occurred predominantly within the brittle resin coat on the pipe surface. Hence, this layer appears to be the weakest link of the current joint design. In order to improve the prototype pipe the manufacturing process was altered as to remove excess resin from the pipe surface.

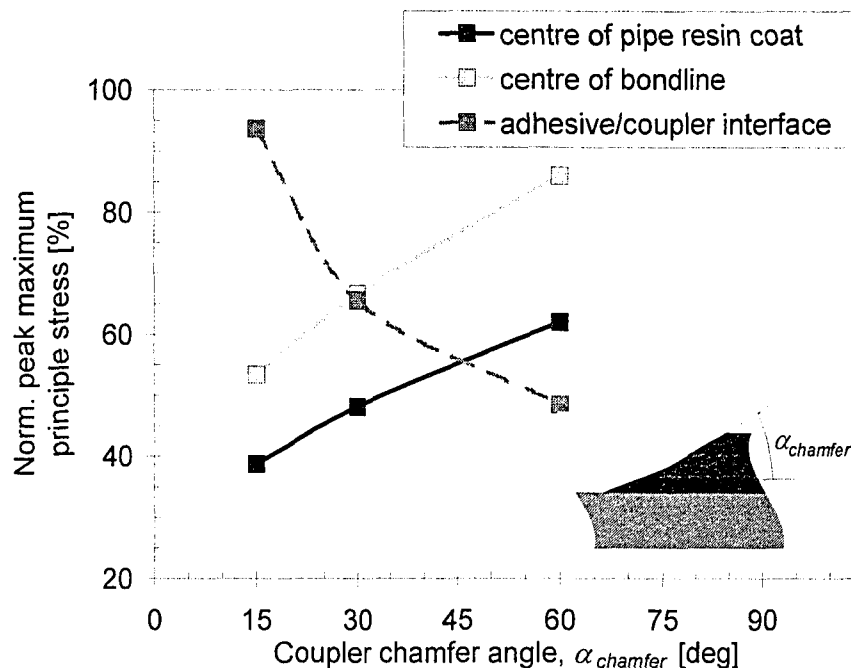


Figure 5.7.22: Normalised peak maximum principle stresses for models with 15°, 30° and 60° coupler chamfers. Stress data originates from three locations within the bondline, and were normalised with respect to the average pipe axial stress, σ_{axial} .

Procedure for excess resin removal:

After the winding process had been completed a porous nylon peel-ply was wrapped around the part, followed by an absorbent breather fleece. Finally, a polymer heat shrink tape was applied consolidating the underlying cloth layers. This configuration allowed the peel-ply to be penetrated by excess resin, which was then absorbed within the breather fleece. This process was further intensified in the curing stage, during which the influence of heat lowered resin viscosity and caused the shrink tape to contract, thus imposing radial compression evenly about the part. Consequently, excess resin was taken away from the pipe surface. The radial pressure applied by the shrink tape also caused further consolidation of the fibre architecture, resulting in an increase of fibre volume fraction to 63.6%. (Without shrink tape wrapping fibre volume fraction was 60.2%.)

Due to poor adhesion between the nylon and epoxy material the peel-ply allowed for easy removal of the cloth layers after curing. The procedure successfully removed any resin coat of appreciable thickness from the pipe surface. Furthermore, a substantially improved evenness of the exterior surface was obtained compared to the previous resin-coated pipe. The porous structure of the peel-ply also resulted in a rough surface finish. Therefore it was unnecessary to prepare the pipe surface by machining and grid-blasting, which were previously employed to improve adhesion for the bonding of coupler sleeves and specimen end connections.

Validation of altered fabrication process:

Utilising improved prototype pipe, specimens were fabricated and tested according to the procedures outlined in previous sections of this thesis. Tests under pure axial and closed-end loading conditions were performed on joined prototypes (i.e. [0H:1A] and [2H:1A]). As shown in Fig.5.8.1, results were added to the previously shown prototype failure envelope. It can be observed that the altered fabrication procedure, and thus the changed surface properties and the higher fibre volume fraction, did not have any noticeable influence on functional failure strength under closed-end loading. Under pure axial loading, however, joint strength increased by 16.5%. This was attributed to the improved pipe surface properties.

Note that higher fibre compaction and the removed resin cover reduced the wall thickness of improved prototype pipe by 0.24 mm to 4.39 mm, compared to previous specimens. The preceding parametric study showed that a decrease in thickness of the resin coat on the pipe surface improved joint performance. Yet, since coupler dimensions remained unchanged, the altered manufacturing procedure caused an increase in bondline thickness. Hence, the observed increase in joint strength cannot be attributed exclusively to the change in surface properties.

In conclusion, the altered fabrication method not only substantially increased joint strength, but it also improved overall manufacturing efficiency. The introduced procedures reduced the number of pipe preparation steps required for joint application (i.e. grid-blasting and machining of bonding surfaces). Moreover, fabrication steps that were added to the winding process offer high potential for automation, since wrapping of the cloth materials and shrink tape can be accomplished with the existing winding equipment. An added benefit is that pipe sections could remain wrapped until reaching the installation site, as the wrap protects the pipe surface from damage and substance contaminations (e.g. oil or dirt).

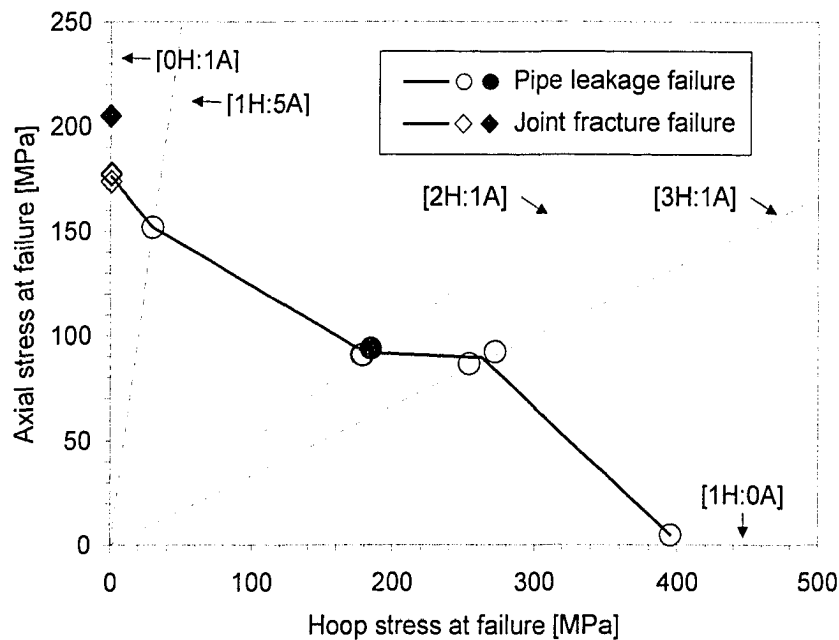


Figure 5.8.1: Experimental biaxial failure envelope of prototype specimens.

Solid symbols mark specimens utilizing improved prototype pipe.

CHAPTER 6

CONCLUSIONS

The main objective of this thesis was to evaluate the feasibility of an all-composite high-pressure pipe system. Such a system ought to be economically superior compared to conventional metallic ones. A unique approach was utilised to achieve this objective; namely, the fabrication, design and damage behaviour were jointly investigated. Filament winding was employed for the manufacturing of components because of its quality and cost-effectiveness in producing tubular parts. Within this framework, solutions for the design were developed and optimised, and a simple, yet innovative joining technique was proposed allowing for the integration of pipe sections. In the following, findings from the preceding research work are highlighted individually.

- A state-of-the-art filament winding facility was employed for the fabrication of specimens. Advantages and constraints of the filament winding technique were addressed. In order to achieve efficient manufacturing, i.e. to avoid fibre slippage or excessively small winding bandwidths, intermediate winding angles were favoured ranging from 30° to 60° . Tow tensioning was found ineffective for controlling winding bandwidth; however, a considerable effect on fibre compaction was ascertained. Fibre tow of reduced linear weight was found to also promote increased fibre compaction. For the selected material system and manufacturing processes the average void contents was found to be within quality limits ($\sim 1\%$).
- Analytical techniques for the determination of the degree of winding band interweaving, engineering moduli and wall thickness of the tubular structures were presented. The usefulness of these techniques for the design and comparison of various tubular structures was demonstrated. Structural and material parameters found by these methods were shown to be in good agreement with the experimental results. The predictive capabilities of these methods therefore allow for more efficient design processes by lessening the need for experimental work.

- Two specimen sizes were employed for the experimental analysis. Small-scale model specimens proved to be effective for preliminary investigations on optimal fibre architectures and manufacturing conditions. Large-scale prototypes were also tested to verify the influence of scale and the viability of the proposed pipe joining technique.
- Two types of failure were observed for composite tubular specimens subjected to combined axial load and internal pressure, i.e. functional failure (loss of fluid) and structural failure (burst). Small-scale specimens under axial-dominated loadings and prototype pipe exhibited functional failure. Structural failures only occurred in small-scale specimens under hoop-dominated loading ratios. (Note that functional failure was always followed by structural failure in small-scale specimens that were equipped with a liner system.)
- Testing of small-scale specimens revealed that increased winding tension and fibre compaction has a detrimental effect on component strength under matrix-dominated loading conditions. Thus, only moderate fibre tensioning is required during manufacturing to achieve adequate degrees of fibre compaction.
- From experiments with $[\pm 60_3]_T$ model specimens functional failure was observed to occur approximately at an average value of 0.3% transverse strain independent from the applied loading ratios ranging from (approximately) pure axial to [3H:1A].
- Tubular composite structures most likely have to sustain variable biaxial loading conditions during installation and service. Fibre architectures limited to a specific winding angle were shown to severely compromise desired high strength properties. Multi-angle lay-ups exhibited significantly better performance. A fibre architecture employing $\pm 60^\circ$ and $\pm 30^\circ$ winding angles was found to produce most advantageous results while maintaining good manufacturability.
- The stacking sequence of multi-angle fibre architectures was also found to influence component strength. This was attributed to the individual deformation of each cover. Under certain loading conditions a constraining effect of outside covers acting upon subjacent covers, may be realised. A delay in damage development was attributed to this effect. Based on these findings a $[\pm 60_3, \pm 30]_T$ lay-up was selected for the

large-scale prototypes. Since the selected combination of $\pm 60^\circ$ and $\pm 30^\circ$ covers already provides high strength under hoop-dominated loadings, the stacking sequence was chosen as to cause strength improvements under axial-dominated loading conditions.

- To compare leakage failure in small-scale and large-scale specimens a permeability damage criterion was adapted. A significant strength size effect for leakage thresholds was ascertained between the two specimen sizes. For the same permeability level, small-scale specimens were found to sustain higher degrees of (matrix) damage than the large-scale ones. This effect could not be explained by inherent differences between the two specimen sizes (such as moderate differences in the degree of interweaving and fibre compaction). Consequently, experimental testing of prototypes remains essential for the determination of absolute strength.
- A joining methodology employing adhesive bonding and an overlap sleeve design was proposed for prototype specimens. Cylindrical sleeve couplers with a $[\pm 30, \pm 60_2]_T$ lay-up were mounted to the extremities of pipe sections, and adhesive was injected forming the bondline in between the pipe components. This joining methodology is considered advantageous due to the simple coupler geometry and the uncomplicated application procedure.
- Experimental testing revealed that the proposed technique for integrating prototype structures produced joint strength that exceeded prototype pipe strength for all but pure axial loading conditions. Joint failure consistently occurred by debonding within the region in between the adhesive bondline and the pipe structure. Stable crack growth commenced from the coupler edge and grew towards the joint centre, which eventually led to joint separation. The crack did not extend into the pipe or coupler adherends, but was contained within the brittle resin coat on the pipe surface. This was attributed to a crack shielding effect of the neighbouring $\pm 30^\circ$ covers of coupler and pipe.
- Joint failure was modelled numerically employing a strength-of-materials and a fracture mechanics approach. In both cases linear elastic material properties were

assumed. The virtual crack closure technique was utilised for the fracture analysis. Good agreement between theoretical and experimental results was ascertained within the elastic range of the materials.

- Employing both numerical models a parametric study was completed for the investigation of various characteristic joint geometry features. This produced the following findings: (a) A minimum overlap length exists, below which crack growth occurs in an unstable manner. (b) Decreasing bondline thickness was determined to increase fracture resistance. Increasing bondline thickness beyond the dimensions of the prototype structure was shown to delay fracture initiation; however, fracture would occur more rapidly once a crack has initiated. Hence, a decrease in bondline thickness was considered most beneficial for improving joint performance. (c) The numerical models indicated that reducing coupler thickness improves joint strength. A $[\pm 30, \pm 60]_T$ coupler lay-up was therefore considered a favourable joint improvement. (d) The influence of coupler chamfering was also analysed. A chamfer angle of approximately 30° was shown to produce best performance.
- The resin coat on the pipe surface (formed by the accumulation of excess resin during manufacturing) was the weakest link within prototype joints. The manufacturing of prototype pipe was therefore altered as to remove this resin coat with an absorbent polymer cloth. This resulted in a significant increase in joint strength of about 16%. Moreover, the application of the absorbent cloth resulted in a textured pipe surface with increased evenness, which provides for good adhesion properties and allows for thinner adhesive bondlines respectively.

Major contributions to the field:

The present study should not be understood as the validation of a specific design solution. Rather this work provides a comprehensive framework for the design of filament-wound all-composite pipe structures. Important characteristics of such structures were discussed beginning with the manufacturing procedure and extending to include essential features such as the fibre architecture and joining technique.

In this thesis appropriate investigative methodologies, both experimental and theoretical in nature were adapted or developed for the determination of material and

dimensional properties of filament-wound components. Comparison of the analytical results with the experimental data indicated good predictive capabilities of the employed methods.

Finally, the thesis furthered the understanding of the involved damage mechanisms. Distinct damage modes were described depending on the applied loading condition. The observed strength discrepancy between model and prototype specimens confirmed that there is a lack of other analytical methodologies for the prediction of failure in pressurised composite structures. It was shown that failure is dominated by matrix damage events on a micro-level and the ensuing permeability characteristics.

Suggested future research direction:

Clearly, considerable efforts have been reported in the technical literature for the analysis of fibre-composite structures. Yet, the leakage behaviour has not been fully understood, and as shown earlier, predictive capabilities remain inadequate. This limits the utilisation of fibre-composites for industrial applications, despite the otherwise favourable properties of these materials. Leakage in fibre-composite structures is governed by micro-damage events and by the permeability properties of the damaged material. This indicates a possible research direction, i.e. an approach that uses micro and macro-damage mechanics in conjunction with suitable permeability criteria for the description and prediction of leakage in fibre-composite structures.

The development of pressurised composite structures for a particular application requires further research that is related once more to the damage behaviour of fibre-composites; namely, these are the material degradation due to environmental conditions (e.g. moisture), and the modification of the polymer matrix phase for the reduction of micro-damage susceptibility. The former aims at describing the effects and mechanisms that cause the properties of fibre-composites to deteriorate during long-term exposure to certain environments. Typically, environmental conditions are rather unique since they strongly depend on the application. This requires a research program to be tailored to the application under consideration. The goal of the latter, i.e. the polymer matrix modification, is to improve the matrix properties as to increase the ultimate stress/strain.

BIBLIOGRAPHY

- 3M (2002). Product Information: Scotch-Weld™ Epoxy Adhesives DP-460 Off-White . DP-460 NS. Publication number: 78-6900-9780-9. 3M Engineered Adhesives Division, St. Paul, MN, USA.
- Abdel Wahab, M.M., Ashcroft, I.A., Crocombe, A.D., Hughes, D.J. and Shaw, S.J. (2001). The effect of environment on the fatigue of bonded composite joints. Part 2: fatigue threshold prediction. *Composites Part A*, Vol. 32, 59-69.
- Adams, R.D. and Davies, R. (1996). Strength of joints involving composites. *Journal of Adhesion*, Vol. 59, 171-182.
- Adams, R.D. and Peppiatt, N.A. (1977). Stress analysis of adhesive bonded tubular lap joints. *Journal of Adhesion*, Vol. 9, 1-18.
- Amaldi, A. and Marchetti, M. (1992). Mechanical behaviour of filament wound carbon fibre reinforced epoxy resin tubes. In: *Proceedings of the 3rd International Conference on Computer Aided Design in Composite Material Technology – CADCOMP 92* (Advani S.G. et al., Eds.), pages 79-88, Delaware, DE, USA. Computational Mechanics Publications, Southampton.
- Anlaş, G., Ardiç, E.S. and Gediz, A. (1997). Calculation of effective moduli of filament wound tubes. *Journal of Reinforced Plastics and Composites*, Vol. 16, 1566-1574.
- Anonymous (2003). TransCanada installs demonstration section of composite reinforced line pipe. *Pipeline & Gas Journal*, June 2003, 50-54.
- ANSYS® Multiphysics (2002). HTML Online Documentation, Release 7.0.
- Ardiç, E.S., Anlaş, G. and Eraslanoglu, G. (1999). Failure prediction for laminated composites under multiaxial loading. *Journal of Reinforced Plastics and Composites*, Vol. 18, 138-150.
- Ashbee, K.H.G. (1993). *Fundamental Principles of Fibre Reinforced Composites*. Technomic Publishing, Lancaster.
- Ashby, M.F. and Jones, D.R.H. (1980). *Engineering Materials*. Pergamon Press, Oxford.

- Ashcroft, I.A., Abdel Wahab, M.M., Crocombe, A.D., Hughes, D.J. and Shaw, S.J. (2001). The effect of environment on the fatigue of bonded composite joints. Part 1: testing and fractography. *Composites Part A*, Vol. 32, 45-58.
- Asp, L.E., Berglund, L.A. and Gudmundson, P. (1995). Effects of a composite-like stress state on the fracture of epoxies. *Composite Science and Technology*, Vol. 53, 27-37.
- Asp, L.E., Berglund, L.A. and Talreja, R. (1996a). Prediction of matrix-initiated transverse failure in polymer composites. *Composites Science and Technology*, Vol. 56, 1089-1097.
- Asp, L.E., Berglund, L.A. and Talreja, R. (1996b). A criterion for crack initiation in glassy polymers subjected to a composite-like stress state. *Composites Science and Technology*, Vol. 56, 1291-1301.
- ASTM Standard Specification D792 (2000). Standard test methods for density and specific gravity (relative density) of plastics by displacement. American Society for Testing and Materials, Philadelphia.
- ASTM Standard Specification D1505 (1998). Standard test method for density of plastics by the density-gradient technique. American Society for Testing and Materials, Philadelphia.
- ASTM Standard Specification D2584 (1994, 2002). Standard test method for ignition loss of cured reinforced resins. American Society for Testing and Materials, Philadelphia.
- ASTM Standard Specification D2734 (2003). Standard test methods for void content of reinforced plastics. American Society for Testing and Materials, Philadelphia.
- ASTM Standard Specification D3171 (1999). Standard test methods for constituent content of composite materials. American Society for Testing and Materials, Philadelphia.
- ASTM Standard Specification D3299 (1995). Standard specification for filament-wound glass-fiber-reinforced thermoset resin corrosion-resistant tanks. American Society for Testing and Materials, Philadelphia.
- ASTM Standard Specification D3800 (1999). Standard test method for density of high-modulus fibers. American Society for Testing and Materials, Philadelphia.

- Bai, J., Hu, G. and Bompard, P. (1997). Micromechanical modelling of the damage initiation and the competition between different mechanisms of $\pm 55^\circ$ filament-wound glass-fibre/epoxy-resin tubes. In: Proceedings of the 11th International Conference on Composite Materials – ICCM-11 (Scott, M., Ed.), Vol. 5, pages 540-551, Gold Coast, Australia. Woodhead Publishing Ltd, Cambridge.
- Baldan, A. (2004). Review – Adhesively-bonded joints and repair in metallic alloys, polymers and composite materials: Adhesives, adhesion theories and surface pre-treatment. *Journal of Materials Science*, Vol. 39, 1-49.
- Baldwin, D.D., Newhouse, N.L., Lo, K.H. and Burden, R.C. (1997). Composite production riser design. In: Proceedings of the 29th Offshore Technology Conference – OTC'97, paper No. OTC 8431, Vol. 3, pages 11-18, Houston, TX, USA. Offshore Technology Conference, Richardson.
- Banerjee, A., Sun, L., Mantell, S.C. and Cohen, D. (1998). Model and experimental study of fiber motion in wet filament winding. *Composites Part A*, Vol. 29A, 251-263.
- Barkatt, A. (2001). Issues in predicting long-term environmental degradation of fiber-reinforced plastics. In: *Environmental Effects on Engineered Materials* (Jones, R.H., Ed.), pages 419-458. Marcel Dekker, New York.
- Bates, P.J., Taylor, D. and Cunningham, M. (2000). Transverse permeability of direct glass rovings. *Journal of Reinforced Plastics and Composites*, Vol. 19, 1217-1226.
- Bazant, Z.P., Daniel, I.M. and Li, Z. (1996). Size effect and fracture characteristics of composite laminates. *Journal of Engineering Materials and Technology, Transactions of the ASME*, Vol. 118, 317-324.
- Bazant, Z.P. (2000). Size effect. *International Journal of Solids and Structures*, Vol. 37, 69-80.
- Bishop, S.M. and Gilmore, R.B. (1989). Fatigue crack growth in adhesively-bonded and co-cured CFRP joints. In: *Proceedings of Bonding and Repair of Composites* (Heriot, J., Ed.), pages 67-74, Birmingham, UK. Butterworth Scientific, Guildford.
- Calius, E.P., Lee, S.Y. and Springer, G.S. (1990). Filament winding cylinders: II. Validation of process model. *Journal of Composite Materials*, Vol. 24, 1299-1343.

- Carey, J., Munro, M. and Fahim, A. Longitudinal elastic modulus prediction of 2-D braided fiber composite. *Journal of Reinforced Plastics and Composites*, Vol. 22, 813-831.
- Carlsson, L.A. and Pipes, R.B. (1997). *Experimental Characterization of Advanced Composite Materials*, 2nd Edition. Technomic Publishing, Lancaster.
- Carroll, M., Ellyin, F., Kujawski, D. and Chiu, A.S. (1995a). The rate-dependent behaviour of $\pm 55^\circ$ filament-wound glass-fibre/epoxy tubes under biaxial loading. *Composite Science and Technology*, Vol. 55, 391-403.
- Carroll, M., Ellyin, F. and Kujawski, D. (1995b). Stacking sequence effect on tensile and fatigue strength of symmetric laminates. *Polymers and Polymer Composites*, Vol. 3, 1-10.
- Chen, Y., Xia, Z., Ellyin, F. (2001). Evolution of residual stresses induced during curing processing using a viscoelastic model. *Journal of Composite Materials*, Vol. 35, 522-542.
- Cheremisinoff, N.P. and Cheremisinoff, P.N. (1978). *Fibreglass-Reinforced Plastics Deskbook*. Ann Arbor Science Publishers, Ann Arbor.
- Chouchaoui, C.S. and Ochoa, O.O. (1999a). Similitude study for a laminated cylindrical tube under tension, bending, internal and external pressure. Part I: governing equations. *Composite Structures*, Vol. 44, 221-229.
- Chouchaoui, C.S., Parks, P. and Ochoa, O.O. (1999b). Similitude study for a laminated cylindrical tube under tension, bending, internal and external pressure. Part II: scale models. *Composite Structures*, Vol. 44, 231-236.
- Clark, J.D. and McGregor, I.J. (1993). Ultimate tensile stress over a zone: a new failure criterion for adhesive joints. *Journal of Adhesion*, Vol. 42, 227-245.
- Cohen, D. (1997). Influence of filament winding parameters on composite vessel quality and strength. *Composites Part A*, Vol. 28A, 1035-1047.
- Cohen, D., Mantell, S.C. and Zhao, L. (2001). The effect of fibre volume fraction on filament wound composite pressure vessel strength. *Composites Part B*, Vol. 32B, 413-429.

- Darcy, H. (1983). Determination of the laws of flow of water through sand. In: *Physical Hydrogeology, Benchmark Papers in Geology* (Freeze, R.A. and Black, W., Eds.), Vol. 72, pages 8-20. Hutchinson & Ross, Stroudsburg.
- De Goeij, W.C., van Tooren, M.J.L. and Beukers, A. (1999). Composite adhesive joints under cyclic loading. *Materials and Design*, Vol. 20, 213-221.
- De Kok, J.M.M and Meijer, H.E.H. (1999). Deformation, yield and fracture of unidirectional composites in transverse loading: 1. Influence of fibre volume fraction and test-temperature. *Composites Part A*, Vol. 30A, 905-916.
- Ellsworth, P.G. and Bauer, D.B. (1992). Composite thread coupling for reinforced pipe. United States Patent, No. 5,106,130.
- Ellyin, F. and Fawaz, Z. (1995). A new methodology for the prediction of fatigue failure in multidirectional fiber-reinforced laminates. *Composites Science and Technology*, Vol. 53, 47-56.
- Ellyin, F., Carroll, M., Kujawski, D. and Chiu, A.S. (1997). The behaviour of multidirectional filament wound fibreglass/epoxy tubulars under biaxial loading. *Composites Part A*, Vol. 28A, 781-790.
- Ellyin, F. and Wolodko, J.D. (1997). Testing facilities for multiaxial loading of tubular specimens. In: *Multiaxial Fatigue and Deformation Testing Techniques*, ASTM STP 1280 (Kalluri, S. and Bonacuse, P.J., Eds.), pages 7-24. American Society for Testing and Materials, Philadelphia.
- Ellyin, F. and Rohrbacher, C. (2000). Effect of aqueous environment and temperature on glass-fibre epoxy resin composites. *Journal of Reinforced Plastics and Composites*, Vol. 19, 1-23.
- Ellyin, F., Wolodko, J., Dorling, D., Glover, A. and Jack, T. (2000). Fibre reinforced composites in pipeline applications: Design issues and current research. In: *Proceedings of the 3rd International Pipeline Conference – IPC 2000* (Ellwood, J.R., Ed.), Vol. 1, pages 491-500, Calgary, Canada. American Society of Mechanical Engineers (ASME), New York.
- Ellyin, F. and Rohrbacher, C. (2003). The influence of aqueous environment, temperature and cyclic loading on glass-fibre/epoxy composite laminates. *Journal of Reinforced Plastics and Composites*, Vol. 22, 615-635.

- Ellyin, F. and Maser, R. (2004). Environmental effects on the mechanical properties of glass-fiber epoxy composite tubular specimens. *Composites Science and Technology*, Vol. 64, 1863-1874.
- Estrada, H. and Parsons, I.D. (1997). A fiber reinforced plastic joint for filament wound pipes: analysis and design. A report on a research project sponsored by the National Science Foundation, Washington, D.C. Published by: National Technical Information Service, Springfield, VA, Technical report number PB97-205512, 186 pages.
- Foral, R.F. (1988). Local damage effects on performance of filament wound composite tubes. In: *Proceedings of the Joint ASME/SES Applied Mechanics and Engineering Sciences Conference: Mechanics of Composite Materials, AMD Symposia Series*, Vol. 92, pages 135-142, Berkeley, CA, USA. American Society of Mechanical Engineers (ASME) – Applied Mechanics Division, New York.
- Friedrich, R., Kuo, M. and Smyth, K. (1996). High-pressure fiber reinforced composite pipe joint. United States Patent, No. 5,520,422.
- Frost, S.R. and Cervenka, A. (1994). Glass fibre-reinforced epoxy matrix filament-wound pipes for use in the oil industry. *Composite Manufacturing*, Vol. 5, 72-81.
- Funck, R. and Fuchs, H.P. (2001). Development of all-composite compressed natural gas (CNG) pressure vessel for vehicle use. In: *Proceedings of the 13th International Conference on Composite Materials – ICCM-13*, paper #1155 (CD ROM), Beijing, China. ICCM-13 Organising Committee.
- Gamstedt, E.K. and Talreja, R. (1999). Fatigue damage mechanics in unidirectional carbon-fibre-reinforced plastics. *Journal of Materials Science*, Vol. 34, 2535-2546.
- Gamstedt, E.K. (2000). Effects of debonding and fiber strength distribution on fatigue-damage propagation in carbon fiber-reinforced epoxy. *Journal of Applied Polymer Science*, Vol. 76, 457-474.
- Gargiulo, C., Marchetti, M. and Rizzo, A. (1996). Prediction of failure envelopes of composite tubes subjected to biaxial loadings. *Acta Astronautica*, Vol. 39, 355-368.
- Garbassi, F. and Occhiello, E. (2001). Surfaces and their modification. In: *Performance of Plastics* (Brostow, W., Ed.), pages 373-400. Hanser Publishers, Munich.

- Gdoutos, E.E. (2000). Failure mechanisms and failure criteria of fiber reinforced composites. In: *Failure Analysis of Industrial Composite Materials* (Gdoutos, E.E., Pilakoutas, K. and Rodopoulos, C.A., Eds.), pages 51-108. McGraw-Hill, New York.
- Giacoletto, H.L. (2002). The art of filament winding. *Reinforced Plastics*, Vol. 46, No. 10, 30-32.
- Gleich, D.M., Van Tooren, M.J.L. and Beukers, A. (2001). Analysis and evaluation of bondline thickness effects on failure in adhesively bonded structures. *Journal of Adhesion Science and Technology*, Vol. 15, 1091-1101.
- Graves, S.R. and Adams, D.F. (1981). Analysis of a bonded joint in a composite tube subjected to torsion. *Journal of Composite Materials*, Vol. 15, 211-224.
- Griffin, S.A., Pang, S.S. and Yang, C. (1991). Strength model of adhesive bonded composite pipe joints under tension. *Polymer Engineering and Science*, Vol. 31, 533-538.
- Grove, S. (1999). Optimum fiber orientation in filament wound structures. *Journal of Materials Science Letters*, Vol. 18, 1203.
- Groves, S., Sanchez, R., Lyon, R. and Magness, F. (1992). Evaluation of cylindrical shear joints for composite materials. *Journal of Composite Materials*, Vol. 26, 1134-1150.
- Guess, T.R., Reedy, E.D., Jr. and Slavin, A.M. (1995). Testing composite-to-metal tubular lap joints. *Journal of Composites Technology & Research*, Vol. 17, 117-124.
- Guild, F.J., Potter, K.D., Heinrich, J., Adams, R.D. and Wisnom, M.R. (2001). Understanding and control of adhesive crack propagation in bonded joints between carbon fibre composite adherends: II. Finite element analysis. *International Journal of Adhesion & Adhesives*, Vol. 21, 445-453.
- Gürdal, Z., Haftka, R.T. and Hajela, P. (1999). *Design and Optimization of Laminated Composite Materials*. John Wiley & Sons, New York.
- Gustafson, C.G., Semb, G. and Moursund, B. (1993). Fatigue from waterhammer on filament wound GRE-pipes and adhesive bonded joints. In: *Proceedings of the 9th International Conference on Composite Materials – ICCM-9* (Miravete, A., Ed.), Vol. 4, pages 63-73, Madrid, Spain. Woodhead Publishing, Cambridge.

- Halpin, J.C. and Kardos, J.L. (1976). The Halpin-Tsai equations: a review. *Polymer Engineering and Science*, Vol. 16, 344-352.
- Halpin, J.C. (1984). *Primer on Composite Materials: Analysis*. Technomic Publishing, Lancaster.
- Harte, A.M., McNamara, J.F. and Roddy, I.D. (2003). Application of optimisation methods to the design of high performance composite pipelines. *Journal of Materials Processing Technology*, Vol. 142, 58-64.
- Hart-Smith, L.J. (1987). Design of adhesively bonded joints. In: *Joining Fibre-Reinforced Plastics* (Matthews, F.L., Ed.), pages 271-311. Elsevier Applied Science Publishing, New York.
- Hashim, S.A., Cowling, M.J. and Lafferty, S. (1998). The integrity of bonded joints in large composite pipes. *International Journal of Adhesion & Adhesives*, Vol. 18, 421-429.
- Hashin, Z. and Rotem, R. (1973). A fatigue failure criterion for fibre reinforced materials. *Journal of Composite Materials*, Vol. 7, 448-464.
- Hashin, Z. (1983). Analysis of composite materials – a survey. *Journal of Applied Mechanics*, Vol. 50, 481-505.
- Hipol, P.J. (1984). Analysis and optimization of a tubular lap joint subjected to torsion. *Journal of Composite Materials*, Vol. 18, 298-311.
- Hu, Y., Xia, Z. and Ellyin, E. (2003). Deformation behaviour of an epoxy resin subject to multiaxial loadings, Part I: Experimental investigations. *Polymer Engineering and Science*, Vol. 43, 721-733.
- Hull, D., Legg, M.J. and Spencer, B. (1978). Failure of glass/polyester filament wound pipe. *Composites*, Vol. 9, 17-24.
- Hull, D. and Clyne, T.W. (1996). *An Introduction to Composite Materials*, 2nd Edition. Cambridge University Press, Cambridge.
- Hoover, J., Kujawski, D. and Ellyin, F. (1997). Transverse cracking of symmetric and unsymmetric glass-fibre/epoxy resin laminates. *Composites Science and Technology*, Vol. 57, 1513-1526.

- Huysmans, G., Marsol, J.F., Verpoest, I., De Roeck, G., De Ridder, L. and Vansant, J. (1996). A field-friendly rigid composite coupler for GRP pipes. In: Proceedings of the 7th European Conference on Composite Materials – ECCM-7, Vol. 2, pages 349-354, London, UK. Woodhead Publishing Ltd, Cambridge.
- Huysmans, G., Marsol, J.F., Verpoest, I., De Roeck, G., De Ridder, L. and Vansant, J. (1997). A field-friendly rigid composite coupler for GRP pipes. *Composite Structures*, Vol. 37, 155-164.
- Huysmans, G., Verpoest, I. and De Roeck, G. (1998). Structural analysis of GRP pipe couplers by using a fracture mechanical approach. *Composites Part B*, Vol. 29B, 477-487.
- Hyer, M.W. (1998). *Stress Analysis of Fiber-Reinforced Composite Materials*. WCB/McGraw Hill, New York.
- Ishikawa, T. and Chou, T. W. (1982a). Elastic behavior of woven hybrid composites. *Journal of Composite Materials*, Vol. 16, 2-19.
- Ishikawa, T. and Chou, T. W. (1982b). Stiffness and strength behaviour of woven fabric composites. *Journal of Materials Science*, Vol. 17, 3211-3220.
- Ishikawa, T. and Chou, T. W. (1983). One-dimensional analysis of woven fabric composites. *AIAA Journal*, Vol. 21, 1714-1721.
- ISO International Standard 11439 (2000). High pressure cylinders for the on-board storage of natural gas as a fuel for automotive vehicles. International Organization for Standardization, Geneva.
- Jackson, K.E., Kellas, S. and Morton, J. (1992). Scale effects in the response and failure of fiber reinforced composite laminates loaded in tension and in flexure. *Journal of Composite Materials*, Vol. 26, 2674-2705.
- Jang, B.Z. (1994). *Advanced Polymer Composites*. ASM International, Materials Park.
- Johnson, W.S. and Mall, S. (1986). Influence of interface ply orientation on fatigue damage of adhesively bonded composite joints. *Journal of Composites Technology and Research*, Vol. 8, 3-7.
- Jones, D.L. (1989). Composite tubing connector assembly. United States Patent, No. 4,810,010.

- Kaempfen, C.E. (1983). Composite laminate joint structure and method and apparatus for making same. United States Patent, No. 4,385,644.
- Kaempfen, C.E. (1993). Double-wall composite pipe and coupling structure assembly. United States Patent, No. 5,222,769.
- Kalman, M. and Loper, C. (1998). Development of composite-armored flex risers for deep water. *World Oil*, November 1998, 103-106.
- Kaw, A.K. (1997). *Mechanics of Composite Materials*. CRC Press, Boca Raton.
- Kies, J.A. (1962). Maximum strains in the resin of fibreglass composites. NRL Report 5752, AD-274560. Washington, DC: US Naval Research Laboratory.
- Kim, H. (2003). The influence of adhesive bondline thickness imperfections on stresses in composite joints. *Journal of Adhesion*, Vol. 79, 621-642.
- Kim, W.T. and Lee, D.G. (1995). Torque transmission capability of adhesively bonded tubular lap joints for composite drive shafts. *Composite Structures*, Vol. 30, 229-240.
- Kliger, H.S. and Wilson, B.A. (1990). Continuous fiber molding processes A. Filament winding. In: *Composite Materials Technology* (Mallick, P.K. and Newman, S., Eds.), pages 179-210. Hanser Publishers, Munich.
- Knox, E.M., Cowling, M.J. and Hashim, S.A. (2000a). Creep analysis of adhesively bonded connections in GRE pipe including the effect of defects. *Composites Part A*, Vol. 31A, 583-590.
- Knox, E.M., Cowling, M.J. and Hashim, S.A. (2000b). Fatigue performance of adhesively bonded connections in GRE pipes. *International Journal of Fatigue*, Vol. 22, 513-519.
- Knox, E.M., Lafferty, S., Cowling, M.J. and Hashim, S.A. (2001). Design guidance and structural integrity of bonded connections in GRE pipes. *Composites Part A*, Vol. 32A, 231-241.
- Kollár, L.P. and Springer, G.S. (2003). *Mechanics of Composite Structures*. Cambridge University Press, Cambridge.

- Koschmieder, M. and Michaeli, W. (2000). On-line tow width measurement in filament winding. In: Proceedings of the 45th International SAMPE Symposium and Exhibition (Loud, S., et al., Eds.), Vol. 2, pages 1417-1426, Long Beach, CA, USA. Society for the Advancement of Material and Process Engineering (SAMPE) Publishing, Covina.
- Krishnamachari, S.I. (1993). Applied Stress Analysis of Plastics. Van Nostrand Reinhold, New York.
- Krueger, R., Cvitkovich, M.K., O'Brien, T.K. and Minguet, P.J. (2000). Testing and analysis of composite skin/stringer debonding under multi-axial loading. *Journal of Composite Materials*, Vol. 34, 1263-1300.
- Krueger, R. (2002). The virtual crack closure technique: History, approach and applications. A NASA contractor report, Hampton, VA. Published by: National Aeronautics and Space Administration (NASA), Hampton, VA, Report number CR-2002-211628, 59 pages.
- Krueger, R., Minguet, P.J. and O'Brien, T.K. (2003). Implementation of interlaminar fracture mechanics in design: An overview. In: Proceedings of the 14th International Conference on Composite Materials – ICCM-14, paper #1456 (CD ROM), San Diego, CA, USA. Society of Manufacturing Engineers, Dearborn.
- Kujawski, D., Ellyin, F. and Culen, M.S. (1998). The fatigue behaviour of filament-wound fiberglass/epoxy tubes under cyclic pressure. *Journal of Reinforced Plastics and Composites*, Vol. 17, 268-281.
- Lang, T.P. and Mallick, P.K. (1998). Effect of spew geometry on stresses in single lap adhesive joints. *International Journal of Adhesion & Adhesives*, Vol. 18, 167-177.
- Lavoie, J.A., Soutis, C. and Morton, J. (2000). Apparent strength scaling in continuous fiber composite laminates. *Composites Science and Technology*, Vol. 60, 283-299.
- Lea, R.H. and Yang, C. (1998). Improving the mechanical properties of composite pipe using multi-angle filament winding. In: Proceedings of the Corrosion/98 NACE Annual Conference & Exposition, pages 458/1-458/6, San Diego, CA, USA. National Association of Corrosion Engineers (NACE), Houston.
- Lee, S.M. (1997). Mode II delamination failure mechanisms of polymer matrix composites. *Journal of Materials Science*, Vol. 32, 1287-1295.

- Lee, S.Y. and Springer, G.S. (1990a). Filament winding cylinders: I. Process model. *Journal of Composite Materials*, Vol. 24, 1270-1298.
- Lee, S.Y. and Springer, G.S. (1990b). Filament winding cylinders: III. Selection of the process variables. *Journal of Composite Materials*, Vol. 24, 1344-1366.
- Li, S., Reid, S.R. and Soden, P.D. (1998). A continuum damage model for transverse matrix cracking in laminated fibre-reinforced composites. *Transactions of the Royal Society London*, Vol. 356, 2379-2412.
- Liang, Y.D., Luo, G., Chen, Y. and Qiu, K.X. (1996). Graphical representation and calculation of interweaving degrees of filament winding patterns. In: *Proceedings of the 41st International SAMPE Symposium and Exhibition*, Vol. 1, pages 486-495, Anaheim, CA, USA. Society for the Advancement of Material and Process Engineering (SAMPE) Publishing, Covina.
- Liang, Y.D. and Luo, G. (1997). Two-dimensional non-axisymmetric filament winding patterns. In: *Proceedings of the 29th International SAMPE Technical Conference*, pages 505-514, Orlando, FL, USA. Society for the Advancement of Material and Process Engineering (SAMPE) Publishing, Covina.
- Liechti, K., Johnson, W.S. and Dillard, D.A. (1987). Experimentally determined strength of adhesively bonded joints. In: *Joining Fibre-Reinforced Plastics* (Matthews, F.L., Ed.), pages 105-184. Elsevier Applied Science Publishing, New York.
- Loewenstein, K.L. (1983). *The Manufacturing Technology of Continuous Glass Fibres*, 2nd Edition. Elsevier Science Publishing, Amsterdam.
- Lossie, M., Peters, J. and Van Brussel, H. (1989). Influence of winding strategy on the characteristics of filament wound structures. *Revue-M.-Mecanique*, Vol. 33, 107-117.
- Lubkin, J.L. and Reissner, E. (1956). Stress distribution and design data for adhesive lap joints between circular tubes. *Journal of Applied Mechanics*, *Transactions of the ASME*, Vol. 78, 1213-1221.
- Mallick, P.K. (1990). Sheet molding compounds. In: *Composite Materials Technology* (Mallick, P.K. and Newman, S., Eds.), pages 27-65. Hanser Publishers, Munich.
- Martens, M. and Ellyin, F. (2000). Biaxial monotonic behaviour of a multidirectional glass fiber epoxy pipe. *Composites Part A*, Vol. 31A, 1001-1014.

- Martens, M. and Ellyin, F. (2001). Biaxial fatigue behaviour of a multidirectional filament-wound glass-fiber/epoxy pipe. *Composite Science and Technology*, Vol. 61, 491-502.
- McAllister, E.W. (1998). *Pipeline Rules of Thumb*. Gulf Publishing Company, Houston.
- Mertiny, P. (1999). *Joint Technology for Fiber Reinforced Polymer Pipes*. Diploma Thesis, Institute of Mechanics, Department of Mechanical Engineering, Hannover University, Germany.
- Mertiny, P. and Ellyin, F. (2001). Selection of optimal processing parameters in filament winding. In: *Proceedings of 33rd International SAMPE Technical Conference* (Falcone, A., et al., Eds.), pages 1084-1095, Seattle, WA, USA. Society for the Advancement of Material and Process Engineering (SAMPE) Publishing, Covina.
- Mertiny, P. and Ellyin, F. (2002). Influence of the filament winding tension on physical and mechanical properties of reinforced composites. *Composite Part A*, Vol. 33A, 1615-1622.
- Mertiny, P., Ellyin, F. and Hothan, A. (2004a). An experimental investigation on the effect of multi-angle filament winding on the strength of tubular composite structures. *Composite Science and Technology*, Vol. 64, 1-9.
- Mertiny, P., Ellyin, F. and Hothan, A. (2004b). Stacking sequence effect of multi-angle filament wound tubular composite structures. *Journal of Composite Materials*, Vol. 38, 1095-1113.
- MIL-HDBK 17, *Composite Materials Handbook* (1999). Vol. 3: Materials Usage, Design, and Analysis. Technomic Publishing, Lancaster.
- Müller de Almeida, S.F. and dos Santos Nogueira Neto, Z. (1994). Effect of void content on the strength of composite laminates. *Composite Structures*, Vol. 28, 139-148.
- O'Brien, T.K. (1982). Characterization of delamination onset and growth in a composite laminate. In: *Damage in Composite Materials*, ASTM STP 775 (Reifsnider, K.L., Ed.), pages 140-167. American Society for Testing and Materials, Philadelphia.

- O'Brien, T.K. (1994). Damage and strength of composite materials: trends, predictions, and challenges. In: Proceedings of the Workshop of Scaling Effects in Composite Materials and Structures, NASA conference publication 3271, pages 145-158, Hampton, Virginia, USA. National Aeronautics and Space Administration (NASA), Hampton.
- O'Brien, T.K. (1998). Composite interlaminar shear fracture toughness, G_{IIc} : shear measurement or sheer myth? In: Composite Materials: Fatigue and Fracture, 7th Volume, ASTM STP 1330 (Bucinell, R.B., Ed.), pages 3-18. American Society for Testing and Materials, Philadelphia.
- O'Brien, T.K. (2001). Characterization, analysis and prediction of delamination in composites using fracture mechanics. In: Proceedings of the 10th International Congress of Fracture – ICF-10, paper #0942 (CD ROM), Honolulu, Hawaii, USA. Elsevier, Oxford.
- Okabe, T. and Takeda, N. (2002). Size effect on tensile strength of unidirectional CFRP composite – experiment and simulation. Composites Science and Technology, Vol. 62, 2053-2064.
- Owens Corning (1996). Product Information: Fiberglas® Brand 158B Type 30® Single End Roving. Publication number: 17111-D. Owens Corning, Toledo, OH, USA.
- Owens Corning (1997). Filament winding of glass fibre composites. Owens Corning, Toledo, OH, USA.
- Owens Corning (1998). Technical Paper: A New Era in Glass Fiber Composites. Publication number: 22862. Owens Corning, Toledo, OH, USA.
- Pantelakis, S. and Labeas, G. (2000). Constant and variable amplitude fatigue damage of laminated fibrous composites. In: Failure Analysis of Industrial Composite Materials (Gdoutos, E.E., Pilakoutas, K. and Rodopoulos, C.A., Eds.), pages 247-298. McGraw-Hill, New York.
- Perreux, D and Thiebaud, F. (1994). Comportement mécanique quasi-statique sous sollicitations biaxiales de tubes composite stratifiés. La Recherche Aéronautique, Vol. 2, 115-124.

- Perreux, D and Thiebaud, F. (1995). Damaged elasto-plastic behaviour of $[+\phi, -\phi]_n$ fibre-reinforced composite laminates in biaxial loading. *Composite Science and Technology*, Vol. 54, 275-285.
- Perreux, D. and Joseph, E. (1997). The effect of frequency on the fatigue performance of filament-wound pipes under biaxial loading: experimental results and damage model. *Composites Science and Technology*, Vol. 57, 353-364.
- Perreux, D. and Suri, C. (1997). A study of the coupling between the phenomena of water absorption and damage in glass/epoxy composite pipes. *Composites Science and Technology*, Vol. 57, 1403-1413.
- Perreux, D., Choqueuse, D. and Davies, P. (2002). Anomalies in moisture absorption of glass fibre reinforced epoxy tubes. *Composites Part A*, Vol. A33, 147-154.
- Peters, S.T., Humphrey, W.D. and Foral, R.F. (1999). *Filament Winding Composite Structure Fabrication*, 2nd Edition. Society of the Advancement for Material and Process Engineering (SAMPE) Publishing, Covina.
- Plumtree, A. and Cheng, G.X. (1999). A fatigue damage parameter for off-axis unidirectional fibre-reinforced composites. *International Journal of Fatigue*, Vol. 21, 849-856.
- Potter, K.D., Guild, F.J., Harvey, H.J., Wisnom, M.R. and Adams, R.D. (2001). Understanding and control of adhesive crack propagation in bonded joints between carbon fibre composite adherends: I. Experimental. *International Journal of Adhesion & Adhesives*, Vol. 21, 435-443.
- Pradhan, S.C., Iyengar, N.G.R. and Kishore, N.N. (1994). Parametric study of interfacial debonding in adhesively bonded composite joints. *Composite Structures*, Vol. 29, 119-125.
- Raju, L.S. (1987). Calculation of strain-energy release rates with higher order and singular finite elements. *Engineering Fracture Mechanics*, Vol. 28., 251-274.
- Reedy, E.D., Jr. and Guess, T.R. (1991). Tubular lap joints for wind turbine applications: test and analysis. In: *Proceedings of the 10th ASME Wind Energy Symposium*, pages 47-52, Houston, TX, USA. American Society of Mechanical Engineers (ASME), New York.

- Reedy, E.D., Jr. and Guess, T.R. (1993). Composite-to-metal tubular lap joints: strength and fatigue resistance. *International Journal of Fracture*, Vol. 63, 351-367.
- Resolution Performance (2001). Technical Bulletin SC:2441-01: EPON Resin 826 with EPI-CURE Curing Agent 9551. Resolution Performance Products LLC, Houston, TX, USA.
- Rispler, A.R., Tong, L., Steven, G.P. and Wisnom, M.R. (2000). Shape optimisation of adhesive fillets. *International Journal of Adhesion & Adhesives*, Vol. 20, 221-231.
- Rodopoulos, C.A. (2000). Theoretical and experimental composite strength evaluation. In: *Failure Analysis of Industrial Composite Materials* (Gdoutos, E.E., Pilakoutas, K. and Rodopoulos, C.A., Eds.), pages 3-50. McGraw-Hill, New York.
- Rosen, B.W. and Hashin, Z. (1987). Analysis of material properties. In: *Engineered Materials Handbook Vol.1: Composites* (Dostal, C.A., et al., Eds.), pages 185-205. ASM International, Materials Park.
- Rosenow, M.W.K. (1984). Wind angle effects in glass fibre-reinforced polyester filament wound pipes. *Composites*, Vol. 15, 144-152.
- Rousseau, J. (1997). Une approche expérimentale et théorique de l'effet de procédé de fabrication sur les performances d'une structure composite: cas de l'enroulement filamentaire. *Diplôme de Docteur thèses, Sciences pour l'Ingénieur, l'Université de Franch-Comté.*
- Rousseau, J., Perreux, D. and Verdière, N. (1997). Motifs d'enroulement et endommagement dans les tubes composites verre/epoxy. *Mécanique Industrielle et Matériaux*, Vol. 50, 155-159.
- Rousseau, J., Perreux, D. and Verdière, N. (1999). The influence of winding patterns on the damage behaviour of filament-wound pipes. *Composite Science and Technology*, Vol. 59, 1439-1449.
- Rybicki, and Kanninen, (1977). A finite element calculation of stress intensity factors by a modified crack closure integral. *Engineering Fracture Mechanics*, Vol. 9, 931-938.

- Semb, G., Nygard, P. and Gustafson, C.G. (1995). Optimization of adhesive bonded joints in GRP pressure piping. In: Proceedings of the 10th International Conference on Composite Materials – ICCM-10 (Poursartip, A. and Street, K.N., Eds.), Vol. 3, pages 503-509, Whistler, BC, Canada. Woodhead Publishing Ltd, Cambridge.
- Shi, Y.P. and Cheng, S. (1993). Analysis of adhesive-bonded cylindrical lap joints subjected to axial load. *Journal of Engineering Mechanics*, Vol. 119, 584-602.
- Simmons, P. (1990). Threaded pin and box construction for composite tubulars. United States Patent, No. 4,943,094.
- Simmons, P. (1995). Composite threaded pipe connectors and method. United States Patent, No. 5,398,975.
- Smith, L.V. and Swanson, S.R. (1995). Failure of braided composite cylinders under biaxial tension. *Journal of Composite Materials*, Vol. 29, 766-784.
- Smith, L.V. and Swanson, S.R. (1997). Design of a cylindrical specimen for biaxial testing of composite materials. *Journal of Reinforced Plastics and Composites*, Vol. 16, 550-565.
- Soden, P.D., Leadbetter, D., Griggs, P.R. and Eckold, G.C. (1978). The strength of filament wound composite under biaxial loading. *Composites*, Vol. 9, 247-250.
- Soden, P.D., Kitching, R. and Tse, P.C. (1989). Experimental failure stresses for $\pm 55^\circ$ filament wound glass fibre reinforced plastic tubes under biaxial loading. *Composites*, Vol. 20, 125-135.
- Soden, P.D., Kitching, R., Tse, P.C., Tsavalas, Y. and Hinton, M.J. (1993). Influence of winding angle on the strength and deformation of filament-wound composite tubes subjected to uniaxial and biaxial loads. *Composites Science and Technology*, Vol. 46, 363-378.
- Soden, P.D., Hinton, M.J. and Kaddour, A.S. (1998). A comparison of the predictive capabilities of current failure theories for composite laminates. *Composites Science and Technology*, Vol. 58, 1225-1254.
- Soden, P.D., Kaddour, A.S. and Hinton, M.J. (2004). Recommendations for designers and researchers resulting from the world-wide failure exercise. *Composites Science and Technology*, Vol. 64, 589-604.

- Spencer, B. and Hull, D. (1978). Effect of winding angle on the failure of filament wound pipe. *Composites*, Vol. 9, 263-271.
- Srinivas, M.V., Dvorak, G.J. and Prochazka, P. (1999). Design and fabrication of submerged cylindrical laminates – II. Effect of fibre pre-stress. *International Journal of Solids and Structures*, Vol. 36, 3945-3976.
- Stubblefield, M.A., Yang, S., Pang, S.S. and Lea, R.H. (1998). Development of heat-activated joining technology for composite-to-composite pipe using prepreg fabric. *Polymer Engineering and Science*, Vol. 38, 143-149.
- Strong, A.B. (2000). *Plastics: Materials and Processing*, 2nd Edition. Prentice Hall, Upper Saddle River.
- Sundt, J.L. (1993). Fire water systems in composite materials. In: *Proceedings of the 12th International Conference on Offshore Mechanics & Arctic Engineering – OMAE'93*, Vol. 3-A, pages 293-302. American Society of Mechanical Engineers (ASME) – Ocean, Offshore and Arctic Engineering (OOAE) Division, New York.
- Swanson, S.R., Christoforou, A.P. and Colvin, G.E. Jr. (1988). Biaxial testing of fiber composites using tubular specimens. *Experimental Mechanics*, Vol. 28, 238-243.
- Swanson, S.R. (1994). Interpretation of scaling of damage and failure in fiber composite laminates. *Journal of Thermoplastic Composite Materials*, Vol. 7, 155-164.
- Swanson, S.R. (1996). *Introduction to Design and Analysis with Advanced Composite Materials*. Prentice Hall, Upper Saddle River.
- Takayanagi, H., Xia, M. and Kemmochi, K. (2002). Stiffness and strength of filament-wound fiber-reinforced composite pipes under internal pressure. *Advanced Composite Materials*, Vol. 11, 137-149.
- Tarnopol'skii, Y.M., Kulakov, V.L., Zakrzhevskii, A.M and Mungalov, D.D. (1996). Textile composite rods operating in torsion. *Composite Science and Technology*, Vol. 56, 339-345.
- Tew, B.W. (1995). Preliminary design of tubular composite structures using netting theory and composite degradation factors. *Journal of Pressure Vessel Technology, Transitions of the ASME*, Vol. 117, 390-394.

- Thornton, D.J. (1999). Finite element analysis of fibre-reinforced composite pipeline. MSc Thesis, Department of Mechanical Engineering, University of Alberta.
- Thomsen, O.T. (1992). Elasto-static and elasto-plastic stress analysis of adhesive bonded tubular lap joints. *Composite Structures*, Vol. 21, 249-259.
- Tomblin, J., Harter, P., Seneviratne, W. and Yang, C. (2002). Characterisation of bondline thickness effects in adhesive joints. *Journal of Composites Technology and Research*, Vol. 24, 332-344.
- Tong, L, Mouritz, A.P. and Bannister, M.K. (2002). *3D Fibre Reinforced Polymer Composites*. Elsevier Science Publishing, Amsterdam.
- Tong, L. and Steven, G.P. (1999). *Analysis and Design of Structural Bonded Joints*. Kluwer Academic Publishers, Norwell.
- Toombes, G.R., Swanson, S.R. and Cairns, D.S. (1985). Biaxial testing of composite tubes. *Experimental Mechanics*, Vol. 25, 186-192.
- True, W.R. (1995). Composite wrap approved for U.S. gas-pipeline repairs. *Oil & Gas Journal*, October 1995, 67-71.
- Vasiliev, V.V. and Morozov, E.V. (2001). *Mechanics and Analysis of Composite Materials*. Elsevier Science Publishing, Amsterdam.
- Wisnom, M.R. (1999). Size effects in the testing of fibre-composite materials. *Composites Science and Technology*, Vol. 59, 1937-1957.
- Whitcomb, J.D. and Woo, K. (1993). Analysis of debond growth in tubular joints subjected to tension and flexural loads. *Computers & Structures*, Vol. 46, 323-329.
- Wolodko, J.D. (1999). Biaxial Fatigue and Leakage Characterisation of Fiber Reinforced Composite Tubes. PhD thesis, Department of Mechanical Engineering, University of Alberta.
- Wolodko, J.D., Mertiny, P., Meijer, G., Martens, M. and Ellyin, F. (2001). Development of a facility for filament winding. In: *Proceedings of the 46th International SAMPE Symposium and Exhibition* (Repecka, L. and Saremi, F.F., Eds.), Vol. 1, pages 1271-1282, Long Beach, CA, USA. Society for the Advancement of Material and Process Engineering (SAMPE) Publishing, Covina.

- Xia, M., Takayanagi, H. and Kemmochi, K. (2001). Analysis of multi-layered filament-wound composite pipes under internal pressure. *Composite Structures*, Vol. 53, 483-491.
- Xia, Z., Zhang, Y. and Ellyin, F. (2003). A unified periodical boundary conditions for representative volume elements of composites and application. *International Journal of Solids and Structures*, Vol. 40, 1907-1921.
- Zang, C. (2000). Design and analysis of composite pipe joints under tensile loading. *Journal of Composite Materials*, Vol. 34, 332-349.
- Yuceoglu, U. and Updike, D.P. (1980). Stresses in two-layer bonded orthotropic cylindrical shells. In: *Emerging technologies in aerospace structures, design, structural dynamics, and materials: presented at the Aerospace conference, Century 2-Emerging Technology conferences*, pages 53-65, San Francisco, CA, USA. American Society of Mechanical Engineers (ASME) – Aerospace Division, New York.
- Zakrzhevskii, A.M and Khitov, V.V. (1988). Effect of interweaving on the load-carrying capacity of wound thick-walled rods of composites in torsion. Translated from *Mekhanika Kompozitnykh Materialov*, Vol. 4, 676-683.
- Zhang, Y., Xia, Z. and Ellyin, F. (2004). Evolution and influence of residual stresses/strains of fiber reinforced laminates. *Composites Science and Technology*, Vol. 64, 1613-1621.

APPENDIX A

FILAMENT WINDING FACILITY¹

A.1 Overview of Winding Facility

A large capacity (production quality) filament winding facility was acquired for the fabrication of tubular composite specimens. The objectives for the facility design were to enable research oriented, efficient and complete onsite manufacturing. It was anticipated to provide a flexible production system for a wide range of part geometries, lay-up configurations and resin/fibre material systems. The largest projected prototype structures are of a total length of 3.6 m and an inside diameter of 0.6 m. As a research facility a high degree of controllability and reproducibility of manufacturing parameters is considered essential. Hence, numerical control capabilities are required for resin bath temperature, active fibre tensioning, winding paths and curing. Providing user-friendly operations, and a safe and healthy work environment were further objectives during the facility conceptualisation.

The facility consists of three core components, i.e. a computer controlled filament winding machine (McClellan-Anderson WMS-4 Axis), a computer controlled fibre-tensioning system for dispensing 10 fibre tows, and a custom designed industrial curing oven with rotating part and digital control capabilities (Wisconsin Oven). The production facility is centred around the computer controlled filament winder (shown in Fig.A.1.1), which has a maximum part/mandrel capacity of 900 kg. Handling of large parts/mandrels is made possible by the overhead beam design of this machine. The winding machine provides 4-axis computer motion control (rotation, traversing carriage,

¹ A version this chapter appeared as: Wolodko, J., Mertiny, P., Meijer, G., Martens, M. and Ellyin, F. (2001). Development of a facility for filament winding. Proceedings of the 46th International SAMPE Symposium and Exhibition, pages 1271-1282, Long Beach, CA, USA. Society for the Advancement of Material and Process Engineering.

pay-out eye feed and pay-out eye rotation). Manufacturer-provided software is available for the offline generation of winding patterns and winding control code.

The facility layout was designed to occupy an 8.5 m by 10.5 m workspace as presented in Fig.A.1.2. The following stations are passed along the fibre path: Fibre creels are mounted onto the fibre-tensioning unit providing tension for 10 creels simultaneously (item 1a). A redirection stand (item 1b) guides the fibre strands to a common level and changes their direction by 90° towards the temperature controlled drum-type resin bath (item 2), where resin impregnation occurs. From the resin bath, fibres run to the carriage arm of the filament winder (item 3a), through the pay-out eye and finally onto the mandrel (item 4) mounted in the chucks of the filament winder.

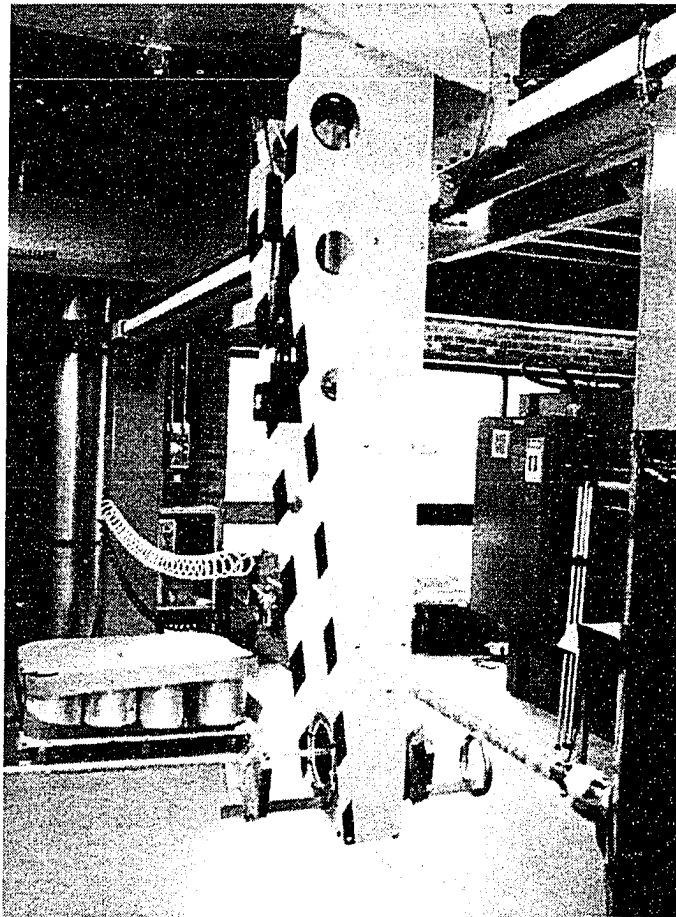


Figure A.1.1: 4-axis computer controlled filament winding machine.

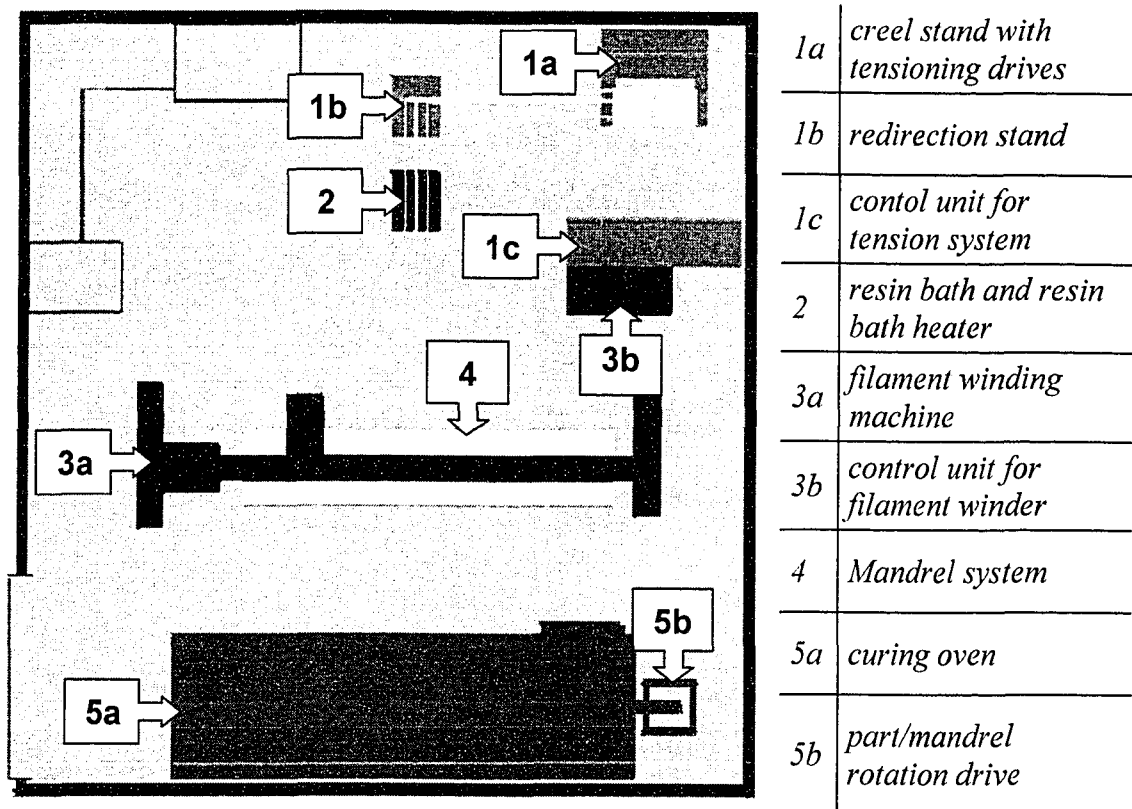


Figure A.1.2: Overview of filament winding facility (Wolodko et al., 2001).

After completion of the winding process, the winding mandrel is removed from the winder and placed onto a cart, which also serves as a mandrel support inside the curing oven (item 5a). The curing oven is digitally controlled thus allowing for a wide range of thermal cure profiles. A drive system was installed to rotate mandrel and part during the curing process (item 5b). This is to avoid ovality and excessive resin drip-off, and to promote a uniform surface finish. After the completion of curing, parts are allowed to cool down before they are taken to another laboratory for mandrel extraction and testing.

A.2 Detailed Description of Facility

2.1 Fibre-tensioning System

Installation of glass-fibre creels:

Glass fibre creels are conventionally prepared for centre-pull procedures with stationary creel packages. Such a setup enables the transfer from package to package by

splicing the inside fibre end of a new creel to the outside fibre end of the creel currently in use. The main benefit of this arrangement is to reduce machine downtime. Hence, centre-pull procedures are most suited for continuous production processes. On the downside, centre-pull procedures introduce strand twist. In order to avoid strand twist the present winding facility was designed to utilise outside-pull creels. Centre-pull creels, which are commonly supplied along with glass-fibre materials, were therefore equipped with disposable 76.2 mm diameter cardboard cores. The creels are mounted onto the drive shaft with centring rings, and are clamped into place using faceplates and a lock nut system. Utilising outside-pull creels also facilitated tow tensioning by applying torque to the creel core instead of applying friction to the fibres. Fibre damage such as filament breakage and fuzzing is thus minimised which enhances the quality of the fabrication process.

Fibre-tensioning drive and control system:

For the application and control of tow tension and take-up during winding a fibre-tensioning unit was developed and fabricated in-house (shown on the left-hand-side of Fig.A.2.1). Tension of up to 90 N can be imposed upon each individual tow. Fibres are tensioned by applying torque to the creels using a series of cost-effective, but reliable, 746 W asynchronous AC motors. Each motor is connected to a creel drive shaft via a cogged belt (shown in the middle of Fig.A.2.1). Motors are powered by RISC-processor driven controller units that regulate the power feed to the motors and receive feed back such as motor position. This motor/controller combination is ideal for speed, torque and position control. A Control Techniques AC regenerative drive unit was also incorporated into the system to absorb the energy from the braking process, which is fed back into the power supply system.

The controller units have a menu-based I/O interface to directly input controller parameters and use a common format programming language to code logical operations. Both parameters and programs may be set and monitored from a personal computer. The 10 controller units and the personal computer communicate via a serial port RS232 connection. Custom designed software was employed to provide a user-friendly interface for the operation of the tensioning system. Using the control panel software on the

personal computer, an operator can start or stop all or individual creel drives, set tension values in real time, adjust a tow breakage detection criteria and monitor each drive status. Tensioning system calibration is done on separate control panels that allow independent control of each creel drive motor parameter, motor direction control, and input and saving of calibration data.

The controller units are programmed to regulate tension via torque control. The outside creel radius, R_{creel} , is measured close to the nip point using a follower arm that is directly coupled to a rotational potentiometer (see right-hand-side of Fig.A.2.1). The resulting voltage signal, U_r , is received by the corresponding controller unit and converted to a radius value based on calibration data according to the following equation:

$$R_{creel} = B_2 U_r^2 + B_1 U_r + B_0 \quad (\text{A.2.1})$$

where B_i are the corresponding calibration constants.

The radius value is multiplied by the requested tension, F_{tow} , to provide an ideal torque value at the creel, T_{ideal} , for a frictionless system according to

$$T_{ideal} = F_{tow} R_{creel} \quad (\text{A.2.2})$$

Due to bearing/belt/motor friction as well as friction along the fibre path the required actual creel torque, T_{actual} , is determined using a second order calibration function, i.e.

$$T_{actual} = C_2 T_{ideal}^2 + C_1 T_{ideal} + C_0 \quad (\text{A.2.3})$$

where C_i are the calibration constants.

Calibration constants were determined utilising a specialised large-diameter calibration mandrel. As shown in the schematic in Fig.A.2.2 the calibration mandrel is equipped with a torsion load cell, which is located in between the actual mandrel body and the shaft to be connected to winding machine drive. During winding of fibre onto the calibration mandrel the fibre tension is monitored in real time, and the measured torque (converted to fibre tension) is sent to a data acquisition system via a telemetry unit mounted on the shaft near the load cell.

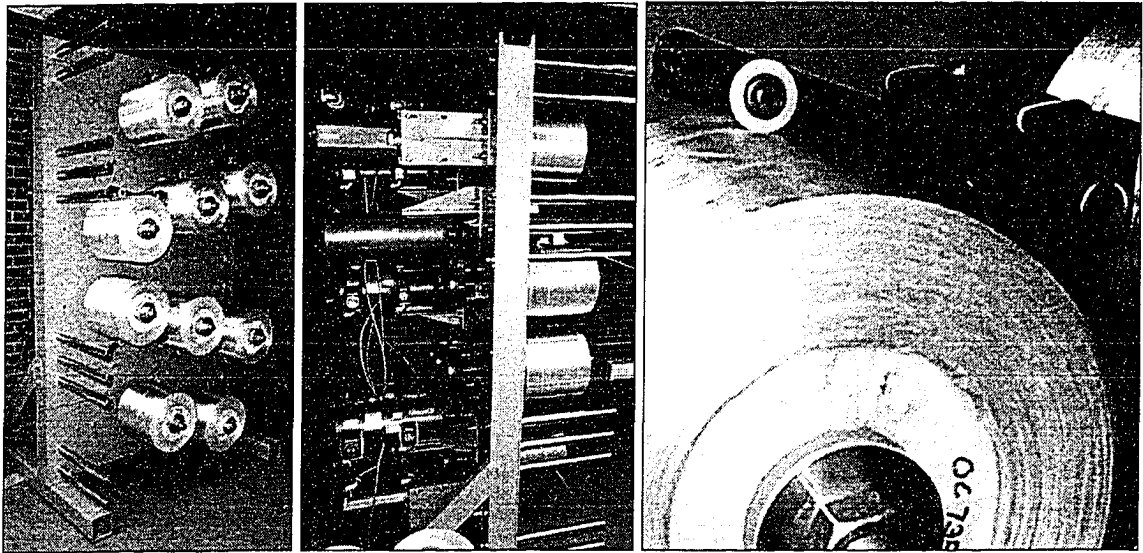


Figure A.2.1: Creel stand with modified centre-pull creels and follower arm system (tensioning motors on backside) (Wolodko et al., 2001).

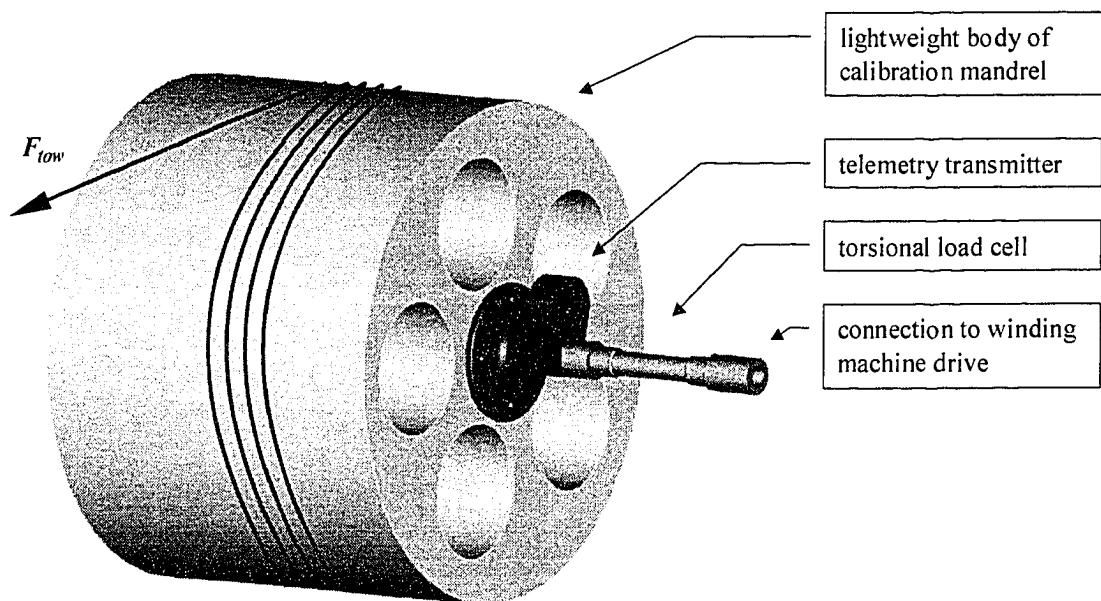


Figure A.2.2: Schematic of fibre tension calibration unit (Wolodko et al., 2001).

Besides determining motor torque requirements the developed controller program was designed to detect irregular conditions, i.e. tow breakage and the need for creel replacement. Tow breakage is detected when the direction of creel rotation reverses for a specific angular displacement during a program cycle, $\alpha_{critical}$. The position sensors of the fibre tensioning motors constantly measure direction of creel rotation and angular displacement, and corresponding data are fed to the controller units. The second alarm condition, i.e. the creel replacement alarm was incorporated to allow for the replacement of an exhausted fibre supply with only minor interruption of the winding sequence. This condition is detected when the creel radius falls below a critical value. Values for triggering these alarm conditions are fully adjustable for various creel sizes and fibre tensions. Either of the alarm conditions causes the stoppage of the affected creel drive system, whereas the remaining drives stay activated, meaning tow tensioning is maintained. At the same time the filament winding machine is automatically put into a hold condition. The flowchart schematic in Fig.A.2.3 illustrates the underlying logic. After a creel has been replaced or the broken tow has been repaired (i.e. broken ends are

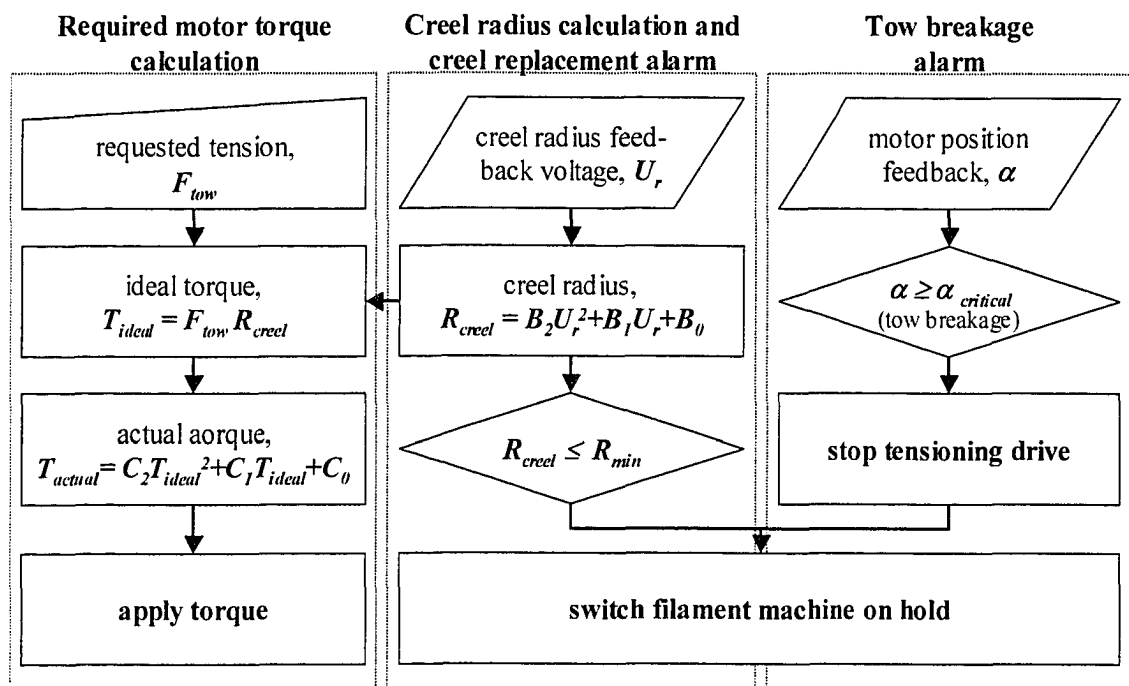


Figure A.2.3: Flowchart of tensioning system control operation (Wolodko et al., 2001).

spliced together), both the tensioning system and the winding machine can be enabled from their respective control panels. The winding sequence resumes at the same location on the mandrel, hence avoiding incomplete coverage or removal of wet fibre strands.

Redirection stand:

The main purpose of the redirection stand is to maximise the fibre path length in the limited workspace. As shown in Fig.A.1.1, the critical distance between the resin bath and winding machine is maximised due to the use of the redirection stand, i.e. the maximum change in angle of the fibre path is ultimately reduced (particularly for long parts). Consequently, forces acting transverse to the tows and associated friction causing fibre damage are decreased.

Redirection is accomplished using two sets of 76.2 mm diameter pulleys (see Fig.A.2.4). Chrome-plated guide bars on the tensioning stand ensure that each of the fibre tows enter the redirection stand at the appropriate height. These pulleys are surface treated (powder coated) to prevent wear and damage to the fibres. In the redirection stand, cantilevered pulleys are used to redirect the upper five tows vertically downward and the lower five tows vertically upwards. (Note that these cantilevered pulleys were also designed to allow for an alternative method of tow tension measurement by using cantilever beam load cells.) At the midpoint, the tows are redirected towards the resin bath (i.e. at 90° to the input fibre direction), spaced at a uniform distance of 12.7 mm.

Bobbins with coloured glass fibre threads (i.e. Fil-Tec 66 ^g/_{1000m} dyed fibreglass yarn) are also mounted onto the redirection stand. These fine threads are tensioned by a simple friction system, and introduced into the fibre path and impregnated with resin. The dyed yarns join the winding band while passing through the filament winder pay-out eye, where they precisely mark each side of the winding band. This allows for an optical identification of winding bandwidths, and for the detection of overlapping and gapping during processing and after curing.

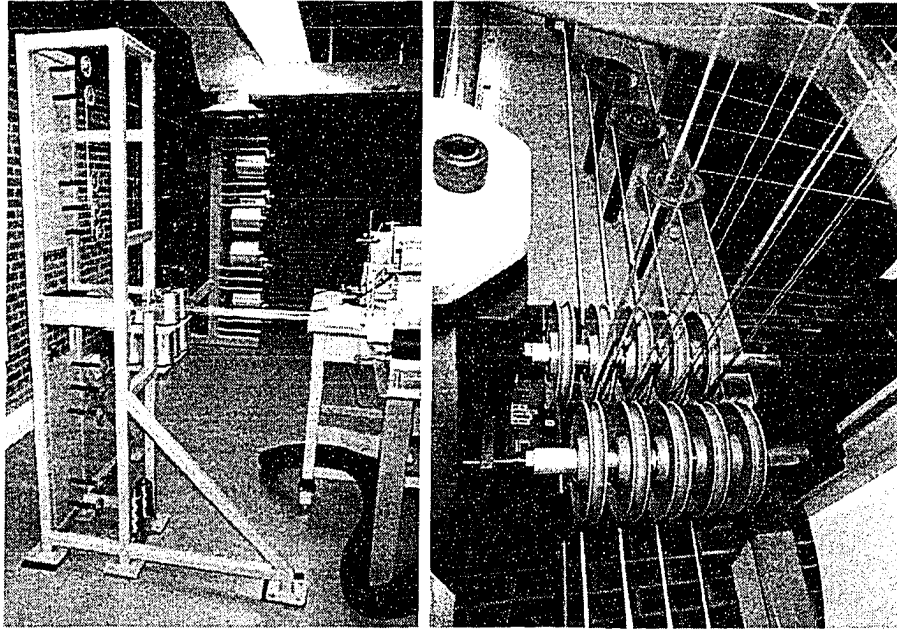


Figure A.2.4: Fibre redirection stand; (left) overall view and (right) close-up of cantilevered pulley assembly (Wolodko et al., 2001).

2.2 Resin Bath

A commercially available (McClellan-Anderson) drum type resin bath with a capacity of 3 litres was reengineered to meet the quality requirements of this facility (see Fig.A.2.5). The resin bath is equipped with a water jacket connected to a computer controlled heating system. This allows for the adjustment of a constant resin temperature, and thus resin viscosity. Bath temperatures can be controlled ranging from room temperature ($\sim 20^{\circ}\text{C}$) to 90°C . The resin bath is not permanently mounted to the laboratory floor, but is movable to accommodate various mandrel lengths.

The resin bath features a flat aluminium inlet roller, which guides the individual tows towards the drum. This roller replaced an initially stationary bar-type guide and comb, which were found to produce a fair amount of fibre breakage, leading to fuzzing and spooling of filaments around the drum. From the inlet roller, tows pass over the drum, which is kept rotating due to the friction between fibres and drum, picking up a thin resin film from the resin tank. The thickness of the resin film depends on the adjustable gab

between the drum and a so-called doctor blade. Fibre tows are spread out over the drum surface and consequently coated with resin material. At the fibre outlet of the resin bath, a stationary bar-type guide and comb are located. The latter is required to prevent tows from horizontal sliding motions caused by the carriage movement of the FW-machine. Due to the lubricating effect of the liquid resin material, fibre damage caused by this bar and comb pair was found to be insignificant.

A ventilation system was installed to the resin bath to remove any harmful fumes. To ease cleaning and to reduce the amount of solvents a polymeric insert was used to line the resin bath. Inserts were custom vacuum moulded and are disposable after use. For improved heat transfer the gap between the metal tub containing the water jacket heating and the polymer liner was filled with water.

2.3 Mandrel System and Curing

Even though the filament winding facility and the curing oven were conceptualised for large-scale parts up to lengths of 3.6 m, a flexible mandrel system was required to accommodate various mandrel sizes. A unique interlocking mandrel system was designed that facilitates the production of large-scale specimens and also allows for simultaneous curing of multiple mandrels of short lengths. Used for the fabrication of model size specimens, mandrels of short length were utilised to ease handling and lower mandrel extraction forces. Moreover, multiple specimen configurations are producible in one winding session, thus providing ideal conditions for a research environment.

As shown in Fig.A.2.6, several mandrels can be connected for curing. Coupler flanges are attached to each end of a mandrel using a pin-connection. The coupler flanges are also used to mount a mandrel into the chucks of the winding machine; clamping onto the mandrel surface is therefore avoided. After winding of an individual part has been completed the part/mandrel is removed from the filament winding machine and is placed onto roller blocks on the oven cart. The cart is then pushed into the oven, and the outermost mandrel coupler is attached to a rotating shaft of the part/mandrel rotation device. Subsequent parts/mandrels are connected to the preceding mandrel in the same fashion. After the last part/mandrel has been added to the string of mandrels, the curing

oven is closed and the curing cycle is started. Parts are kept in constant rotation avoiding resin dripping and ovality of the final product.

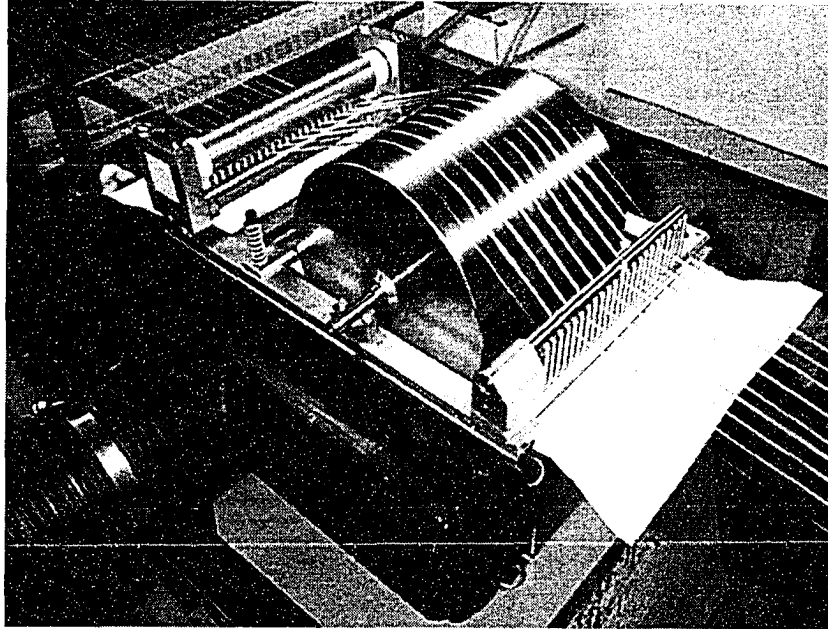


Figure A.2.5: Heated drum-type resin bath with ventilation nozzle, inlet roller and polymeric liner (Wolodko et al., 2001).

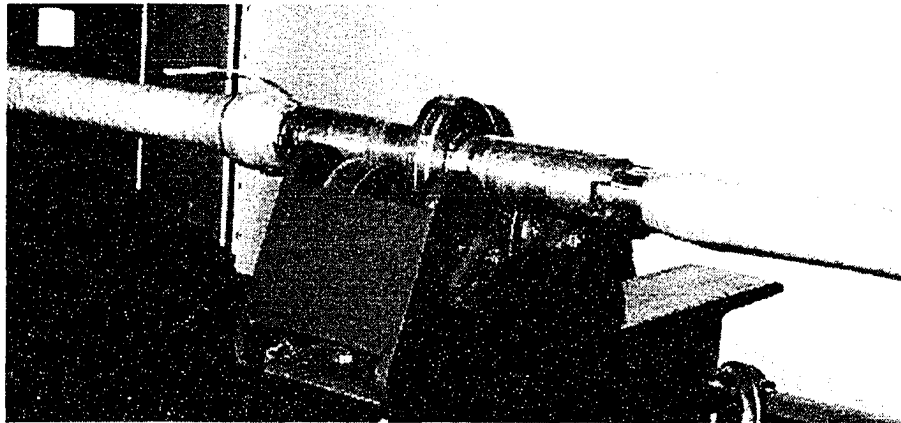


Figure A.2.6: Roller blocks and coupled mandrels on oven cart (Wolodko et al., 2001).

APPENDIX B

BANDWIDTH MEASUREMENT TECHNIQUES¹

B.1 Bandwidth Measurement using Tracer Threads

To enable the measurement of winding bandwidths and the amount of overlap or gapping between adjacent winding bands, several 38.1 mm diameter specimens were permanently marked during winding. A blue and a green tracer thread indicated each shoulder of a deposited band respectively. Two different coloured glass-fibre threads of 0.066 g/m linear weight were passed through the resin bath. In contrast to the active tension control of the much heavier fibre tows, the threads were only slightly tensioned by a simple friction system. To ensure that the threads precisely mark the shoulders of a band and do not get entangled with the heavier glass-fibre tows, the threads were separated from the tows by a large gap. At the last possible stage, while passing through the last comb located before the pay-out eye of the filament winder, the threads were positioned adjacent to the outermost tows. This resulted in the tracing of the band shoulders.

After curing, the translucent nature of the fibre/resin compound allowed for a manual bandwidth measurement. Using a calliper gauge, the width of the different bands along the tube length could be determined even in subjacent layers. It is of great importance to identify the corresponding tracers and band. It requires an experienced operator to locate the proper pair of tracer threads knowing the interweaving structure and an estimated bandwidth. It is worth pointing out that this measurement procedure is time consuming, and mistakes are easily made if work is not performed with the necessary care.

¹A version of this chapter appeared as: Mertiny, P. and Ellyin, F. (2001). Selection of optimal processing parameters in filament winding. In: Proceedings of 33rd International SAMPE Technical Conference, pages 1084-1095, Seattle, WA, USA. Society of the Advancement of Material and Process Engineering.

Furthermore, this technique can only be applied to fibre types and resin systems with a high degree of translucency. Knowing these shortcomings, a more sophisticated method using image analysis was developed.

B.2 Bandwidth Measurement using Image Analysis

For improved repeatability and automated processing of winding bandwidth measurements, an image analysis system was developed. The analysis process can be divided into two operations: (a) in-situ image acquisition and storage during the winding procedure, and (b) a post processing operation. The installed hardware for the imaging system is shown in Fig.B.2.1.

In-situ image acquisition:

A colour CCD camera was mounted onto an adjustable fixture attached to the carriage arm of the filament winding machine. By these means, images of the mandrel and part were taken at the carriage arm position. Also mounted onto the same fixture was a photodiode, which travelled along the bottom of the carriage bed (crossbeam) of the filament winding machine. Using reflective marker tape the photodiode was triggered at certain positions along the axis of mandrel rotation. The exact position was determined by a permanent measuring tape applied to the crossbeam.

Video images were taken continuously and were displayed on a monitor at the winding system control stand. A PC based image acquisition system read the video signal via a frame grabber card and the signal from the photodiode via the PC parallel port. In the event of triggering, the momentary image was transferred from the frame grabber buffer to the computer extended memory allowing for the storage of 120 images (620×476 pixels resolution, 24 bit per pixel, TGA file format). After completion of the winding sequence, images were written to a hard drive for batch mode post processing.

Post processing operation:

In the first step of post processing, images were converted to the TIFF file format to facilitate the use of the Scion Image[®] analysis software. This software supports many standard image-processing functions (e.g., spatial calibration, measuring user-defined

regions-of-interest, editing functions). Most advantageous is the built-in Pascal-like macro language, which allows Scion Image[®] to be customised by the user. A program routine (macro) was programmed for the imaging software that automatically determines bandwidth values from a specified number of images. Before the start of the batch mode operation the operator was prompted to determine and enter into the program: a scale factor (i.e. amount of pixels per length scale), the mandrel diameter, the winding angle, a colour threshold value and certain coordinates (i.e. a reference line, which is the mandrel face closest to the pay-out eye; positions of two line selections for later bandwidth measurements; and an offset value for the geometrical fibre/mandrel contact point).

It was found that the green component of an RGB (red, green, blue colour coded) image provides the best contrast for image analysis. During batch mode operation the green component was therefore separated and converted into a B/W (black-and-white) image based on the entered threshold value that was adjusted in such a way as to provide a 100% black background. Note that in this study the captured background was simply a black cover on the floor space under the filament winding machine. A typical image before and after conversion into the B/W mode is shown in Fig.B.2.2.

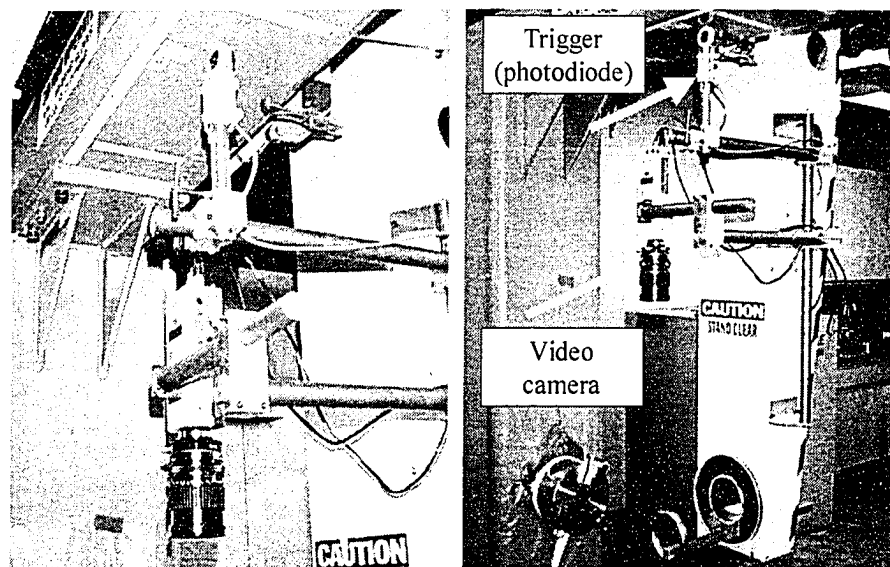
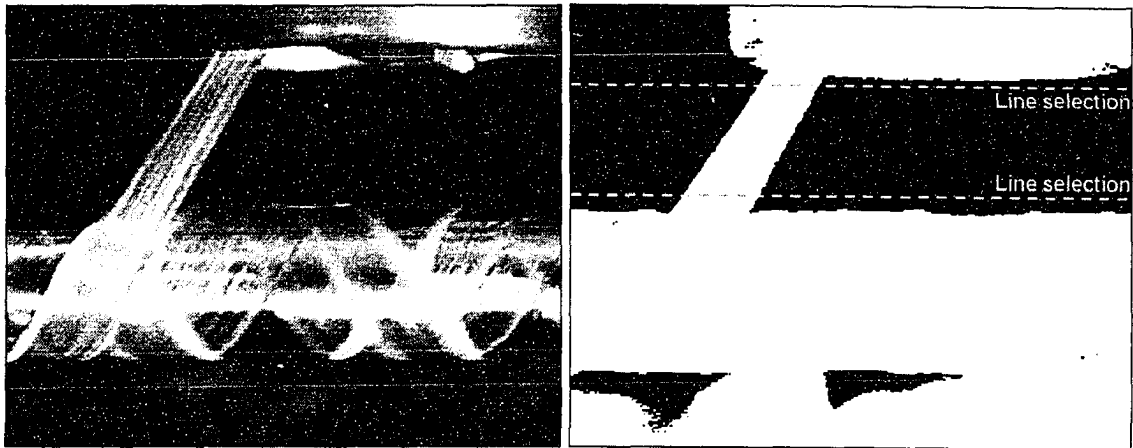


Figure B.2.1: Input devices of image system mounted on carriage arm of filament winder (Mertiny and Ellyin, 2001).



*Figure B.2.2: Image before (left) and after conversion into black-and-white mode (right)
(Mertiny and Ellyin, 2001).*

An average colour value was determined along two line selections, which were placed across images according to the values entered by the operator (i.e. located in between the pay-out eye and the mandrel/part as shown in Fig.B.2.2). In these B/W images the average colour value of the line selections (of which the length is known by the entered scale factor and the image width) is directly proportional to the bandwidths at the given line position. Using this length information and the applied winding angle an 'apparent bandwidth' (i.e. at the geometrical fibre/mandrel contact point) was determined from certain basic geometrical considerations. Before proceeding to the analysis of the subsequent image the bandwidth data were added to a list of results. After completion of the batch mode operation, the list of data was exported to a spreadsheet program for further evaluation.

Bandwidth values from the image analysis were plotted versus the travelled carriage distance (or an index position) resulting in a continuous graph as shown in Fig.B.2.3. In this study, five images were taken evenly spaced between two turnaround points of the carriage (for 38.1 mm diameter mandrels with 787 mm length). Generally the bandwidth recording was not constant. In fact it varied significantly depending on the position at which the images were taken.

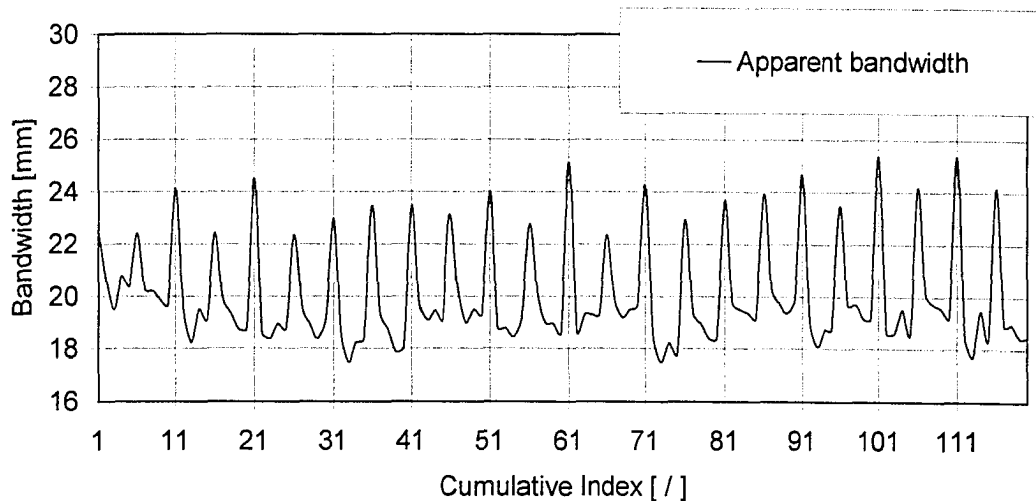


Figure B.2.3: Bandwidth values from image analysis plotted versus the travelled carriage distance given as an index number (Mertiny and Ellyin, 2001).

Peaks in Fig.B.2.3 indicate the first image taken after a carriage direction reversal. Here the carriage and the pay-out eye were already in the final position and speed for travelling along the mandrel, but the fibre band is still in an adjustment period and is therefore significantly larger than in the following four positions. To illustrate the bandwidth adjustment, the average bandwidth values were calculated for every position of the carriage travelling away from and towards the home position of the machine. Such a graph is shown in Fig.B.2.4. For further analysis only bandwidth values taken at positions #2-5 were used to calculate an average bandwidth for a particular specimen. Values obtained from position #1 were omitted (Note that sections affected by the mandrel turnaround and bandwidth adjustment were not used for testing but discarded.).

B.3 Comparison of Bandwidth Measurement Routines

From Fig.B.3.1 it can be observed that different camera and lighting settings (e.g. lens aperture, illumination) resulted in significant changes in image contrast. In order to precisely detect the edge of a band, a high contrast is favourable. But, different camera and lighting settings also influenced the bandwidth measurement when using the image

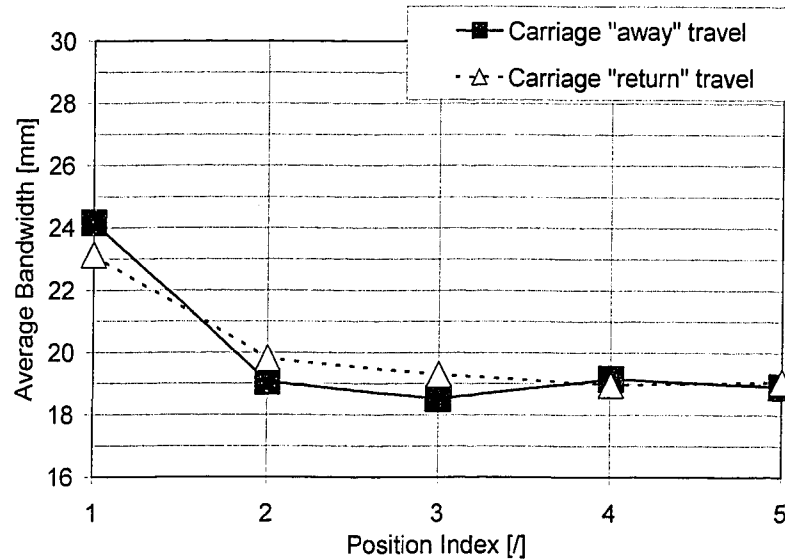


Figure B.2.4: Average bandwidth values calculated for every position of the carriage travelling away from and towards to the home position of the machine (Mertiny and Ellyin, 2001).

analysis system. From Fig.B.3.2 it can be observed that a change in the camera and lighting setting from “A” (low light intensity) to “B” (high light intensity) resulted in an increase of the measured average bandwidth of approximately 1 mm. Hence, attention was paid to keep settings constant and to provide a uniform illumination for bandwidth analysis and control.

In Fig.B.3.2 results from two $[\pm 60_3]_T$ specimens (38.1 mm diameter mandrel, made from tows of 0.735 g/m) wound with two different winding tensions are presented. It can be observed that bandwidth measurements obtained using tracer threads were lower than the results from image analysis. This difference was attributed to the fact that the image system does not capture any fibre motion after the fibres have been placed onto the mandrel. Furthermore, a calculated ‘apparent bandwidth’ is only based on geometrical considerations. Fibre deposition altered by the resin wedge at the fibre/mandrel contact point, as well as fibre motion due to the deposition of subsequent layers and lag winding (i.e. winding against an already deposited fibre band) cannot be captured by the presented image analysis system. Hence, results from the two measurement routines are not

unconditionally comparable. However, the image analysis system provided extended capabilities for repeatable, automated bandwidth measurement at distinct locations.

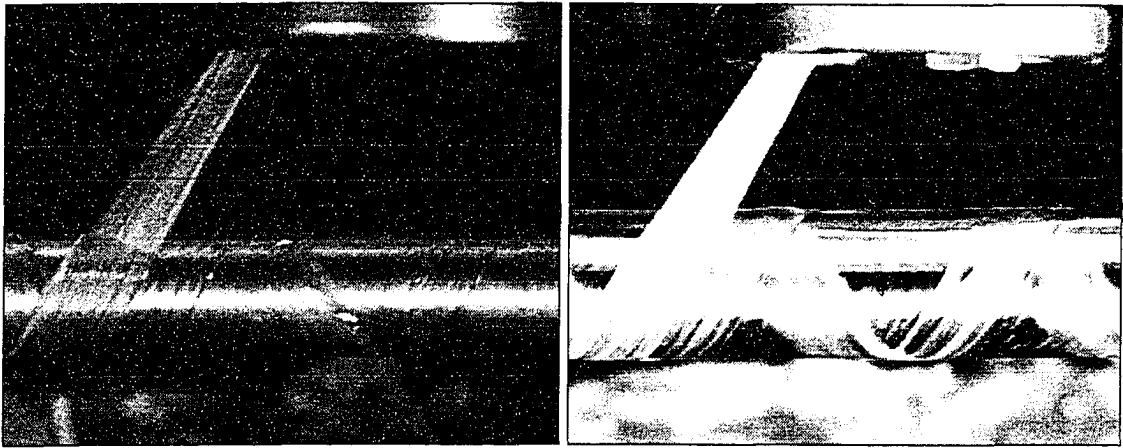


Figure B.3.1: Images taken at identical positions with camera and lighting settings “A” (left, low light intensity) and “B” (right, high light intensity) (Mertiny and Ellyin, 2001).

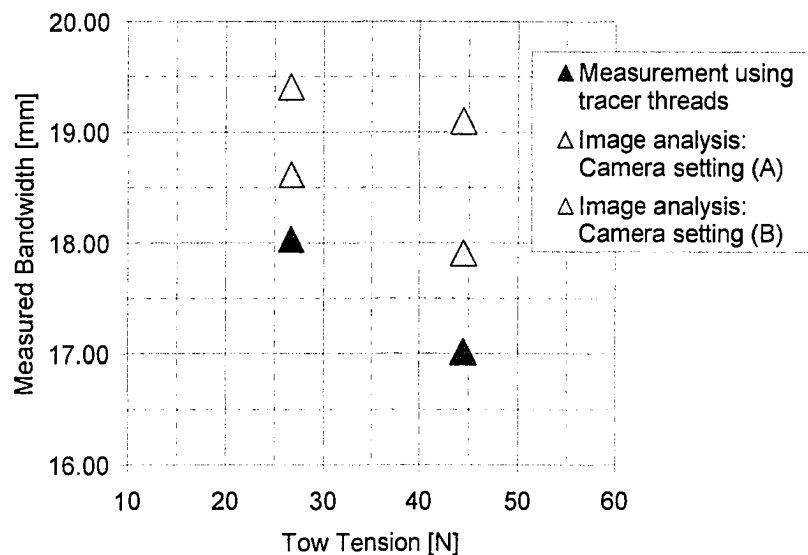


Figure B.3.2: Bandwidths for various tow tensions using different measurement techniques (Mertiny and Ellyin, 2001).

APPENDIX C

PROTOTYPE-SCALE TESTING APPARATUS

C.1 Design Requirements

Due to the greatly increased dimensions of prototype pipe a large-scale testing apparatus was required for the completion of an experimental study. Such a device basically has to emulate the functionality of the testing apparatus employed for the testing of model-scale specimens (see Chapter 3: Subsection 3.2.1, as well as Ellyin and Wolodko, 1997; and Wolodko, 1999). Namely, the device is to impose biaxial stress states upon tubular specimens using internal pressurisation and axial loading. In addition to biaxial testing the large-scale testing apparatus is also to be used for the extraction of mandrels from prototype-size parts. It was a design requirement to provide for maximum specimen dimensions of 0.6 m and 3.7 m in diameter and length respectively, and the ability to subject specimens to internal pressures of up to 70 MPa.

For safety reasons a liquid medium must be used for pressurisation. Since specimens are to be tested up to failure (i.e. the fluid cannot be recovered after testing), water was chosen as the hydraulic medium based on cost and environmental considerations. Providing cyclic test capabilities with reasonably high loading frequencies was found to be prohibitive. This is due to high pressures, potentially large internal specimen volumes and associated high flow rates that would require substantial pumping power and control capacities (i.e. pressure intensifier). It was therefore considered sufficient to provide for monotonic test capabilities. It was considered desirable that the large-scale testing device permits for single-handed operation. Finally, the safety of the operator and any bystanders had to be ensured during specimen installation and testing.

It was determined that the testing machine's control system must provide accurate and repeatable control of biaxial loading ratios and a wide range of data acquisition

capabilities. To provide an operator with a high degree of flexibility regarding test conditions, a programmable control software environment was considered essential.

C.2 Apparatus Description

Following the above requirements a testing apparatus was developed and fabricated in-house. (In addition to the author the following individuals were primarily involved in the conceptualisation, design and fabrication of this testing device: F. Ellyin, B. Faulkner, K. Graf, G. Meijer, R. Petersen, J. Wolodko, and Z. Xia.) The testing apparatus consists of three basic components: the load frame, the load application system and the control and data acquisition computer. In the following the various components of the testing apparatus are presented. Note that a brief overview of the testing device was given earlier, see Chapter 3: Subsection 3.2.3.

C.2.1 Structural Components

Load frame:

The experimental investigation of high-pressure large-diameter pipe requires the testing machine to sustain substantial axial forces (e.g. under pure hoop or axial tensile loading conditions). Moreover, the projected dimensions of prototype structures further increase demands towards stiffness and strength of the load-bearing structure. Hence, a closed load frame of considerable dimensions was designed to house the specimen and the hydraulic actuator. The load frame provides a maximum space for specimen installation of 3.7 m by 0.8 m in length and width respective. Having a horizontal orientation the load frame consists of two crossheads resting on two solid rails (see Fig.C.2.1). The latter are supported by a number of columns that are attached to the concrete foundation. Both rails are equipped with bores, which are used to affix the crossheads utilising 50 mm diameter steel pins. To account for high bearing loads which the pins may impose upon the bore surfaces during testing, the rails feature a rectangular cross section that offers a 229 mm bore length. Moreover, bores and the top surfaces of both rails were precision-machine to ensure parallelism of crossheads and thus proper specimen alignment. One crosshead is fixed at one end of the load frame, where it houses

the hydraulic actuator for the application of axial load. At the other end of the testing machine a moveable crosshead can be equipped with various mounting plates. This crosshead has been designed to accommodate tubular parts up to 600 mm in diameter (i.e. the maximum capacity of the filament winder with respect to parts' outside diameter).

An overhead hoist system was installed to assist during the installation and de-installation of mounting plates and specimens. Sheet metal plates and two hydraulically actuated covers completely enclose the load frame during testing, thus ensuring the protection of personnel from debris in case of a burst failure.

Mounting plates:

For testing and mandrel extraction two different types of mounting plates were provided with the testing machine. For the testing configuration a three-piece mounting plate assembly was designed to accommodate specimen end-tabs. As shown in Fig.C.2.1, this assembly features adapter plates equipped with T-slots for a horizontal and vertical end-tab alignment. Note that the second specimen end-tab is affixed to the ram of the hydraulic actuator. The alignment of both specimen end-connections is eased utilising a laser pointer. Being attached at various locations on the actuator ram the laser pointer's beam is used to mark the proper position of the mounting plate assembly on the movable

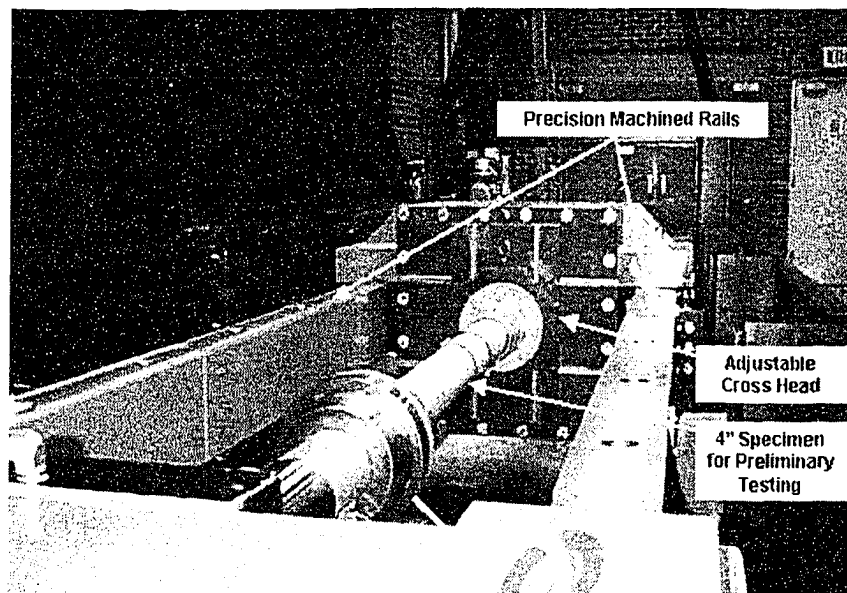


Figure C.2.1: Load frame of large-scale testing apparatus.

crosshead. After the proper coaxial alignment has been accomplished, a 50 mm bolt is used to secure the adapter plates of the mounting plate assembly.

For the mandrel extraction configuration a mounting plate assembly with an aluminium extraction eye is utilised, see Fig.C.2.2. Aluminium is used to protect the polished surfaces of the steel mandrels from scratching. Different adapter plates are available to accommodate various mandrel diameters. Due to limitations in actuator stroke, mandrels with lengths greater than 0.9 m long must be extracted in a multi-step process. This is accomplished by successively re-positioning of the crosshead. Steps denoted (1) to (4) in Fig.C.2.3 illustrate this procedure.

As shown in Fig.C.2.4, an additional load frame can be installed to the moveable crosshead to enable four-point bending tests. However, this feature was not employed in the current experimental study.

C.2.2 Components for Load Application

Biaxial loading conditions are imposed upon specimens using two separate systems: (a) the application of axial loading was accomplished by a hydraulic actuator, and (b) specimen pressurisation was realised utilising a reciprocation air-driven water pump.

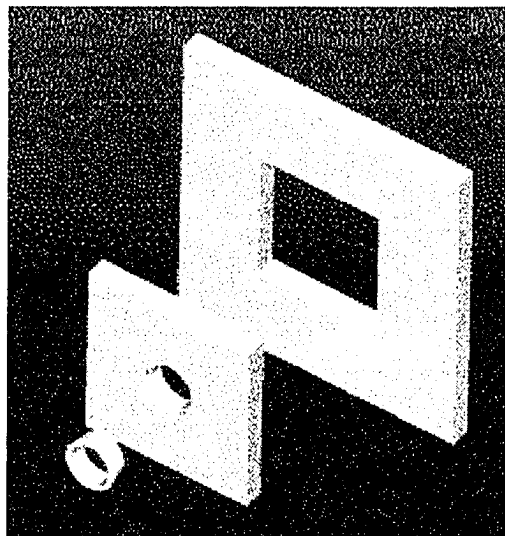


Figure C.2.2: Schematic of mounting plates for mandrel extraction.

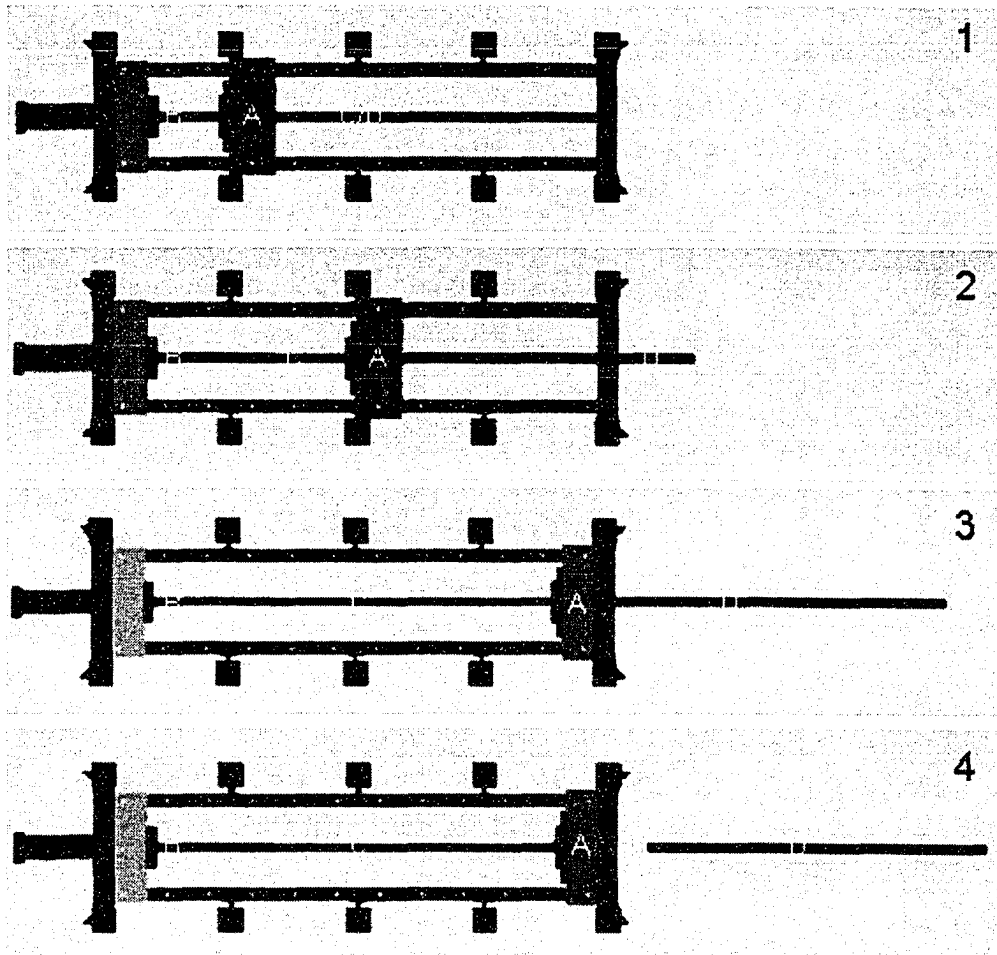


Figure C.2.3: Schematic of the extraction process for large-scale tubular specimens:

- (1) extraction start (crosshead 'A' at inner most position and ram 'B' fully extended);*
- (2) crosshead in second position to begin extraction of next segment;*
- (3) crosshead in final position for extraction of remaining mandrel length;*
- (4) mandrel 'C' completely extracted (within the load frame) and pipe 'D'.*

Axial load application:

The hydraulic actuator is capable of providing a maximum axial pulling and pushing force of 1054 kN and 1112 kN respectively. These values are achieved under 20.7 MPa operating pressure of the supply pump. The actuator is activated using a bi-directional solenoid valve providing three control states: ram extension (compression force), ram retraction (tension force) and ram stop. Depending on the required force the valve

activation time is controlled by the computer control system. The valve also allows for a manual flow rate adjustment, thus enabling the individual setting of ram extension and retraction rates.

Specimen pressurisation:

A reciprocating air-driven water pump (type Haskel ASF150) is used for specimen pressurisation. It has a capacity of 138 MPa based on an air supply pressure of 690 kPa. The air supply pressure is adjusted using an electro/pressure (E/P) transducer (Marsh Bellofram T-1000), or alternatively a manually operated air pressure regulator.

The reciprocating pump was found to cause significant pressure fluctuations in the air supply line, which perturbs the stable operation of the E/P transducer. For that reason an air reservoir (pressure tank) was installed in between transducer and pump to provide damping of the pump feedback; thus, proper transducer operation is ensured. To enable the depressurisation of specimens a pneumatically activated relief valve was incorporated into the high-pressure water line. Figure C.2.5 shows the assembly of water pump, relief valve and gas tank.

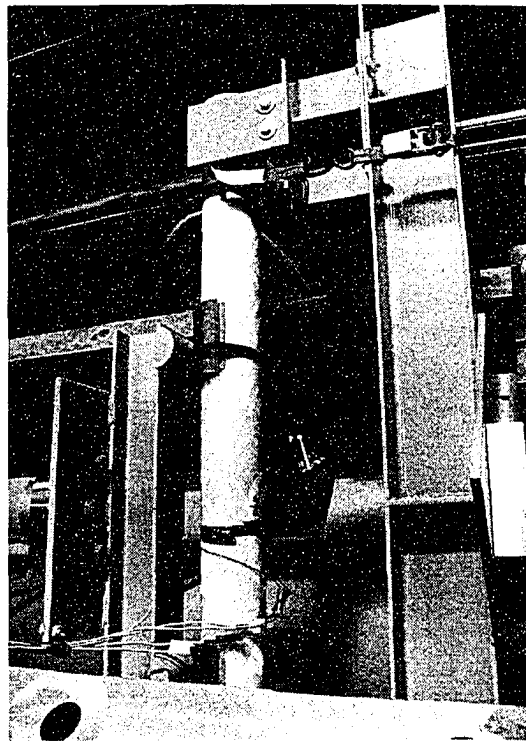


Figure C.2.4: Load frame for four-point bending tests.

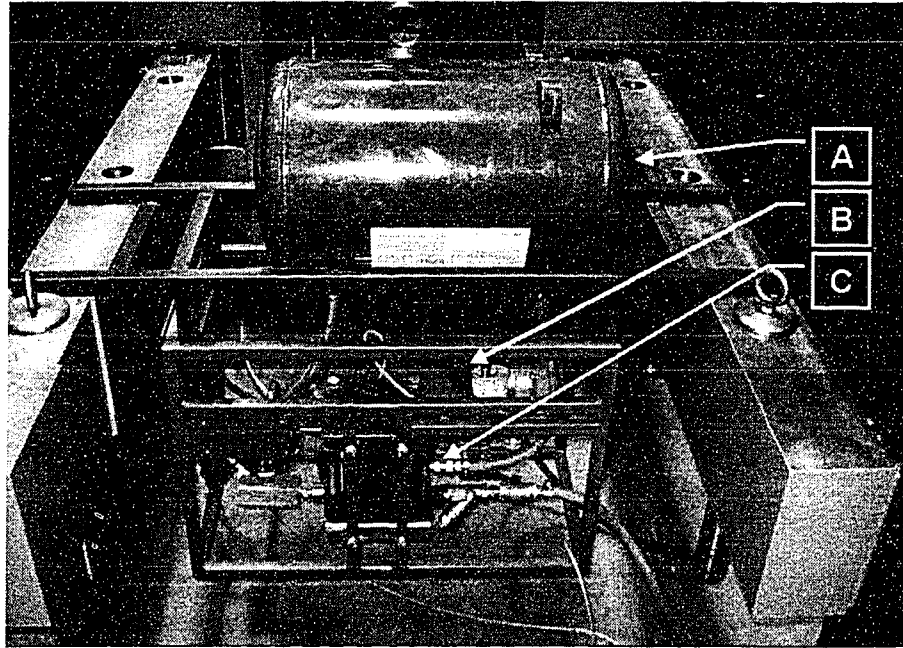


Figure C.2.5: Pump assembly for specimen pressurisation: (A) air reservoir, (B) relief valve and (C) air-driven water pump.

C.2.3 Components for System Control and Data Acquisition

Control and data acquisition computer system:

The platform for the control and data acquisition system is a Pentium-class personal computer (300 MHz P-II). The computer is equipped with a National Instruments 6036E PCI signal input/output (I/O) card. This device provides a capacity of 16 channels of 16-bit analogue input, two channels of 16-bit analogue output and eight digital I/O ports. In addition, the card features a data acquisition system timing controller (DAQ-STC) for time related functions. The maximum timer resolution is 50 ns. The DAC-STC provides general-purpose counter/timer functions that are used to create pulse signals for the control of the bi-directional hydraulic solenoid valve. Signals going to and coming from the testing equipment are interfaced using a custom-made connector box. This accessory provides BNC cable connections for the aforementioned analogue and digital I/O lines.

Instrumentation for the collection of test data:

The computer system is equipped with peripheral instrumentation to record pressure, force and strain data during testing. This is accomplished utilising the computer system's analogue input lines. Each input is adjusted to read a voltage range of ± 10 V. Pressure readings are obtained by connecting a transducer (Omega PX613) to a port machined into one of the specimen end tabs. This facilitates the measurement of internal pressures of up to 103 MPa. A load cell located at the end of the actuator ram produces axial force readings. This load cell was designed and fabricated in-house. Since high-frequency noise renders the load cell's output signal unfit for control purposes, the voltage signal requires conditioning using an electronic filter. The installed low pass filter has a cut-off frequency of about 5 Hz. The filter circuit diagram is shown in Fig.C.2.6. The filter proved to be very effective; fluctuations of the voltage output signal for a constant specimen loading were reduced by more than 75% (measured in terms of the standard deviation).

Since 16 analogue input lines are made available by the I/O card, up to 14 data acquisition devices can be connected in addition to the pressure and force sensors. In the present study, up to five of these lines were employed for the collection of strain data. A 6-channel strain gauge conditioner type Intertechnology 2120 was provided for the conditioning of strain readings. A fully instrumented specimen is shown in Fig.C.2.7.

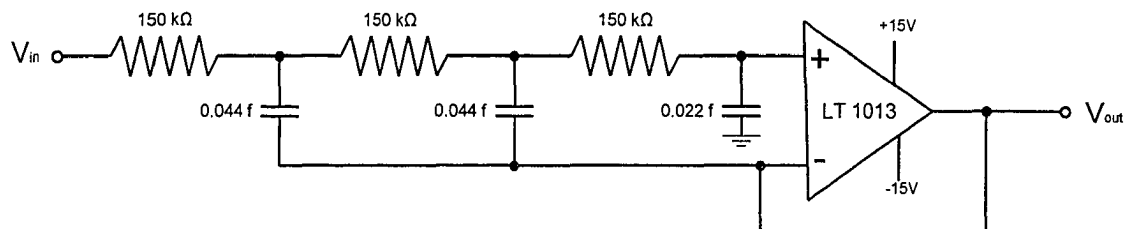


Figure C.2.6: Circuit diagram of the low pass filter for the conditioning of the load cell output signal.

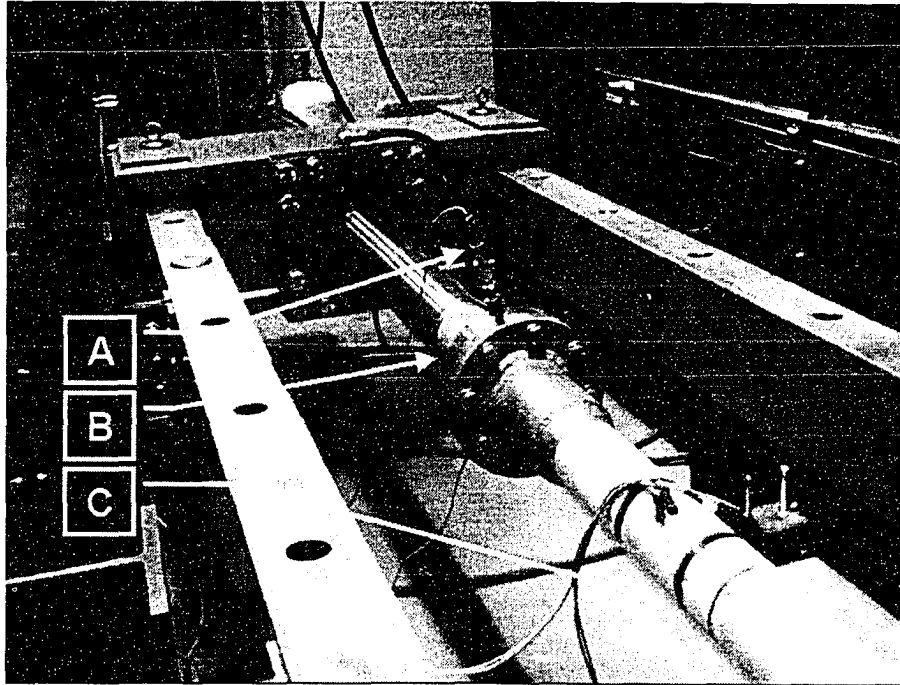


Figure C.2.7: Instrumented prototype specimen: (A) pressure transducer attached to specimen end tab, (B) axial force load cell mounted onto actuator ram, and (C) strain gauges bonded to specimen surface.

C.3 Design of Controller Logic

A controller logic was designed to impose monotonic biaxial loadings upon specimens. This is achieved by increasing either pressure or axial force linearly according to a certain loading rate. A software-based or external function generator (MTS-410) can be employed to produce a force or pressure ramp signal respectively. Generally, it is preferable to utilise the measured pressure signal as the master control signal, which is then used by the controller logic to adjust the force signal to produce the desired biaxial loading ratio. This has the following reasons: Firstly, the force actuator provides a significantly faster reaction time than the pressure pump. This causes the force signal to follow a given set-point much more closely, particularly if sudden pressure fluctuations occur. Secondly, the pressure pump is only able to increase pressurisation; a reduction of pressure is not feasible. Hence, control capabilities using force as the master signal are

considerably compromised. (Note that activating the pressure relief valve causes pressure to diminish entirely.) However, under highly axial dominated loadings, force needs to be chosen as the master signal. Due to the low pressure requirements under such conditions each stroke of the reciprocating pump causes a relatively large and rapid increase in specimen loading. This causes a fast rise of the computed force set point, which generally cannot be matched by the hydraulic system of the force actuator.

Use of pressure as the master control signal:

If pressure constitutes the master control signal the force set point, F_{sp} , is calculated from Eq.(C.3.1), which is based on the biaxial membrane stress equations for a pressurised and axially loaded tube, see Eqs.(3.5.2) and (3.5.3).

$$F_{sp} = \frac{\pi}{4} \left(p_i \left(\frac{A}{H} (D^2 + Ds) + D^2 \left(\frac{A}{H} - 1 \right) \right) + p_o \left((D + s)^2 \left(1 - \frac{A}{H} \right) - \frac{A}{H} (D^2 + Ds) \right) \right) \quad (\text{C.3.1})$$

where $\frac{A}{H}$ is the inverse of the desired biaxial stress ratio [H:A].

According to Fig.C.3.1 the difference between computed force set point, F_{sp} , and force measurements, F , is used as an input for a PID-control algorithm that drives the feedback control loop. This includes the generation of a pulse signal for the activation of the hydraulic bi-directional solenoid valve. Details on pulse generation and PID-control algorithms are given later in this text.

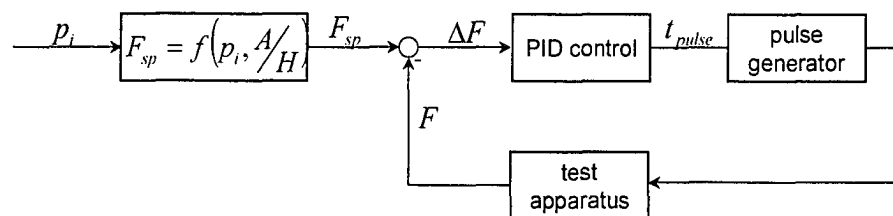


Figure C.3.1: Control schematic for pressure being the master control signal.

Use of force as the master control signal:

An equation for the pressure set point, p_{sp} , is derived analogues to Eq.(C.3.1) if force is selected to be the master control signal:

$$p_{sp} = \frac{\left(\frac{\pi}{4} F - p_o \left((D+s)^2 \left(1 - \frac{A}{H} \right) - \frac{A}{H} (D^2 + Ds) \right) \right)}{\left(\frac{A}{H} \left((D^2 + Ds) + D^2 \left(1 - \frac{H}{A} \right) \right) \right)} \quad (\text{C.3.2})$$

As shown in Fig.C.3.2, the input for the PID-control algorithm is obtained from the difference between computed pressure set point, p_{sp} , and pressure measurements, p_i .

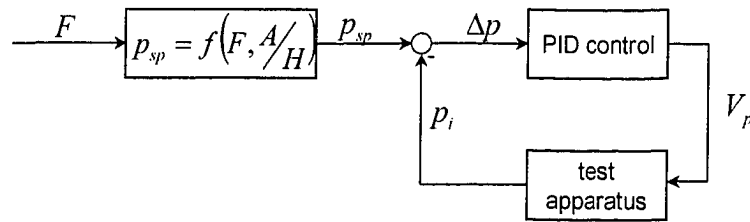


Figure C.3.2: Control schematic for force being the master control signal.

PID-control algorithm:

PID-control algorithms are frequently used for a variety of control applications. They provide three basic functions: a proportionality (P) term provides feedback for the control loop, an integral (I) term eliminates steady state offsets, and a derivative (D) term approximates the future development of the output value.

Using the terminology given in Fig.C.3.3, an output signal is produced by the following equations:

$$I(k) = I(k-1) + K_I x(k) T_{cycle} \quad (\text{C.3.3})$$

$$u(k) = K_P x(k) + I(k) + K_D \left(\frac{x(k) - x(k-1)}{T_{cycle}} \right) \quad (\text{C.3.4})$$

where $x(k)$ and $u(k)$ are the input and output signals respectively, T_{cycle} is the sampling interval, and K_P , K_I and K_D are control parameters. For the current test setup, i.e.

specimen type and test configurations, good results were achieved with control parameters $K_P = 0.5$, $K_I = 0.2$ and $K_D = 0.1$.

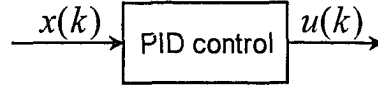


Figure C.3.3: Schematic of PID-controller.

Pulse width modulation:

Although the bi-directional hydraulic valve only allows for three distinct states (i.e. ram extension, retraction and stop), a continuous loading of the specimen can be approximated using pulse width modulation. The pulse duration, t_{pulse} , is computed according to the following equation:

$$t_{pulse} = \frac{u - u_{min}}{u_{max} - u_{min}} T_{cycle} \quad (C.3.5)$$

where u_{max} and u_{min} are maximum and minimum output parameters respectively.

According to this definition the PID-controller output may produce an output signal of $-T_{cycle} < t_{pulse} < T_{cycle}$. In the case of a positive output the pulse generator activates the bi-directional valve for compression loading. In turn, tensile loading is produced for a negative output. To protect the valve from extremely short activation times, any pulse shorter than 15 ms is set to zero, whereas pulse signals greater than 185 ms cause a valve activation for the full sampling interval, T_{cycle} .

User interface:

The National Instruments LabView graphical programming language was employed to code the controller and data acquisition logic. This software also allows for the creation of a convenient user interface by providing the ability to custom design various control panels. These panels allow for the adjustment of all control parameters. Hence, an operator has the ability to tailor the controller logic to various test conditions, which provides a high degree of flexibility with regards to test specimens and loading scenarios.

APPENDIX D

EXPERIMENTAL BIAxIAL STRESS DATA

Model Specimens (S)

Spec. No.	Lay-up	Stress ratio	Experimental stresses at functional failure [MPa]		Experimental stresses at structural failure [MPa]	
			Hoop	Hoop	Hoop	Axial
S017 ¹	[±60 ₃] _T	[2H:1A]	217	105	463	224
S018	[±60 ₃] _T	[1H:0A]	876	0	876	0
S019 ¹	[±60 ₃] _T	[1H:0A]	833	0	840	0
S020 ¹	[±60 ₃] _T	[3H:1A]	NA	NA	629	210
S021	[±60 ₃] _T	[2H:1A]	234	113	NA	NA
S022	[±60 ₃] _T	[2H:1A]	240	116	NA	NA
S023	[±60 ₃] _T	[2H:1A]	205	99	413	200
S026 ¹	[±60 ₃] _T	[2H:1A]	243	117	490	237
S027	[±60 ₃] _T	[3H:1A]	391	131	671	225
S028	[±60 ₃] _T	[1H:15A]	3	56	3	56
S029 ¹	[±60 ₃] _T	[3H:1A]	364	121	556	186
S030 ¹	[±60 ₃] _T	[3H:1A]	283	94	663	222
S031 ¹	[±60 ₃] _T	[1H:15A]	8	71	8	71
S032 ¹	[±60 ₃] _T	[1H:0A]	820	0	820	0
S033	[±60 ₃] _T	[1H:0A]	814	0	834	0
S034	[±60 ₃] _T	[3H:1A]	NA	NA	691	231
S035	[±60 ₃] _T	[2H:1A]	235	114	444	215
S036	[±60 ₃] _T	[3H:1A]	421	141	801	268
S039 ²	[±60 ₂ , ±45] _T	[0H:1A]	1	80	4	129

¹Baseline specimen configuration

²Stiffness reduction method was used to determine functional failure.

Spec. No.	Lay-up	Stress ratio	Experimental stresses at functional failure [MPa]		Experimental stresses at structural failure [MPa]	
			Hoop	Hoop	Hoop	Axial
S040	$[\pm 60_2, \pm 45]_T$	[2H:1A]	361	175	693	335
S041	$[\pm 60_2, \pm 45]_T$	[1H:1A]	148	148	291	292
S042	$[\pm 60_2, \pm 45]_T$	[1H:0A]	585	0	588	0
S043	$[\pm 45, \pm 60_2]_T$	[2H:1A]	321	155	646	312
S044	$[\pm 45, \pm 60_2]_T$	[1H:0A]	658	0	658	0
S045	$[\pm 45, \pm 60_2]_T$	[2H:1A]	346	167	625	302
S046 ²	$[\pm 45, \pm 60_2]_T$	[1H:15A]	0	77	3	112
S051	$[\pm 45, \pm 60_2]_T$	[1H:1A]	132	133	227	228
S052	$[\pm 45, \pm 60_2]_T$	[1H:1A]	133	134	218	218
S059	$[\pm 30, \pm 60_2]_T$	[2H:1A]	NA	NA	662	319
S060	$[\pm 30, \pm 60_2]_T$	[1H:1A]	224	223	424	422
S061	$[\pm 30, \pm 60_2]_T$	[1H:1A]	209	209	408	407
S066	$[\pm 45, \pm 60_2]_T$	[3H:1A]	540	180	857	286
S067	$[\pm 45, \pm 60_2]_T$	[1H:0A]	630	0	636	0
S070	$[\pm 60_2, \pm 45]_T$	[1H:1A]	151	151	333	333
S071	$[\pm 60_2, \pm 45]_T$	[1H:0A]	572	0	572	0
S080	$[\pm 30, \pm 60_2]_T$	[1H:0A]	466	0	540	0
S081	$[\pm 30, \pm 60_2]_T$	[3H:1A]	505	168	588	196
S082	$[\pm 30, \pm 60_2]_T$	[1H:0A]	550	0	559	0
S083	$[\pm 30, \pm 60_2]_T$	[2H:1A]	378	182	649	312
S084	$[\pm 30, \pm 60_2]_T$	[1H:15A]	22	322	22	322
S086	$[\pm 30, \pm 60_2]_T$	[1H:3A]	79	237	115	342
S087	$[\pm 30, \pm 60_2]_T$	[1H:15A]	15	306	16	324
S089	$[\pm 60_2, \pm 45]_T$	[2H:1A]	385	186	757	366
S091	$[\pm 60_2, \pm 45]_T$	[3H:1A]	576	192	812	271

¹Baseline specimen configuration

²Stiffness reduction method was used to determine functional failure.

Prototype Specimens (P) and Joined Prototype Specimens (J)

Spec. No.	Lay-up	Stress ratio	Experimental stresses at functional failure [MPa]	
			Hoop	Axial
P003 ¹	[±60 ₅] _T	[3H:1A]	208	70
P004 ¹	[±60 ₅] _T	[1H:0A]	468	1
P005 ¹	[±60 ₅] _T	[2H:1A]	161	80
P007 ¹	[±60 ₅] _T	[2H:1A]	161	81
P008 ¹	[±60 ₅] _T	[1H:0A]	489	2
P008-03 ¹	[±60 ₅] _T	[1H:5A]	13	54
P009 ¹	[±60 ₅] _T	[2H:1A]	142	72
P010 ¹	[±60 ₅] _T	[3H:1A]	211	71
P012 ¹	[±60 ₃ , ±30] _T	[3H:1A]	254	87
P016 ¹	[±60 ₃ , ±30] _T	[1H:5A]	27	152
P017 ¹	[±60 ₃ , ±30] _T	[2H:1A]	179	91
P018 ¹	[±60 ₃ , ±30] _T	[1H:0A]	396	5
J001-01	[±60 ₃ , ±30] _T	[2H:1A]	177	91
J001-02 ²	[±60 ₃ , ±30] _T	[0H:1A]	1	178
J002-01 ²	[±60 ₃ , ±30] _T	[0H:1A]	1	177
J003-01	[±60 ₃ , ±30] _T	[2H:1A]	Test was stopped at 75/38MPa hoop/axial stress. No damage was observed.	
J003-02	[±60 ₃ , ±30] _T	[3H:1A]	272	92
J003-03 ²	[±60 ₃ , ±30] _T	[0H:1A]	1	174
J004-01 ³	[±60 ₃ , ±30] _T	[2H:1A]	184	94
J004-04 ^{2,3}	[±60 ₃ , ±30] _T	[0H:1A]	0	205

¹First generation control software was employed.

²Test was terminated by joint failure.

³Improved prototype, i.e. pipe surface resin coat was removed during manufacturing.

APPENDIX E

VCCT: DERIVATION AND EXAMPLE CALCULATION

E.1 Example Derivation of VCCT for Mode I SERR

An expression for the mode I strain energy release rate is subsequently derived for 4-noded quadrilateral elements symmetric about the crack tip (shown in Fig.E.1.1). This derivation yields the result of the mode I case of the virtual crack closure technique first presented by Rybicki and Kanninen (1977).

The following stress distribution in front of the crack tip is assumed:

$$\sigma_{\rho}(\xi) = \frac{a_1}{\sqrt{\xi}} + a_2 \text{ for } \xi \geq 0 \quad (\text{E.1.1})$$

$$\sigma_{\rho}(\xi) = 0 \text{ for } \xi < 0 \quad (\text{E.1.2})$$

where a_1 and a_2 are unknown coefficients.

This stress distribution is thought to cause nodal forces $F_{\rho i}$, $F_{\rho j}$, et cetera, acting upon corresponding nodes i, j , and so forth, shown in Fig.E.1.1. Two nodal forces are required to determine the coefficients a_1 and a_2 . These forces were chosen closest and around the crack tip, i.e. $F_{\rho i}$ and $F_{\rho j}$.

$$\mathcal{G}_I = \lim_{\Delta \rightarrow 0} \frac{1}{2\Delta} \int_0^{\Delta} \sigma_{\rho}(\Delta - r, 0) \bar{v}(r, \pi) dr \quad (\text{E.1.3})$$

Based on Irwin's (1958) equation for the calculation of the mode I energy release rate, Eq.(E.1.3), the work associated with the assumed stress distribution, $\sigma_{\rho}(\xi)$, is equated to the work resulting from the forces $F_{\rho i}$ and $F_{\rho j}$, and the displacements \bar{v}_i and \bar{v}_j , i.e.

$$\frac{1}{2} \int_0^{\Delta} \sigma_{\rho}(\xi) \bar{v}(\xi) d\xi = -\frac{1}{2} [F_{\rho i} \bar{v}_i + F_{\rho j} \bar{v}_j] \quad (\text{E.1.4})$$

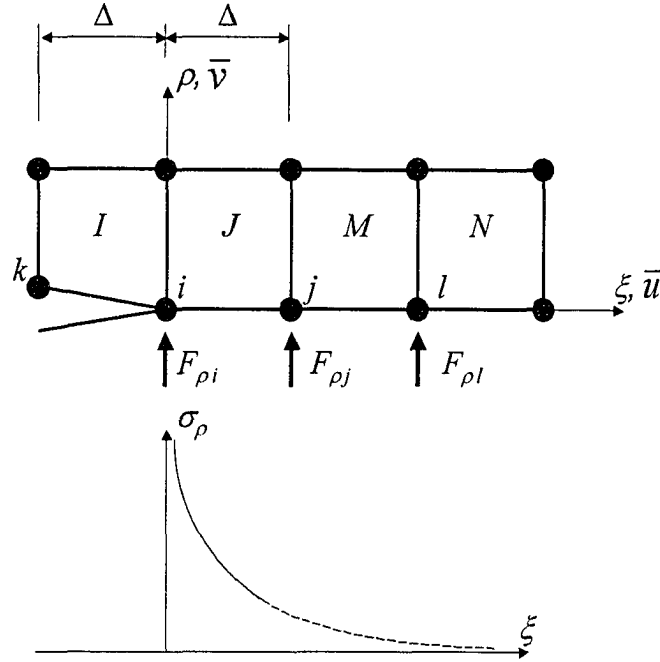


Figure E.1.1: Schematic showing local coordinate system, nodal forces and stress distribution at the crack tip in a 4-noded quadrilateral finite element grid.

In Eq.(E.1.4) $\bar{v}(\xi)$ and Δ are the displacement interpolation (shape) function of the element and the element length respectively. Note that a tensile stress σ_ρ causes forces in negative ρ -direction. For 4-noded quadrilateral elements the displacement interpolation (shape) function for the i - j -side is given by

$$\bar{v}(\xi) = \left(1 - \frac{\xi}{\Delta}\right) \bar{v}_i + \frac{\xi}{\Delta} \bar{v}_j \quad (\text{E.1.5})$$

Substituting Eq.(E.1.5) into Eq.(E.1.4) gives

$$\frac{1}{2} \int_0^\Delta \sigma_\rho(\xi) \left[\left(1 - \frac{\xi}{\Delta}\right) \bar{v}_i + \frac{\xi}{\Delta} \bar{v}_j \right] d\xi = -\frac{1}{2} [F_{\rho i} \bar{v}_i + F_{\rho j} \bar{v}_j] \quad (\text{E.1.5})$$

Separating variables \bar{v}_i and \bar{v}_j yields

$$F_{\rho i} = - \int_0^\Delta \sigma_\rho(\xi) \left(1 - \frac{\xi}{\Delta}\right) d\xi \quad F_{\rho j} = - \int_0^\Delta \sigma_\rho(\xi) \frac{\xi}{\Delta} d\xi \quad (\text{E.1.6a\&b})$$

Substituting Eq.(E.1.1) into Eq.(E.1.6a) and Eq.(E.1.6b) yields

$$\begin{aligned}
 F_{\rho i} &= -\int_0^{\Delta} \left(\frac{a_1}{\sqrt{\xi}} + a_2 \right) \left(1 - \frac{\xi}{\Delta} \right) d\xi = -\int_0^{\Delta} \left(\frac{a_1}{\sqrt{\xi}} + a_2 - a_1 \frac{\sqrt{\xi}}{\Delta} - a_2 \frac{\xi}{\Delta} \right) d\xi \\
 &= -\left[2a_1\sqrt{\xi} + a_2\xi - \frac{2}{3}a_1 \frac{\xi^{3/2}}{\Delta} - \frac{1}{2}a_2 \frac{\xi^2}{\Delta} \right]_0^{\Delta} = -2a_1\sqrt{\Delta} - a_2\Delta + \frac{2}{3}a_1\sqrt{\Delta} + \frac{1}{2}a_2\Delta \\
 &= -\frac{4}{3}a_1\sqrt{\Delta} - \frac{1}{2}a_2\Delta \tag{E.1.7}
 \end{aligned}$$

$$\begin{aligned}
 F_{\rho j} &= -\int_0^{\Delta} \left(\frac{a_1}{\sqrt{\xi}} + a_2 \right) \frac{\xi}{\Delta} d\xi = -\int_0^{\Delta} \left(a_1 \frac{\sqrt{\xi}}{\Delta} + a_2 \frac{\xi}{\Delta} \right) - \left[\frac{2}{3}a_1 \frac{\xi^{3/2}}{\Delta} + \frac{1}{2}a_2 \frac{\xi^2}{\Delta} \right]_0^{\Delta} \\
 &= -\frac{2}{3}a_1\sqrt{\Delta} - \frac{1}{2}a_2\Delta \tag{E.1.8}
 \end{aligned}$$

Equations (E.1.7-8) can be written as

$$\begin{pmatrix} a_1\sqrt{\Delta} \\ a_2\Delta \end{pmatrix} = \frac{1}{2} \begin{bmatrix} -3 & 3 \\ 4 & -8 \end{bmatrix} \begin{pmatrix} F_{\rho i} \\ F_{\rho j} \end{pmatrix} \tag{E.1.9}$$

In the wake of the crack tip the relative crack opening displacement, $\bar{v}_R(r)$, is given by the displacements of nodes i , k , and k' and the element shape function:

$$\bar{v}_R(r) = \left(1 - \frac{r}{\Delta} \right) \bar{v}_i + \frac{r}{\Delta} (\bar{v}_k - \bar{v}_{k'}) \tag{E.1.10}$$

Now the displacements in the wake of the crack tip and the stress distribution ahead of the crack tip are determined. Thus, according to Eq.(E.1.3) the mode I strain energy release rate can be calculated as

$$\begin{aligned}
 \mathcal{G}_I &= \lim_{\Delta \rightarrow 0} \frac{1}{2\Delta} \int_0^{\Delta} \sigma_{\rho}(\Delta - r, 0) \bar{v}_R(r, \pi) dr \\
 &= \lim_{\Delta \rightarrow 0} \frac{1}{2\Delta} \int_0^{\Delta} \left[\frac{a_1}{\sqrt{\Delta - r}} + a_2 \right] \left[\left(1 - \frac{r}{\Delta} \right) \bar{v}_i + \frac{r}{\Delta} (\bar{v}_k - \bar{v}_{k'}) \right] dr \tag{E.1.11}
 \end{aligned}$$

with $r = \Delta - \xi$. In the following the integration of Eq.(E.1.11) is performed.

$$\begin{aligned}
\mathcal{G}_I &= -\lim_{\Delta \rightarrow 0} \frac{1}{2\Delta} \int_0^\Delta \left[\frac{a_1}{\sqrt{\Delta-r}} + a_2 \right] \left[\left(1 - \frac{\Delta-\xi}{\Delta} \right) \bar{v}_i + \frac{\Delta-\xi}{\Delta} (\bar{v}_k - \bar{v}_{k'}) \right] d\xi \\
&= -\lim_{\Delta \rightarrow 0} \frac{1}{2\Delta} \int_0^\Delta \left[\frac{a_1}{\sqrt{\xi}} + a_2 \right] \left[\frac{\xi}{\Delta} \bar{v}_i + \left(1 - \frac{\xi}{\Delta} \right) (\bar{v}_k - \bar{v}_{k'}) \right] d\xi \\
&= -\lim_{\Delta \rightarrow 0} \frac{1}{2\Delta} \int_0^\Delta \left[\frac{a_1}{\sqrt{\xi}} + a_2 \right] \left[\frac{\xi}{\Delta} \bar{v}_i + \left(1 - \frac{\xi}{\Delta} \right) (\bar{v}_k - \bar{v}_{k'}) \right] d\xi \\
&= -\lim_{\Delta \rightarrow 0} \frac{1}{2\Delta} \int_0^\Delta \left[\frac{a_1}{\sqrt{\xi}} \frac{\xi}{\Delta} \bar{v}_i + \frac{a_1}{\sqrt{\xi}} (\bar{v}_k - \bar{v}_{k'}) - \frac{a_1}{\sqrt{\xi}} \frac{\xi}{\Delta} (\bar{v}_k - \bar{v}_{k'}) \right. \\
&\quad \left. + a_2 \frac{\xi}{\Delta} \bar{v}_i + a_2 (\bar{v}_k - \bar{v}_{k'}) - a_2 \frac{\xi}{\Delta} (\bar{v}_k - \bar{v}_{k'}) \right] d\xi \\
&= -\lim_{\Delta \rightarrow 0} \frac{1}{2\Delta} \left[\frac{2}{3} \frac{a_1}{\Delta} \xi^{2/3} \bar{v}_i + 2a_1 \sqrt{\xi} (\bar{v}_k - \bar{v}_{k'}) - \frac{2}{3} \frac{a_1}{\Delta} \xi^{2/3} (\bar{v}_k - \bar{v}_{k'}) \right. \\
&\quad \left. + \frac{a_2}{\Delta} \frac{\xi^2}{2} \bar{v}_i + a_2 \xi (\bar{v}_k - \bar{v}_{k'}) - \frac{a_2}{\Delta} \frac{\xi^2}{2} (\bar{v}_k - \bar{v}_{k'}) \right]_0^\Delta \\
\mathcal{G}_I &= -\lim_{\Delta \rightarrow 0} \frac{1}{2\Delta} \left[\frac{2}{3} a_1 \sqrt{\Delta} \bar{v}_i + \frac{4}{3} a_1 \sqrt{\Delta} (\bar{v}_k - \bar{v}_{k'}) + \frac{1}{2} a_2 \Delta \bar{v}_i + \frac{1}{2} a_2 \Delta (\bar{v}_k - \bar{v}_{k'}) \right] \quad (\text{E.1.12})
\end{aligned}$$

Using Eq.(E.1.9), and substituting results for coefficients a_1 and a_2 into Eq.(E.1.12),

$$\begin{aligned}
\mathcal{G}_I &= -\lim_{\Delta \rightarrow 0} \frac{1}{2\Delta} \left[\frac{2}{3} \left(-\frac{3}{2} F_{\rho_i} + \frac{3}{2} F_{\rho_j} \right) \bar{v}_i + \frac{4}{3} \left(-\frac{3}{2} F_{\rho_i} + \frac{3}{2} F_{\rho_j} \right) (\bar{v}_k - \bar{v}_{k'}) \right. \\
&\quad \left. + \frac{1}{2} (2F_{\rho_i} - 4F_{\rho_j}) \bar{v}_i + \frac{1}{2} (2F_{\rho_i} - 4F_{\rho_j}) (\bar{v}_k - \bar{v}_{k'}) \right] \\
&= -\lim_{\Delta \rightarrow 0} \frac{1}{2\Delta} \left[-F_{\rho_j} \bar{v}_i - F_{\rho_i} (\bar{v}_k - \bar{v}_{k'}) \right] \quad (\text{E.1.13})
\end{aligned}$$

Since the displacement \bar{v}_i at the crack tip is zero, Eq.(E.1.13) reduces to

$$\mathcal{G}_I = \lim_{\Delta \rightarrow 0} \left[\frac{1}{2\Delta} F_{\rho_i} (\bar{v}_k - \bar{v}_{k'}) \right] \quad (\text{E.1.14})$$

Equation (E.1.14) is identical to the result presented by other researchers, e.g. Rybicki and Kanninen (1977), and Krueger (2002). An expression for the mode II energy release rate is found in a similar fashion.

E.2 Calculation of Parabolic Displacement Interpolation Function

The present calculation demonstrates the equivalence of the following two equations: (a) the parabolic displacement interpolation function defined along nodes i - j - k according to Raju (1988), i.e. Eq.(5.6.7), and (b) the shape function for 8-noded quadrilateral solids (PLANE82) provided by the documentation of the finite elements software (ANSYS[®], 2002), i.e. Eq.(5.6.8). In that order, Eqs.(5.6.7) and (5.6.8) are repeated below for convenience. The corresponding element coordinate systems are provided in Fig.E.2.1.

$$\bar{v}(\xi) = \left(1 - \frac{3\xi}{\Delta} + \frac{2\xi^2}{\Delta^2}\right)\bar{v}_i + \left(4\frac{\xi}{\Delta} - 4\frac{\xi^2}{\Delta^2}\right)\bar{v}_j + \left(-\frac{\xi}{\Delta} + 2\frac{\xi^2}{\Delta^2}\right)\bar{v}_k$$

$$\begin{aligned}\bar{v}(s,t) = & \frac{1}{4}[\bar{v}_i(1-s)(1-t)(-s-t-1) + \bar{v}_k(1+s)(1-t)(s-t-1) \\ & + \bar{v}_m(1+s)(1+t)(s+t-1) + \bar{v}_o(1-s)(1+t)(-s+t-1)] \\ & + \frac{1}{2}[\bar{v}_j(1-s^2)(1-t) + \bar{v}_l(1+s)(1-t^2) + \bar{v}_n(1-s^2)(1+t) + \bar{v}_p(1-s)(1-t^2)]\end{aligned}$$

A relationship between the s - t and ρ - ξ coordinates is established in the following.

For $\xi = 0 \Rightarrow s = -1$, $\xi = \frac{\Delta}{2} \Rightarrow s = 0$, and $\xi = \Delta \Rightarrow s = 1$.

$$\text{Hence,} \quad \xi = \frac{\Delta}{2}s + \frac{\Delta}{2} \Leftrightarrow s = \frac{2}{\Delta}\xi - 1 \quad (\text{E.2.1})$$

On the element side with i - j - k -nodes, $t = -1$.

APPENDIX F

ANSYS BATCH FILES

F.1 Stress Analysis Model

```
C*** ANSYS FE MECHANICAL ANALYSIS OF COUPLED TUBES
C*** STRESS ANALYSIS
C*** 2-D axis-symmetrical model, midplane symmetry
C*** cylinder#1 w/ 60deg covers (=2 interwoven layers) tube structure
C*** cylinder#2 w/ 60deg covers (=2 interwoven layers) tube structure
C*** cylinder#3 w/ 30deg covers (=2 interwoven layers) tube structure
C*** cylinder#A w/ resin coat of tube structure
C*** cylinder#4 w/ 30deg covers (=2 interwoven layers) coupler
structure
C*** cylinder#5 w/ 60deg covers (=2 interwoven layers) coupler
structure
C*** cylinder#6 w/ 60deg covers (=2 interwoven layers) coupler
structure
C*** coupler structure provides for tapering
C*** 1 layer adhesive structure
C*** 1 taper for adhesive structure
C*** Material 1: orthotropic pipe material; GFRP 60 angle-ply lamina;
C*** Material 2: orthotropic pipe material; GFRP 30 angle-ply lamina;
C*** Material 3: isotropic; adhesive material;
C*** Material 4: isotropic; neat resin material;
C*** Material 5: orthotropic coupler material; GFRP 30 angle-ply
lamina;
C*** Material 6: orthotropic coupler material; GFRP 60 angle-ply
lamina;
C*** Material 7: friction coefficient for contact elements
C***
/FILENAME, JOINT_PIPE_MODEL
/TITLE, JOINT_PIPE_MODEL
/OUTPUT, JOINT_PIPE_MODEL, OUT
/UNITS, SI
C***
*AFUN, DEG
C*****
C***
C*** INPUT PARAMETERS (SI units: m, kg, s, N)
C***
C*****
C*** TUBE GEOMETRY
C***
id_tube=0.1016          !*Inside diameter of tube
l_tube=7.5*id_tube     !*Length of tube
l_grip=0.2032          !*Length of grip section
```

```

C***
C*** CYLINDER#1
t_c1_tube=2.235e-3          !*Thickness of cylinder#1
C***
C*** CYLINDER#2
t_c2_tube=1.082e-3          !*Thickness of cylinder#2
C***
C*** CYLINDER#3
t_c3_tube=1.312e-3          !*Thickness of cylinder#3
C***
C*** CYLINDER#A
t_cA_tube=0.2e-3           !*Thickness of cylinder#A
C***
dummy=id_tube+2*t_c1_tube
dummy=dummy+2*t_c2_tube
dummy=dummy+2*t_c3_tube
oD_tube=dummy+2*t_cA_tube   !*Outside diameter of tube
C*****
C*** ADHESIVE LAYER GEOMETRY
C***
t_adhesive=1.013e-3        !*Thickness of adhesive layer
iD_adhesive=oD_tube        !*Inside diameter of adh. layer
C*****
C*** COUPLER GEOMETRY
C***
gamma_taper=30             !*Angle of coupler tapering
iD_coupler=oD_tube+2*t_adhesive !*Inside diameter coupler
l_coupler=0.155575        !*Coupler length
C***
C*** CYLINDER#4
t_c4_coupler=1.192e-3      !*Thickness of cylinder#4
step=t_c4_coupler/TAN(gamma_taper)
l_c4_coupler=l_coupler-step !*Top length of coupler cylinder#4
C***
C*** CYLINDER#5
t_c5_coupler=0.944e-3      !*Thickness of cylinder#5
step=t_c5_coupler/TAN(gamma_taper)
l_c5_coupler=l_c4_coupler-step !*Top length of coupler cylinder#5
C***
C*** CYLINDER#6
t_c6_coupler=0.928e-3      !*Thickness of cylinder#6
step=t_c6_coupler/TAN(gamma_taper)
l_c6_coupler=l_c5_coupler-step !*Top length of coupler cylinder#6
C***
od_coupler=iD_coupler+2*t_c4_coupler !*Outside diameter coupler
od_coupler=od_coupler+2*t_c5_coupler
od_coupler=od_coupler+2*t_c6_coupler
C***
C*****
C*** CALCULATE TUBE LENGTH SECTION
C***
beta_taper=gamma_taper/2+5 !*Angle of adh. layer tapering
l_tube_section=l_coupler+t_adhesive/TAN(beta_taper)
C*****
C*** LOADS (Pa)

```

```

C***
R=0 !*Loading ratio
sigma_A=25e6 !*Axial stress in pipe
iP=sigma_A*R*(od_tube-id_tube)/id_tube !*Internal pressure
C*****
C*** MESHING PARAMETERS
C***
esize1=t_adhesive/3 !*Element size at coupler end
esize2=(od_tube-id_tube)/6 !*Element size in coupler area
esize3=(od_tube-id_tube)/5 !*Element size in pure tube area
C*****
C*** DISPLAY PARAMETERS FOR PLOTTING RESULTS
C***
max_s=100e6
min_s=0
C*****
C*** PATH OPERATION PARAMETERS
C***
interface_dist=0.05e-3
C*****
C*** PREPROCESSOR
C***
C*****
/PREP7
C*****
C*** DEFINE COORDINATE SYSTEM / ELEMENT ORIENTATION
C***
C*** 2-Model with Cartesian C.S.
C*** X, Y, Z refer to Radial (R), Axial(Z), Hoop(THETA) directions.
C***
CSYS,1
LOCAL,11,0
ESYS,11
C*****
C*** DEFINE ELEMENT TYPES
C***
ET,1,PLANE82 !*Elements for solid body
KEYOPT,1,3,1 !*Axisymmetric analysis
KEYOPT,1,5,0
KEYOPT,1,6,0
C*****
C*** DEFINE REAL CONSTANTS
C***
C***R,1,0,3.4E09
C*****
C*** DEFINE MATERIAL CONSTANTS
C***
C*** MATERIAL #1
MP,EX,1,15.288E09
MP,EY,1,13.067E09
MP,EZ,1,26.870E09
MP,GXY,1,5.757E09
MP,GYZ,1,12.117E09
MP,GXZ,1,4.999E09

```

```
MP,NUXY,1,0.176
MP,NUXZ,1,0.137
MP,NUYZ,1,0.697
C***
C*** MATERIAL #2
MP,EX,2,15.288E09
MP,EY,2,26.870E09
MP,EZ,2,13.067E09
MP,GXY,2,4.999E09
MP,GYZ,2,12.117E09
MP,GXZ,2,5.757E09
MP,NUXY,2,0.137
MP,NUXZ,2,0.176
MP,NUYZ,2,0.339
C***
C*** MATERIAL #3
MP,EX,3,4.8E09
MP,EY,3,4.8E09
MP,EZ,3,4.8E09
MP,GXY,3,1.8E09
MP,GYZ,3,1.8E09
MP,GXZ,3,1.8E09
MP,PRXY,3,0.34
MP,PRXZ,3,0.34
MP,PRYZ,3,0.34
C***
C*** MATERIAL #4
MP,EX,4,3.4E09
MP,EY,4,3.4E09
MP,EZ,4,3.4E09
MP,GXY,4,1.2E09
MP,GYZ,4,1.2E09
MP,GXZ,4,1.2E09
MP,PRXY,4,0.42
MP,PRXZ,4,0.42
MP,PRYZ,4,0.42
C***
C*** MATERIAL #5
MP,EX,5,16.648E09
MP,EY,5,14.551E09
MP,EZ,5,29.075E09
MP,GXY,5,6.375E09
MP,GYZ,5,12.898E09
MP,GXZ,5,5.636E09
MP,NUXY,5,0.171
MP,NUXZ,5,0.143
MP,NUYZ,5,0.693
C***
C*** MATERIAL #6
MP,EX,6,16.648E09
MP,EY,6,29.075E09
MP,EZ,6,14.551E09
MP,GXY,6,5.636E09
MP,GYZ,6,12.898E09
MP,GXZ,6,6.375E09
```



```

MP,NUXY,6,0.143
MP,NUXZ,6,0.171
MP,NUYZ,6,0.332
C***
C*** MATERIAL #7
C***MP,MU,7,0
C*****
C*** DEFINE KEYPOINTS
C***
C*** AT ORIGIN (ZERO X)
K,,iD_tube/2,0,0           !Keypoint #1
K,,iD_tube/2+t_c1_tube,0,0 !Keypoint #2
dummy=iD_tube/2+t_c1_tube
dummy=dummy+t_c2_tube
K,,dummy,0,0             !Keypoint #3
K,,oD_tube/2-t_cA_tube,0,0 !Keypoint #4
K,,oD_tube/2-t_cA_tube/2,0,0 !Keypoint #5
K,,oD_tube/2,0,0         !Keypoint #6
K,,iD_coupler/2,0,0      !Keypoint #7
K,,iD_coupler/2+t_c4_coupler,0,0 !Keypoint #8
dummy=iD_coupler/2+t_c4_coupler
dummy=dummy+t_c5_coupler
K,,dummy,0,0             !Keypoint #9
K,,oD_coupler/2,0,0     !Keypoint #10
C***
C*** AT MESH REFINEMENT SECTION
dummy=l_c6_coupler-0.001
K,,iD_tube/2,dummy,0     !Keypoint #11
K,,iD_tube/2+t_c1_tube,dummy,0 !Keypoint #12
dummx=iD_tube/2+t_c1_tube
dummx=dummx+t_c2_tube
K,,dummx,dummy,0       !Keypoint #13
K,,oD_tube/2-t_cA_tube,dummy,0 !Keypoint #14
K,,oD_tube/2-t_cA_tube/2,dummy,0 !Keypoint #15
K,,oD_tube/2,dummy,0   !Keypoint #16
K,,iD_coupler/2,dummy,0 !Keypoint #17
K,,iD_coupler/2+t_c4_coupler,dummy,0 !Keypoint #18
dummx=iD_coupler/2+t_c4_coupler
dummx=dummx+t_c5_coupler
K,,dummx,dummy,0       !Keypoint #19
K,,oD_coupler/2,dummy,0 !Keypoint #20
C***
C*** AT TUBE SECTION
dummy=l_tube_section
K,,iD_tube/2,dummy,0     !Keypoint #21
K,,iD_tube/2+t_c1_tube,dummy,0 !Keypoint #22
dummx=iD_tube/2+t_c1_tube
dummx=dummx+t_c2_tube
K,,dummx,dummy,0       !Keypoint #23
K,,oD_tube/2-t_cA_tube,dummy,0 !Keypoint #24
K,,oD_tube/2-t_cA_tube/2,dummy,0 !Keypoint #25
K,,oD_tube/2,dummy,0   !Keypoint #26
C***
C*** AT COUPLER END
K,,iD_coupler/2,l_coupler,0 !Keypoint #27

```

```

dummy=id_coupler/2+t_c4_coupler
K,,dummy,l_c4_coupler,0           !Keypoint #28
dummy=dummy+t_c5_coupler
K,,dummy,l_c5_coupler,0           !Keypoint #29
dummy=dummy+t_c6_coupler
K,,dummy,l_c6_coupler,0           !Keypoint #30
C***
C*** AT TUBE END
K,,id_tube/2,l_tube,0             !Keypoint #31
K,,id_tube/2+t_c1_tube,l_tube,0   !Keypoint #32
dummy=id_tube/2+t_c1_tube
dummy=dummy+t_c2_tube
K,,dummy,l_tube,0                 !Keypoint #33
K,,oD_tube/2-t_cA_tube,l_tube,0   !Keypoint #34
K,,oD_tube/2-t_cA_tube/2,l_tube,0 !Keypoint #35
K,,oD_tube/2,l_tube,0             !Keypoint #36
C*****
C*** DEFINE AREAS
C***
A,1,11,12,2                       !*Section (A) Cylinder#1 (area1)
A,2,12,13,3                       !*Section (A) Cylinder#2 (area2)
A,3,13,14,4                       !*Section (A) Cylinder#3 (area3)
A,4,14,15,5                       !*Section (A) Cylinder#A (area4)
A,5,15,16,6                       !*Section (A) Cylinder#A (area5)
A,6,16,17,7                       !*Section (A) Adhesive Layer (area6)
A,7,17,18,8                       !*Section (A) Cylinder#4 (area7)
A,8,18,19,9                       !*Section (A) Cylinder#5 (area8)
A,9,19,20,10                      !*Section (A) Cylinder#6 (area9)
A,11,21,22,12                    !*Section (C) Cylinder#1 (area10)
A,12,22,23,13                    !*Section (C) Cylinder#2 (area11)
A,13,23,24,14                    !*Section (C) Cylinder#3 (area12)
A,14,24,25,15                    !*Section (C) Cylinder#A (area13)
A,15,25,26,16                    !*Section (C) Cylinder#A (area14)
A,16,26,27,17                    !*Section (C) Adhesive Layer
    (area15)
A,17,27,28,18                    !*Section (C) Cylinder#4 (area16)
A,18,28,29,19                    !*Section (C) Cylinder#5 (area17)
A,19,29,30,20                    !*Section (C) Cylinder#6 (area18)
A,21,31,32,22                    !*Section (B) Cylinder#1 (area19)
A,22,32,33,23                    !*Section (B) Cylinder#2 (area20)
A,23,33,34,24                    !*Section (B) Cylinder#3 (area21)
A,24,34,35,25                    !*Section (B) Cylinder#A (area22)
A,25,35,36,26                    !*Section (B) Cylinder#A (area23)
C***
C*** Generation of arc-shaped adhesive fillet
ADELE,15                          !*Delete area adhesive layer
dummy=id_coupler/2+(l_tube_section-l_coupler)/TAN(gamma_taper)
K,,dummy,l_tube_section,0         !*Keypoint #37, origin of arc
r=dummy-oD_tube/2                 !*Radius of arc-shaped adhesive
    fillet
LARC,26,27,37,r                   !*Draw arc-shaped adhesive fillet
AL,39,17,41,59                    !*Adhesive Layer w/ arc-shaped
    fillet
C*****
C*** MESHING

```

```

C***
MSHAPE,,2D
C***
C***Define Element Sizes
ASEL,S,AREA,,1,14           !*Element size in coupler vicinity
ASEL,A,AREA,,16,18
AESIZE,ALL,esize2
ASEL,S,AREA,,19,23         !*Element size in pure tube area
AESIZE,ALL,esize3
LSEL,S,LINE,,30           !*Element size at coupler end
LSEL,A,LINE,,32
LSEL,A,LINE,,34
LSEL,A,LINE,,42
LSEL,A,LINE,,44
LSEL,A,LINE,,46
LESIZE,ALL,,,2
LSEL,S,LINE,,59
LESIZE,ALL,,,12
dummy=l_c6_coupler-0.001
KSEL,S,LOC,Y,dummy
KESIZE,ALL,esize1
KSEL,S,KP,,21,30
KESIZE,ALL,esize1
C***
C*** Mesh entire structure
MSHKEY,1                   !*Choose mapped meshing
ASEL,S,AREA,,1,14
ASEL,A,AREA,,16,17
ASEL,A,AREA,,19,23
AMESH,ALL
MSHKEY,0                   !* Mesh adhesive layer
ASEL,S,AREA,,15
AESIZE,ALL,esize1/4
AMESH,ALL
MSHKEY,0                   !* Mesh remaining areas
ASEL,S,AREA,,18
AMESH,ALL
ASEL,S,AREA,,1,23
NROTAT,ALL
C***
C*****
C*** ATTACH ELEMENT ATTRIBUTES
C***
ASEL,S,AREA,,1             !*Tube section (A) Cylinder#1
ASEL,A,AREA,,10           !*Tube section (C) Cylinder#1
ASEL,A,AREA,,19           !*Tube section (B) Cylinder#1
ESLA,S
EMODIF,ALL,MAT,1
EMODIF,ALL,TYPE,1
EMODIF,ALL,ESYS,11
C***
ASEL,S,AREA,,2             !*Section (A) Cylinder#2
ASEL,A,AREA,,11           !*Section (C) Cylinder#2
ASEL,A,AREA,,20           !*Section (B) Cylinder#2
ESLA,S

```

```

EMODIF,ALL,MAT,1
EMODIF,ALL,TYPE,1
EMODIF,ALL,ESYS,11
C***
ASEL,S,AREA,,3                !*Section (A) Cylinder#3
ASEL,A,AREA,,12              !*Section (C) Cylinder#3
ASEL,A,AREA,,21              !*Section (B) Cylinder#3
ESLA,S
EMODIF,ALL,MAT,2
EMODIF,ALL,TYPE,1
EMODIF,ALL,ESYS,11
C***
ASEL,S,AREA,,4,5            !*Section (A) Cylinder#A
ASEL,A,AREA,,13,14          !*Section (C) Cylinder#A
ASEL,A,AREA,,22,23          !*Section (B) Cylinder#A
ESLA,S
EMODIF,ALL,MAT,4
EMODIF,ALL,TYPE,1
EMODIF,ALL,ESYS,11
C***
ASEL,S,AREA,,6                !*Section (A) Adhesive layer
ASEL,A,AREA,,15              !*Section (C) Adhesive layer
ESLA,S
EMODIF,ALL,MAT,3
EMODIF,ALL,TYPE,1
EMODIF,ALL,ESYS,11
C***
ASEL,S,AREA,,7                !*Section (A) Cylinder#4
ASEL,A,AREA,,16
ESLA,S
EMODIF,ALL,MAT,5
EMODIF,ALL,TYPE,1
EMODIF,ALL,ESYS,11
C***
ASEL,S,AREA,,8                !*Section (A) Cylinder#5
ASEL,A,AREA,,17
ESLA,S
EMODIF,ALL,MAT,6
EMODIF,ALL,TYPE,1
EMODIF,ALL,ESYS,11
C***
ASEL,S,AREA,,9                !*Section (A) Cylinder#6
ASEL,A,AREA,,18
ESLA,S
EMODIF,ALL,MAT,6
EMODIF,ALL,TYPE,1
EMODIF,ALL,ESYS,11
C*****
C***
C*** SOLUTION
C***
C*****
/SOLU
C*****
C*** APPLY DISPLACEMENT BOUNDARY CONDITIONS

```

```

C***
C*** Note: Tolerances for node selection is set to 1e-12**2
ESEL,ALL
NSEL,S,LOC,Y,0                !* Symmetry at coupler centre
dummy=iD_coupler/2+t_c4_coupler
dummy=dummy+t_c5_coupler
dummy=dummy+t_c6_coupler
NSEL,R,LOC,X,iD_tube/2,dummy
D,ALL,UY,0
dummy=oD_tube/2+1e-4          !* B.C. for grip at tube end
NSEL,S,LOC,X,oD_tube/2,dummy
dummy=l_tube-l_grip
NSEL,R,LOC,Y,dummy,l_tube
D,ALL,UX,0                    !* Simplified B.C. for grip area
C*****
C*** APPLY EXTERNAL LOADING
C***
dummy=l_tube+1e-4            !*Axial load
NSEL,S,LOC,Y,l_tube,dummy
SF,ALL,PRES,-sigma_A
dummy=iD_tube/2+1e-4        !*Internal pressure
NSEL,S,LOC,X,iD_tube/2,dummy
SF,ALL,PRES,iP
C*****
C*** DISPLAY MODEL
C***
NSEL,ALL
ESEL,ALL
/NUMBER,1                    !*Indicate materials by colour
/PNUM,MAT,1
/PSF,PRES,NORM,2,,1        !*Indicate pressure loads
/PBC,ALL,,1                !*Show all B.C.
/DSCALE,1,OFF              !*Set displacement scaling to zero
/AUTO,1                     !*Zoom model to screen
C*****
C*** SOLVE MODEL
C***
SOLVE
C*****
C*** POSTPROCESSOR
C***
C*****
/POST1
C*****
C*** PLOT RESULTS
C***
/EFACET,1
/CONTOUR,1,128,AUTO
/REP
C***GET,max_s,PLNSOL,0,MAX    !*Find max value in last contour
plot
C***GET,min_s,PLNSOL,0,MIN    !*Find min value in last contour
plot
step=(max_s-min_s)/10        !*Adjust contour colours

```

```

v1=min_s+2*step
v2=v1+2*step
v3=v2+2*step
v4=v3+step/2
v5=v4+step/2
v6=v5+step/2
v7=v6+step/2
/CVAL,1,v1,v2,v3,v4,v5,v6,v7,max_s
PLNSOL,S,1,0,1          !*Contour plot principle stress
      nodal solution
C***/REP
C*****
C*** PATH OPERATIONS
C***
C*** Note: The "PMAP,ACCURATE,MAT" command should be executed when
C*** discontinuities at material interfaces are to be shown.
/FORMAT,,,16,8,400
/OUTPUT,J00X,PTH          !Redirect output to file
C***
PATH,pipe,2,,200          !Path through pipe at centre of
      gauge section
PPATH,1,,id_tube/2,l_coupler+l_tube/2,0
PPATH,2,,od_tube/2,l_coupler+l_tube/2,0
PMAP,ACCURATE,MAT
PDEF,sigma_X,S,X,AVG
PDEF,sigma_Y,S,Y,AVG
PDEF,sigma_Z,S,Z,AVG
PDEF,sigma_XY,S,XY,AVG
PDEF,sigma_XZ,S,XZ,AVG
PDEF,sigma_YZ,S,YZ,AVG
PDEF,sigma_PR1,S,1,AVG
PDEF,sigma_EQV,S,EQV,AVG
PDEF,eps_X,EPTO,X,AVG
PDEF,eps_Y,EPTO,Y,AVG
PDEF,eps_Z,EPTO,Z,AVG
PDEF,eps_XY,EPTO,XY,AVG
PDEF,eps_XZ,EPTO,XZ,AVG
PDEF,eps_YZ,EPTO,YZ,AVG
PDEF,eps_PR1,EPTO,1,AVG
PDEF,eps_PR1,EPTO,2,AVG
PDEF,eps_PR1,EPTO,3,AVG
PDEF,eps_EQV,EPTO,EQV,AVG
PRPATH,sigma_X,sigma_Y,sigma_Z,sigma_PR1,sigma_EQV
PRPATH,eps_X,eps_Y,eps_Z,eps_XY
PRPATH,eps_PR1,eps_PR2,eps_PR3,eps_EQV
C***
FINISH

```

F.2 Fracture Analysis Model

```

C*** ANSYS FE MECHANICAL ANALYSIS OF COUPLED TUBES
C*** FRACTURE MECHANICS ANALYSIS
C*** 2-D axis-symmetrical model, midplane symmetry
C*** cylinder#1 w/ 60deg covers (=2 interwoven layers) tube structure
C*** cylinder#2 w/ 60deg covers (=2 interwoven layers) tube structure
C*** cylinder#3 w/ 30deg covers (=2 interwoven layers) tube structure
C*** cylinder#A w/ resin coat of tube structure
C*** cylinder#4 w/ 30deg covers (=2 interwoven layers) coupler
structure
C*** cylinder#5 w/ 60deg covers (=2 interwoven layers) coupler
structure
C*** cylinder#6 w/ 60deg covers (=2 interwoven layers) coupler
structure
C*** coupler structure provides for tapering
C*** 1 layer adhesive structure
C*** 1 taper for adhesive structure
C*** Material 1: orthotropic pipe material; GFRP 60 angle-ply lamina;
C*** Material 2: orthotropic pipe material; GFRP 30 angle-ply lamina;
C*** Material 3: isotropic; adhesive material;
C*** Material 4: isotropic; neat resin material;
C*** Material 5: orthotropic coupler material; GFRP 30 angle-ply
lamina;
C*** Material 6: orthotropic coupler material; GFRP 60 angle-ply
lamina;
C*** Material 7: friction coefficient for contact elements
C***
/FILENAME,JOINT_PIPE_MODEL
/TITLE,JOINT_PIPE_MODEL
/OUTPUT,JOINT_PIPE_MODEL,OUT
/UNITS,SI
C***
*AFUN,DEG
C*****
C***
C*** INPUT PARAMETERS (SI units: m,kg,s,N)
C***
C*****
C*** TUBE GEOMETRY
C***
id_tube=0.1016                !*Inside diameter of tube
l_tube=7.5*id_tube            !*Length of tube
l_grip=0.2032                 !*Length of grip section
C***
C*** CYLINDER#1
t_c1_tube=2.235e-3           !*Thickness of cylinder#1
C***
C*** CYLINDER#2
t_c2_tube=1.082e-3           !*Thickness of cylinder#2
C***
C*** CYLINDER#3

```

```

t_c3_tube=1.312e-3          !*Thickness of cylinder#3
C***
C*** CYLINDER#A
t_cA_tube=0.2e-3          !*Thickness of cylinder#A
C***
dummy=iD_tube+2*t_c1_tube
dummy=dummy+2*t_c2_tube
dummy=dummy+2*t_c3_tube
oD_tube=dummy+2*t_cA_tube  !*Outside diameter of tube
C*****
C*** ADHESIVE LAYER GEOMETRY
C***
t_adhesive=1.013e-3       !*Thickness of adhesive layer
iD_adhesive=oD_tube       !*Inside diameter of adh. layer
C*****
C*** COUPLER GEOMETRY
C***
gamma_taper=30            !*Angle of coupler tapering
iD_coupler=oD_tube+2*t_adhesive !*Inside diameter coupler
l_coupler=0.155575       !*Coupler length
C***
C*** CYLINDER#4
t_c4_coupler=1.192e-3     !*Thickness of cylinder#4
step=t_c4_coupler/TAN(gamma_taper)
l_c4_coupler=l_coupler-step !*Top length of coupler cylinder#4
C***
C*** CYLINDER#5
t_c5_coupler=0.944e-3     !*Thickness of cylinder#5
step=t_c5_coupler/TAN(gamma_taper)
l_c5_coupler=l_c4_coupler-step !*Top length of coupler cylinder#5
C***
C*** CYLINDER#6
t_c6_coupler=0.928e-3     !*Thickness of cylinder#6
step=t_c6_coupler/TAN(gamma_taper)
l_c6_coupler=l_c5_coupler-step !*Top length of coupler cylinder#6
C***
od_coupler=iD_coupler+2*t_c4_coupler !*Outside diameter coupler
od_coupler=od_coupler+2*t_c5_coupler
od_coupler=od_coupler+2*t_c6_coupler
C*****
C*** LOADS (Pa)
C***
R=0 !*Loading ratio
sigma_A=100e6             !*Axial stress in pipe
iP=sigma_A*R*(oD_tube-iD_tube)/iD_tube !*Internal pressure
C*****
C*** MESHING PARAMETERS
C***
esize1=t_adhesive/2      !*Element size at coupler end
esize2=(oD_tube-iD_tube)/5 !*Element size in coupler area
esize3=(oD_tube-iD_tube)/5 !*Element size in bare tube area
      (PLANE42)
C*****
C*** FRACTURE ANALYSIS PARAMETERS
C***

```



```

a=l_coupler/2                !*Crack length
beta_initial_fracture=10     !*Angle of crack initiation
numbercracknodes=621        !*Number of nodes along crack plane
C*****
C*** DISPLAY PARAMETERS FOR PLOTTING RESULTS
C***
max_s=0
min_s=0
C*****
C***
C*** PREPROCESSOR
C***
C*****
/PREP7
C*****
C*** DEFINE COORDINATE SYSTEM / ELEMENT ORIENTATION
C***
C*** 2-Model with Cartesian C.S.
C*** X, Y, Z refer to Radial (R), Axial(Z), Hoop(THETA) directions.
C***
CSYS,1
LOCAL,11,0
ESYS,11
C*****
C*** DEFINE ELEMENT TYPES
C***
ET,1,PLANE82                !*Elements for solid body
KEYOPT,1,3,1                !*Axisymmetric analysis
KEYOPT,1,5,0
KEYOPT,1,6,0
C*****
C*** DEFINE REAL CONSTANTS
C***
C*****
C*** DEFINE MATERIAL CONSTANTS
C***
C*** MATERIAL #1
MP,EX,1,15.288E09
MP,EY,1,13.067E09
MP,EZ,1,26.870E09
MP,GXY,1,5.757E09
MP,GYZ,1,12.117E09
MP,GXZ,1,4.999E09
MP,NUXY,1,0.176
MP,NUXZ,1,0.137
MP,NUYZ,1,0.697
C***
C*** MATERIAL #2
MP,EX,2,15.288E09
MP,EY,2,26.870E09
MP,EZ,2,13.067E09
MP,GXY,2,4.999E09
MP,GYZ,2,12.117E09
MP,GXZ,2,5.757E09
MP,NUXY,2,0.137

```

```

MP,NUXZ,2,0.176
MP,NUYZ,2,0.339
C***
C*** MATERIAL #3
MP,EX,3,4.8E09
MP,EY,3,4.8E09
MP,EZ,3,4.8E09
MP,GXY,3,1.8E09
MP,GYZ,3,1.8E09
MP,GXZ,3,1.8E09
MP,PRXY,3,0.34
MP,PRXZ,3,0.34
MP,PRYZ,3,0.34
C***
C*** MATERIAL #4
MP,EX,4,3.4E09
MP,EY,4,3.4E09
MP,EZ,4,3.4E09
MP,GXY,4,1.2E09
MP,GYZ,4,1.2E09
MP,GXZ,4,1.2E09
MP,PRXY,4,0.42
MP,PRXZ,4,0.42
MP,PRYZ,4,0.42
C***
C*** MATERIAL #5
MP,EX,5,16.648E09
MP,EY,5,29.075E09
MP,EZ,5,14.551E09
MP,GXY,5,5.636E09
MP,GYZ,5,12.898E09
MP,GXZ,5,6.375E09
MP,NUXY,5,0.143
MP,NUXZ,5,0.171
MP,NUYZ,5,0.332
C***
C*** MATERIAL #6
MP,EX,6,16.648E09
MP,EY,6,14.551E09
MP,EZ,6,29.075E09
MP,GXY,6,6.375E09
MP,GYZ,6,12.898E09
MP,GXZ,6,5.636E09
MP,NUXY,6,0.171
MP,NUXZ,6,0.143
MP,NUYZ,6,0.693
C*****
C*** DEFINE KEYPOINTS
C***
C*** AT ORIGIN (ZERO X)
K,,iD_tube/2,0,0           !Keypoint #1
K,,iD_tube/2+t_c1_tube,0,0 !Keypoint #2
dummy=iD_tube/2+t_c1_tube
dummy=dummy+t_c2_tube
K,,dummy,0,0             !Keypoint #3

```

```

K,,oD_tube/2-t_cA_tube,0,0      !Keypoint #4
K,,oD_tube/2-t_cA_tube/2,0,0    !Keypoint #5
K,,oD_tube/2,0,0                !Keypoint #6
K,,iD_coupler/2,0,0             !Keypoint #7
K,,iD_coupler/2+t_c4_coupler,0,0 !Keypoint #8
dummy=iD_coupler/2+t_c4_coupler
dummy=dummy+t_c5_coupler
K,,dummy,0,0                    !Keypoint #9
K,,oD_coupler/2,0,0             !Keypoint #10
C***
C*** AT CRACK SECTION
dummy=-TAN(beta_initial_fracture)
dummy=dummy*(t_adhesive+t_cA_tube/2)
dummy=dummy+l_coupler-a
K,,iD_tube/2,dummy,0            !Keypoint #11
K,,iD_tube/2+t_c1_tube,dummy,0  !Keypoint #12
dummx=iD_tube/2+t_c1_tube
dummx=dummx+t_c2_tube
K,,dummx,dummy,0               !Keypoint #13
K,,oD_tube/2-t_cA_tube,dummy,0  !Keypoint #14
K,,oD_tube/2-t_cA_tube/2,dummy,0 !Keypoint #15
K,,oD_tube/2,dummy,0           !Keypoint #16
K,,iD_coupler/2,dummy,0        !Keypoint #17
K,,iD_coupler/2+t_c4_coupler,dummy,0 !Keypoint #18
dummx=iD_coupler/2+t_c4_coupler
dummx=dummx+t_c5_coupler
K,,dummx,dummy,0               !Keypoint #19
K,,oD_coupler/2,dummy,0        !Keypoint #20
C***
C*** AT TUBE SECTION
dummy=-TAN(beta_initial_fracture)
dummy=dummy*(oD_tube/2+t_adhesive-iD_tube/2)
dummy=dummy+l_coupler
K,,iD_tube/2,dummy,0            !Keypoint #21
dummy=-TAN(beta_initial_fracture)
dummy=dummy*(oD_tube/2+t_adhesive-iD_tube/2-t_c1_tube)
dummy=dummy+l_coupler
K,,iD_tube/2+t_c1_tube,dummy,0  !Keypoint #22
dummx=iD_tube/2+t_c1_tube
dummx=dummx+t_c2_tube
dummy=-TAN(beta_initial_fracture)
dummy=dummy*(oD_tube/2+t_adhesive-iD_tube/2-t_c1_tube-t_c2_tube)
dummy=dummy+l_coupler
K,,dummx,dummy,0               !Keypoint #23
dummy=-TAN(beta_initial_fracture)
dummy=dummy*(t_adhesive+t_cA_tube)
dummy=dummy+l_coupler
K,,oD_tube/2-t_cA_tube,dummy,0  !Keypoint #24
dummy=-TAN(beta_initial_fracture)
dummy=dummy*(t_adhesive+t_cA_tube/2)
dummy=dummy+l_coupler
K,,oD_tube/2-t_cA_tube/2,dummy,0 !Keypoint #25
K,251,oD_tube/2-t_cA_tube/2,dummy,0 !Keypoint #25_1
dummy=-TAN(beta_initial_fracture)
dummy=dummy*(t_adhesive)

```

```

dummy=dummy+l_coupler
K,,oD_tube/2,dummy,0          !Keypoint #26
K,261,oD_tube/2,dummy,0      !Keypoint #26_1
C***
C*** AT COUPLER END
K,,iD_coupler/2,l_coupler,0   !Keypoint #27
dummy=iD_coupler/2+t_c4_coupler
K,,dummy,l_c4_coupler,0      !Keypoint #28
dummy=dummy+t_c5_coupler
K,,dummy,l_c5_coupler,0      !Keypoint #29
dummy=dummy+t_c6_coupler
K,,dummy,l_c6_coupler,0      !Keypoint #30
C***
C*** AT TUBE END
K,,iD_tube/2,l_tube,0         !Keypoint #31
K,,iD_tube/2+t_c1_tube,l_tube,0 !Keypoint #32
dummy=iD_tube/2+t_c1_tube
dummy=dummy+t_c2_tube
K,,dummy,l_tube,0            !Keypoint #33
K,,oD_tube/2-t_cA_tube,l_tube,0 !Keypoint #34
K,,oD_tube/2-t_cA_tube/2,l_tube,0 !Keypoint #35
K,,oD_tube/2,l_tube,0        !Keypoint #36
C*****
C*** DEFINE AREAS
C***
A,1,11,12,2                   !*Section (A) Cylinder#1 (area1)
A,2,12,13,3                   !*Section (A) Cylinder#2 (area2)
A,3,13,14,4                   !*Section (A) Cylinder#3 (area3)
A,4,14,15,5                   !*Section (A) Cylinder#A (area4)
A,5,15,16,6                   !*Section (A) Cylinder#A (area5)
A,6,16,17,7                   !*Section (A) Adhesive Layer (area6)
A,7,17,18,8                   !*Section (A) Cylinder#4 (area7)
A,8,18,19,9                   !*Section (A) Cylinder#5 (area8)
A,9,19,20,10                  !*Section (A) Cylinder#6 (area9)
A,11,21,22,12                 !*Section (C) Cylinder#1 (area10)
A,12,22,23,13                 !*Section (C) Cylinder#2 (area11)
A,13,23,24,14                 !*Section (C) Cylinder#3 (area12)
A,14,24,25,15                 !*Section (C) Cylinder#A (area13)
A,15,25,26,16                 !*Section (C) Cylinder#A (area14)
A,16,26,27,17                 !*Section (C) Adhesive Layer
                               (area15)
A,17,27,28,18                 !*Section (C) Cylinder#4 (area16)
A,18,28,29,19                 !*Section (C) Cylinder#5 (area17)
A,19,29,30,20                 !*Section (C) Cylinder#6 (area18)
A,21,31,32,22                 !*Section (B) Cylinder#1 (area19)
A,22,32,33,23                 !*Section (B) Cylinder#2 (area20)
A,23,33,34,24                 !*Section (B) Cylinder#3 (area21)
A,24,34,35,25                 !*Section (B) Cylinder#A (area22)
A,25,35,36,26                 !*Section (B) Cylinder#A (area23)
C*****
C*** MESHING
C***
C*** DEFINE NODES AT CRACK PLANE
MSHAPE,0,2D

```

```

/INPUT,JFrac002_1mm,txt,,5      !*Read crack plane corner nodes from
      file
C***                             !*(These nodes are numbered
C*** !*consecutively starting with 1)
C***
C***Define Element Sizes
ASEL,S,AREA,,1,18                !*Element size in coupler vicinity
AESIZE,ALL,esize2
ASEL,S,AREA,,19,23                !*Element size in pure tube area
AESIZE,ALL,esize3
LSEL,S,LINE,,30,34,2             !*Element size at coupler end
LSEL,S,LINE,,43,47,2
LESIZE,ALL,,,2
LSEL,S,LINE,,36,39,3
LSEL,A,LINE,,60
LESIZE,ALL,,,1
LSEL,S,LINE,,41
LESIZE,ALL,,,3
KSEL,S,KP,,11,30
KSEL,A,KP,,251
KSEL,A,KP,,261
KESIZE,ALL,esize1
C***
C*** Mesh entire structure
MSHKEY,1                          !*Choose mapped meshing
NUMSTR,NODE,1001                  !*Offset consecutive node numbers
NUMSTR,ELEM,1001                  !*Offset consecutive element numbers
ASEL,S,AREA,,13
AMESH,ALL
NUMSTR,NODE,2001                  !*Offset consecutive node numbers
NUMSTR,ELEM,2001                  !*Offset consecutive element numbers
ASEL,S,AREA,,14
AMESH,ALL
NUMSTR,NODE,3001                  !*Offset consecutive node numbers
NUMSTR,ELEM,3001                  !*Offset consecutive element numbers
ASEL,S,AREA,,1,12
ASEL,A,AREA,,15,23
AMESH,ALL
ASEL,S,AREA,,1,23
NROTAT,ALL
C***
C*** Couple DOF at crack plane nodes
C***                             !*(These node pairs will be
C*** !*used to grow the crack)
LSEL,S,LINE,,37,39
LSEL,A,LINE,,60
NSLL,S,1
NWRITE,JFrac,Node                !*Write crack plane corner nodes to
      file
C*** !*initially reorder and renumber crack
C*** !*plane nodes using external software)
*DO,i,5,numbercracknodes-2,2     !*Do-loop to couple DOF
NSEL,S,NODE,,i,i+1
CP,i,ALL,ALL
C***NUMSTR,ELEM,20001            !*Offset consecutive element numbers

```

```

*ENDDO
C***
C*** Merge coinciding nodes of upper and lower crack plane
C***                                     !*(Note that nodes from FE mesh
C*** !*are not associated with the
C*** !*initially placed nodes yet)
LSEL,S,LINE,,37                               !*Merge nodes on lower plane
NSLL,S,1
NSEL,A,NODE,,5,numbercracknodes-2,2
NUMMRG,NODE,1e-6,,,LOW
LSEL,S,LINE,,38                               !*Merge nodes on upper plane
NSLL,S,1
NSEL,A,NODE,,6,numbercracknodes-1,2
NUMMRG,NODE,1e-6,,,LOW
C***
C*****
C*** ATTACH ELEMENT ATTRIBUTES
C***
ASEL,S,AREA,,1                               !*Tube section (A) Cylinder#1
ASEL,A,AREA,,10                              !*Tube section (C) Cylinder#1
ASEL,A,AREA,,19                              !*Tube section (B) Cylinder#1
ESLA,S
EMODIF,ALL,MAT,1
EMODIF,ALL,TYPE,1
EMODIF,ALL,ESYS,11
C***
ASEL,S,AREA,,2                               !*Section (A) Cylinder#2
ASEL,A,AREA,,11                              !*Section (C) Cylinder#2
ASEL,A,AREA,,20                              !*Section (B) Cylinder#2
ESLA,S
EMODIF,ALL,MAT,1
EMODIF,ALL,TYPE,1
EMODIF,ALL,ESYS,11
C***
ASEL,S,AREA,,3                               !*Section (A) Cylinder#3
ASEL,A,AREA,,12                              !*Section (C) Cylinder#3
ASEL,A,AREA,,21                              !*Section (B) Cylinder#3
ESLA,S
EMODIF,ALL,MAT,2
EMODIF,ALL,TYPE,1
EMODIF,ALL,ESYS,11
C***
ASEL,S,AREA,,4,5                             !*Section (A) Cylinder#A
ASEL,A,AREA,,13,14                          !*Section (C) Cylinder#A
ASEL,A,AREA,,22,23                          !*Section (B) Cylinder#A
ESLA,S
EMODIF,ALL,MAT,4
EMODIF,ALL,TYPE,1
EMODIF,ALL,ESYS,11
C***
ASEL,S,AREA,,6                               !*Section (A) Adhesive layer
ASEL,A,AREA,,15                              !*Section (C) Adhesive layer
ESLA,S
EMODIF,ALL,MAT,3
EMODIF,ALL,TYPE,1

```

```

EMODIF,ALL,ESYS,11
C***
ASEL,S,AREA,,7                !*Section (A) Cylinder#4
ASEL,A,AREA,,16
ESLA,S
EMODIF,ALL,MAT,5
EMODIF,ALL,TYPE,1
EMODIF,ALL,ESYS,11
C***
ASEL,S,AREA,,8                !*Section (A) Cylinder#5
ASEL,A,AREA,,17
ESLA,S
EMODIF,ALL,MAT,6
EMODIF,ALL,TYPE,1
EMODIF,ALL,ESYS,11
C***
ASEL,S,AREA,,9                !*Section (A) Cylinder#6
ASEL,A,AREA,,18
ESLA,S
EMODIF,ALL,MAT,6
EMODIF,ALL,TYPE,1
EMODIF,ALL,ESYS,11
C*****
C***
C*** SOLUTION
C***
C*****
/SOLU
C*****
C*** APPLY DISPLACEMENT BOUNDARY CONDITIONS
C***
C*** Note: Tolerances for node selection is set to 1e-12**2
ESEL,ALL
NSEL,S,LOC,Y,0                !* Symmetry at coupler centre
dummy=iD_coupler/2+t_c4_coupler
dummy=dummy+t_c5_coupler
dummy=dummy+t_c6_coupler
NSEL,R,LOC,X,iD_tube/2,dummy
D,ALL,UY,0
dummy=oD_tube/2+1e-4          !* B.C. for grip at tube end
NSEL,S,LOC,X,oD_tube/2,dummy
dummy=l_tube-l_grip
NSEL,R,LOC,Y,dummy,l_tube
D,ALL,UX,0                    !* Simplified B.C. for grip area
C*****
C*** APPLY EXTERNAL LOADING
C***
dummy=l_tube+1e-4             !*Axial load
NSEL,S,LOC,Y,l_tube,dummy
SF,ALL,PRES,-sigma_A
C*** dummy=iD_tube/2+1e-4     !*Internal pressure
C*** NSEL,S,LOC,X,iD_tube/2,dummy
C*** SF,ALL,PRES,iP
C*****
C*** SOLVE MODEL AND OUTPUT NODAL DATA

```

```

C***
C*** Solve for first step of crack propagation
NSEL,ALL
ESEL,ALL
ANTYPE,STATIC,NEW
SOLVE
/POST1
NSEL,S,NODE,,5,8
/FORMAT,,16,8,400
/OUTPUT,JFrac,solF
PRNLD,F
/FORMAT,,16,8,400
/OUTPUT,JFrac,solU
PRNSOL,U,COMP
/OUTPUT
C***
C*** Solve for consecutive steps of crack propagation - small steps
*DO,i,9,41,8                !*Do-loop to release coupled crack
    plane nodes
NSEL,ALL
ESEL,ALL
/SOLU
CPDELE,i-8,i-1,,ANY
ANTYPE,STATIC,NEW
SOLVE
/POST1
NSEL,S,NODE,,i-4,i+3
/OUTPUT,JFrac,solF,,APPEND
PRNLD,F                    !*Note that nodal forces are on a
    360deg basis.
/OUTPUT
/OUTPUT,JFrac,solU,,APPEND
PRNSOL,U,COMP
/OUTPUT
*ENDDO
C***
C*** Solve for consecutive steps of crack propagation - large steps
*DO,i,57,(numbercracknodes-16),16 !*Do-loop to release coupled crack
    plane nodes
NSEL,ALL
ESEL,ALL
/SOLU
CPDELE,i-16,i-1,,ANY
ANTYPE,STATIC,NEW
SOLVE
/POST1
NSEL,S,NODE,,i-4,i+3
/OUTPUT,JFrac,solF,,APPEND
PRNLD,F                    !*Note that nodal forces are on a
    360deg basis.
/OUTPUT
/OUTPUT,JFrac,solU,,APPEND
PRNSOL,U,COMP
/OUTPUT
*ENDDO

```